Acoustical Physics, Vol. 51, No. 3, 2005, pp. 239–245. Translated from Akusticheskiĭ Zhurnal, Vol. 51, No. 3, 2005, pp. 293–300.

Comparison of the Efficiencies of Fourier and Wavelet Expansions in Passive Acoustic Thermal Tomography

K. M. Bograchev

ELDIS Research Center, Institute of Radio Engineering and Electronics, Russian Academy of Sciences, Starosadskii per. 8, Moscow, 101000 Russia

e-mail: homeinternet@eircom.net

Received December 30, 2003

Abstract—A comparison of the accuracy achieved in temperature-distribution reconstruction by the Fourier and wavelet expansions in passive acoustic tomography is carried out. Since the use of focused ultrasound in hyperthermia leads to local heating of the tissue, the wavelet representation of such temperature distributions with local fluctuations is more compact than their Fourier representation. It is demonstrated that the compactness of the wavelet representation provides an opportunity to reduce considerably the number of unknown quantities in solving the inverse problem of acoustic thermal tomography and to increase the accuracy of the temperature-distribution reconstruction in comparison with the case of using the Fourier representation. A method for choosing a compact wavelet basis for temperature distributions obtained in the hyperthermia process is proposed. © *2005 Pleiades Publishing, Inc.*

Temperature within a human body is an important characteristic. Measuring and monitoring this temperature is especially important in medicine, in particular, in cases of hyperthermia in oncology, hypothermia, and ultrasonic surgery. To measure the in-depth temperature, it is possible to use the information carried by thermal acoustic radiation in the megahertz frequency range that comes from a depth of 2–10 cm under the surface of the body, depending on the frequency of the received radiation [1]. On the basis of a set of measurements of thermal acoustic radiation by piezoelectric transducers positioned on the surface of the body, it is possible to reconstruct the spatial distribution of the in-depth temperature, i.e., to implement thermal acoustic tomography. In our previous studies [2–6], we evaluated the quality of a 2D reconstruction of the temperature distribution by the method of thermal acoustic tomography using a computer simulation. Since the purpose was to monitor the temperature within a human body in the hyperthermia process, the actual temperature distribution was assumed to be typical of such a process, namely, to be in the form of a locally heated region with temperature decreasing away from the center of heating in such way that the typical temperature distribution had the form of a peak.

The problem was formulated as follows: in the process of simulation, we assumed that measurements of the acoustic brightness temperature (directly proportional to the intensity of the received thermal acoustic radiation) were performed by piezoelectric transducers on the surface of the body (Fig. 1). In this case, the temperature distribution within a square area of 10×10 cm^2 was reconstructed. This area was covered by a grid dividing the area into $15 \times 15 = 225$ subareas. In fact, this study considered the reconstruction of the temperature values (Fig. 2a) at the corresponding 225 nodes of the grid (the number of unknowns was equal to 225).

To ensure the smoothness of the reconstructed temperature distribution, we assumed this distribution to be equal to a finite sum of harmonic functions. In the case of such a distribution, the 2D Fourier spectrum contains $15 \times 15 = 225$ unknown components. Therefore, an intermediate stage existed in the algorithm; i.e., the values of these 225 components were assumed to be the unknowns in a system of linear equations. To represent the problem in the form of a system of linear equations, these components were extended into a one-dimensional vector of 225 elements [5]. After their determination, we performed the inverse procedure of constructing the 2D Fourier spectrum from the vector. After that, the inverse Fourier transformation was performed and a reconstructed two-dimensional temperature distribution was obtained (Fig. 2b).

We assumed that the coefficient of ultrasound absorption γ does not depend on the coordinate and the frequency in the reception band of piezoelectric transducers and that the spread function of a piezoelectric transducer can be approximated as a beam l (this is admissible in the case of the use of focused piezoelectric transducers). In each measurement (or scan), the value of the acoustic temperature is represented by an integral, to which all points of the studied region that lie on the beam contribute:

$$T_A = \gamma \int_0^\infty T(l) \exp(-\gamma l)\, dl, \qquad (1)$$

1063-7710/05/5103-0239$26.00

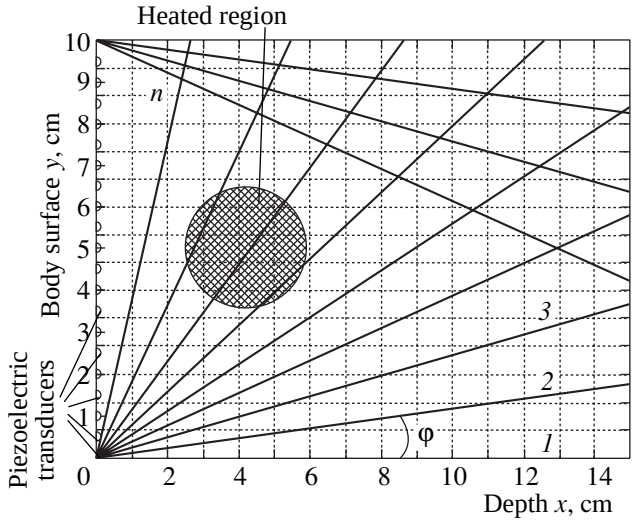

Fig. 1. Scheme of scanning for the region under investigation L with the dimensions 10×10 cm^2 in the (x, y) plane. The x coordinate is directed inside the body (the coordinate $x = 0$ is at the body surface), and the y coordinate is oriented along the body surface. The region L is divided into N_x points along the x axis and N_y points along the y axis (the division is shown by the thin dashed lines of the grid). Temperature readings in the medium were taken at $N_H = N_x N_y$ points. Half-circles denote piezoelectric transducers, and numbers 1, 2, 3, …, n are the numbers of the transducer scanning angles measured with respect to the x axis. At $0 \le y < 5$ cm, the rotation angle is $\alpha = 0°$–$80°$ (where α is measured counter clockwise); at $5 < y \le 10$ cm, $\alpha = -80°$ to $0°$; and at $y = 5$ cm, $\alpha = -80°$ to $80°$; $N_x = N_y = 15$.

where l is the coordinate along the acoustic axis of the piezoelectric transducer (the point $l = 0$ coincides with the transducer position), $T(l)$ is the temperature distribution along the acoustic axis of the piezoelectric transducer, and the factor $\exp(-\gamma l)$ determines the absorption of an acoustic wave in the process of its propagation from the source (located at the point l on the acoustic axis of the transducer) to the piezoelectric transducer.

In the Fourier analysis, the 2D distribution of thermodynamic temperature $T(x, y)$ is expanded in harmonics $f_1(x, y), \ldots, f_n(x, y)$, where $n = 1, \ldots, N_{\max}$, in such a way that

$$T(x, y) = \sum_{n=1}^{N_f} k_n^f f_n(x, y), \tag{2}$$

where $f_n(x, y)$ are the harmonic functions of the Fourier expansion and k_n^f are the corresponding expansion coefficients. Substituting Eq. (2) into Eq. (1), we obtain a formula describing the contribution of each harmonic to the acoustic temperature measured for a given scan:

$$T_A = \gamma \sum_{n=1}^{N_f} k_n^f \int_0^\infty f_n^{sc}(l) \exp(-\gamma l) dl. \tag{3}$$

Here, $f_n^{sc}(l)$ is the value of the function $f_n(x, y)$ at the point lying on the acoustic axis of the piezoelectric transducer at the distance l from the transducer. As experiments demonstrated, the acoustic temperature can be measured with a certain error (noise) with an average value of ~0.1 K. Taking into account this noise, Eq. (3) takes on the form

$$T_A^e = \gamma \sum_{n=1}^{N_f} k_n^f \int_0^\infty f_n^{sc}(l) \exp(-\gamma l) dl, \tag{4}$$

where T_A^e is the value of the acoustic temperature with allowance for the measurement noise. Applying Eq. (4) to all scans (numbers $i = 1, \ldots, N_s$), we obtain a system of linear equations, where the unknowns are the components of the Fourier spectrum of the peak under reconstruction:

$$\begin{cases} T_{A1}^e = \gamma \sum_{n=1}^{N_f} k_n^f \int_0^\infty f_{n1}^{sc}(l) \exp(-\gamma l) dl, \\ \ldots \\ T_{Ai}^e = \gamma \sum_{n=1}^{N_f} k_n^f \int_0^\infty f_{ni}^{sc}(l) \exp(-\gamma l) dl. \\ \ldots \end{cases} \tag{5}$$

Here, T_{Ai}^e is the value of the acoustic temperature measured experimentally for the ith scan. We assumed the number of acoustic temperature measurements (i.e., equations) to be equal to $N_s = 253$, which is somewhat greater than the number of unknowns (225).

The problem of solving system of Eqs. (5), i.e., the inverse problem of thermoacoustic tomography, is ill-defined because of the presence of noise in the measurements, and it is necessary to use Tikhonov's regularization method to solve it. As was demonstrated in [2–5], this method provides an opportunity to solve the inverse problem and reconstruct the 2D temperature distribution. The modification known as local regularization is especially efficient in this case (Fig. 2b). The local regularization takes into account the thermophysical properties of the tissue and the presence of blood flow. This modification is used if, in solving the inverse problem, the coefficients of the 2D Fourier expansion of the desired temperature distribution are unknown. The local regularization consists in that, in the process of solving a set of equations, the value of the regularizing parameter depends on the coefficient number. The temperature distribution reconstructed by this method is sufficiently close to the actual one (Fig. 2b). However, a systematic error introduced by the regularization exists. This systematic error leads to the fact that the recon-

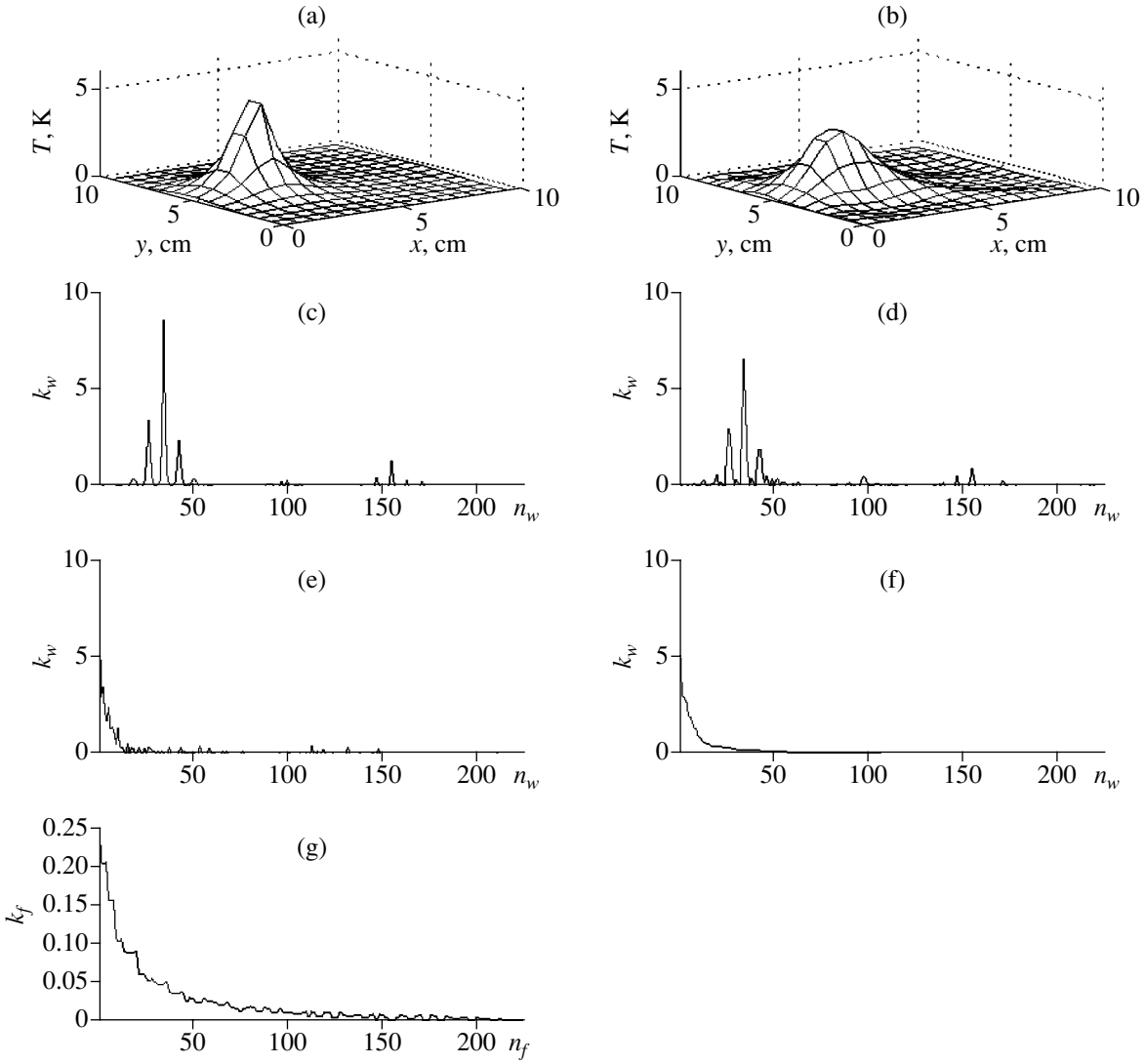

Fig. 2. An example of ordering of the wavelet expansion components: (a) the actual temperature peak; (b) the temperature peak reconstructed by the method of Tikhonov's local regularization; (c) the wavelet expansion of the actual peak (a); (d) the wavelet expansion of the reconstructed peak (b); (f) the wavelet expansion of the reconstructed peak ordered in decreasing order (b); (e) the wavelet expansion of peak (a) that is resorted in the same way as wavelet expansion (f); and (g) the Fourier spectrum of peak (a) that is presented in the form of a one-dimensional vector. In all images of wavelet expansions, the first 225 (of 256) components are shown (wavelet expansions differ from wavelet spectra by a possible change in the order of components). In all images of wavelet and Fourier expansions, the ordinate axis represents the absolute values of components.

structed distribution is distorted in comparison with the actual one. In particular, the reconstructed peak is lower and wider than the actual peak. This is caused by the fact that, the greater the harmonic number is, the stronger the regularization process underestimates the values of the Fourier spectrum. This effect is especially important in the case when the center of the heated region is located far from the body surface. In this case, as one can see from Fig. 2g, the spectrum of a typical temperature peak is sufficiently wide and contains many high-frequency components. Underestimating these components due to the regularization produces considerable distortion of the peak in the course of the reconstruction.

The Fourier transformation is a representation of a function in the form of a sum of harmonics, i.e., periodic functions. It is clear that this technique is most convenient for representation of the functions that are periodic themselves. The Fourier spectrum of such functions looks most compact. In this case, the Fourier spectrum of an explicitly local function, like the local temperature peak under reconstruction, will be sufficiently wide.

It was demonstrated earlier [7] that taking into account the physical features of the process provides an opportunity to use a wavelet expansion, for example, to reduce noise in the measured signal.

The temperature peak obtained in the hyperthermia process is an explicitly local function. Taking into account this feature of the function under reconstruction, an expansion in basic functions, which are local themselves, i.e., wavelets, must be convenient for such a peak.

In the wavelet analysis, an expansion of the form

$$T(x, y) = \sum_{\mathbf{k} \in \mathbf{Z}^2} w^{i_0}_{m,\mathbf{k}} \varphi^{i_0}_{m,\mathbf{k}}(x, y) + \sum_{i=i_0}^{\infty} \sum_{m=1}^{2} \sum_{\mathbf{k} \in \mathbf{Z}^2} n^i_{m,\mathbf{k}} \psi^i_{m,\mathbf{k}}(x, y), \; i_0 \in \mathbf{Z},$$

is performed [8], where $\varphi^{i_0}_{m,\mathbf{k}}$ is the scaling function, $\psi^i_{m,\mathbf{k}}$ is the wavelet function, $w^{i_0}_{m,\mathbf{k}}$, $n^i_{m,\mathbf{k}}$ are the expansion coefficients corresponding to these functions and $\mathbf{Z}$ is a set of integers. If we take into account that we look for the values of the function $T(x, y)$ only at the grid nodes, i.e., a discrete wavelet transformation is implemented, we obtain that the expansion given by Eq. (6) has a finite number of terms, which is close to the number of the grid nodes, and it can be represented in the form

$$T(x, y) = \sum_c w_c \varphi_c(x, y) + \sum_d n_d \psi_d(x, y). \qquad (6)$$

Substituting Eq. (6) into Eq. (1), we obtain a formula describing the contribution of each wavelet component to the acoustic temperature measured for a given scan:

$$T_A = \gamma \sum_c w_c \int_0^\infty \varphi^{sc}_c(l) \exp(-\gamma l) dl + \gamma \sum_d n_d \int_0^\infty \psi^{sc}_d(l) \exp(-\gamma l) dl, \qquad (7)$$

where $\varphi^{sc}_c(l)$ is the value of the function $\varphi_c(x, y)$ at the point lying on the acoustic axis of the piezoelectric transducer at the distance l from the transducer (the meaning of the notation ψ^{sc}_d is analogous). Taking into account the noise in the acoustic temperature measurements, we arrive at the expression

$$T^e_A = \gamma \sum_c w_c \int_0^\infty \varphi^{sc}_c(l) \exp(-\gamma l) dl + \gamma \sum_d n_d \int_0^\infty \psi^{sc}_d(l) \exp(-\gamma l) dl. \qquad (8)$$

For all scans, we obtain a set of linear equations, where the unknowns are the coefficients of the wavelet expansion of the temperature peak under reconstruction:

$$\begin{cases} T^e_{A1} = \gamma \sum_c w_c \int_0^\infty \varphi^{sc}_{c1}(l) \exp(-\gamma l) dl \\ \quad + \gamma \sum_d n_d \int_0^\infty \psi^{sc}_{d1}(l) \exp(-\gamma l) dl, \\ \ldots \\ T^e_{Ai} = \gamma \sum_c w_c \int_0^\infty \varphi^{sc}_{ci}(l) \exp(-\gamma l) dl \\ \quad + \gamma \sum_d n_d \int_0^\infty \psi^{sc}_{di}(l) \exp(-\gamma l) dl, \\ \ldots. \end{cases} \qquad (9)$$

In solving sets of equations (5) or (9), i.e., in solving the inverse problem of acoustic thermography, an important role is played by the number of unknowns. The wavelet transformation of the temperature peak must be supposedly more compact than its Fourier spectrum. The narrower the temperature peak, the stronger this difference must be. The compactness of the wavelet expansion provides an opportunity to reduce the number of unknowns and, in such a way, to increase the accuracy of the solution of the inverse problem of thermal acoustic tomography and to improve the quality of the temperature reconstruction. Here, we study the comparative efficiencies of the wavelet and Fourier expansions in the reconstruction of 2D temperature peaks. We have studied the expansion in only one type of wavelets (the Daubechies-2 wavelets).

Figure 2a demonstrates an actual two-dimensional temperature distribution. Its Fourier spectrum and wavelet expansion "extended into a vector" are shown in Figs. 2g and 2c, respectively. One can see that the number of significant components of the wavelet expansion is rather small, although they are scattered over the whole spectrum.

Employment of the wavelet expansion must be efficient if, in solving Eqs. (9), we assume the unknowns to be only the significant wavelet components. This provides an opportunity to reduce the number of unknowns in Eqs. (9) and, therefore, to increase the accuracy of the reconstruction. In solving the inverse problem, the regularization is efficient if the significant components are collected at the beginning of the spectrum and it is desirable for them to follow in descending order of their value, i.e., if the wavelet expansion is resorted. Since the temperature distribution under reconstruction is unknown, one does not know which of the components

of its wavelet expansion are significant; i.e., the desired order of its resorting (ordering) is unknown. However, it is possible to estimate the positions of these significant components using the temperature distribution reconstructed by the method of Tikhonov's local regularization [2–5]. Although the peak reconstructed by this method is distorted to a certain extent in comparison with the actual one, the position of its maximum approximately corresponds to the position of the maximum of the actual peak. As numerical analysis has demonstrated, there is a close similarity in the positions of the significant components in the wavelet expansion of the actual peak and the peak reconstructed by the method of Tikhonov's local regularization. Thus, a certain stability of the positions of the significant components of the wavelet expansion of the temperature peak exists with respect to the transformation of this peak, which occurs in the process of the reconstruction by the method of Tikhonov's local regularization. This provides an opportunity to use the wavelet expansion of the peak (Fig. 2b) reconstructed by the method of Tikhonov's local regularization as the reference one in the processes of resorting (ordering) of the components of the wavelet expansion of the peak under reconstruction (Fig. 2a) and the determination of the significant components of this expansion. Approximately, this means that, if only n_{comp} components with certain numbers (for example, $n_{comp} = 20$) are significant in the wavelet expansion of the peak reconstructed by the method of Tikhonov's local regularization (Fig. 2b), then, as a rule, the same n_{comp} components are significant in the wavelet expansion of the actual peak (Fig. 2a). These components can be considered to be unknowns, while the other ones can be taken equal to zero.

Thus, the algorithm of solving Eqs. (9) is as follows:

1. The reconstruction by the method of Tikhonov's local regularization is carried out (a reconstructed peak is shown in Fig. 2b).

2. Its wavelet spectrum "extended into a vector" is calculated (Fig. 2d).

3. The order of its resorting for ordering in the decreasing order of its components is determined (Fig. 2f).

4. The number of "significant" components is selected (for example, $n_{comp} = 20$, Fig. 2f).

5. Only the terms corresponding to these "significant" components are kept in the set of Eqs. (9). In this way, the number of unknowns is reduced to $n_{comp} = 20$ (instead of 225).

6. Set of Eqs. (9) is solved by the method of Tikhonov's global regularization. As a result, the values of the "significant" components of the wavelet expansion are obtained (their number is $n_{comp} = 20$). All other components are taken to be equal to zero.

7. The inverse wavelet transformation is performed, and a reconstructed temperature peak is obtained.

A detailed scheme of solving the inverse problem of acoustic thermography using such wavelet filtration is shown in Fig. 3.

The efficiency of this approach can be seen from Fig. 2e, where the wavelet expansion demonstrated in Fig. 2c is resorted (ordered); the order of resorting is determined by the wavelet expansion (Fig. 2d) of the peak reconstructed by the method of Tikhonov's local regularization. One can see that such a resorting technique provides a basic opportunity to position the wavelet components of the actual distribution in decreasing order (Fig. 2e). The Fourier spectrum of the actual peak that is extended into a vector is also shown for comparison (Fig. 2g). Its components were used as unknowns in the reconstruction by the method of Tikhonov's local regularization. One can see that the wavelet expansion (Fig. 2e) of the actual peak is much more "compact," for example, the decrease in the absolute value of the Fourier spectrum component by a factor of e occurs only at number 10, while, in the case of the wavelet expansion, it occurs already at number 2. Precisely this "compactness" provides an opportunity to increase the accuracy of solving the inverse problem.

An example of the temperature reconstruction according to this scheme (Fig. 3) is shown in Fig. 4. The parameters of the actual temperature distribution are as follows (Fig. 4a): the depth of the heat source is 2.5 cm, the lateral coordinate of the heat source is 5 cm, its characteristic width is $d = 0.4$ cm, its characteristic length (the thermophysical parameter of the tissue) is $x_D = 1$ cm, and the maximum value of the internal temperature increment is $T_{max} = 5$ K.

Convenient criteria of the reconstruction accuracy are the maximum value of the reconstructed temperature T_{max}^{REC} and the root-mean-square error of reconstruction dT_R over all 225 nodes of the grid where the temperature values were reconstructed:

$$dT_R = \sqrt{\sum_{i=1}^{225} (T(x_i, y_i) - T^{REC}(x_i, y_i))^2/225},$$

where $T(x_i, y_i)$ and $T^{REC}(x_i, y_i)$ are the values of the actual and reconstructed temperatures at the grid node of number i. One can see from Fig. 4 that the method of Tikhonov's local regularization (Fig. 4b) produces a large error for both these parameters ($T_{MAX}^{REC} = 3.46$ K and $dT_R = 0.24$ K) in comparison with the method of wavelet filtration (Fig. 4c), where $T_{MAX}^{REC} = 4.39$ K and $dT_R = 0.17$ K.

To perform the statistical analysis, the above parameters T_{MAX}^{REC} and dT_R are calculated for the actual temperature distribution (Fig. 4a) with 20 different realizations of noise in the measurements. The average values

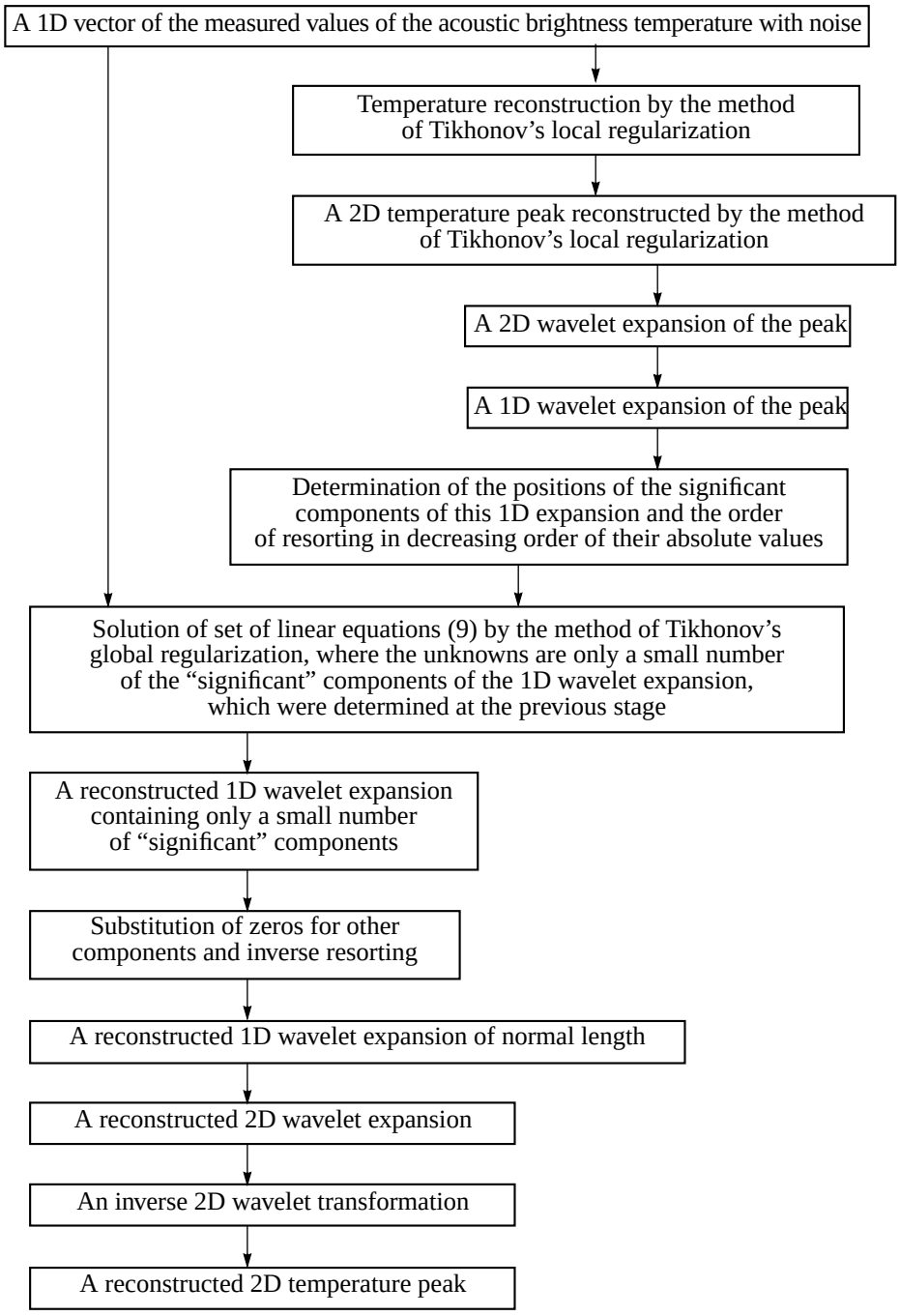

Fig. 3. Scheme of solving the inverse problem of acoustic thermography with the use of the wavelet transformation.

of these parameters are given in the table. Although the reconstruction by the method of Tikhonov's local regularization using Fourier analysis was carried out in all 20 cases, the reconstruction by the method of wavelet analysis (regularization) was impossible in ten cases (i.e., 50% of cases). Thus, the method of wavelet analysis is less stable in comparison with the method of Fourier analysis with respect to the possibility of regularization. The problem of the stability of the wavelet reconstruction and the factors that determine it need additional investigation.

One can see from the table that the use of the wavelet expansion provides an opportunity to improve the quality of the temperature distribution reconstruction according to both criteria. This comparative improvement must be more clear the narrower the peak under reconstruction is. Here, the reconstruction method

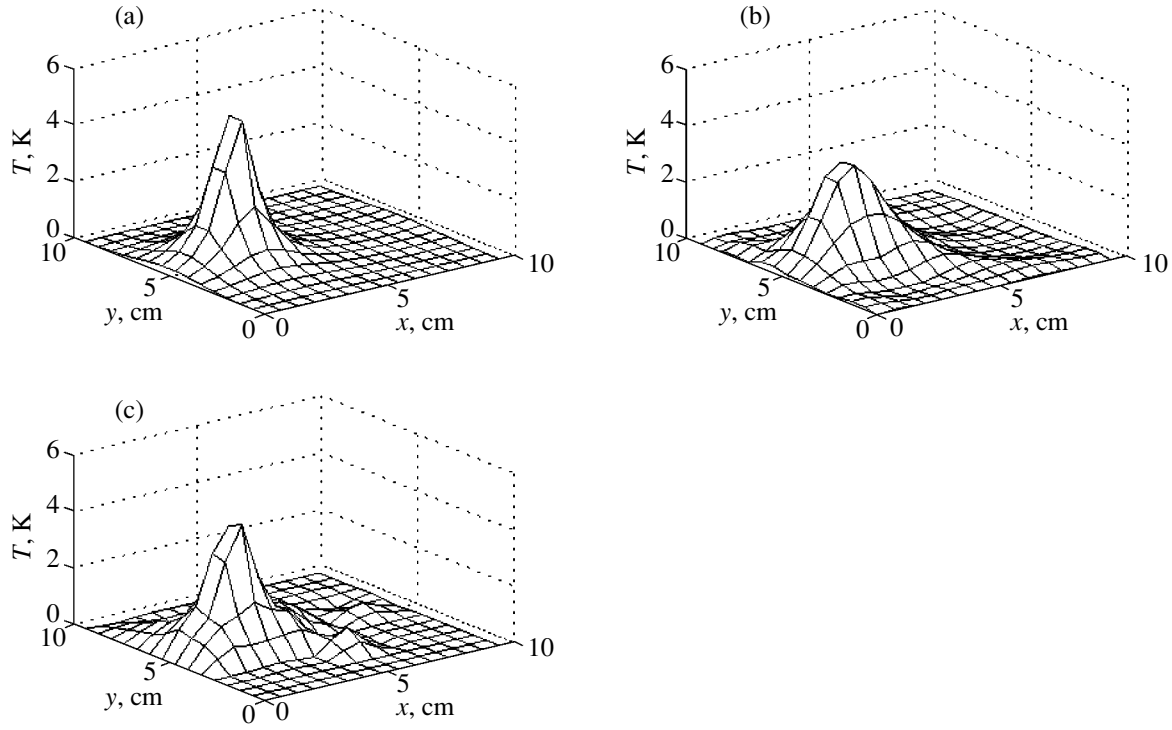

Fig. 4. An example of reconstruction of (a) an actual temperature peak by (b) the method of Tikhonov's local regularization and (c) the method of wavelet filtration. The increment of internal temperature is given along the ordinate axis.

developed earlier (the method of Tikhonov's local regularization) is used as an intermediate stage.

Thus, it has been demonstrated that the use of the wavelet expansion provides an opportunity to improve the accuracy of reconstruction of the temperature distribution within a human body in the course of hyperthermia using focused ultrasound. It was assumed that, in the focal region, the heat source has a Gaussian intensity distribution. However, the problems of the efficiency of the wavelet analysis in the case of other types of heat sources, other positions of the sources that differ from those considered here, and the problems of choosing the most efficient type of wavelet all need further investigation. The data obtained in this study allow us to expect that the use of the wavelet analysis may occupy one of the most important places among the methods of solving ill-defined inverse problems of thermal acoustic tomography.

Comparison of the average statistical accuracy of reconstructing the temperature distribution by the methods of the Fourier and wavelet expansions

Reconstruction criterion	Reconstruction by the method of Tikhonov's local regularization	Reconstruction by the method of wavelet filtrations
$\langle T_{\max}^{REC} \rangle$, K	3.3 ± 0.14	4.3 ± 0.25
$\overline{dT_R}$, K	0.26 ± 0.013	0.21 ± 0.019

ACKNOWLEDGMENTS

This work was supported by the Russian Foundation for Basic Research, project nos. 03-01-00723 and 02-02-17371.

REFERENCES

1. V. I. Passechnik, A. A. Anosov, and M. G. Isrefilov, Ultrasonics **34**, 511 (1996).
2. Yu. V. Gulyaev, K. M. Bograchev, I. P. Borovikov, *et al.*, Radiotekh. Élektron. (Moscow) **43**, 1140 (1998) [J. Commun. Technol. Electron. **43**, 1061 (1998)].
3. V. I. Pasechnik, A. A. Anosov, and K. M. Bograchev, Biomed. Radioélektron., No. 2, 3 (1999).
4. K. M. Bograchev and V. I. Pasechnik, Akust. Zh. **45**, 742 (1999) [Acoust. Phys. **45**, 667 (1999)].
5. K. M. Bograchev, Candidate's Dissertation in Physics and Mathematics (Inst. of Radio Engineering and Electronics, Russ. Acad. Sci., Moscow, 2000).
6. K. M. Bograchev and V. I. Pasechnik, Akust. Zh. **48**, 467 (2002) [Acoust. Phys. **48**, 406 (2002)].
7. M. S. Bosnyakov and Yu. V. Obukhov, Pattern Recogn. Image Anal. **13** (1), 74 (2003).
8. A. V. Pereberin, Vychisl. Metody Program. **2**, 15 (2001).

Translated by M. Lyamshev

Acoustical Physics, Vol. 51, No. 3, 2005, pp. 246–254. Translated from Akusticheskiĭ Zhurnal, Vol. 51, No. 3, 2005, pp. 301–310.

Optical Breakdown in a Liquid: The Slow Phase of the Dynamics of Cavity Collapse and a Noncontact Technique for Pressure Measurement in a Liquid

N. F. Bunkin*, A. M. Lomonosov*, G. A. Lyakhov*, N. V. Suyazov*, S. I. Bakum, and L. M. Dorozhkin****

** Wave Research Center, Prokhorov General Physics Institute, Russian Academy of Sciences, ul. Vavilova 38, Moscow, 119991 Russia*

e-mail: nbunkin@kapella.gpi.ru

*** Institute of General and Inorganic Chemistry, Russian Academy of Sciences, Leninskii pr. 31, Moscow, 117907 Russia*

Received June 17, 2004

Abstract—It is demonstrated that, in the case of optically probing the breakdown region, a pulsed signal is formed due to the acoustic pulses produced by the breakdown and collapse of the cavitation cavity. The measured dependence of the delay time of the second pulse on the hydrostatic pressure in the liquid and the pressure of saturated vapor agrees well with the theoretical dependence corresponding to the hydrodynamic model of the cavity. On the basis of the optical cavitation effect, a technique is proposed for a noncontact measurement of hydrostatic pressure in a liquid enclosed in a sealed cell. The range of applicability of the technique is evaluated. © *2005 Pleiades Publishing, Inc.*

1. INTRODUCTION

Cavitation, i.e., the formation of a vapor-gas cavity in a liquid, may occur under the effect of a sufficiently intense sound pulse [1], an electric discharge [2], an underwater explosion [3, 4], and also as a result of the optical breakdown of a liquid by a laser pulse [5–7]. In studying cavitation produced by an optical breakdown, most attention is usually given to physical phenomena accompanying the last stage of cavity collapse [8], which is characterized by high values of temperature and pressure inside the cavity and also by high velocities of the boundary motion. At the same time, the dynamics of the cavity in the slow phase of pulsation is of certain interest, which is connected, for example, with measurements of the physical parameters of a liquid. Namely, in the case of laser probing of the optical breakdown region, two pronounced pulses are observed in the oscillogram of scattered radiation [9]. The first (in time) of them corresponds to the instant of breakdown. The delay time Δt of the second pulse relative to the first one is tens of times greater than the durations of the pulses themselves and rather weakly depends on the intensity of the breakdown radiation. For water at atmospheric pressure, $\Delta t \approx 200$ μs. If the pressure in the cell is reduced to several tens of torrs, the value of Δt increases by an order of magnitude or more [9].

Proceeding from these results, it is natural to suppose that the delay time between the first and second pulses of the probe radiation scattering is determined by the dynamics of a spherical cavity (bubble) formed at the instant of breakdown. This cavity first expands, and its radius reaches the maximum value R_{max}; then, the cavity collapses (see [1, 2]). It is the second pulse that, according to our natural assumption, is connected with the instant of the bubble collapse: this pulse is produced by the scattering of the probe light beam by a shock wave generated at the instant of collapse.

Thus, the delay time Δt corresponds to the period of nonlinear pulsation of a bubble [1, 2]. It is mainly determined by the time of the slow phase of the bubble evolution around its maximum dimension, when the cavity radius $R(t)$ is comparable to R_{max} in the order of magnitude. The bubble dynamics in this case can be described by the Rayleigh–Plesset equation [1, 10]

$$\rho\left[R\frac{d^2R}{dt^2} + \frac{3}{2}\left(\frac{dR}{dt}\right)^2\right] = -p_\infty + p_b - \frac{2\sigma}{R} - \frac{4\mu}{R}\frac{dR}{dt}, \quad (1)$$

where ρ, σ, and μ are the density, surface tension, and viscosity of the liquid; p_b is the pressure of vapor and gas within the cavity; and p_∞ is the hydrostatic pressure in the liquid (far from the cavity). In the experiment, the depth of the liquid h was no greater than 3 cm, which corresponded to $\rho gh \lesssim 3 \times 10^{-3}$ atm, and the hydrostatic pressure p_∞ could be changed for the pressure over the liquid surface.

The delay time Δt measured in our experiment in the pressure range $p_\infty = 0.2$–1 atm lies within the limits $\Delta t \approx 200$–900 μs. As it will be demonstrated below, this allows us to ignore the two last terms on the right-hand

side of Eq. (1) (the surface tension and viscosity) and use the formula [1, 11]

$$p_b \approx p_s \tag{2}$$

for the pressure within the cavity, where p_s is the pressure of saturated vapor. Reducing Eq. (1), we obtain

$$\rho\left[R\frac{d^2R}{dt^2} + \frac{3}{2}\left(\frac{dR}{dt}\right)^2\right] = -p_\infty + p_s. \tag{3}$$

Indeed, in the approximation of Eq. (2), the period of nonlinear pulsations Δt, equal to twice the time of collapse of the Rayleigh's cavity [10], is connected with the maximum radius of the cavity R_{max} by the relation

$$\Delta t = \xi R_{max}\sqrt{\frac{\rho}{p_\infty - p_s}}, \tag{4}$$

where $\xi = 6^{1/2}\int_0^1(\tau^{-3}-1)^{-1/2}d\tau \approx 1.83$. Taking into account the values of $\Delta t \approx 200$–900 μs measured within the range $p_\infty = 0.2$–1 atm and at $p_s \approx 2.3\times10^{-2}$ atm (the experiment was conducted at room temperature), from Eq. (4) we obtain the estimates

$$R_{max} \approx 1\text{–}2 \text{ mm}, \quad \frac{2\sigma}{R_{max}(p_\infty - p_s)} = 2\xi\sigma\rho^{1/2}(p_\infty - p_s)^{-3/2}\Delta t^{-1} \approx (1\text{–}4)\times10^{-3}, \tag{5}$$

which allow us to ignore the surface tension within the whole investigated range of hydrostatic pressure p_∞. An estimate for the average velocity of the boundary v_{av} in the slow phase of cavity evolution also follows from Eq. (4):

$$v_{av} = \frac{2R_{max}}{\Delta t} = \sqrt{\frac{p_\infty - p_s}{\rho}}; \tag{6}$$

in the investigated pressure range, $v_{av} \lesssim 4$–10 m/s, which provides an opportunity to ignore the compressibility and viscosity of the liquid. The approximation of Eq. (2) is valid under the condition that the bubble dimensions vary sufficiently slowly in such a way that the pressure within the cavity has time to stabilize at the level p_s. Equation (6) provides an opportunity to clarify the applicability limits for the approximation of Eq. (2). To do this, we consider the equation of state of water vapor within the cavity together with the Hertz–Knudsen approximation for a flow of water molecules through the interface:

$$p_b = \frac{3Nk_bT}{4\pi R^3}, \quad \frac{1}{4\pi R^2}\frac{dN}{dt} = \frac{\beta(p_s - p_b)}{\sqrt{2\pi m k_B T}}. \tag{7}$$

Here, N is the number of vapor molecules in the cavity, m is the mass of a molecule, k_B is the Boltzmann constant, T is the absolute temperature, and β is the condensation coefficient. The value $\beta \approx 0.04$ is commonly adopted for water, but some authors give the value $\beta \sim 1$. The difference can be explained by different models of the liquid–vapor boundary [1]. Set of equations (7) has a solution close to Eq. (2) in the case of validity of the inequality $|dR/dt| \ll v_t$, where

$$v_t = \beta\sqrt{\frac{k_BT}{2\pi m}} \tag{8}$$

is the characteristic rate of mass exchange. Thus, for the slow phase of pulsation, the applicability condition for the approximation of Eq. (2) is reduced to $v_{av} \ll v_t$. The pressure $p_b \approx p_s$ in Eqs. (3) and (4) must be taken into account only if it contributes noticeably in comparison with p_∞. Assuming that $p_s \approx p_\infty/2$ for definiteness, using Eq. (6) for the average velocity in the slow phase, and taking into account Eq. (8), we obtain the following applicability condition for Eq. (4):

$$p_s \ll \max\left\{\beta^2\rho\frac{k_BT}{2\pi m}, p_\infty\right\}. \tag{9}$$

At $\beta = 0.04$, we have $v_t \sim 6$ m/s and $p_s \ll 0.4$ atm, so that Eq. (4) can be used at least at temperatures lower than 60–70°C.

Thus, the estimates following from the experimental values of Δt demonstrate that the approximation of Eq. (3) and relation (4) are valid at room temperature within the whole range of pressures studied: $p_\infty = 0.2$–1 atm. A refinement of the model is needed at sufficiently low pressure, when $p_\infty \approx p_s$, and at sufficiently high temperatures, when the condition given by Eq. (9) is violated.

When the cavity reaches its maximum dimensions, i.e., at $R = R_{max}$ and $dR/dt = 0$, its energy E_b is equal to the work against the forces of external pressure to produce such a cavity:

$$E_b = \frac{4\pi R_{max}^3}{3}(p_\infty - p_s). \tag{10}$$

Using Eq. (10), it is possible to eliminate the quantity R_{max} from Eq. (4):

$$\Delta t = 1.14\rho^{1/2}E_b^{1/3}(p_\infty - p_s)^\alpha, \tag{11}$$

where

$$\alpha = -5/6. \tag{12}$$

Relations (11) and (12) in the approximation of $p_s = 0$ are commonly called the Willis formula [2, 3]. The energy E_b in the order of magnitude also characterizes the energy accumulated in a bubble at the instant of its formation. Moreover, according to [1], $E_b \gtrsim Q_b$, where Q_b is the quantity of heat released in the bubble. This provides an opportunity to estimate the heating ΔT of the liquid in the layer adjoining the bubble with the thickness $\delta \approx \sqrt{\chi\Delta t/2}$:

$$\Delta T \lesssim E_b(4\pi R_{max}^2\delta\rho c_p)^{-1}, \tag{13}$$

where χ and c_p are the thermal diffusivity and capacity of water. Proceeding from this estimate and taking into account Eqs. (4) and (10) and the measured values of Δt, we obtain an estimate

$$\Delta T \lesssim 0.3(p_\infty - p_s)^{3/2}\Delta t^{1/2}p^{-3/2}\chi^{-1/2}c_p^{-1} \lesssim 2^\circ\mathrm{C}, \quad (14)$$

which allows us to ignore the heating of the liquid in the slow phase of pulsation.

The major assumption used in the model that needs experimental verification consists of the fact that the energy of the bubble production E_b is assumed to be constant and independent of the hydrostatic pressure p_∞. The independence (or weak dependence) of E_b on the external parameter, i.e., pressure, agrees well with the model of optical breakdown, where the energy of bubble production is determined by the internal properties of the liquid [12]. (It is necessary to keep in mind that, in our experiment, a bubble results from an optical breakdown.) According to [12], the optical breakdown has two stages. At the first stage, a laser pulse ionizes liquid molecules in the walls of a bubstone cluster. The energy spent by the laser pulse at this stage is just the sum of energies of single ionization of such molecules. A bubstone has a fixed (critical) radius, and the number of bubstones themselves in each cluster is approximately the same (for more details see [13]); therefore, these power inputs are virtually constant. The second stage is the induced optical coalescence. At this stage, electronic pressure and, hence, electron temperature increase in an avalanche-like manner in each single bubstone. The walls between single bubstones are destroyed, and a macroscopic vapor-gas bubble filled with heavy particles (fragments of bubstone walls) is formed. In this case, the energy of the laser pulse is spent for heating of electrons of such a bubble, which is accompanied by their bremsstrahlung (breakdown spark). The pressure within the bubble at this stage is estimated [13] to be equal to hundreds of atmospheres; therefore, the dependence on the external pressure must not manifest itself. It follows from this fact that the assumption that the bubble energy is independent of the external pressure seems to be quite substantiated.

Under this assumption, $\partial E_b/\partial p_\infty \equiv 0$, the dependence of the delay time Δt on the pressure difference $p_\infty - p_s$ according to Eq. (11) has a power-law form with the power index $\alpha = -5/6 = -0.833\ldots$. The definiteness of this dependence of Δt on p_∞ in a liquid provides an opportunity for a noncontact measurement of this pressure with the help of a remote detection of the scattering of probe light radiation in the region of optical breakdown.

The purpose of this work is the experimental verification of the power-law dependence of Δt on the pressure difference $p_\infty - p_s$ and the measurement of the power index α in the pressure range $p_\infty = 0.2$–1 atm, and also the evaluation of the possibility for a remote measurement of the liquid pressure by the method proposed below.

As we have already noted, we used optical breakdown to produce cavitation. The advantage of this method over other ones is the fact that the liquid is irradiated with pulses of calibrated energy under constant focusing conditions. As a result, in the case of a sufficient interval between pulses, the same conditions of cavitation production are reproduced for each pulse. This improves the reproducibility of the measured data. Moreover, an advantage of the proposed method is the absence of direct contact between the measuring device and the cell with the liquid. The experimental scheme described below implements a laser method of pressure measurement.

2. SCHEMES OF THE EXPERIMENTS

2.1. Optical Breakdown: Detection of the Scattering of Optical Radiation and of Acoustic Pulses

The experiment was conducted with double-distilled water filtered by an ion-exchange filter. Its specific resistance was 10 MΩ cm. The cells used in the experiment were manufactured from a pyrex tube with a length of 10 cm and a diameter of 3 cm. A quartz window was welded onto one end of the tube to transmit the laser radiation into the cell. The other end of the cell was covered by a teflon stopper, which contained platinum electrodes for monitoring the purity of the liquid. The stopper was grinded in the pyrex tube and fixed by springs on the external side of the tube. A thermistor in a quartz capillary was located near the electrodes for monitoring the temperature in the cell. The volume of the liquid in the cell was 180 ml, and the free volume was 100 ml.

Before the experiments, the cells were checked for impermeability: a vacuum was created in empty cells, and they stayed connected to an external pressure gauge for a week. If the pressure increased, the cell was marked unfit. Production of the necessary pressure in a cell was performed in the following way. The cell was connected to a forevacuum pump with the help of a set of vacuum hoses (a vacuum line), the end of one hose being open to the atmosphere. When the forevacuum pump producing a pressure $p = 3$ torr was switched on, the diameter of the output orifice of this hose was changed with the help of a clamp. In this way, it was possible to vary the pressure in the vacuum line. Thus, the pressure $p_\infty = 0.2$, 0.4, 0.5, 0.6, and 0.8 bar was produced sequentially in the cell.

After that, the cell was positioned on an optical bench and irradiated by laser pulses. The scheme of the experimental setup is given in Fig. 1. (*1*) Radiation of a single-mode pulsed-periodic Nd^{3+}:YAG laser (wavelength $\lambda = 1.06$ μm and a pulse length of 50 ns at the level of the pulse half-height) was directed with the help of a telescope and a system of lenses into (*2*) the cell with the liquid, where the optical breakdown was produced. The pulse energy varied within the range $E_L = 35$–105 mJ. The breakdown occurred at a depth of 5 mm. The lens focusing the radiation into the cell had a focal distance of 2 cm, and the diameter of the light spot at this lens was 0.5 cm.

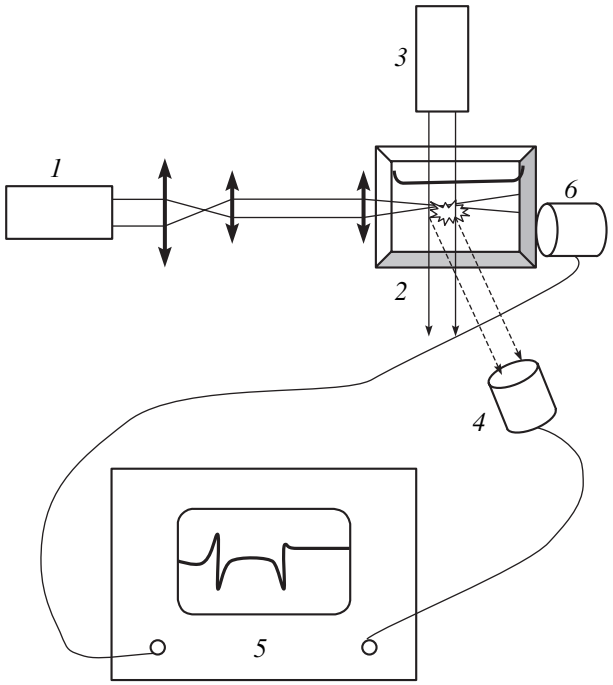

Fig. 1. Scheme of the experiment with the detection of the scattered optical radiation and the acoustic signal.

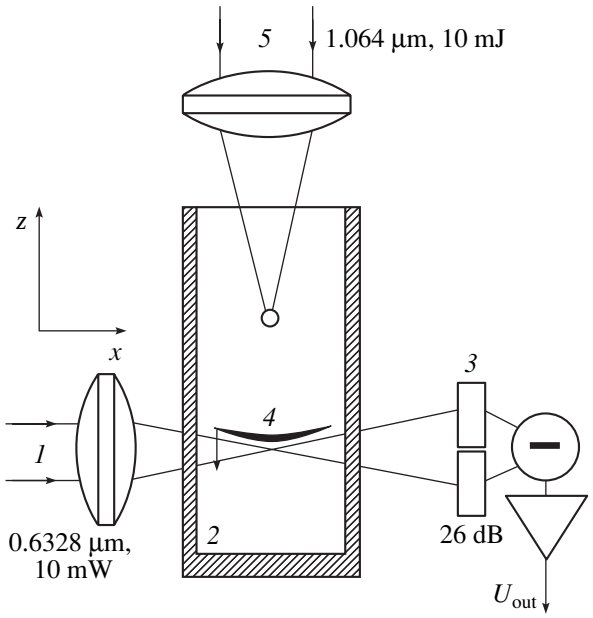

Fig. 2. Scheme of the experiment with the detection of the refraction of radiation of a He–Ne laser by acoustic cavitation pulses.

The pulsed laser radiation initiated an optical breakdown and the formation of a cavitation bubble. To measure the pulsation time of this bubble, the breakdown region was illuminated by (*3*) the probe radiation of the second harmonic of a single-mode CW Nd^{3+}:YAG laser (wavelength $\lambda = 0.53$ μm, power of 1 W, and beam diameter of 0.2 cm at the level of $1/e^2$) perpendicularly to the beam of the first harmonic. (*4*) A photodiode was installed under the angle of 30° to the axis of the second harmonic radiation; it transmitted a signal to the input of one of the channels of (*5*) a storage oscilloscope (Tektronix TDS 540). It is necessary to note that the choice of the angle between the photodiode orientation and the axis of the second harmonic beam is arbitrary to a large extent. It was important to us only that the direct laser radiation not hit the photodiode. (*6*) An acoustic sensor on the basis of a texturized piezoelectric film described in [14, 15] was pressed to the cell. The thickness of this film was 20 μm, and its resonance frequency was 22 MHz. The signal from this sensor was fed to the input of another channel of the oscilloscope. Thus, we had an opportunity to observe simultaneously the signals of scattering of probe optical radiation and the sound propagation for a single laser pulse. The oscilloscope was triggered by the same pulse that opened the electrooptic shutter of the pulsed laser, i.e., synchronously with the laser pulse. The oscilloscope was coupled to a computer via a GPIB card to provide the experimental data accumulation and numerical processing. This data array was composed from the signals of sensors (*4*) and (*6*).

2.2. Differential Optical Detection and the Estimation of the Acoustic Pulse Intensity at Cavitation

To verify the acoustic mechanism underlying the formation of the scattering pulses of probe optical radiation (Fig. 1), we conducted an additional series of experiments with a modified detection scheme. In this case, a method based on refraction of a probe beam of a CW laser in the field of a sound wave was used to detect short acoustic pulses excited in the process of laser breakdown of water. The scheme of the method is given in Fig. 2. Radiation of a 1-mW He:Ne laser was used as (*1*) a probe beam. The beam was directed normally to the axis of (*2*) a cell and focused at its center. In this case, the beam diameter at the focus did not exceed 50 μm. The sound ((*4*) is its propagation front) arising due to the breakdown and the subsequent bubble collapse modulates the refraction index of water, which causes a deviation of the probe beam. This deviation is measured by a differential sensor consisting of (*3*) two photodiodes, which is sensitive to deviations of the probe beam with respect to its initial direction. The positive values of the signal correspond to a beam deviation towards the sound source, i.e., a pressure increase. The length of each pulse is determined by the time of passage of the front of a sound wave through the cross section of the probe beam $t = c/h$, which constitutes ~30 ns. The time resolution of this method is limited by the value of t.

In the approximation of geometrical optics, the transmission of a probe beam through a medium is

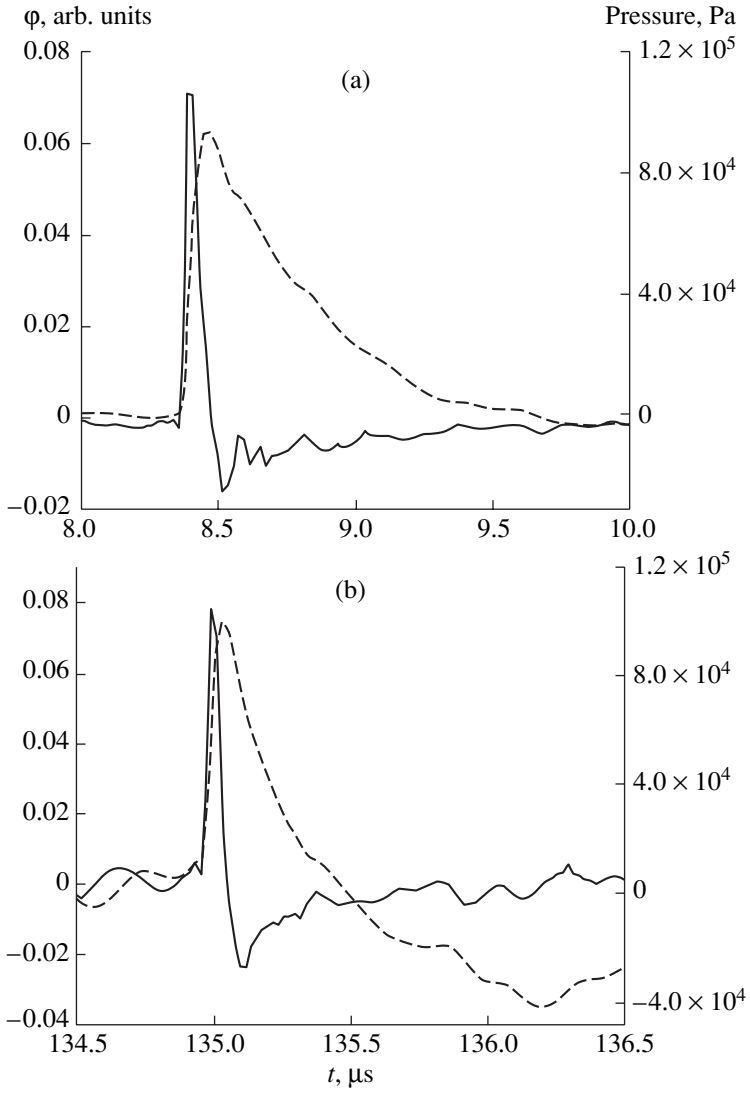

Fig. 3. The solid lines show the typical signal from the optical sensor for the differential detection scheme in Fig. 2 in the case of optical breakdown: (a) bubble formation and (b) bubble collapse. The dashed lines show the calculated pressure pulses.

described by the eikonal equation

$$\frac{d}{ds}\left(n\frac{d\mathbf{r}}{ds}\right) = \nabla n,$$

where $\mathbf{r}$ is the radius vector of the beam point, s is the beam length to the point $\mathbf{r}$, and $n = n(\mathbf{r})$ is the refraction index of the medium. Ignoring small deviations of the beam in the transverse direction, the eikonal equation can be reduced to an equation for the angle φ between the tangent to the beam and the x axis, $\partial\varphi/\partial x \approx n^{-1}\partial n/\partial z$. The difference $n - 1$ is assumed to be proportional to the density ρ of the liquid. In this case, at a large distance from the sound source, where the front of a sound wave can be considered to be plane, the total angular deviation of the probe beam leaving the medium can be estimated as

$$\varphi \approx \frac{h}{n}\frac{\partial}{\partial z}n \approx \frac{(n-1)h}{n\rho}\frac{\partial\rho}{\partial z} \approx \frac{(n-1)h}{n\rho c^3}\frac{\partial p}{\partial t}, \qquad (15)$$

where h is the transverse dimension of the cell and c is the sound velocity. Thus, the sound pressure is proportional to the integral of the differential sensor signal. The output signal of this sensor is proportional to the difference of photocurrents $\Delta i = i_1 - i_2 = \frac{4}{\sqrt{\pi}}\eta W\varphi/\theta$, where $i_{1,2}$ are the photocurrents of the first and second photodiodes, η is their quantum efficiency, W is the power of probe radiation, and θ is the convergence angle of the probe beam in the case of focusing. At the given experimental conditions, we have $\Delta i = 4.5 \times 10^{-2}\varphi$. The load of the photodiodes was 100 Ω, and, after a preamplifier for 26 dB, the output signal is equal to $U_{out} = \varphi 90$ V. To determine the pressure, we integrate the quantity U_{out} over time according to Eq. (15). The pressure pulses obtained in this way are given in Fig. 3 by dashed lines. Estimation of the amplitude of the

pressure pulses yields a value of the order of magnitude of 1 atm. This value of the amplitude of an acoustic pulse evidently does not exceed theoretical estimates for the distances of the order of magnitude of several millimeters from the region of collapse of cavitation bubbles (e.g., see [1, 16]).

An experiment according to the scheme given in Fig. 2 was conducted at atmospheric pressure p_∞ and the energy of (*5*) a laser pulse that was close to the optical breakdown threshold E_L = 4–10 mJ. The signal was detected at the distances of 4.8, 7.4, and 12.7 mm from the source, which provided an opportunity to determine the propagation velocity of the detected disturbance from the cavitation region and to identify it as an acoustic one. The dependence of the arrival time of the first observed pulse out of the two of them on the position of the probe beam with respect to the breakdown region (the focus of the pulsed laser) is demonstrated in Fig. 4. The propagation velocity of the disturbance was 1500 ± 40 m/s, which corresponded to the acoustic nature of the disturbance.

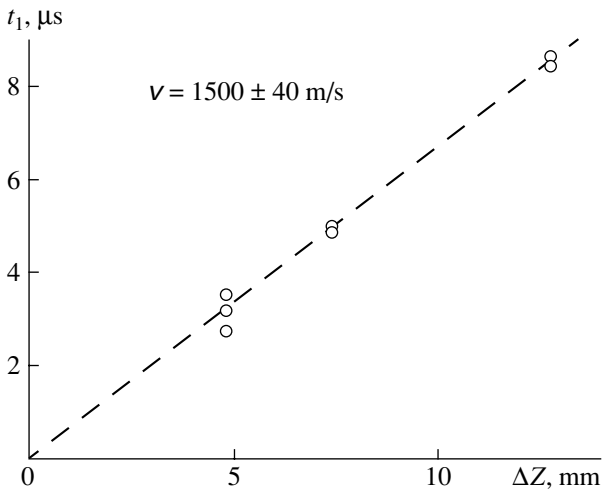

Fig. 4. Dependence of the arrival time t_1 of the first pulsed signal (optical breakdown) on the position of the probe beam Δz with respect to the focus of the pulsed laser for the differential detection scheme in Fig. 2. The slope of the approximating line corresponds to the velocity of the disturbance propagation of 1500 ± 40 m/s.

3. EXPERIMENTAL RESULTS

Experiments according to the scheme given in Fig. 1 were conducted at pressures p_∞ = 0.2, 0.4, 0.5, 0.6, 0.8, and 1 atm. Ten measurements at each pressure value were performed with the energy of a laser pulse E_L = 68 mJ. Moreover, at the pressure p_∞ = 1 atm, the values of Δt were measured for various values of the energy of laser pulses. In the absence of a cavitation bubble (as well as in the absence of the breakdown itself), there were no signals at the sensors (*4*) and (*6*). A characteristic pattern of the distribution of electric signals at the optical and acoustic sensors in the case of optical breakdown is given in Fig. 5. Zero on the abscissa axis corresponds to the front of the laser pulse (oscilloscope triggering). Within a short time $t_1 \sim 20$ μs after the laser pulse, the first pulse appears in both oscilloscope tracks, and, after that, the second pulse follows within the time Δt (Δt = 270 μs in Fig. 5). The interval between the first and second pulses Δt was measured in each experiment. It is necessary to note that exact correspondence of data obtained from the optical and acoustic sensors was not observed for every laser pulse: the number of pulses in an acoustic signal may be much greater than two. In these cases, the pulse clearly distinguished by the maximum amplitude was selected, and, when many pulses with approximately equal amplitudes were present, the selection of the second pulse in the oscilloscope track of the acoustic signal was determined by the condition of the maximum correspondence to the optical analog.

The array of the values of the delay time Δt for the second pulse selected in the indicated way was processed to calculate the index α in the dependence of Δt on the difference $p_\infty - p_s$ (Eq. (11)). The results of statistical processing of the data obtained for the (a) optical and (b) acoustic detection channels at a fixed energy of laser pulses E_L = 68 mJ are presented in Fig. 6. Here, we presumed the pressure of saturated vapor p_s to be equal to 17.2 torr. The broken line in Fig. 6 corresponds to such a processing employing the least-squares method. In this case, all values of Δt, including the ones measured at different pressures, are taken into account with equal statistical weights. The values obtained for the refraction index almost coincide for the optical and acoustic channels ($\alpha_{opt} = -0.88 \pm 0.05$ and $\alpha_{ac} = -0.87 \pm 0.04$) and, within the limits of estimated error, agree well with the theoretical value $\alpha = -5/6$ (Eq. (12)). The solid line in Fig. 6 shows the results of sequential processing, when the average value of Δt and an error for each fixed pressure value were calculated first, and then, in the process of calculating α, the pressure values with larger errors were taken into account with smaller weights (the statistical weight of a point is inversely proportional to variance; see [17] for an example). Since measurements for different pressure values were conducted at different times and, technically, in some cases experimental conditions could vary within certain limits (e.g., the cell temperature could vary for several degrees), the implementation of this processing technique seemed to be more adequate. The values of the power index α obtained in this case for the dependence of the delay time Δt of the second pulse on the pressure difference $p_\infty - p_s$ were $\alpha_{opt} = \alpha_{ac} = -0.84 \pm 0.03$. The measurements in both channels practically coincided with the theoretical value (Eq. (12)).

The coincidence of the results for optical and acoustic channels in measuring Δt testifies to the acoustic origin of the disturbance providing for the scattering of the probe optical radiation. Additional arguments in favor of this hypothesis, as well as evaluation of the ampli-

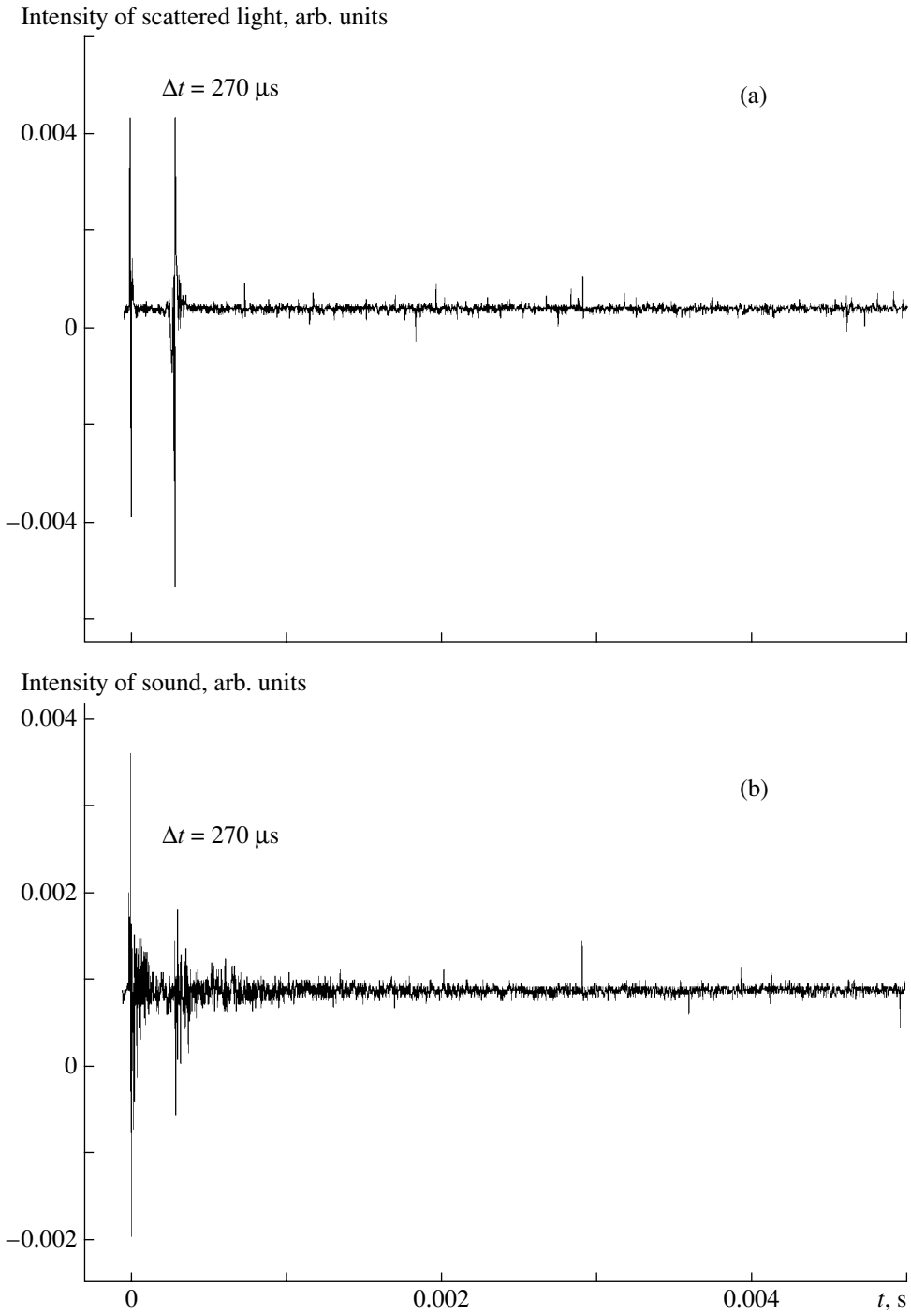

Fig. 5. Oscillograms for the (a) optical and (b) acoustic sensors of the detection scheme in Fig. 1 at $p_\infty = 0.6$ atm and $E_L = 68$ mJ.

tude of the acoustic pulse, were obtained in a series of experiments conducted using the differential scheme of optical detection (Fig. 2).

In the theoretical model described in Section 1, the power dependence given by Eq. (11) is a consequence of the fact that the energy of cavity production E_b (Eq. (10)) does not depend on the pressure p_∞ in the liquid. The measured values of Δt provide an opportunity to estimate this energy: $E_b \approx (650 \pm 100)$ μJ. A relatively high error of this estimate is a consequence of the rather "slow" dependence of Δt on E_b: Δt is proportional to $E_b^{1/3}$ (Eq. (11)).

The results of measurements of the delay time Δt at different values of the energy of the laser pulse are given in Fig. 7. These results demonstrate that, if the

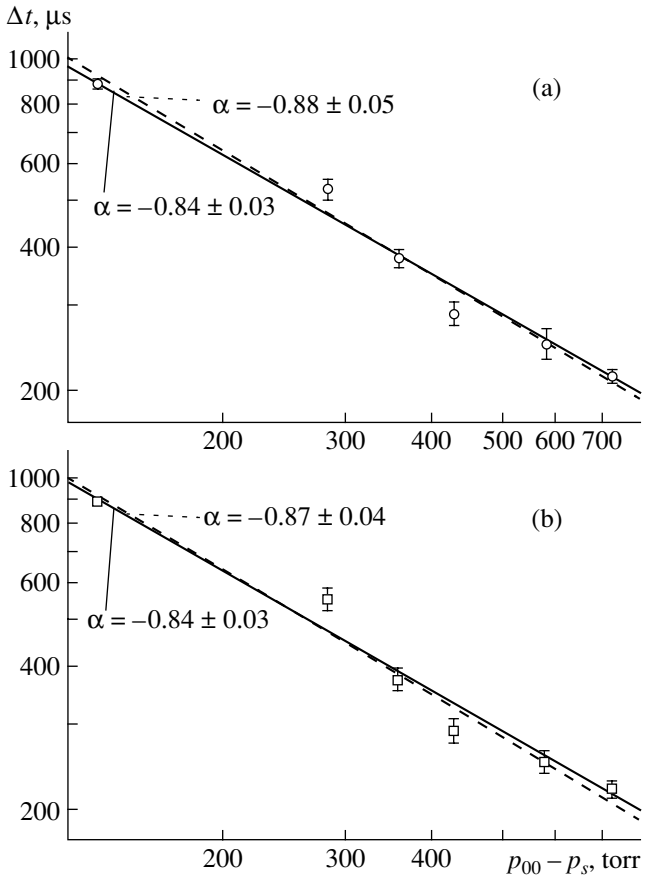

Fig. 6. Dependence of the delay time Δt for the second pulse relative to the first one on the pressure difference $p_\infty - p_s$ for the (a) optical and (b) acoustic sensors. The energy of the laser pulse initiating the optical breakdown is E_L = 68 mJ, and p_s = 17.2 torr. The broken line is the result of statistical processing when all experimental values of Δt are taken into account with equal weight. The solid line is the result of sequential processing. The statistical weight of the value of Δt at a fixed pressure is inversely proportional to the squared error.

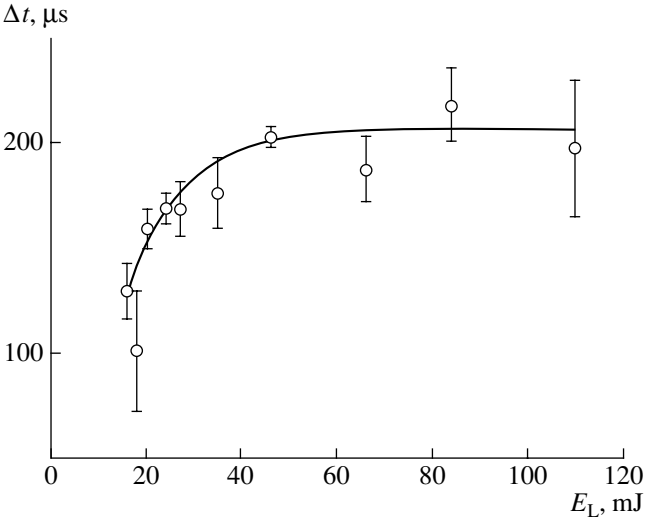

Fig. 7. Delay time for the second pulse Δt at p_∞ = 1 atm and different values of the energy of laser pulses E_L.

values of E_L are noticeably higher than the optical breakdown threshold, the dependence of the delay time Δt on the energy of the laser pulse E_L is fairly weak. The energy of cavity production E_b here also depends weakly on E_L. Thus, in the case of the use of optical breakdown for remote detection of pressure p_∞, an essentially over-threshold mode of operation is preferable, since, at sufficiently high values of E_L, the instability of this parameter less strongly affects the measured value of the delay time Δt.

4. CONCLUSIONS

Let us formulate the main results of the experiment on studying the cavitation in the case of the optical breakdown of water.

(i) It is demonstrated that short (no longer than 10-μs) pulses of the scattering of probe acoustic radiation at angles of several tens of degrees result from its scattering by the acoustic perturbations accompanying the optical breakdown and collapse of a cavitation bubble.

(ii) The measured values of the power index characterizing the dependence of the delay time Δt on the pressure difference $p_\infty - p_s$ (Fig. 6), $\alpha = -0.84 \pm 0.03$, agree well with the theoretical dependence given by Eqs. (11) and (12).

(iii) The results obtained substantiate the assumption concerning the constancy of E_b under varying hydrostatic pressure p_∞ in the liquid, which is used in the theoretical model. This fact is the basis for the proposed method of remote pressure measurement in liquids.

(iv) A weak dependence of the collapse time Δt on the energy of the laser pulse E_L in the case of its multiple excess over the threshold of optical breakdown is demonstrated experimentally.

(v) The estimate of the range of applicability of the employed theoretical model (Eqs. (11) and (12)) and, therefore, the range of applicability of the proposed method of remote pressure measurement gives a wide range of variation of the pressure p_∞ and the temperature of the liquid T, except for the regions where $p_\infty \approx p_s$ or where the condition of Eq. (9), $p_s \ll \max\left\{\beta^2\rho\frac{k_B T}{2\pi m}, p_\infty\right\}$, fails. In the case of water, the proposed method can be used at least up to the temperature of 60–70°C, except for the low-pressure region $p_\infty \approx p_s$. The extension of the method beyond the limits of the indicated range requires an improvement of the theoretical model.

The proposed method of pressure measurement can be effective in cases where pressure measurement by direct methods is impossible for some reason. The major advantage of the proposed method is the fact that it is contactless; therefore, it can be used for the processes of chemical and biological technologies. It is

necessary to note that the main requirement imposed on the liquids under test is their transparency to probe radiation.

ACKNOWLEDGMENTS

This work was supported in part by the Russian Foundation for Basic Research (project nos. 03-02-16589 and 02-02-16184) and by the Foundation for Support of Domestic Science.

REFERENCES

1. G. V. Flinn, in *Physical Acoustics. Principles and Methods*, Ed. by W. P. Mason (Academic, New York, 1964; Mir, Moscow, 1967), Vol. 1, Part B.
2. K. A. Naugol'nykh and N. A. Roĭ, *Electric Discharges in Water* (Nauka, Moscow, 1971) [in Russian].
3. R. H. Cole, *Underwater Explosions* (Princeton Univ. Press, Princeton, N.J., 1948; Inostrannaya Literatura, Moscow, 1950).
4. V. K. Kedrinskiĭ, *Hydrodynamics of Explosions: Experiment and Models* (Ross. Akad. Nauk, Novosibirsk, 2000) [in Russian].
5. A. Vogel, W. Hentschel, J. Holzfuss, and W. Lauterborn, Ophtalmologie **93**, 1259 (1986).
6. A. Vogel, W. Lauterborn, and R. Timm, J. Fluid Mech. **206**, 299 (1989).
7. A. Vogel and W. Lauterborn, Appl. Opt. **27**, 1869 (1988).
8. O. Baghdassarian, H.-Ch. Chu, B. Tabbert, and G. A. Williams, Phys. Rev. Lett. **86**, 4934 (2001).
9. S. I. Bakum, N. F. Bunkin, and A. M. Lomonosov, Phys. Wave Phenom. **11**, 96 (2003).
10. H. Lamb, *Hydrodynamics*, 6th ed. (Dover, New York, 1945; Gostekhizdat, Moscow, 1947).
11. M. A. Margulis, Usp. Fiz. Nauk **170**, 263 (2000) [Phys. Usp. **43**, 259 (2000)].
12. N. F. Bunkin and F. V. Bunkin, Laser Phys. **3**, 63 (1993).
13. N. F. Bunkin and F. V. Bunkin, Zh. Éksp. Teor. Fiz. **123**, 828 (2003) [JETP **96**, 730 (2003)].
14. I. A. Veselovskiĭ, L. M. Dorozhkin, V. V. Lazarev, *et al.*, Akust. Zh. **33**, 834 (1987) [Sov. Phys. Acoust. **33**, 483 (1987)].
15. K. I. Maslov, L. M. Dorozhkin, V. S. Doroshenko, and R. G. Maev, IEEE Trans. Ultrason. Ferroelectr. Freq. Control **44**, 380 (1997).
16. J. Holzfuss, M. Rüggeberg, and A. Billo, Phys. Rev. Lett. **81**, 5434 (1998).
17. D. J. Hudson, *Statistics. Lectures on Elementary Statistics and Probability* (Geneva, 1964; Mir, Moscow, 1970).

Translated by M. Lyamshev

Acoustical Physics, Vol. 51, No. 3, 2005, pp. 255–264. Translated from Akusticheskiĭ Zhurnal, Vol. 51, No. 3, 2005, pp. 311–322.

Spectral–Morphological Analysis of Acoustical Images of Biological Tissues and Composite Structures: II. Test Classification of Acoustomicroscopic Images

V. A. Burov, E. L. Kim, and O. D. Rumyantseva

Faculty of Physics, Moscow State University, Vorob'evy gory, Moscow, 119992 Russia

e-mail: burov@phys.msu.ru

Received June 10, 2004

Abstract—Results of numerical classification of different structure types in acoustomicroscopic images of real biological tissues and composite structures are reported. The classification is based on the Bayesian statistical hypothesis testing method. General realizations of this method in the form of the spatial-spectrum and spectral–morphological approaches are considered. The spatial-spectrum approach cannot discriminate between morphologically different structures with statistically identical power spectra. This disadvantage is eliminated in the spectral–morphological approach, which uses information on the spectral properties of the structure type being classified, as well as on the particular form of its characteristic features. The general approaches and their particular realizations (Bartlett's and Pisarenko's methods) are compared as applied to practical problems. © *2005 Pleiades Publishing, Inc.*

The purpose of this work is to numerically solve the problem of classification of tissues and structures by spectral and morphological methods. A solution to the problem under study can find a wide application in different fields: in geology and metallurgy for metallographic section analysis, in materials science, and also for many medical biological purposes. The latter include conventional biological microscopy and dermatology and the morphological analysis of normal and pathological parts of biological tissues (including cancer tumors), which has become topical in recent years. The issue of particular interest is the classification of images of biological tissues and composite structures obtained by acoustomicroscopic methods. The classification of biological tissues is primarily intended for additional medical diagnostics.

A detailed theoretical consideration of the proposed methods of spectral and morphological analysis is given in [1]. In this paper, the main statements and relationships underlying the numerical classification are given to make the presentation logically consistent.

1. SPECTRAL–MORPHOLOGICAL CLASSIFICATION OF IMAGES FROM THE VIEWPOINT OF STATISTICAL HYPOTHESIS TESTING THEORY

The brightness image of a complex structure to be classified is described by a two-dimensional nonnegative function $\Gamma_0(\mathbf{r})$, from which the average brightness Γ_0 is subtracted: $\Gamma_{\text{dif}}(\mathbf{r}) \equiv \Gamma_0(\mathbf{r}) - \Gamma_0$. It is necessary to separate regions that belong to one of the two image types indicated by superscripts I and II. The criterion for a current fragment $X_\mathbf{r}$ ($\mathbf{r}$ is the fragment's center) of image $\Gamma_{\text{dif}}(\mathbf{r})$ to belong to one of the given types relies on the current likelihood ratio function: $L(X_\mathbf{r}) \equiv L(\mathbf{r}) = P(X_\mathbf{r}|\text{I})/P(X_\mathbf{r}|\text{II})$. Here, $P(X_\mathbf{r}|\text{I})$ and $P(X_\mathbf{r}|\text{II})$ are the conditional probability densities of the events that $X_\mathbf{r}$ belongs to the structure of the first or second type, respectively. A learning set is specified, which consists of samples $u(\mathbf{r})$, i.e., of regions of an image of the given type with its average value $\bar{u}$ subtracted: $u_{\text{dif}}(\mathbf{r}) \equiv u(\mathbf{r}) - \bar{u}$. Each sample is characterized by brightness values at $N \times N$ discrete spatial points. The autocovariance matrix $A(\mathbf{r}, \mathbf{r}')$ for the structures of the given types is unknown. Therefore, we assume that the image is spatially homogeneous and ergodic and use an estimate of the autocovariance matrix in the form of an $N^2 \times N^2$ block-Toeplitz Hermitian matrix $A(\mathbf{r}, \mathbf{r}') = A(\mathbf{r}' - \mathbf{r}) \approx K(\boldsymbol{\rho} = \mathbf{r}' - \mathbf{r})$, where $K(\boldsymbol{\rho})$ is the sample autocovariance function for samples u_{dif}. Below, we use Dirac's notation: $u_{\text{dif}} \equiv |T^\text{I}\rangle$ and $u_{\text{dif}} \equiv |T^\text{II}\rangle$ are the column vectors for structure types I and II. To construct $L(\mathbf{r})$, we use the Karhunen–Loéve basis in the form of orthonormal eigenvectors $\{\varphi_i\}$ and eigenvalues $\{\lambda_i\}$ for the structure type I ($A = A^\text{I}$) and also $\{\psi_j\}$, $\{\mu_j\}$ for the structure type II ($A = A^\text{II}$): $A^\text{I}|\varphi_i\rangle = \lambda_i|\varphi_i\rangle$ and $A^\text{II}|\psi_j\rangle = \mu_j|\psi_j\rangle$, where $i, j = 1, \ldots, N^2$. The basis $\{\varphi_i\}$ is an eigen basis for structure $|T^\text{I}\rangle$ and a "foreign" basis for structure $|T^\text{II}\rangle$. For the basis $\{\psi_j\}$, the situation is the opposite. Expansion coefficients of the structure in its proper and alternative bases have the form $a_i^\text{I} \equiv \langle\varphi_i|T^\text{I}\rangle$, $b_j^\text{I} \equiv \langle\psi_j|T^\text{I}\rangle$; $a_j^\text{II} \equiv \langle\psi_j|T^\text{II}\rangle$, $b_i^\text{II} \equiv$

1063-7710/05/5103-0255$26.00 © 2005 Pleiades Publishing, Inc.

$\langle\varphi_i|T^{\mathrm{II}}\rangle$. The fragment $|X_{\mathbf{r}}\rangle$ is characterized by column vectors $|(X_{\mathbf{r}})^{\mathrm{I}}_{\mathrm{II}}\rangle = \begin{pmatrix}\{c_i^{\mathrm{I}}\}_{i=1,\ldots,N^2}\\ \{c_j^{\mathrm{II}}\}_{j=1,\ldots,N^2}\end{pmatrix}$ and $|(X_{\mathbf{r}})^{\mathrm{II}}_{\mathrm{I}}\rangle = \begin{pmatrix}\{c_j^{\mathrm{II}}\}_{j=1,\ldots,N^2}\\ \{c_i^{\mathrm{I}}\}_{i=1,\ldots,N^2}\end{pmatrix}$, where $c_i^{\mathrm{I}}(\mathbf{r}) \equiv \langle\varphi_i|X_{\mathbf{r}}\rangle$ and $c_j^{\mathrm{II}}(\mathbf{r}) \equiv \langle\psi_j|X_{\mathbf{r}}\rangle$. For both structure types, matrices of correlation coefficients are constructed. For structure $|T^{\mathrm{I}}\rangle$, elements of these matrices (described by the indices $m, n = 1, \ldots, N^2$) have the form

$$\begin{aligned}(K^{\mathrm{I}}_{aa})_{mn} &\equiv \overline{a^{\mathrm{I}}_m(a^{\mathrm{I}}_n)^*} = \overline{\langle\varphi_m|T^{\mathrm{I}}\rangle\langle T^{\mathrm{I}}|\varphi_n\rangle};\\ (K^{\mathrm{I}}_{bb})_{mn} &\equiv \overline{b^{\mathrm{I}}_m(b^{\mathrm{I}}_n)^*} = \overline{\langle\psi_m|T^{\mathrm{I}}\rangle\langle T^{\mathrm{I}}|\psi_n\rangle};\\ (K^{\mathrm{I}}_{ab})_{mn} &\equiv \overline{a^{\mathrm{I}}_m(b^{\mathrm{I}}_n)^*} = \overline{\langle\varphi_m|T^{\mathrm{I}}\rangle\langle T^{\mathrm{I}}|\psi_n\rangle};\\ (K^{\mathrm{I}}_{ba})_{mn} &\equiv \overline{b^{\mathrm{I}}_m(a^{\mathrm{I}}_n)^*} = (K^{\mathrm{I}}_{ab})^*_{nm}.\end{aligned} \tag{1}$$

The overbar means averaging over an ensemble of structures of the corresponding type. For the structure $|T^{\mathrm{II}}\rangle$, elements $(K^{\mathrm{II}})_{mn}$ are obtained from $(K^{\mathrm{I}})_{mn}$ by replacing T^{I} with T^{II} and interchanging the vectors φ and ψ. The combined matrices $K^{\mathrm{I}}_{\mathrm{comb}}$ and $K^{\mathrm{II}}_{\mathrm{comb}}$ consist of four blocks: $K^{\mathrm{I}}_{\mathrm{comb}} \equiv \begin{pmatrix}K^{\mathrm{I}}_{aa}; & K^{\mathrm{I}}_{ab}\\ K^{\mathrm{I}}_{ba}; & K^{\mathrm{I}}_{bb}\end{pmatrix}$. They characterize the statistical properties of structures of both types themselves and their cross properties. As a result, under the assumption that the random vectors $|(X_{\mathbf{r}})^{\mathrm{I}}_{\mathrm{II}}\rangle$ and $|(X_{\mathbf{r}})^{\mathrm{II}}_{\mathrm{I}}\rangle$ obey the multidimensional zero-mean Gaussian distribution, we obtain

$$L(\mathbf{r}) = \frac{P(X_{\mathbf{r}}|\mathrm{I})}{P(X_{\mathbf{r}}|\mathrm{II})} = \frac{\det^{1/2}(K^{\mathrm{II}}_{\mathrm{comb}})\exp\left(-\frac{1}{2}\langle(X_{\mathbf{r}})^{\mathrm{I}}_{\mathrm{II}}|(K^{\mathrm{I}}_{\mathrm{comb}})^{-1}|(X_{\mathbf{r}})^{\mathrm{I}}_{\mathrm{II}}\rangle\right)}{\det^{1/2}(K^{\mathrm{I}}_{\mathrm{comb}})\exp\left(-\frac{1}{2}\langle(X_{\mathbf{r}})^{\mathrm{II}}_{\mathrm{I}}|(K^{\mathrm{II}}_{\mathrm{comb}})^{-1}|(X_{\mathbf{r}})^{\mathrm{II}}_{\mathrm{I}}\rangle\right)}. \tag{2}$$

A decision is made by comparing $\Lambda'(\mathbf{r}) \equiv \Lambda(\mathbf{r}) - \ln(L_0)^{\mathrm{I}}_{\mathrm{II}}$ with zero, where $\Lambda(\mathbf{r}) \equiv \ln L(\mathbf{r})$ and $(L_0)^{\mathrm{I}}_{\mathrm{II}}$ is the threshold.

The spatial-spectrum approach performs averaging over the complete hypothetic ensemble of all images whose correlation properties are described by the given matrix A. Then, $\overline{|T^{\mathrm{I}}\rangle\langle T^{\mathrm{I}}|} = A^{\mathrm{I}}$, and the matrices K^{I}_{aa}, K^{II}_{aa} in (1) are diagonal:

$$\begin{aligned}(K^{\mathrm{I}}_{aa})_{mn} &= \lambda_n\delta_{mn} = \begin{Bmatrix}\lambda_n, & m = n\\ 0, & m \neq n\end{Bmatrix};\\ (K^{\mathrm{I}}_{ab})_{mn} &= \lambda_m\langle\varphi_m|\psi_n\rangle;\\ (K^{\mathrm{I}}_{bb})_{mn} &= \sum_{i=1}^{N^2}\lambda_i\langle\psi_m|\varphi_i\rangle\langle\varphi_i|\psi_n\rangle.\end{aligned} \tag{3}$$

A number of particular methods, which are sufficiently efficient under certain conditions and are computationally simpler, follow from the general optimal approach. The modified Bartlett's method classifies structures in terms of a statistical feature that is pronounced in the structure being classified and is weak in the alternative type. Specifically, to classify a type-I structure, from all $\{\varphi_i\}_{i=1,\ldots,N^2}$ are taken only the vectors $\varphi_{i=i_0}$ that satisfy the condition

$$\begin{aligned}&\sqrt{\overline{|\langle\varphi_{i_0}|T^{\mathrm{I}}\rangle|^2}} \gg \sqrt{\overline{|\langle\varphi_{i_0}|T^{\mathrm{II}}\rangle|^2}}, \text{ i.e.,}\\ &h_0\sqrt{\lambda_{i_0}} \geq \sqrt{\sum_{j=1}^{N^2}\mu_j|\langle\varphi_{i_0}|\psi_j\rangle|^2},\end{aligned} \tag{4}$$

where the coefficient $h_0 < 1$. To classify a type-II structure, from all $\{\psi_j\}_{j=1,\ldots,N^2}$ are taken only the vectors $\psi_{j=j_0}$ that satisfy the condition

$$\begin{aligned}&\sqrt{\overline{|\langle\psi_{j_0}|T^{\mathrm{II}}\rangle|^2}} \gg \sqrt{\overline{|\langle\psi_{j_0}|T^{\mathrm{I}}\rangle|^2}}, \text{ i.e.,}\\ &h_0\sqrt{\mu_{j_0}} \geq \sqrt{\sum_{i=1}^{N^2}\lambda_i|\langle\psi_{j_0}|\varphi_i\rangle|^2} \quad (h_0 < 1).\end{aligned} \tag{5}$$

Then, the resultant responses $R^{\mathrm{I}}_{\mathrm{Bt}}(\mathbf{r})$ and $R^{\mathrm{II}}_{\mathrm{Bt}}(\mathbf{r})$ are high in regions with structure type I or II, respectively, and are low in regions of the alternative type:

$$\begin{aligned}R^{\mathrm{I}}_{\mathrm{Bt}}(\mathbf{r}) &\equiv \frac{1}{N^{\mathrm{I}}_{\mathrm{Bt}}}\sum_{i_0}\left|F^{\mathrm{I}}_{i_0}(\mathbf{r})\right|; \quad R^{\mathrm{II}}_{\mathrm{Bt}}(\mathbf{r}) \equiv \frac{1}{N^{\mathrm{II}}_{\mathrm{Bt}}}\sum_{j_0}\left|F^{\mathrm{II}}_{j_0}(\mathbf{r})\right|;\\ F^{\mathrm{I}}_{i_0}(\mathbf{r}) &\equiv \int\Gamma_{\mathrm{dif}}(\mathbf{r}')\varphi_{i_0}(\mathbf{r}'-\mathbf{r})d\mathbf{r}';\\ F^{\mathrm{II}}_{j_0}(\mathbf{r}) &\equiv \int\Gamma_{\mathrm{dif}}(\mathbf{r}')\psi_{j_0}(\mathbf{r}'-\mathbf{r})d\mathbf{r}',\end{aligned} \tag{6}$$

where $N^{\mathrm{I}}_{\mathrm{Bt}}$ and $N^{\mathrm{II}}_{\mathrm{Bt}}$ are the total numbers of the selected vectors φ_{i_0} and ψ_{j_0}, respectively.

To classify a structure as type I or II, the modified Pisarenko's method selects eigenvectors φ_{i_0} or ψ_{j_0} that produce a weak response:

$$\begin{aligned}&\varphi_{i_0}:\ \sqrt{\overline{\left|\langle\varphi_{i_0}|T^{\mathrm{I}}\rangle\right|^2}} \ll \sqrt{\overline{\left|\langle\varphi_{i_0}|T^{\mathrm{II}}\rangle\right|^2}},\\ &\text{i.e.,}\quad H_0\sqrt{\lambda_{i_0}} \le \sqrt{\sum_{j=1}^{N^2}\mu_j\left|\langle y_{j_0}|\psi_j\rangle\right|^2};\end{aligned} \tag{7}$$

$$\begin{aligned}&\psi_{j_0}:\ \sqrt{\overline{\left|\langle\psi_{j_0}|T^{\mathrm{II}}\rangle\right|^2}} \ll \sqrt{\overline{\left|\langle\psi_{j_0}|T^{\mathrm{I}}\rangle\right|^2}},\\ &\text{i.e.,}\quad H_0\sqrt{\mu_{j_0}} \le \sqrt{\sum_{i=1}^{N^2}\lambda_i\left|\langle\psi_{j_0}|\varphi_i\rangle\right|^2}\quad (H_0>1).\end{aligned} \tag{8}$$

In this case, the resultant responses $R^{\mathrm{I}}_{\mathrm{Ps}}(\mathbf{r})$ and $R^{\mathrm{II}}_{\mathrm{Ps}}(\mathbf{r})$ reach their maximum in the region whose structure belongs to the corresponding type:

$$\begin{aligned}R^{\mathrm{I}}_{\mathrm{Ps}}(\mathbf{r}) &\equiv \left[\left\{\frac{1}{N^{\mathrm{I}}_{\mathrm{Ps}}}\sum_{i_0}\left|F^{\mathrm{I}}_{i_0}(\mathbf{r})\right|\right\} + \eta^{\mathrm{I}}_{\mathrm{Ps}}\right]^{-1};\\ R^{\mathrm{II}}_{\mathrm{Ps}}(\mathbf{r}) &\equiv \left[\left\{\frac{1}{N^{\mathrm{II}}_{\mathrm{Ps}}}\sum_{j_0}\left|F^{\mathrm{II}}_{j_0}(\mathbf{r})\right|\right\} + \eta^{\mathrm{II}}_{\mathrm{Ps}}\right]^{-1},\end{aligned} \tag{9}$$

where $N^{\mathrm{I}}_{\mathrm{Ps}}$ and $N^{\mathrm{II}}_{\mathrm{Ps}}$ are the total numbers of the selected vectors φ_{i_0} and ψ_{j_0} and $\eta^{\mathrm{I}}_{\mathrm{Ps}}$ and $\eta^{\mathrm{II}}_{\mathrm{Ps}}$ are the regularization coefficients. The difference $R^{\mathrm{I}}_{\mathrm{Ps}}(\mathbf{r}) - R^{\mathrm{II}}_{\mathrm{Ps}}(\mathbf{r})$ plays the role of the logarithm of the likelihood ratio. Unlike general classification approach (2), Bartlett's and Pisarenko's methods are only capable of extracting the structures when eigenvectors with the necessary contrast properties can be found.

The spatial-spectrum version (3) of the optimal method uses the complete hypothetic ensemble of images of the given type. Therefore, the classification only relies on the power spectrum characteristics and ignores morphological features of the structure. The spectral–morphological approach additionally accounts for morphological features that manifest themselves in correlation relations between the expansion coefficients. The bases $\{\varphi_i\}$ and $\{\psi_j\}$ and coefficients $|(X_{\mathbf{r}})^{\mathrm{I}}_{\mathrm{II}}\rangle$ and $|(X_{\mathbf{r}})^{\mathrm{II}}_{\mathrm{I}}\rangle$ remain the same, but the averaging in formulas (1) for the correlation matrices is performed over a subset of the complete hypothetic ensemble. This subset is composed of all realizations of the structure images that possess the specified morphological features. The numerical implementation performs the averaging in Eqs. (1) over a subset in the form of learning samples of type I or II (q is the sample number) $u_{\mathrm{dif}} = |T^{\mathrm{I}}_q\rangle_{q=1,\ldots,Q_1}$ or $u_{\mathrm{dif}} = |T^{\mathrm{II}}_q\rangle_{q=1,\ldots,Q_2}$:

$$\begin{aligned}(K^{\mathrm{I}}_{aa})_{mn} &\equiv \overline{a^{\mathrm{I}}_m(a^{\mathrm{I}}_n)^*} = \frac{1}{Q_1}\sum_{q=1}^{Q_1}\langle\varphi_m|T^{\mathrm{I}}_q\rangle\langle T^{\mathrm{I}}_q|\varphi_n\rangle;\\ (K^{\mathrm{I}}_{bb})_{mn} &\equiv \overline{b^{\mathrm{I}}_m(b^{\mathrm{I}}_n)^*} = \frac{1}{Q_1}\sum_{q=1}^{Q_1}\langle\psi_m|T^{\mathrm{I}}_q\rangle\langle T^{\mathrm{I}}_q|\psi_n\rangle;\\ (K^{\mathrm{I}}_{ab})_{mn} &\equiv \overline{a^{\mathrm{I}}_m(b^{\mathrm{I}}_n)^*} = \frac{1}{Q_1}\sum_{q=1}^{Q_1}\langle\varphi_m|T^{\mathrm{I}}_q\rangle\langle T^{\mathrm{I}}_q|\psi_n\rangle;\\ (K^{\mathrm{I}}_{ba})_{mn} &= (K^{\mathrm{I}}_{ab})^*_{nm}\end{aligned} \tag{10}$$

and similar formulas for structure type II. Here, the correlation matrices K^{I}_{aa} and K^{II}_{aa} lose their diagonal form (Eq. (3)); i.e., coefficients a_m and a_n ($n \neq m$) become correlated due to the morphological features of the structure.

2. NUMERICAL IMPLEMENTATION OF CLASSIFICATION METHODS FOR ACOUSTOMICROSCOPIC IMAGES OF BIOLOGICAL TISSUES AND COMPOSITE STRUCTURES

Below, we present the results of classifying acoustomicroscopic images of various biological tissues and composite structures on the basis of the optimal method in its spatial-spectrum version, including modified Bartlett's and Pisarenko's methods, and also in the spectral–morphological version, its limiting case being Capon's method. It can be seen that images produced by an acoustic microscope in certain cases display the structural features more clearly than those produced by an optical microscope [2–6] or an ultrasonic scanning system [7, 8]. Therefore, in these situations, acoustomicroscopic images are preferable for classification of biological tissues.

The brightness function $\Gamma_{00}(\mathbf{r})$ of the initial image of a real object is preliminarily processed as follows. First, to provide for the highest relative contrast of the fine structure features and, therefore, the maximum sharpness of response, we subtract the minimum value from the image and assume that $\min_{\mathbf{r}}\Gamma_{00}(\mathbf{r}) = 0$. Second, to eliminate the effect of brightness on the classification process, we normalize the image $\Gamma_{00}(\mathbf{r})$ by the result of smoothing it via the convolution with the function $S_0(-\mathbf{r})$, whose volume equals unity. This function describes a homogeneous structureless element: a small area on which $S_0(\mathbf{r})$ is positive and constant (or almost constant) and zero outside it. The size of this area must be comparable

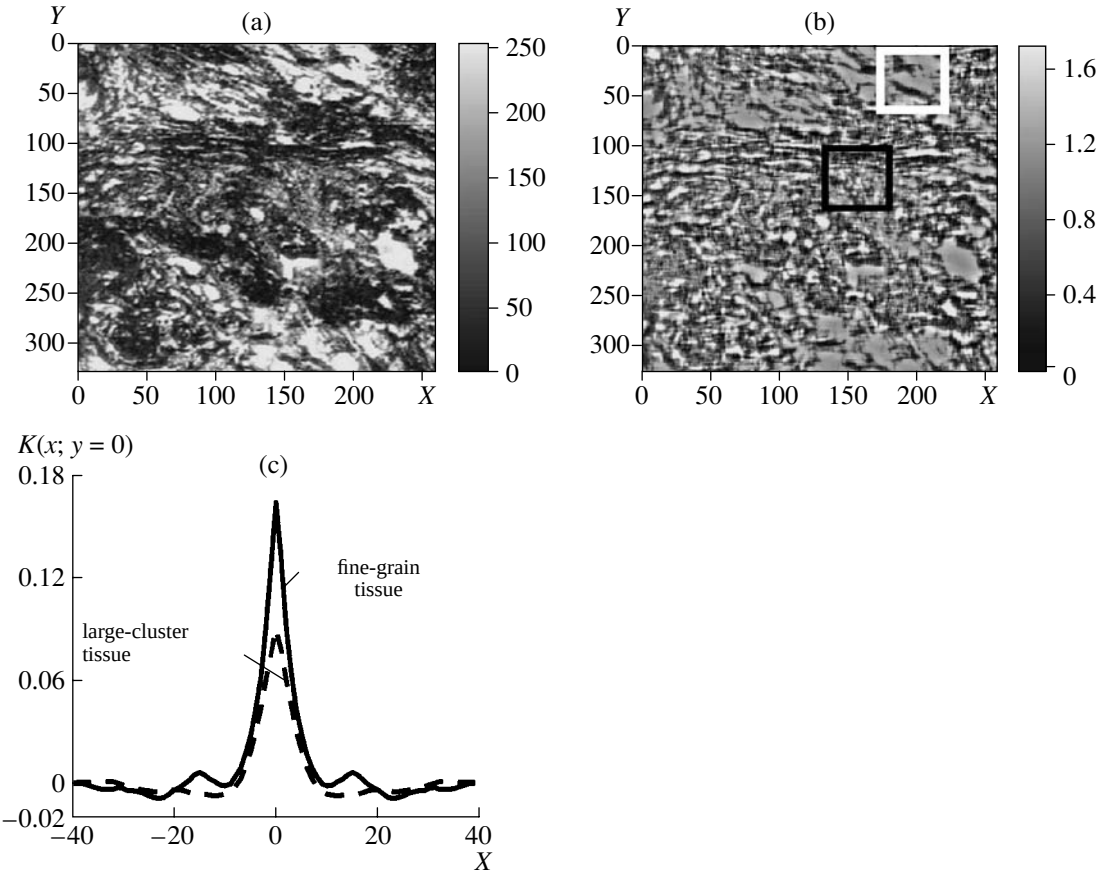

Fig. 1. Structure types of a cancerous mammary gland: (a) initial image of the mammary gland obtained with a scanning acoustic microscope, (b) the image normalized by the locally averaged brightness (the two structure types to be classified are the large-cluster tissue (outlined by the white contour) and fine-grain tissue (black contour)), and (c) the central section of the sample autocovariance function along the *x* axis for the large-cluster (dashed line) and fine-grain (solid line) tissues.

to the size of the regions of the image that constitute the learning set. Due to the normalization

$$\Gamma_0(\mathbf{r}) \equiv \frac{\Gamma_{00}(\mathbf{r})}{\int \Gamma_{00}(\mathbf{r}')S_0(\mathbf{r}'-\mathbf{r})d\mathbf{r}'}, \text{ where } \int S_0(\mathbf{r}')d\mathbf{r}' = 1, \quad (11)$$

the locally averaged (over the uniform area) brightness function $\Gamma_0(\mathbf{r})$ differs from the background (which is almost the same throughout the image and is close to 1) by the local brightness variation alone. These variations characterize intrinsic morphological features of the image structure.

2.1. Initial Images and Structure Types to Be Classified

The initial image $\Gamma_{00}(\mathbf{r})$ of cancerous mammary gland tissue (Fig. 1a) is borrowed from [2]. The full size of this image is about 410×480 μm^2, which corresponds to 260×330 pixels. In this and further examples, the image was normalized according to Eq. (11) by a moving locally averaged brightness $\int \Gamma_{00}S_0 d\mathbf{r}'$ calculated over a square region, in which S_0 was assumed to be constant. For the mammary gland tissue, the size of this region was 20×20 pixels. Two types of tissue were selected in the brightness-normalized gland tissue image $\Gamma_0(\mathbf{r})$ to be classified. Typical regions of these tissues are outlined in Fig. 1b: the first type is a tissue containing large clusters (white contour), and the second type is the small-grain tissue (black contour). The learning set for each of these tissue types contained from one to nine 40×40-pixel learning regions cut out from the image $\Gamma_0(\mathbf{r})$. Central sections (along the horizontal axis) of the sample autocovariance functions $K(\boldsymbol{\rho})$, which result from averaging over a set of five samples of the corresponding type, are shown in Fig. 1c. The block-Toeplitz autocovariance matrix constructed of $K(\boldsymbol{\rho})$ for a structure of a fixed type has $N^2 = 40^2 = 1600$ eigenvectors.

A similar scheme was used on the preparatory classification stage for other images. Specifically, we considered an acoustomicroscopic image of a tooth tissue with the dimensions $\approx(385 \times 385)$ μm^2, which corresponds to 210×210 pixels (Fig. 4a). This image, bor-

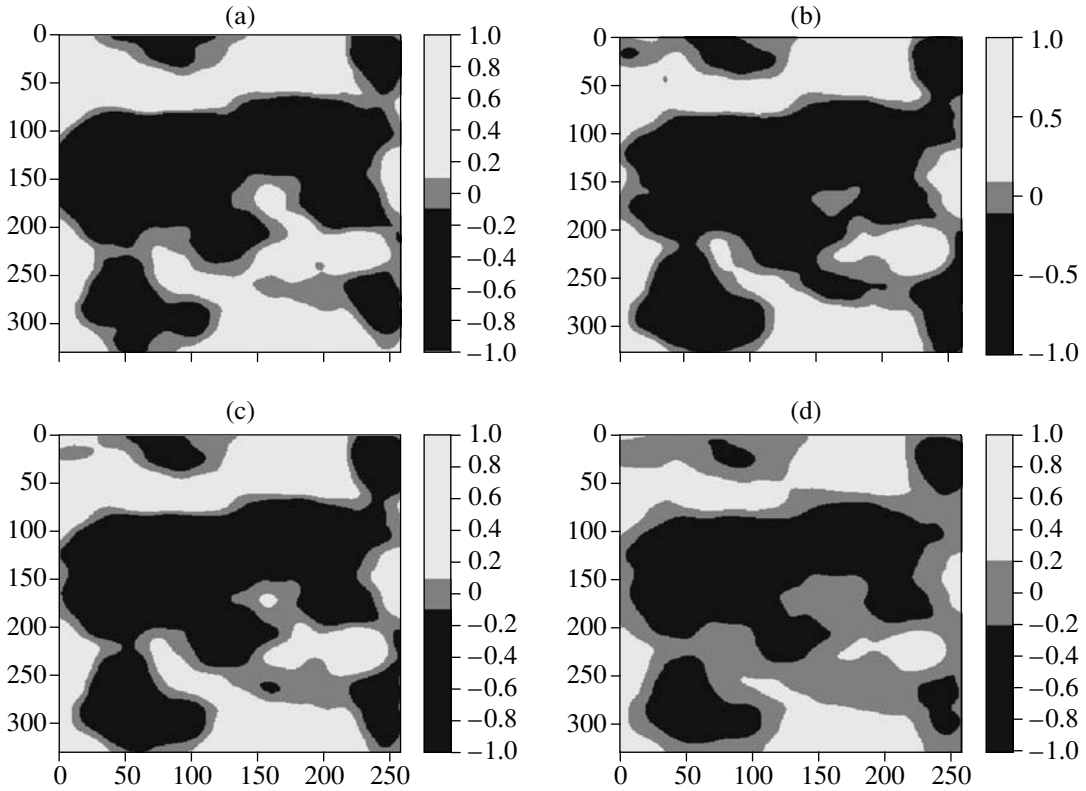

Fig. 2. Results of classification of large-cluster (white regions) and fine-grain (black regions) mammary gland tissues by the spatial-spectrum method based on (a) four, (b) five, and (c, d) nine learning samples of each type at the ambiguity zone level of (a, b, c) ±0.1 and (d) ±0.2.

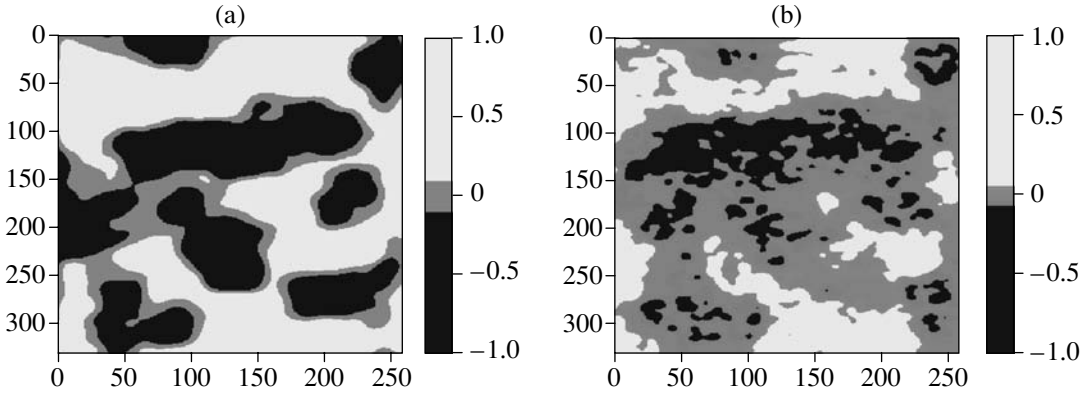

Fig. 3. Comparison of classification methods: (a) the destructive combination of results obtained by Pisarenko's and Bartlett's methods and (b) the comparison of results obtained by the spectral and spectral–morphological methods.

rowed from [6], consists of the enamel (the left, lighter, part of the figure) and dentine (the right, darker, part) tissues, which clearly differ in brightness. However, after normalization by the moving locally averaged brightness, the difference in the enamel and dentine tissues almost disappeared (Fig. 4b). Consequently, enamel and dentine are close in their structure and differ mostly in their "packing" density, which creates the brightness contrast (Fig. 4a). This circumstance is corroborated by earlier studies [4, 6]. Therefore, the two structure types to be classified were selected as follows. The first type was the general enamel–dentine tissue structure, whose typical region is outlined by the white contour in Fig. 4b. This type of structure fills the entire image except for the region of the immediate enamel–dentine interface, which has a more anisotropic struc-

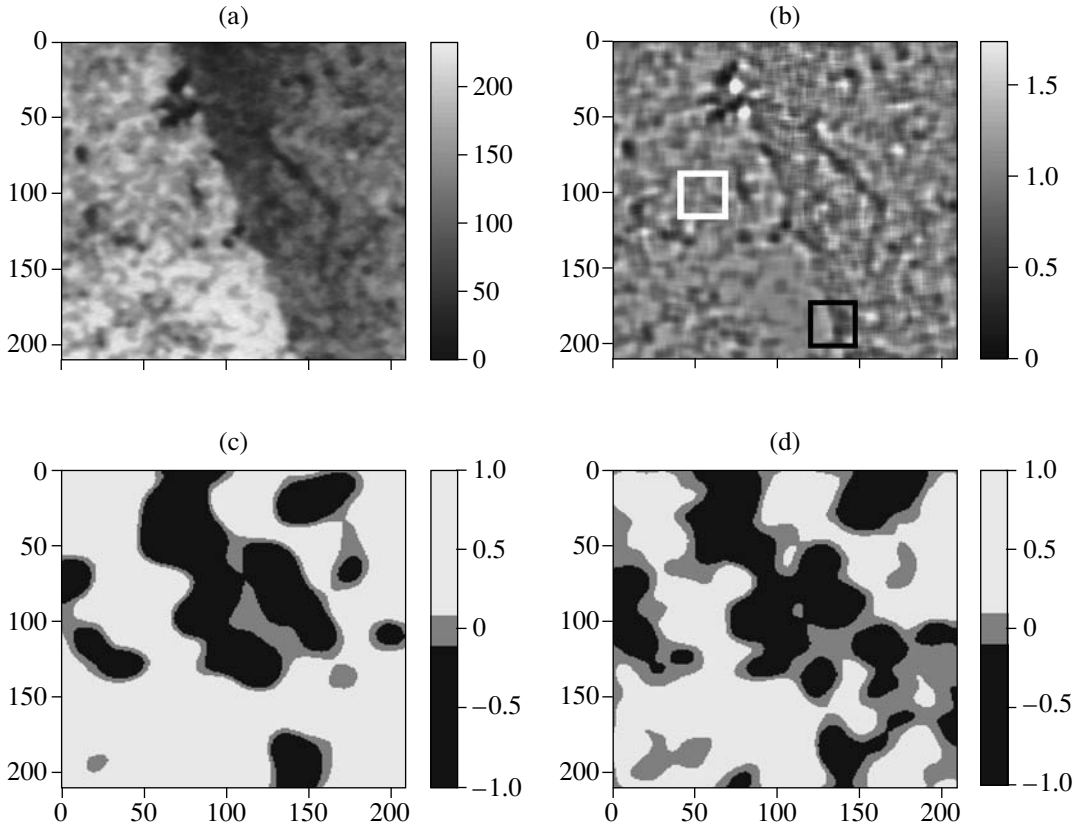

Fig. 4. Classification of the tooth tissue structures: (a) initial image of the tooth tissue obtained with a scanning acoustic microscope, (b) the image normalized by the locally averaged brightness (the two structure types to be classified are the enamel–dentine tissue (outlined by the white contour) and intermediate tissue (black contour)), (c) classification by the spatial-spectrum method, and (d) a destructive combination of results obtained by Pisarenko's and Bartlett's methods.

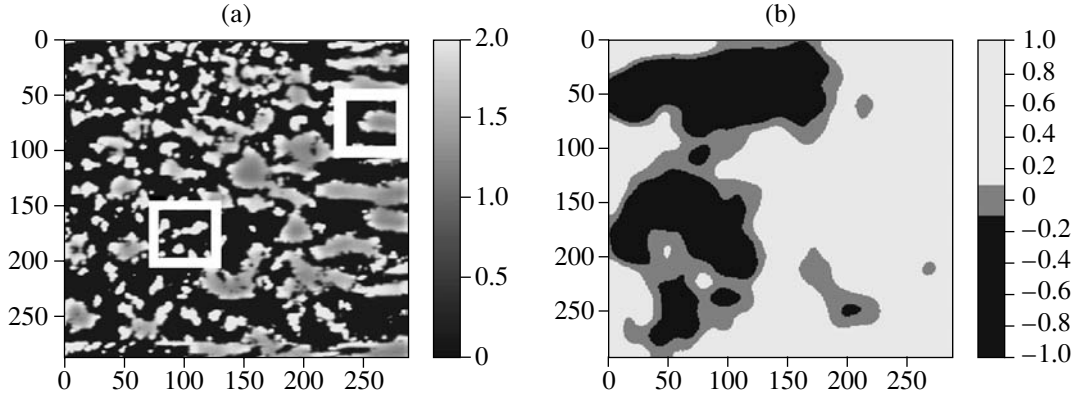

Fig. 5. Classification of the composite structure: (a) polymer image obtained with a scanning acoustic microscope and normalized by the locally averaged brightness (the two structure types to be classified are the large-scale structure (outlined by the thicker white contour in the upper right corner) and small-scale structure (white contour in the lower left corner)) and (b) the result of classification by the spatial-spectrum method.

ture with elements extending along it (the typical region outlined by the black contour in Fig. 4b) and is considered to be tissue of the second type. The learning sets contained five 20×20-pixel samples of the corresponding type, which allowed us to construct sample autocovariance functions. Thus, $N^2 = 20^2 = 400$ eigenvectors are available for classifying the image of tooth tissue.

The acoustomicroscopic image of the composite structure (consisting of a structured polyethylene and

polysterene PÉNP : PS = 80% : 20% mixture) [4] does not actually change after the normalization (Fig. 5a). Its full size is ≈(630 × 630) μm, which corresponds to 290 × 290 pixels. The large-scale (thick white contour in Fig. 5a) and small-scale structures (thinner white contour) were taken as the two types to be classified. Functions $K(\boldsymbol{\rho})$ constructed from four 40 × 40-pixel learning samples of each type produce $N^2 = 40^2 = 1600$ eigenvectors.

2.2. Spatial-Spectrum Approach

To better visualize the classification pattern obtained, for example, on the basis of likelihood ratio (2), we additionally smooth the estimated distribution $\Lambda'(\mathbf{r})$ and normalize it by its maximum value, reducing it to the function $\Lambda'_{\text{norm}}(\mathbf{r})$. The final classification decision is made in terms of a three-level scheme determined by the conditions on the validity of the decision. A fragment of the image is classified as type I if $\Lambda'_{\text{norm}}(\mathbf{r}) > \alpha_1 > 0$ (such regions are shown in the classification pattern in white) or as type II if $\Lambda'_{\text{norm}}(\mathbf{r}) < \alpha_2 < 0$ (black regions). Making a decision can also be impossible if $\alpha_2 \le \Lambda'_{\text{norm}}(\mathbf{r}) \le \alpha_1$; in these regions of indefinite classification (referred to as the ambiguity zone), shown in grey, the algorithm does not classify the structure as either of the two given types. Here, the thresholds $0 < \alpha_1 < 1$ and $-1 < \alpha_2 < 0$ are determined by the costs of the corresponding errors. Note that, unlike Wald's sequential analysis scheme [9], in this problem, there is no possibility of a further accumulation of data for the region in which making a decision was impossible.

Classification by Bartlett's and Pisarenko's methods. The structure types in the mammary gland and tooth tissue images described above were first classified by modified Bartlett's and Pisarenko's methods. Selection rules (4) and (5) allowed us to use Bartlett's method (response $R^{\text{II}}_{\text{Bt}}(\mathbf{r})$ in formulas (6)) to classify the small-grain mammary gland tissue, for which three (among the total of N^2) eigenvectors ψ_{j_0} were found at $h_0 = 0.35$, and the intermediate tooth tissue (two vectors ψ_{j_0} at $h_0 = 0.35$). At the same time, for these tissue types, there were no eigenvectors that satisfied condition (8) for the applicability of Pisarenko's method. Conversely, for the alternative tissue types, there were no eigenvectors necessary for Bartlett's method; however, classification was found to be possible by Pisarenko's method (condition (7), response $R^{\text{I}}_{\text{Ps}}(\mathbf{r})$ in formulas (9)). In particular, for the large-cluster mammary gland tissue, three eigenvectors φ_{i_0} were found at $H_0 = 3.5$; for the enamel–dentine tissue in the tooth image, two vectors φ_{i_0} were at $H_0 = 2.3$. The regions identified by Bartlett's and Pisarenko's methods were complementary and did not intersect. This fact corroborates that alternative tissue types were actually selected in this case. To facilitate the comparison of these results with results of classification by the spectral and spectral–morphological methods discussed below, the direct responses of Bartlett's and Pisarenko's methods were destructively combined, and Figs. 3a and 4d show the difference $R^{\text{I}}_{\text{Ps}}(\mathbf{r}) - R^{\text{II}}_{\text{Bt}}(\mathbf{r})$, smoothed out and normalized by its maximum value and fitted to the three-level scheme numerically characterized by the brightness scale.

Numerical estimates of the likelihood ratio. A more general classification method represented by the spatial-spectrum and spectral–morphological approaches constructs the combined matrices $K^{\text{I}}_{\text{comb}}$ and $K^{\text{II}}_{\text{comb}}$ with the use of the combined basis $\{\varphi_i\} \cup \{\psi_j\}$. Because this basis is overdetermined [1], the combined matrices appear to be singular. Therefore, these methods use the regularized combined matrices $K^{\text{I}}_{\text{reg}}$ and $K^{\text{II}}_{\text{reg}}$ in formulas (2) instead of $K^{\text{I}}_{\text{comb}}$ and $K^{\text{II}}_{\text{comb}}$, respectively. In the simplest case, $K^{\text{I}}_{\text{reg}} = K^{\text{I}}_{\text{comb}} + \eta_{\text{comb}}\hat{\text{E}}$ and $K^{\text{II}}_{\text{reg}} = K^{\text{II}}_{\text{comb}} + \eta_{\text{comb}}\hat{\text{E}}$, where $\hat{\text{E}}$ is the unit matrix. In classification of real images, the regularization coefficient η_{comb} as a rule was $\eta_{\text{comb}} \cong (0.1\text{–}5)(\nu^{\text{I}}_{\min} + \nu^{\text{II}}_{\min})/2$, where $\nu^{\text{I}}_{\min}$ and $\nu^{\text{II}}_{\min}$ are the smallest nonzero eigenvalues of the nonregularized matrices $K^{\text{I}}_{\text{comb}}$ and $K^{\text{II}}_{\text{comb}}$, respectively.

The spatial-spectrum approach constructs the correlation matrices of expansion coefficients involved in the combined matrices by formulas (3). The classification based on image processing by this method was found to be stable to parameters of the algorithm, which may be varied within sufficiently wide limits without noticeably changing the result. These parameters include the number of samples in the learning set, the number of eigenvectors of each type used to construct the combined matrices, and the relative regularization coefficient for these matrices. In particular, the logarithm of classification likelihood ratio $\Lambda(\mathbf{r})$ was calculated using only N' (out of the total of N^2) eigenvectors, which corresponded to essentially nonzero eigenvalues. For the image of the mammary gland tissue $N' = 400$ vectors out of $N^2 = 1600$ were taken; for the tooth tissue, $N' = 150$ vectors out of $N^2 = 400$ were taken; and for the polymer, $N' = 400$ vectors out of $N^2 = 1600$ were taken. The results of classification using these numbers N' of the eigenvectors were actually the same as those with the use of all N^2 vectors. However, the ranks of combined matrices in these two cases are indicative. When all N^2 eigenvectors of each type are used, the rank of matrices $K^{\text{I}}_{\text{comb}}$ and $K^{\text{II}}_{\text{comb}}$ in the spectral approach is

N^2, because each of the bases $\{\varphi_i\}$ and $\{\psi_j\}$ $(i, j = 1, \ldots, N^2)$, which form these matrices, is complete. Whereas if, for the mammary gland, for example, only $N' = 400$ eigenvectors are used, the rank appears to be considerably higher than N', decreasing from 790 for learning sets consisting of only one sample to 770 for sets of nine samples. This fact indicates that, when the classification relies on an overdetermined basis, supplementing 400 vectors of one type with 400 vectors of the alternative type is fundamentally necessary for the reliable classification of the alternative type of structure.

Investigation of real images of different structure types revealed that their brightness distribution histograms differ little from the Gaussian distribution used in classification scheme (2). The numerical implementation of this scheme suggested that all structure types are equiprobable and the error costs are equal; i.e., $(L_0)^{\mathrm{I}}_{\mathrm{II}} = 1$, $\ln(L_0)^{\mathrm{I}}_{\mathrm{II}} = 0$, and $\Lambda'(\mathbf{r}) = \Lambda(\mathbf{r})$. Results of classification that are smoothed and normalized by their maximum values are shown in Figs. 2a–2c for the mammary gland; in Fig. 4c for the tooth; and in Fig. 5b for the polymer. The decision was made in terms of the three-level scheme described above, and the ambiguity zone was specified by the level of ±0.1 ($\alpha_1 = 0.1$ and $\alpha_2 = -0.1$). It can be seen that the general spectral approach, which makes the most use of the statistical spectral information about the given structure types, and the more specific Bartlett's and Pisarenko's methods yield similar classification results. However, the optimal method simultaneously recognizes both tissue types, and the classification result better agrees with a purely visual (intuitive) structure separation of the initial image. The above-mentioned stability of results to such a parameter as length of the learning set and to particular realizations of the learning samples in it at a sufficient amount of statistical data is illustrated by the example of the mammary gland tissue. Specifically, Figs. 2a–2c differ only in the number of learning samples of a fixed type used to construct the classification bases: the structure type of these samples is the same. Even in the limiting case of the learning set consisting of a single sample, the classification is capable of identifying tissue regions of the corresponding types.

Estimation of the width of the ambiguity zone. Levels α_1 and α_2 of the ambiguity zone, in which the algorithm fails to be decisive, can be estimated for each particular classification method and set of basis functions used. To this end, one should analyze a test structure whose spatial–spectrum properties cannot be ascribed to any of the two types that are classified in the image, thereby placing it at an intermediate position in terms of spectrum. Also, the brightness variance of the test structure must be the same as the brightness variance of the image. Then, the standard deviation σ of the output response of the classification algorithm to such a test structure will give estimates for the levels α_1 and α_2.

For example, for the image of the mammary gland tissue (Fig. 1b), a Gaussian random structure was synthesized. We set the low- and high-frequency components of its spatial spectrum equal to zero, which caused the size of typical spatial features of the test structure to be intermediate between those of tissue types I and II in the image of the mammary gland tissue. The brightness variance of this structure was additionally made equal to the variance of the whole locally normalized image $\Gamma_0(\mathbf{r})$ of the mammary gland. This synthesized random structure was subjected to classification by the spectral method with the help of the same bases as earlier. The result $\Lambda(\mathbf{r}) = \Lambda_{\mathrm{rand}}(\mathbf{r})$ of classifying the random structure was smoothed out and normalized by the maximum value of a similar result of classifying the mammary gland image. The spread in the classification quantity $\Lambda_{\mathrm{rand}}(\mathbf{r})$ was in the range with a total width of $6\sigma \approx 1.2$; therefore, the ambiguity level was $\alpha_1 \approx -\alpha_2 \approx \sigma \approx 0.2$. The result of classifying the mammary gland tissue for the ambiguity level of ±0.2 is shown in Fig. 2d, which corresponds to Fig. 2c plotted for an ambiguity level of ±0.1.

2.3 Spectral–Morphological Approach

Unlike engineering structures, biological tissues usually do not feature a clearly defined structure pattern. In this regard, the morphological analysis of images whose structure is more or less random implies that a sufficiently large learning set is available; i.e., the learning set is a representative set of realizations. To eliminate morphological properties associated with orientation alone, the set must contain samples of all possible orientations of the typical structure. In this regard, the morphological classification can be referred to as "soft" classification, in contrast to "hard" classification provided by the matched spatial filtering or Capon's method. From the viewpoint of statistical hypotheses testing theory, Capon's method modified for the classification problem is the limiting case of the spectral–morphological approach when the classification relies on the morphological criterion formulated as the requirement of an almost complete coincidence of types of elementary structures constituting the image with the type of the given reference structure [10–12]. Thus, in the modified Capon's method, the structure type to be classified is definitely specified. This is a limiting case, in which the correlation matrices of expansion coefficients (10) are formed from the learning sets, each of the two of which consists of a single sample $|T^{\mathrm{I}}\rangle$ or $|T^{\mathrm{II}}\rangle$, respectively ($Q_1 = Q_2 = 1$). The modified Capon's method demonstrated a high efficiency in classifying images with a clearly defined (also in terms of orientation) type of their characteristic elements [11, 12]. However, its efficiency is not always high in classifying real images. As compared with the optimal method, Capon's method separates regions of type I and II less clearly and the result of the classification is not very stable, because it is noticeably affected by sec-

ondary features of the classification process. This is associated with an insufficiently full use of characteristic features of the structure when classification relies on a single particular region.

The specific properties and advantages of the most general—spectral–morphological—approach as compared to both the purely spectral and purely morphological methods are illustrated below by the example of classification of the mammary gland tissue discussed above (Figs. 1a and 1b). In all cases considered below, the number of samples of both types in the learning set was the same and equal to $Q \equiv Q_1 = Q_2$. The rank of combined matrices $K^{\mathrm{I}}_{\mathrm{comb}}$ and $K^{\mathrm{II}}_{\mathrm{comb}}$ constructed on the basis of correlation matrices (10) of expansion coefficients was equal to the number of samples Q. This is determined by the fact that the matrix $|\overline{T}\rangle\langle\overline{T}| = \frac{1}{Q}\sum_{q=1}^{Q}|T_q\rangle\langle T_q|$ is a sum of dyadic matrices $|T_q\rangle\langle T_q|$, each of which has a rank of 1.

When the learning set consists of a small number of samples, response of the spectral–morphological algorithm is most pronounced in regions of the image that have the same shape and orientation as the samples present in the set. Thus, if the learning set is constructed from insufficient statistical data, the response of the spectral–morphological algorithm is similar to the sharp response of the modified Capon's method when the image region being classified is almost exactly the same as the given standard element of the structure in its shape, orientation, and proportions.

A fuller learning set can be obtained by directly increasing the number of samples of the given type, as well as by including different orientations of the samples available. As we noted above, the presence of samples in the learning set that are oriented at different angles excludes from classification criteria those morphological features that are associated with orientation of the anisotropic structure alone. Specifically, each of the nine learning samples of the given type was rotated about six discrete angles in the range from 10° to 90°, and the set was thereby extended to 54 samples. Angles near 0° were not considered; i.e., the learning set contained no samples that coincided or almost coincided with particular regions of the image being classified. This measure prevented an extremely sharp response of the algorithm. The result $\Lambda = \Lambda_{\mathrm{morph}}(\mathbf{r})$ of the spectral–morphological classification of the mammary gland image is, in general terms, the same as the result of classification of this image by the spectral method, $\Lambda = \Lambda_{\mathrm{spectr}}(\mathbf{r})$. However, the spectral–morphological analysis separates the regions of the given type more finely, i.e., on a smaller scale. To illustrate the comparison of the results of the spectral and spectral–morphological classification, we used the function $D(\mathbf{r}) \equiv 0.5[\,\mathrm{sgn}(\Lambda_{\mathrm{spectr}}(\mathbf{r})) + \mathrm{sgn}(\Lambda_{\mathrm{morph}}(\mathbf{r}))\,]\Lambda_{\mathrm{spectr}}(\mathbf{r})\Lambda_{\mathrm{morph}}(\mathbf{r})$. If $\Lambda_{\mathrm{spectr}}(\mathbf{r})$ and $\Lambda_{\mathrm{morph}}(\mathbf{r})$ have different signs at a particular point $\mathbf{r}$, i.e., the spectral and spectral–morphological methods identify the structure type differently, then, $D(\mathbf{r}) = 0$. Otherwise, when they classify the structure type identically, the sign of $D(\mathbf{r})$ uniquely specifies the type. Figure 3b shows the normalized and smoothed comparison function $D(\mathbf{r})$ for the case when the learning set consists of nine samples for the spectral method and of 54 samples for the spectral–morphological method. The pattern of light and dark spots corroborates the spectral classification but is not identical to it.

2.4. Comparative Analysis of Classification Methods

The results of image classification by the different methods discussed above allow us to draw the following conclusions. An unquestionable advantage of the general (both, the spectral and spectral–morphological) approach is the fact that it relies on the statistical hypothesis testing method. A disadvantage of the purely spectral approach is that it is incapable of discriminating between structures of different morphological types if they have the same average spatial power spectrum [1]. The purely morphological Capon's method, which works directly with learning samples and also is the least laborious of all the methods considered, is free from this disadvantage. However, this method in essence is a rigid morphological analysis, which gives a strong response only when the object has a particular shape and orientation. Therefore, it should be used when the reference structure element is known a priori. Note that it may be difficult to reflect all statistical features of the structure in this reference element.

Thus, none of the purely spectral or purely morphological methods is quite perfect from the viewpoint of providing the maximum classification reliability. However, the results presented in this paper allow us to expect that the spectral–morphological approach is the most promising approach for classifying biological tissues. The following aspects are fundamentally important here. The matrix K_{aa}, which is constructed in this method through directly averaging the cross products of expansion coefficients of the members of the learning set in the proper basis (see formula (10)), is not diagonal. The off-diagonal matrix elements introduce morphological features of the given structure into the classification process. At the same time, the diagonal part of the spectral–morphological matrix K_{aa} was found to be close to the exactly diagonal matrix K_{aa} in the spectral approach (see formula (3)). These circumstances show that the learning set over which the spectral–morphological approach performs the averaging is a subset belonging to the complete hypothetical ensemble of structures with given spatially homogeneous spectral properties.

An image constructed as a collage of two random images with the same spectral properties as those of the true structures is classified by the spectral approach identically with these structures, whereas the spectral–morphological approach classifies it as a neutral image,

because its two parts do not correspond to any of the given types [1].

The spectral and spectral–morphological approaches both exhibit a weak dependence of the result on particulars and characteristics of the classification algorithm. The classification result is stable, and its quality improves to a certain limit with an increase in the size of the learning set. As its length increases further, the quality remains almost unchanged.

ACKNOWLEDGMENTS

We are grateful to R.G. Maev and L.A. Denisova for supplying us with images and for invaluable encouragement.

This work was supported by a grant from the President of the Russian Federation (grant no. NSh-1575.003.2) and by the Russian Foundation for Basic Research (project no. 04-02-16043).

REFERENCES

1. V. A. Burov, E. L. Kim, and O. D. Rumyantseva, Akust. Zh. **51** (1), 68 (2005) [Acoust. Phys. **51** (1), 52 (2005)].
2. R. A. Lemons and C. F. Quate, Science **188**, 905 (1975).
3. J. J. Jones, Newsl. Acoust. Soc. Am. Echoes **10** (2), 1 (2000).
4. R. G. Maev, Doctoral Dissertation in Physics and Mathematics (Inst. of Biochemical Physics, Russian Academy of Sciences, Moscow, 2003).
5. L. A. Denisova, Doctoral Dissertation in Biology (Inst. of Biochemical Physics, Russian Academy of Sciences, Moscow, 2003).
6. R. Gr. Maev, L. A. Denisova, E. Yu. Maeva, and A. F. Denisov, Acoust. Imaging **25**, 501 (2000).
7. B. Todd and M. Ravi, Am. J. Surg. **185**, 416 (2003).
8. P. M. Lamb, N. M. Perry, S. J. Vinnicombe, and C. A. Wells, Clin. Radiol. **55**, 40 (2000).
9. A. Wald, *Sequential Analysis* (Wiley, New York, 1947; Fizmatgiz, Moscow, 1960).
10. S. M. Kay and S. L. Marple, Jr., Proc. IEEE **69**, 1380 (1981).
11. V. A. Burov and E. L. Kim, in *Proceedings of XI Session of the Russian Acoustical Society* (GEOS, Moscow, 2001), Vol. 2, pp. 26–29; http://akin.ru/Rao/sess11/sect9me.htm.
12. V. A. Burov and E. L. Kim, Acoust. Imaging **26**, 273 (2002).

Translated by A. Khzmalyan

Acoustical Physics, Vol. 51, No. 3, 2005, pp. 265–270. Translated from Akusticheskiĭ Zhurnal, Vol. 51, No. 3, 2005, pp. 323–329.

On the Predictability of the Positions of the Convergence Zones in the Ocean

R. A. Vadov

Andreev Acoustics Institute, Russian Academy of Sciences, ul. Shvernika 4, Moscow, 117036 Russia

e-mail: vadov@akin.ru

Received June 30, 2004

Abstract—The disagreement between the experimental and calculated positions of the first convergence zone are known from many publications. The most probable cause for such a disagreement, namely, the incorrect specification of the input data for the calculations, is considered. The lack of simultaneity between the hydrological surveys of the region and the acoustic experiments is emphasized. The experimental data obtained by the author in five ocean regions are presented. These data characterize the diurnal variability of the distance from the source to the nearest boundary of the convergence zone. The relations proposed by different researchers for calculating the sound speed from the temperature, salinity, and hydrostatic pressure are analyzed. It is shown that these relations lead to a substantial difference in the estimated depth dependence of the hydrostatic gradient of the sound speed. The position of the first convergence zone is calculated for the propagation conditions determined by vertical temperature and salinity profiles with the subsequent recalculation of these profiles into sound speed profiles by using eight different formulas known from the literature. It is shown that different formulas lead to different values of the distance to the first zone; this difference is substantially greater than that between the calculations and experiment. The necessity of improving the recalculation relations in view of the experimental data on sound propagation in natural oceanic waveguides, including the data on the actual positions of the convergence zones, is emphasized. © *2005 Pleiades Publishing, Inc.*

One of the "unsolvable" problems of underwater acoustics, which was repeatedly addressed in many publications (e.g., [1–4]) over several decades, consists in the discrepancy between the experimental and calculated positions of the first convergence zone. The difference in the measured and theoretical values of the distance from the source to the nearest boundary of the zone reaches 1–2 km. As a rule (though not always), the calculations lead to an overestimated distance in comparison with experiment.

This paper analyzes the most probable reason for such a discrepancy, namely, the incorrect specification of the input data for the calculations. The following factors are emphasized: the diurnal variability of the propagation conditions, the lack of simultaneity in the hydrological survey of the propagation path and the acoustic experiments, and the substantial difference in the relations proposed by different researchers for recalculating the temperature, salinity, and hydrostatic pressure into the sound speed.

1. In many cases, a hydrological survey of the propagation path is carried out either before or after the acoustic experiment. As a rule, a survey of the ocean medium is performed up to a depth of 1000–2000 m (deep-water stations, down to the bottom, are rare). The missing part of the sound speed profile, $c(z)$, is reconstructed by using archive data. The diurnal variability of the propagation conditions and the nonsimultaneous hydrological and acoustic measurements are possible sources of the observed disagreement between the calculated and measured distances to the convergence zone. The time separation of the acoustic experiment and the hydrological survey is usually 8 to 20 h.

In several expeditions by the research vessels of the Acoustics Institute, diurnal studies of the geometry and the intensity structure of the first convergence zone were carried out. The experiments were performed in five regions of the World Ocean: the Norwegian and Mediterranean Seas, the Sea of Japan, the central part of the Atlantic Ocean, and the central part of the Indian Ocean. Figure 1 shows the sound speed profiles that characterize the propagation conditions in all these regions.

In all the experiments, the same technique [5, 6] was used. The receiving vessel drifted with omnidirectional receivers deployed to the chosen depths. The transmitting vessel, with a sound source at the chosen depth, went 2 to 3 knots away from the receiving vessel or towards it and crossed the first convergence zone several times a day. In crossing the convergence zone, a continuous noiselike signal was transmitted within a 1/3-octave frequency band. The central frequency of the transmission was about 3 kHz. Periodically (every 5–10 minutes), the distance between the source and the receivers was measured. To do so, dedicated instruments [7] were used. The distance was also periodically

1063-7710/05/5103-0265$26.00 © 2005 Pleiades Publishing, Inc.

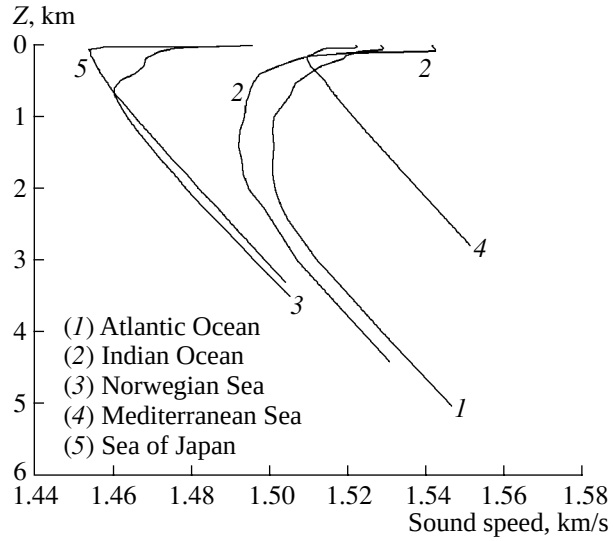

Fig. 1. Sound speed profiles characterizing the propagation conditions in the regions of the experiments.

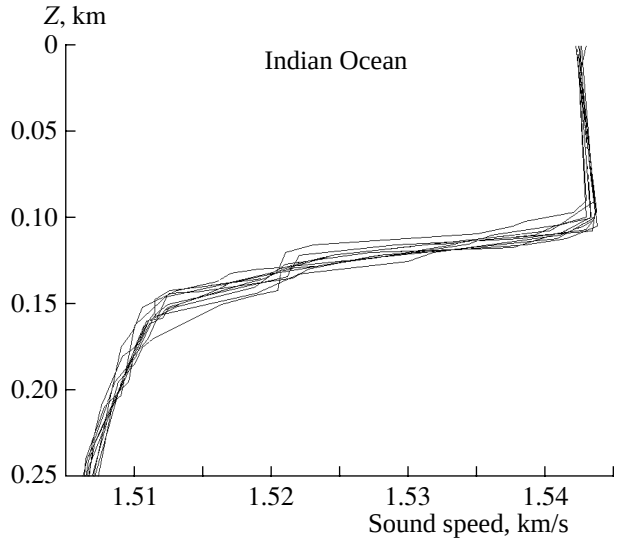

Fig. 2. Diurnal variations of the propagation conditions in the Indian Ocean.

(every 1–2 h) measured with the use of a satellite navigation system. Upon leaving the convergence zone, the transmitting vessel turned around to cross the zone again. At that time, the receiving vessel was used to measure the sound speed profile $c(z)$. The maximal depth of the survey was no greater than 500 m. The diurnal variations in the $c(z)$ profile are illustrated in Fig. 2, where a set of profiles measured in one of the experiments is presented. The greatest changes in the $c(z)$ profiles were observed in the temperature discontinuity layer, the layer where the maximal absolute value of the negative gradient in the sound speed occurred: both the value of the gradient and the position of the layer varied. The main cause of the changes observed is the presence of internal waves.

As the initial experimental data for estimating the diurnal variations in the position of the first convergence zone and for determining its intensity structure, the sound field levels measured by a 2307 Bruel&Kjar device were used. The measurements were performed in a mode of recording the absolute arithmetic mean values with running averaging over 1- to 2-s intervals.

After digitization, the sound field levels varying with distance were stored in a computer memory. Thus, the initial data for the subsequent processing had the form of a set of arrays that contained the mean sound field levels repeatedly measured in different parts of the first convergence zone within 24 h. The data arrays were adjusted to each other in distance. The step in distance, which was used in creating the arrays, was 10 to 25 m, depending on the particular experiment and the reception depth. Figure 3 shows the variations in the sound field level within the first convergence zone, as measured in one of the experiments. The sound field levels (in dB re $2 \cdot 10^5$ Pa) that are represented by the ordinate axis refer to the upper curve. All other curves are artificially spaced in vertical.

The position of the nearest boundary of the convergence zone and the distance from the source to this boundary were determined for a level of –3 dB relative to the maximum measured at the initial part of the zone. In analyzing the bulk of the experimental data, the mean values obtained for the position of the convergence zone were corrected within some limits of the above threshold level to obtain a minimal scatter in the values of the distance to the zone boundary. The data of these measurements are summarized in Table 1. The following notations are used in the table: Z_0 for the depth of the towed source, Z_1 for the depth of the receiver, R_0 for the experimental mean distance to the nearest boundary of the convergence zone, R_{01} for the same distance calculated with the $c(z)$ profiles measured in the experiments, and S_R for the standard deviation of the distance to the zone.

The aforementioned study revealed diurnal variations in the position of the nearest boundary of the convergence zone.

The standard deviation of the distance to the zone varied from 150 to 300 m. The exception is the Sea of Japan, where a maximal standard deviation of 700 m was observed.

The mean value of the distance to the nearest shadow zone differed by 0.5–2.5 km from the calculated value averaged over the sound speed profiles measured during the experiment. The calculations led to a shorter distance (than the experimental one) for the Norwegian Sea and to a longer distance for other ocean regions. All the calculations were carried out with the use of Tebyakin's computer code [8] by using the sound speed profiles measured in the experiment as the input data. The sound speed profiles were continued down to

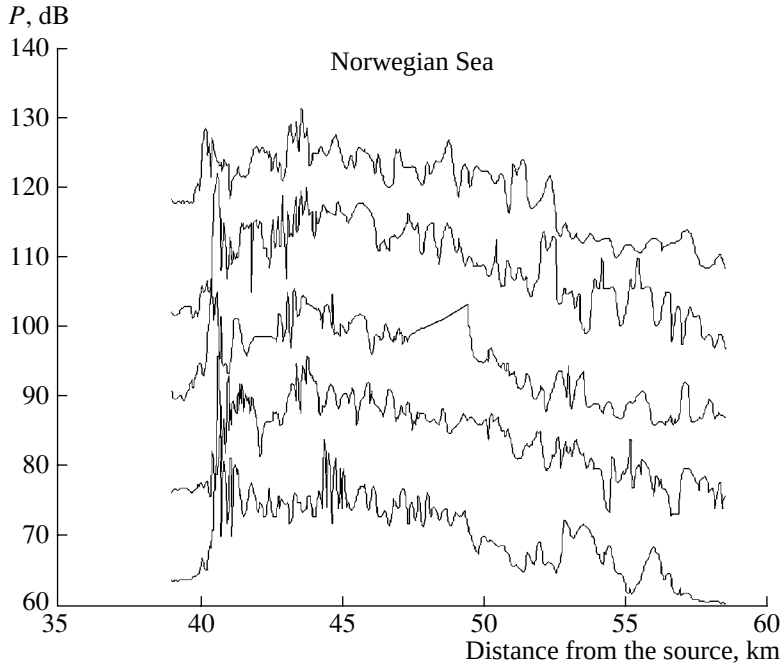

Fig. 3. Diurnal variability of the intensity structure of the sound field in the vicinity of the first convergence zone in the Norwegian Sea. The depths of the source and receiver are 120–125 and 150 m, respectively.

the bottom according to the data of deep-water hydrological surveys nearest to the shallow ones in space and time.

2. Some early studies [1, 3] that reported on the discrepancy between the measured and calculated positions of the convergence zone focused on the problem of the best choice of the relations (known at that time) between the sound speed and the temperature, salinity, and hydrostatic pressure, rather than on the reason for the discrepancy. In these studies, the quality criterion for the relation chosen was the agreement between the measured and calculated distances to the zone. Such an approach, the estimation of the agreement between the calculated propagation time of the probing signal and the sea depth measured by echo sounding, was also used by Meinen and Watts [9], who performed a comparison of the expressions proposed by Del Grosso [10] and by Chen and Millero [11] for calculating the sound speed.

Normally, the sound speed is obtained by recalculating the salinity and temperature of the sea water at certain depths. In recalculations, the relations between the

Table 1. Data of 12- to 24-h observations on the position of the nearest boundary of the first convergence zone in different ocean regions

Ocean regions	Z_0, m	Z_1, m	R_0, km	S_R, m	R_{01}, km
Indian Ocean (24 h)	120–125	160	56.4	240	59.0
		470	54.6	220	56.6
Atlantic Ocean (24 h)	110	200	58.7	232	59.5
		500	57.0	280	57.4
Atlantic Ocean (24 h)	20	150	60.8	220	62.0
		500	59.6	200	60.0
Norwegian Sea (24 h)	120–125	15	44.0	300	43.9
		60	41.4	170	40.2
		150	40.5	150	39.2
		500	36.3	100	35.6
Mediterranean Sea (12 h)	84–88	15	28.4	200	30.3
Sea of Japan (24 h)	70–85	20	42.1	700	43.1

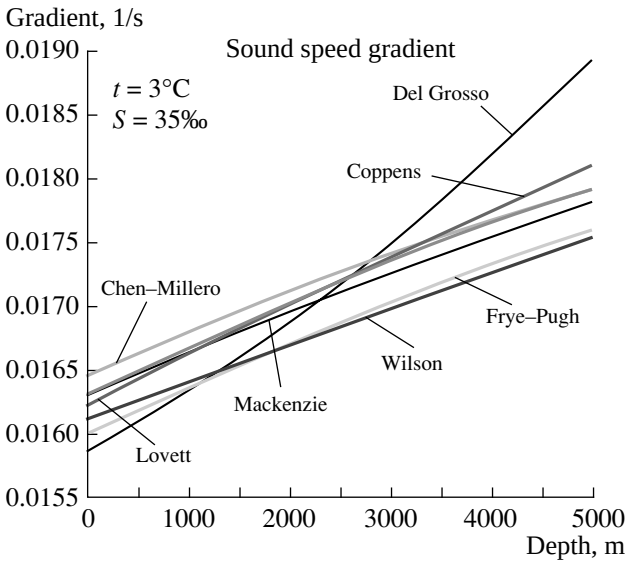

Fig. 4. Calculated depth dependences of the sound speed gradient at constant temperature and salinity (3°C and 35‰, respectively); the formulas proposed by different researchers are used.

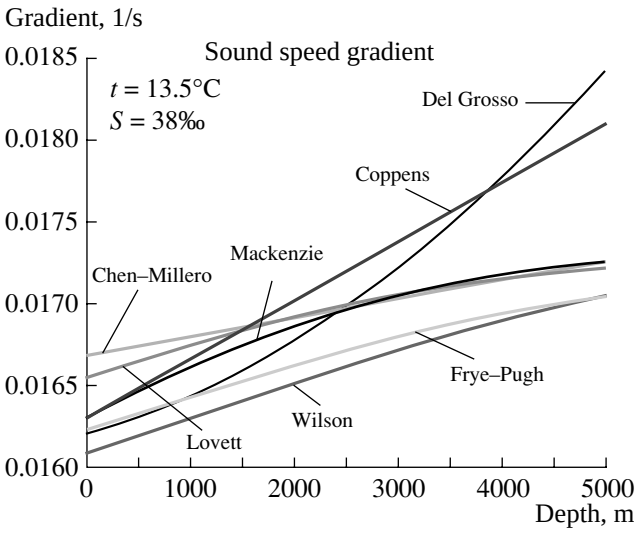

Fig. 5. Calculated depth dependences of the sound speed gradient at constant temperature and salinity (13.5°C and 38‰, respectively); the formulas proposed by different researchers are used.

sound speed, salinity, temperature, and hydrostatic pressure (or depth), which are derived from a bulk of experimental data, are used.

The six formulas proposed by several researchers [10–15] for recalculating the temperature, salinity, and hydrostatic pressure into the sound speed were analyzed. All of these formulas were obtained on the basis of experimental data characterizing the dependence of the sound speed on the hydrological parameters. In different studies, different parameters were used as the initial ones, namely, the temperature, salinity, and depth or the temperature, salinity, and hydrostatic pressure. To bring these relations into a common form $c(t, S, z)$, the hydrostatic pressure was converted into the depth by using the formula proposed by Polosin [16].

To compare different relations, a set of calculations was performed for different values of the parameters of the sea medium. The most demonstrative results were obtained for the sea medium with constant temperature and salinity in depth [17].

Figure 4 shows the resulting gradients of the sound speed. The calculations were performed for depths from 0 to 5000 m with temperature and salinity of 3°C and 35‰, respectively. The scatter in the gradient values calculated with different formulas reaches 0.0005 s^{-1} at smaller depths and is even greater for depths of 3–4 km and over. Such changes in the gradient of the sound speed are quite sufficient to displace the convergence zone by more than 1 km. This was a somewhat unexpected result.

Figure 5 shows the results of similar calculations performed for a temperature of 13.5°C and a salinity of 38‰, which are characteristic of the Mediterranean Sea. The scatter in the sound speed gradients calculated by using different formulas is not at all lower. Therefore, the calculations were continued in a somewhat different way.

3. A set of calculations was carried out in connection with the diurnal observations of the position of the convergence zone. The $c(z)$ profiles were calculated for each of the five ocean regions. In the calculations, depth dependences of the temperature and salinity measured in the experiments were used (for depths greater than 1500–2000 m, the temperature and salinity were taken from the archive data). Eight relations published by different researchers in different years [10–15, 18, 19] were used to recalculate the temperature, salinity, and hydrostatic pressure (depth) into the sound speed. For each region, eight $c(z)$ profiles were obtained. These profiles were used to calculate the sound field and the distance from the source to the nearest boundary of the first convergence zone. The positions of the source and receiver were specified according to the experimental layouts. The results obtained are summarized in Table 2.

For nearly all the regions, the minimal distance to the zone is obtained by the use of the Kuwahara–Mackenzie relations. These relations (in contrast to other ones used) are based on the results of recalculating the dependences of the modulus of the volume elasticity and the density of the sea medium on the temperature, salinity, and hydrostatic pressure into the sound speed. These results were presented in the form of tables by Kuwahara [20] in the late 1930s and in the form of empirical relations proposed by Mackenzie [19] in 1960.

Table 2. Distance from the source to the nearest boundary of the convergence zone. The calculations of the sound field are performed for a number of sea regions with the $c(z)$ profiles obtained by using different formulas. Comparison of the calculations with the experiment

Sea region	Transmission depth	Reception depth	Kuwahara and Mackenzie 1960	Wilson 1962	Frye and Pugh 1971	Del Grosso 1974	Chen and Millero 1977	Lovett 1978	Coppens 1981	Mackenzie 1981	Experiment
Indian Ocean	120 m	160 m	55.575	58.225	57.975	56.675	56.925	56.925	57.125	57.475	56.4 km
		470 m	53.575	56.275	55.975	54.725	54.875	54.925	55.175	55.475	54.6 km
Atlantic Ocean	110 m	200 m	57.725	60.175	59.975	58.475	59.025	59.025	59.025	59.425	58.7 km
		500 m	55.525	58.175	57.975	56.625	57.025	57.075	57.125	57.475	57.0 km
Norwegian Sea	122 m	15 m	41.425	44.425	44.425	44.075	43.525	43.725	44.875	43.875	44.0 km
		60 m	38.175	40.775	41.125	40.925	40.375	40.375	40.375	40.625	41.4 km
		150 m	36.975	39.325	39.425	39.475	38.875	39.125	38.775	39.175	40.5 km
		500 m	33.575	35.725	35.825	35.875	35.325	35.625	35.325	35.625	36.3 km
Sea of Japan	80 m	20 m	41.825	45.725	44.825	45.275	43.875	43.925	44.125	44.275	42.1 km
Mediterranean Sea	86 m	15 m	27.775	30.475	27.525	30.325	29.675	29.325	29.975	29.775	28.4 km

For seven $c(z)$ profiles (except for one obtained with the Kuwahara–Mackenzie formula), the minimal scatter in the calculated distances to the zone was 0.5 km for a reception depth of 500 m in the Norwegian Sea. The maximal scatter, 2.9 km, was obtained for the Mediterranean Sea. In the Indian and Atlantic oceans, the scatter in the calculated distances to the zone was 1.5–1.7 km.

For the sake of comparison, the experimentally measured distances to the zone are presented in the last column of Table 2. The best agreement between the measured and calculated distances is obtained with the Del Grosso formula [10] for the Indian Ocean and with the Chen–Millero formula [11] for the Atlantic Ocean. Note that the difference between the experimental and calculated distances given by both methods is lower than 0.4–0.5 km for these regions. It is worth mentioning that the relation proposed by Chen and Millero in the early 1980s was recommended by UNESCO for oceanological calculations.

The Del Grosso relation leads to the best agreement between the experiment and the calculations for the Norwegian Sea. In this case, the distance calculated according to Del Grosso differs from that calculated according to Chen and Millero by about 0.55 km, independently of the reception depth.

For the Sea of Japan and the Mediterranean Sea, the best agreement between the experiment and the calculations corresponds to the sound speed estimated according to Kuwahara. For the Mediterranean Sea, the experimental value of the distance to the zone falls between the values calculated with the Kuwahara and Lovett formulas (the difference between these two calculated values is 1.55 km). Such a result agrees well with the experimental data of other researchers. According to English [1] (1963), in the experiments performed by Hace (Woods Hole) in the Mediterranean Sea, the experimental distance to the convergence zone falls between the values calculated with the formulas of Kuwahara and Wilson. From the statements of English, it also follows that the experimental value of the distance is closer to that given by the Kuwahara relation.

The studies performed show that none of the relations tested can be treated as a universal one for the calculation of the sound speed in the sea medium. At the same time, for all the ocean regions at hand, a relation exists that leads to a satisfactory agreement between the calculated and measured distances to the convergence zone. It seems that such a situation is a consequence of some individual properties of the propagation conditions in these regions.

What is the fundamental difference in the regions at hand from the viewpoint of the mechanisms of the sound field formation in the vicinity of the first convergence zone?

The first difference consists in the position of the axes of the underwater sound channel (USC). In the Atlantic and Indian oceans, the depth of the USC axis is about 1500 m. The beginning of the zone is formed by the rays whose lower turning point is at depths of 3–4 km. In this case, the distance to the zone strongly depends on the hydrostatic gradient of the sound speed at these depths. In the Mediterranean Sea and in the Sea of Japan, the USC axis is at depths of 150–250 m. The beginning of the convergence zone is formed by the rays with turning points at 1–2 km. For these ocean regions, the distance to the zone depends on the hydrostatic gradient at much shallower horizons (0.5–2 km). The Norwegian Sea is intermediate in this respect.

The second difference consists in the temperature of the water bulk below the USC axis. This temperature is 2–4°C in the Atlantic and Indian oceans, lower than 0°C in the Sea of Japan and the Norwegian Sea, and 13–13.5°C in the Mediterranean Sea. One should keep in mind that, apart from the direct dependence of the hydrostatic gradient on the depth, the relations proposed by different researchers contain the cross terms determining the temperature dependence.

Such fundamental differences between the regions could be used for correcting the formulas for calculating the sound speed from the temperature, salinity, and hydrostatic pressure in view of the experimental data on the position of the first convergence zone. The need for such a correction is beyond question.

From the studies performed, the following conclusions can be drawn regarding the main reasons for the discrepancies between the experimental and calculated positions of the first convergence zone:

(i) The diurnal variability of the propagation conditions leads to substantial changes in the distance from the source to the nearest boundary of the convergence zone. However, the lack of simultaneity in the hydrological and acoustic measurements, which is one of the reasons for the difference between experiment and calculations, can only partially account for the discrepancies observed.

(ii) The substantial difference in the relations proposed by different researchers for calculating the sound speed from the temperature and salinity measured at different depths seems to be the main cause of the difference in the experimental and calculated distances to the zone. The calculations of the sound field with the $c(z)$ profiles obtained by using different formulas for recalculating the temperature and salinity at different depths into the sound speed lead to a scatter in the distance to the zone within the same range of values (in order of magnitude) as those reported by different researchers.

(iii) From all the relations proposed for recalculating the temperature, salinity, and hydrostatic pressure into the sound speed, one cannot select a universal one that leads to the best agreement between the experimental and calculated distances to the zone (at least, for the five regions analyzed). In constructing such a relation, the experimental data on the position of the first convergence zone should be taken into account.

ACKNOWLEDGMENTS

This work was supported by the Russian Foundation for Basic Research, project nos. 04-02-16959 and 04-05-64557.

REFERENCES

1. M. Greenspan and C. E. Tschiegg, in *Underwater Acoustics*, Ed. by V. M. Albers (Plenum, New York, 1963; Mir, Moscow, 1965).
2. N. S. Ageeva and L. S. Raĭskaya, Morsk. Priborostr., No. 1, 8 (1972).
3. V. P. Shevtsov, Okeanologiya (Moscow) **12** (3), 575 (1972).
4. O. P. Galkin, E. A. Kharchenko, and L. V. Shvachko, in *Proceedings of IX All-Union Acoustical Conference* (Moscow, 1977), Sect. D, pp. 1–4.
5. R. A. Vadov, Akust. Zh. **41**, 202 (1995) [Acoust. Phys. **41**, 172 (1995)].
6. R. A. Vadov, Akust. Zh. **49**, 278 (2003) [Acoust. Phys. **49**, 230 (2003)].
7. A. E. Vedeneev, O. P. Galkin, I. S. Rogozhkin, and L. M. Filippov, Vopr. Sudostr., Ser. Akust., No. 15, 122 (1982).
8. V. P. Tebyakin *et al.*, *A Report of Institute of Acoustics, USSR Acad. Sci.* (Moscow, 1990).
9. C. S. Meinen and D. R. Watts, J. Acoust. Soc. Am. **102**, 2058 (1997).
10. V. A. Del Grosso, J. Acoust. Soc. Am. **56**, 1084 (1974).
11. C. T. Chen and F. J. Millero, J. Acoust. Soc. Am. **62**, 1129 (1977).
12. W. D. Wilson, J. Acoust. Soc. Am. **32**, 1357 (1960).
13. J. R. Lovett, J. Acoust. Soc. Am. **63**, 1713 (1978).
14. A. B. Coppens, J. Acoust. Soc. Am. **69**, 862 (1981).
15. K. W. Mackenzie, J. Acoust. Soc. Am. **70**, 807 (1981).
16. A. S. Polosin, Vestn. Mosk. Univ., No. 3, 101 (1967).
17. R. A. Vadov, in *Proceedings of 13th Session of the Russian Acoustical Society* (GEOS, Moscow, 2003), Vol. 4, pp. 27–32.
18. H. W. Frye and J. D. Pugh, J. Acoust. Soc. Am. **50**, 384 (1971).
19. K. W. Mackenzie, J. Acoust. Soc. Am. **32**, 100 (1960).
20. S. Kuwahara, Hydrogr. Rev. **16** (2), 123 (1939).

Translated by E. Kopyl

Acoustical Physics, Vol. 51, No. 3, 2005, pp. 271–281. Translated from Akusticheskiĭ Zhurnal, Vol. 51, No. 3, 2005, pp. 330–341.

Signal Travel Times along Chaotic Rays in Long-Range Sound Propagation in the Ocean

A. L. Virovlyansky

Institute of Applied Physics, Russian Academy of Sciences,
ul. Ul'yanova 46, Nizhni Novgorod, 603600 Russia
e-mail: viro@hydro.appl.sci-nnov.ru

Received May 5, 2004

Abstract—Numerical calculations show that, in the presence of weak fluctuations of sound velocity, ray trajectories in underwater acoustic waveguides exhibit a chaotic behavior. According to the findings of the late 1990s, under the chaotic conditions, the travel times of sound pulses along trajectories connecting the source and receiver form compact clusters. Each cluster is formed by the rays that have the same sign of their launch angles at the source and the same number of turning points. The cluster center is close to the arrival time of an unperturbed ray with a similar topology. The paper presents a quantitative description of this phenomenon. The ray structure of the field is analyzed using the Hamiltonian formalism in terms of the action–angle canonical variables. The width of the cluster and its shift with respect to the unperturbed ray arrival are estimated. The results of the study explain (from the point of view of geometrical optics) the presence of stable maxima in the initial part of a pulse signal, which are observed in the field and in numerical experiments on the long-range sound propagation in the ocean. © *2005 Pleiades Publishing, Inc.*

I. INTRODUCTION

The results of numerical modeling and the data of field experiments demonstrate that the method of geometrical optics allows one to adequately predict a number of sound field characteristics in the deep sea at distances of up to several thousands of kilometers [1–3]. This stimulates the development of ray methods for analyzing long-range sound propagation in the ocean.

In the geometrical optics approximation, the signal in an acoustic waveguide represents a sum of pulses arriving at the observation point along different ray trajectories [4]. For brevity, the travel times of such pulses are called ray travel times. In the late 1970s, it was already known that, even at a distance on the order of 1000 km, the pulses arriving at the receiver along different steep rays form rather steady peaks of the received signal, which often are resolved in time [5]. This is explained by the fact that random inhomogeneities of the medium lead to a splitting of the unperturbed ray into a bundle of microrays with close trajectories and, therefore, with close travel times [6].

However, in the second half of the 1990s, when the appearance of high-performance computers allowed one to model the ray dynamics in realistic models of underwater waveguides, it was found that the situation is much more complicated and interesting [7–10]. It was found that the presence of weak and rather small-scale inhomogeneities of the sound velocity induces ray chaos, which is an analog of the dynamical chaos in mechanics [11]. Ray chaos is a general property of range-dependent waveguides and is observed in various models of underwater sound channels [7–9, 12–16]. Chaotic rays are very unstable: the difference in the vertical coordinates δz of the trajectories with close initial conditions increases with range r, on average, according to the exponential law (as long as this difference is small compared to the transverse size of the waveguide):

$$|\delta z| \sim e^{\lambda r}, \tag{1}$$

where $\lambda > 0$ is the Lyapunov exponent.

Such a behavior of the trajectories is observed in the simplest (however, quite realistic) two-dimensional model of the underwater sound channel in a deep sea [2, 17], where the sound velocity field $c(r, z)$ (r is the distance, z is the depth) is represented as

$$c(r, z) = c_0(z) + \delta c(r, z). \tag{2}$$

Here, $c_0(z)$ is the smooth unperturbed profile and $\delta c(r, z)$ is the random internal-wave-induced perturbation with statistics described by the Garrett–Munk spectrum [6, 18]. In spite of its weakness, this perturbation causes chaotic behavior of the ray trajectories with Lyapunov exponent λ on the order of 1/100 km^{-1} for the flat rays and 1/300 km^{-1} for the steep rays [2, 10]. Because of the exponential divergence of the trajectories at long ranges, one does not deal with bundles of stochastic microrays weakly deviating from the initial unperturbed ray in this case.

Under the chaos conditions, the number of rays connecting the source and the receiver on long tracks is very large. However, their arrival times are unexpectedly grouped in rather compact clusters [2, 9]. Each cluster is formed by the rays with the same iden-

tifier $\pm M$, where $\pm$ is the sign of the launch angle of a ray at the source and M is the number of turning points. The center of the cluster is close to the arrival time of the unperturbed ray with the same identifier. It is important to note that the rays forming a cluster, in spite of the identity of their topology, can considerably diverge in space. A remarkable feature of steep rays is the fact that the clusters formed are resolved in time and form stable maxima in the signals observed in the experiments [2].

The aim of this paper is the statistical description of the clustering effect. For analyzing the ray dynamics, we use an approach developed in [19–21] (the last reference [21] is an e-print that can be found on the Internet at xxx.lanl.gov.). This approach is based on the Hamiltonian formalism expressed in terms of the action–angle canonical variables (I, θ). They are widely used for analyzing the finite motions of particles in mechanics and for studying oscillations of ray trajectories in waveguides [7, 22].

Because of the weakness of sound velocity fluctuations, even at long range the variation of the action variable I remains small compared to the scale typical of the dependence of the unperturbed Hamiltonian on I. The presence of this small parameter of the problem, which can hardly be "discerned" when operating with the standard momentum–coordinate variables, allows one (i) to find an unexpectedly simple approximate formula connecting the variations of the ray arrival times with the action variable variations and (ii) to approximate the fluctuations of the action variable by the Wiener random process, which represents the simplest diffusion model [23, 24]. As a result, one can estimate the width of the cluster and find its shift with respect to the arrival time of the unperturbed ray. It is shown that, on long tracks, this shift is directed toward early times; i.e., the perturbed pulses arrive somewhat earlier than the unperturbed ones.

2. THE HAMILTONIAN FORMALISM FOR THE DESCRIPTION OF RAY TRAJECTORIES

2.1. Momentum–Coordinate Variables

Consider an acoustic waveguide with a sound velocity field given by Eq. (2). Let the z axis be directed upwards and the water surface be at the level $z = 0$. The refractive index is $n(r, z) = c_r/c(r, z)$, where c_r is a constant (we suppose that $|c(r, z) - c_r| \ll c_r$). In the momentum–coordinate variables (p, z), the ray equations have the form of the Hamiltonian equations [7, 10, 13]

$$\frac{dz}{dr} = \frac{\partial H}{\partial p}, \quad \frac{dp}{dr} = -\frac{\partial H}{\partial z}, \tag{3}$$

with the Hamiltonian

$$H = -\sqrt{n^2 - p^2}. \tag{4}$$

The equations

$$p = n\sin\chi, \quad H = -n\cos\chi \tag{5}$$

relate the momentum p and the Hamiltonian H with the ray grazing angle χ. The ray arrival time is $t = \int ds/c$, where ds is the element of the ray trajectory arc. This time can be represented as $t = c_r^{-1} S$, where

$$S = \int (pdz - Hdr) \tag{6}$$

is the eikonal. In optical-mechanical analogy, the role of time is played by the coordinate r while the eikonal S is an analog of the mechanical action [7, 10, 13, 25].

2.2. Action–Angle Variables

The canonical transformation relating the momentum–coordinate (p, z) and the action–angle (I, θ) variables is given by the known relationship [22]

$$dS = pdz - Hdr = dG - \theta dI - Hdr, \tag{7}$$

where $G(I, z, r)$ is the generating function. To determine the function G, we consider the unperturbed waveguide with the refractive index profile $n_0(z) = c_r/c_0(z)$. In such a waveguide, the Hamiltonian

$$H_0 = -\sqrt{n_0^2(z) - p^2} \tag{8}$$

is conserved along the ray trajectory. The action variable I is determined by the integral [7, 22]

$$I = \frac{1}{2\pi}\oint pdz = \frac{1}{\pi}\int_{z_{\min}}^{z_{\max}} dz\sqrt{n_0^2(z) - H_0^2} \tag{9}$$

over the trajectory oscillation cycle. The coordinates $z_{\min}$ and $z_{\max}$ are depths of the ray turning points. At these depths, $n_0(z) = H_0$. Equation (9) defines the Hamiltonian H_0 as a function of the variable I. The ray trajectory in the unperturbed waveguide is a periodic curve with the cycle length $D = 2\pi/\omega$, where

$$\omega(I) = \frac{dH_0(I)}{dI}. \tag{10}$$

Let us assume that the oscillation cycle of the ray trajectory begins at the minimum of the cycle. In the first half-cycle, where the variable θ varies from 0 to π, the canonical transformation is determined by equations [7, 13, 22]

$$p = \frac{\partial G}{\partial z}, \quad \theta = \frac{\partial G}{\partial I}, \tag{11}$$

with the generating function

$$G(I, z) = \int_{z_{\min}}^{z} dz\sqrt{n_0^2(z) - H_0^2(I)}. \tag{12}$$

These formulas define the direct

$$I = I(p, z), \quad \theta = \theta(p, z), \tag{13}$$

and inverse

$$p = p(I, \theta), \quad z = z(I, \theta) \tag{14}$$

canonical transformations. In the second half-cycle, where θ varies from π to 2π, the transformations are continued with the use of the following relationships: $p(I, \theta) = -p(I, 2\pi - \theta)$ and $z(I, \theta) = z(I, 2\pi - \theta)$. At the beginning of each new cycle, θ returns to the value $\theta = 0$ in a jumplike manner.

This transformation can also be used in the perturbed waveguide with $\delta c \neq 0$. In this case, the Hamiltonian can be represented in the form

$$H = H_0 + V, \tag{15}$$

where

$$V(p, z, r) = -\sqrt{n^2(z, r) - p^2} + \sqrt{n_0^2(z) - p^2} \simeq \delta c / c_r. \tag{16}$$

Since generating function (12) does not depend on r, the Hamiltonian H in terms of new variables (I, θ) is expressed by the simple substitution of Eq. (14) into Eqs. (15) and (16). As a result, we obtain

$$H(I, \theta, r) = H_0(I) + V(I, \theta, r). \tag{17}$$

We rewrite Eq. (7) in the form $dS = d(G - I\theta) - Id\theta - Hdr$ and note that, in spite of the jumps of θ from 2π to 0 on passing through each minimum, the combination $G - I\theta$ is a continuous function of distance. At the trajectory minima, i.e., at the origin and end of each cycle, this combination is zero. Integrating dS and taking into account the aforesaid, we obtain the expression for the ray eikonal as the sum (here and below, we assume that the ray trajectories begin at the distance $r = 0$)

$$S = S_a + S_b, \tag{18}$$

where

$$S_a = -G(z_0, I_0) + G(z_1, I_1) + \theta_0 I_0 - \theta_1 I_1 \tag{19}$$

and

$$S_b = \int_0^r (Id\theta - (H + V)dr). \tag{20}$$

Here and in what follows, we use subscripts 0 and 1 to indicate the ray parameters at the initial and terminal points of the trajectory, respectively.

It is convenient to make the angular variable θ be a continuous function of distance. For this purpose, we add $2\pi\nu$ to its values at the νth cycle of the trajectory. In this case, $p(I, \theta)$ and $z(I, \theta)$ become periodic functions of θ with a period of 2π. The transfer to the continuous θ does not change Eq. (20), but, in formula (19), θ_1 is now understood as the terminal value of the angular variable taken modulo 2π. For the trajectory with N cycles, the magnitude of the continuous angular variable at the terminal point is related to θ_0 and θ_1 by the relationship

$$\theta = 2\pi N - \theta_0 + \theta_1. \tag{21}$$

The ray equations (Hamiltonian equations) in terms of the new variables take the form

$$\frac{dI}{dr} = -\frac{\partial V}{\partial \theta} \tag{22}$$

and

$$\frac{d\theta}{dr} = \omega + \frac{\partial V}{\partial I}. \tag{23}$$

The canonical transformation determined by Eqs. (11) and (12) can be expressed analytically in an explicit form only for several specifically chosen profiles $n_0(z)$ [7, 13]. However, in underwater acoustics, we should deal with the refractive index profiles obtained by the spline approximation of the data of measurements performed at a finite number of points. In this case, the calculation of the ray trajectories is carried out using the standard ray codes [26]. The same codes can be used for calculating the variables I and θ. The question about the numerical realization of the canonical transformation determined by Eqs. (11) and (12) is briefly discussed in [21] using the standard ray code. The procedure described in [21] is used in obtaining the numerical results presented in Section 6.

2.3. The Ray Arrival Time Differences

We compare the eikonals of two rays, the trajectory of one of the rays lying in the perturbed waveguide (the "perturbed" ray) and the trajectory of another ray in the unperturbed waveguide (the "unperturbed" ray) ($\sigma c = 0$). The unperturbed ray parameters will be denoted by an overbar. Assume that the perturbation V is proportional to a small parameter ε and that the initial values of the action variables of the compared rays are close to each other. Then, according to Eq. (22), the difference between these variables at any distance will be $\delta I = I - \bar{I} = O(\varepsilon)$. We impose no other restrictions. The rays can be launched from different depths z_0 and $\bar{z}_0$ and arrive at depths z_1 and $\bar{z}_1$. In spite of the fact that the rays propagate over the same distance along the axis r, their trajectories may have different numbers of cycles, namely, N and $\bar{N}$.

The eikonal of the unperturbed ray $\bar{S}$ is determined by formulas (18)–(20), which are simplified due to the fact that $\bar{I}$ does not depend on distance. In particular,

$\bar{I}_1 = \bar{I}_2 = \bar{I}$. Using Eqs. (10) and (11) for the difference in the components of eikonal (19), we find

$$S_a - \bar{S}_a = -[G(z_0, \bar{I}) - G(\bar{z}_0, \bar{I})] + [G(z_1, \bar{I}) - G(\bar{z}_1, \bar{I})] + \bar{I}(\delta\theta_0 - \delta\theta_1) + O(\varepsilon^2). \quad (24)$$

Here, $\delta\theta_{0,1} = \theta_{0,1} - \bar{\theta}_{0,1}$. The difference in the components (20) is accumulated with the distance, and, in estimating this difference, we retain the terms on the order of $O(\varepsilon^2)$. Using the fact that, according to Eq. (23), $d\theta = (\omega(I) + \partial V/\partial I)dr$ and $d\bar{\theta} = \omega(\bar{I})dr$, we obtain

$$S_b - \bar{S}_b = \int_0^r \left(\bar{I}\bar{\omega}'\delta I + \frac{1}{2}(\omega' + \bar{I}\bar{\omega}'')\delta I^2\right)dr + \int_0^r (\bar{I}\partial V/\partial I - V + \delta I \partial V/\partial I)dr + O(\varepsilon^3). \quad (25)$$

The symbols $\bar{\omega}'$ and $\bar{\omega}''$ denote the first and second derivatives of $\omega(\bar{I})$ with respect to $\bar{I}$. The difference in the angular variables for the rays at the track end, with an accuracy up to the terms proportional to ε^2, is equal to

$$\delta\theta = \int_0^r \left(\bar{\omega}'\delta I + \frac{1}{2}\bar{\omega}''\delta I^2 + \partial V/\partial I\right)dr = 2\pi\Delta N - \delta\theta_0 + \delta\theta_1, \quad (26)$$

where $\Delta N = N - \bar{N}$. The last equality in Eq. (26) follows from Eq. (21). Substituting Eq. (26) into Eq. (25) and combining Eq. (25) and Eq. (24), we find

$$\delta S = S - \bar{S} = -[G(z_0, \bar{I}) - G(\bar{z}_0, \bar{I})] + [G(z_1, \bar{I}) - G(\bar{z}_1, \bar{I})] + 2\pi\Delta N\bar{I} + \int_0^r V dr + \frac{\bar{\omega}'}{2}\int_0^r \delta I^2 dr + \int_0^r \delta I \partial V/\partial I dr. \quad (27)$$

In deriving this formula, we have expanded the difference $\omega(I) - \omega(\bar{I})$ in powers of δI and retained only the two first terms. This can be done only in the case when δI is much smaller than the typical scale of the function $\omega(I)$. In other words, the following inequality must be valid:

$$\mu = \left|\frac{d\omega}{dI}\right|\frac{\delta I}{\omega} \ll 1. \quad (28)$$

It should be emphasized that this inequality does not assume that the change in the variable I is small compared to the initial value of I. In [21], it was shown that, in a typical deep-water waveguide with inhomogeneities caused by internal waves, this condition is valid even at distances of the order of several thousands of kilometers. In the same paper, it was also shown that the last term in Eq. (27) can be neglected. In the case when the initial coordinates z_0 and $\bar{z}_0$ are close to each other, as are the terminal coordinates z_1 and $\bar{z}_1$, Eq. (27), with allowance for the first equality (12), can be represented in the form

$$\delta S = -\bar{p}_0\delta z_0 + \bar{p}_1\delta z + 2\pi\Delta N\bar{I} + \frac{\bar{\omega}'}{2}\int_0^r \delta I^2 dr + \int_0^r V dr, \quad (29)$$

where $\bar{p}_0$ and $\bar{p}_1$ are the initial and terminal momenta of the unperturbed ray, respectively, while $\delta z_{0,1} = z_{0,1} - \bar{z}_{0,1}$. In such a form, the expression for δS was obtained in [19] (see also [20, 21]).

For the difference in the arrival times of the rays connecting a point source and a receiver ($z_{0,1} = \bar{z}_{0,1}$), from Eq. (29) with allowance for Eq. (16) we obtain

$$\delta t = t - \bar{t} = \delta t_N + \delta t_V + \delta t_I, \quad (30)$$

where

$$\delta t_N = 2\pi\Delta N\bar{I}/c_r, \quad (31)$$

$$\delta t_V = -\frac{1}{c_r^2}\int_0^r \delta c dr, \quad (32)$$

$$\delta t_I = +\frac{\bar{\omega}'}{2c_r}\int_0^r \delta I^2 dr. \quad (33)$$

In the unperturbed waveguide ($\delta c = 0$), the terms δt_V and δt_I are reduced to zero, and we arrive at the formula previously obtained in [27–29].

In the case when the rays to be compared have the same identifiers (i.e., the same topology), the term δt_N is reduced to zero. The terms δt_V and δt_I have different physical meanings. The first of them predominates at short ranges, where a weak perturbation has no time to cause noticeable distortions of the trajectory shape [5, 6]. At long ranges (several thousands of kilometers), the term δt_I [19, 21] becomes predominant for most rays. It takes into account the variations in the ray arrival times due to the change of the trajectory shape.

A simplified (but less rigorous) derivation of formula (30) in the situation when $\delta t_N = 0$, as well as the results of testing Eq. (30) by a direct numerical solution of the ray equations, are presented in the recent paper [30].

Formulas (27) and (29)–(33) relate the variations of the ray arrival times to variations of other trajectory parameters. For practical use of these results, it is necessary to express the statistical characteristics of the trajectories (determining the statistics of the right-hand parts of the above-mentioned formulas) in terms of the characteristics of the environmental inhomogeneities

causing the ray chaos. In the next section, the approximate method developed in [21, 31] (see also [20]) for solving this problem is briefly discussed.

3. THE STATISTICAL DESCRIPTION OF RAY TRAJECTORIES

Let us use the model of a deep-water acoustic waveguide with an unperturbed sound velocity profile $c_0(z)$ that is shown at the left of Fig. 1. The weak fluctuations of sound velocity $\delta c(r, z)$ are caused by the effect of the random field of internal waves with the statistics given by the empirical Garrett–Munk spectrum [6]. At each point of the waveguide, the mean value (over the ensemble of inhomogeneities) of the perturbation is $\langle \delta c(r, z) \rangle = 0$. For the numerical modeling of specific realizations of perturbation $\delta c(r, z)$, we use the method suggested in [18]. Omitting details (see [19, 21], where this model of the waveguide is described at length), we only note that the rms amplitude $\delta c(r, z)$ near the surface is equal to 0.5 m/s and decays with depth according to the law $\exp(-z/L)$, where $L = 0.66$ km. The spectrum of the dependence of the perturbation on the horizontal coordinate r is concentrated within the interval of spatial frequencies from $2\pi/100$ km^{-1} to $2\pi/4$ km^{-1}. The right-hand part of Fig. 1 shows the vertical sections of the field $\delta c(r, z)$ for three different distances. In such a waveguide model, the rays behave chaotically, and the trajectories with close initial conditions exponentially diverge as r increases. The values of the corresponding Lyapunov exponents are indicated in the Introduction.

Formally, ray equations (3) in a randomly inhomogeneous medium can be considered as stochastic equations whose parameters are determined by a random function δc. The analytical solution to these nonlinear equations can be obtained in the framework of ordinary perturbation theory only for short ranges, where the perturbation has no time to cause noticeable deviations of the trajectory from the unperturbed ray.

However, as is shown in [20], [21], and [31], the situation is simplified with the change to the action–angle variables. Because of the weakness of the perturbation, the variation of the action variable on the horizontal scales of the environmental inhomogeneities is small. Therefore, the right-hand side of Eq. (22) can be considered as a random δ-correlated function. In this case, $I(r)$ will be a Markovian process [23] with a probability density $P(I, r)$ obeying the Fokker–Plank equation

$$\frac{\partial P}{\partial r} = \frac{\partial}{\partial I} B \frac{\partial}{\partial I} P. \tag{34}$$

The calculation of the diffusion coefficient B is discussed in detail in [21], where it is shown that, in our model of the medium, the dependence of B on I is rather weak and the diffusion coefficient can be approximated with a constant to a good accuracy:

$$B = 1.5 \times 10^{-7} \text{ km}. \tag{35}$$

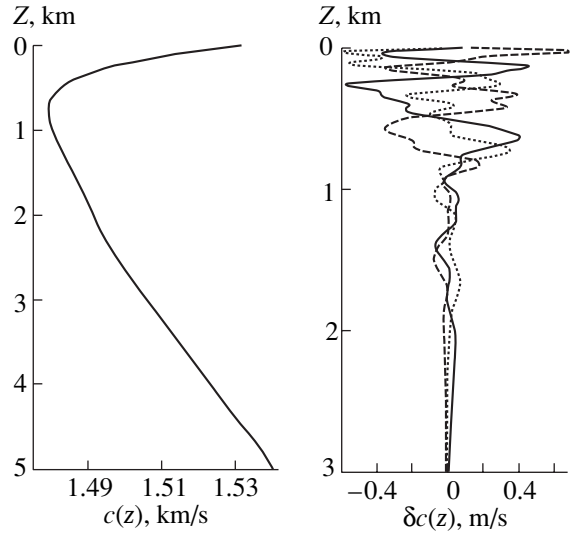

Fig. 1. Unperturbed sound velocity profile $c_0(z)$ (at the left) and the vertical sections of the perturbation $\delta c(r, z)$ for three different distances (at the right).

In this approximation, we have

$$I = I_0 + x, \tag{36}$$

where $x(r)$ is the Wiener random process [23, 24]. It starts at the point $x(0) = 0$ and obeys the stochastic equation

$$\frac{dx}{dr} = \xi(r), \tag{37}$$

where ξ is white noise with a zero mean and a correlation function $\langle \xi(r)\xi(r') \rangle = B\delta(r - r')$. Here and below, the angular brackets mean statistical averaging. Because the Wiener process is of a Gaussian nature, all its statistical characteristics are determined by the mean value and the correlation function:

$$\langle x \rangle = 0, \quad \langle x(r)x(r') \rangle = B\min(r, r'). \tag{38}$$

Some difficulty arises because the random function $I(r)$ given by Eqs. (36) and (37) can take both positive and negative values. However, the action variable is nonnegative by definition. This restriction is easily taken into account by introducing a reflecting boundary at $I = 0$. The solution to the Fokker–Plank equation (34) with the constant diffusion coefficient and the initial condition $P(I, 0) = \delta(I - I_0)$ in the presence of the reflecting boundary has the form [23, 24]

$$P(I, r) = \frac{1}{\sqrt{2\pi B r}} \left[\exp\left(-\frac{(I - I_0)^2}{2Br} \right) + \exp\left(-\frac{(I + I_0)^2}{2Br} \right) \right]. \tag{39}$$

Stochastic equation (37) approximates Hamiltonian equation (22).

For simplifying the second Hamiltonian equation, following [20, 21, 31], we replace $\omega(I)$ by $\omega(I_0) + \omega'(I_0)x$

and neglect the last term on the right-hand side of Eq. (23). Representing the angular variable in the form

$$\theta = \theta_0 + \omega(I_0)r + y, \tag{40}$$

instead of (23) we obtain the equation

$$\frac{dy}{dr} = \omega'(I_0)x \tag{41}$$

with the initial condition $y(0) = 0$. This yields

$$y(r) = \omega'(I_0)\int_0^r x(r')dr'. \tag{42}$$

In the approximation under consideration, which below will be called Wiener process approximation, the statistical moments and many other characteristics of I and of θ are easily expressed in integral form. The formulas obtained make it possible to analytically describe the chaotic ray structure of the field in an inhomogeneous waveguide.

In the following sections, this approach will be used for analyzing the clusters of the ray arrival times. We conditionally divide all rays into steep and flat ones: the steep (flat) rays are those intersecting the channel axis under a grazing angle greater (smaller) than 5°. The idea of this partition is that, for the steep rays, we can ignore the "reflections" of the action variable from the boundary $I = 0$. Then, in formula (39), we can neglect the second term in the square brackets. In this approximation, $\langle I\rangle = I_0$ and the variance of I grows according to the diffusion law

$$\langle (I - I_0)^2\rangle = Br. \tag{43}$$

In what follows, we restrict our consideration to analyzing only the steep rays.

4. RAYS WITH THE SAME IDENTIFIER

Let us choose one of the unperturbed rays connecting the source and the receiver and investigate the statistics of the perturbed (chaotic) rays characterized by the following properties: (i) they should have the same identifier $\pm M$ as that of the chosen unperturbed ray and (ii) they should arrive at the receiver. The arrival times of such rays form one of the clusters, as was mentioned in the Introduction. To solve this problem, we use a simplifying assumption that, on long tracks ($M \gg 1$), condition (ii) imposes weak additional limitations (as compared to condition (i)) on the statistical moments of the action variable, which will be calculated in this section. Therefore, the condition that a chaotic ray belongs to the cluster can be formulated as a rather simple inequality:

$$-\pi/2 < \theta - \theta_0 - (\bar\theta - \bar\theta_0) < \pi/2. \tag{44}$$

As in Subsection 2.3, the parameters of the unperturbed rays are marked with an overbar. From Eq. (44), with allowance for Eqs. (40) and (42), we obtain

$$-\pi/2 < (\omega(I_0) - \omega(\bar I))r + \omega'(I_0)\int_0^r x(r')dr' < \pi/2. \tag{45}$$

The smallness of the parameter μ (see expression (28)) allows one to approximately replace $\omega(I_0) - \omega(\bar I)$ by $\omega'(I_0)(I_0 - \bar I)$. As a result, inequality (45) takes the form

$$-\frac{\pi}{2|\omega'(\bar I)|r} + \bar I - I_0 < g < -\frac{\pi}{2|\omega'(\bar I)|r} + \bar I - I_0, \tag{46}$$

where

$$g = \frac{1}{r}\int_0^r x(r')dr'. \tag{47}$$

The probability density of a random Gaussian quantity g obtained with the help of Eq. (38) is equal to

$$P_g(g) = \sqrt{\frac{3}{2\pi Br}}\exp\left(-\frac{3}{2}\frac{g^2}{Br}\right). \tag{48}$$

The probability for the ray with the initial value of the action I_0 to obey condition (44) (we denote it by $P_0(I_0)$) is determined by the integration of $P_g(g)$ over interval (46). On long tracks, the width of this interval is considerably smaller than the scale of the function $P_g(g)$; i.e.,

$$\frac{\pi}{2|\omega'(\bar I)|r} \ll \sqrt{Br/3}, \tag{49}$$

and we obtain

$$\begin{aligned} P_0(I_0) &= P_g(\bar I - I_0)\frac{\pi}{|\omega'(\bar I)|r} \\ &= \sqrt{\frac{3\pi}{2B|\omega'(\bar I)|^2 r^3}}\exp\left(-\frac{3}{2}\frac{(\bar I - I_0)^2}{Br}\right). \end{aligned} \tag{50}$$

This suggests that the initial values of the action for the cluster-forming rays are concentrated mainly within the interval of width

$$\sigma_{I_0} = \sqrt{Br/3}. \tag{51}$$

To estimate the term δt_I involved in Eq. (30), we need to calculate the moments of the random quantity

$$\delta I(\rho) \equiv I(\rho) - \bar I = I_0 + x(\rho) - \bar I \tag{52}$$

within the interval of distances $0 \le \rho \le r$. Let us denote

$$a_{1,2} \equiv \delta I(\rho_{1,2}) \tag{53}$$

and calculate the correlation function

$$Q(\rho_1, \rho_2) = \langle a_1 a_2\rangle. \tag{54}$$

Here, the averaging is carried out over the rays forming the cluster, which satisfy condition (45).

For clarity, we assume that the rays launched from the source form a dense (in the limit, infinitely dense) fan. The number of rays with initial values of I within the small interval $(I_0, I_0 + dI_0)$ is equal to $\nu(I_0)dI_0$, where $\nu(I_0)$ is the density depending on the directional pattern of the source. We use the symbol $W_{g, a_1, a_2}(g, a_1, a_2)$ to denote the combined probability density of a_1, a_2, and g. The number of rays with the parameters I_0, a_1, and a_2 that belong to the intervals $(I_0, I_0 + dI_0)$, $(a_1, a_1 + da_1)$, and $(a_2, a_2 + da_2)$ is equal to

$$d\tilde{N} = \nu(I_0)W_{g, a_1, a_2}(\bar{I} - I_0, a_1, a_2)\frac{\pi}{|\omega'(\bar{I})|r}dI_0 da_1 da_2.$$

Here, we took into account that, according to inequality (46), the values of g for the cluster-forming rays are within the interval of width $dg = \dfrac{\pi}{|\omega'(\bar{I})|r}$ and assumed that the variations of the function $W_{g, a_1, a_2}(g, a_1, a_2)$ within this interval are small. Assuming that the dependence $\nu(I)$ is sufficiently smooth to replace $\nu(I_0)$ by $\nu(\bar{I})$, we obtain

$$Q(\rho_1, \rho_2) = \frac{\int a_1 a_2 d\tilde{N}}{\int d\tilde{N}} = \int a_1 a_2 W_{g, a_1, a_2}(\bar{I} - I_0, a_1, a_2)dI_0 da_1 da_2. \quad (55)$$

For calculating this integral, it is not necessary to know the explicit form of the function $W_{g, a_1, a_2}(g, a_1, a_2)$. Using the well-known representation of the probability density of the random quantity β in the form

$$P_\beta(b) = \langle \delta(b - \beta)\rangle, \quad (56)$$

where the angular brackets mean averaging over the statistical ensemble of the values of β, leads to the expression

$$W_{g, a_1, a_2}(\bar{I} - I_0, a_1, a_2) = \langle \delta(I_0 - \bar{I} + g)\delta(a_1 - I_0 + \bar{I} - x(\rho_1))\delta(a_2 - I_0 + \bar{I} - x(\rho_2))\rangle, \quad (57)$$

where averaging is carried out over the Wiener process realizations $x(\rho)$. Substituting Eq. (57) into Eq. (55) and using Eq. (38), we find

$$Q(\rho_1, \rho_2) = \langle (x(\rho_1) - g)(x(\rho_2) - g)\rangle = B\left(\frac{r}{3} - \rho_1 - \rho_2 + \frac{\rho_1^2 + \rho_2^2}{2r} + \min(\rho_1, \rho_2)\right). \quad (58)$$

This specifically yields

$$\langle \delta I^2(0)\rangle = \langle \delta I^2(r)\rangle = \frac{Br}{3}. \quad (59)$$

As is seen, at the end of the track (at the point $\rho = r$), the variance is less by a factor of three than that of the value (see Eq. (43)) obtained without allowance for limitation (46).

Because $\delta I(\rho)$ is a Gaussian random process with zero mean, all its statistical moments are expressed in terms of the second moment, i.e., in terms of the function $Q(\rho_1, \rho_2)$ [24, 32]. In particular, the fourth moment is equal to

$$\langle \delta I^2(\rho_1)\delta I^2(\rho_2)\rangle = Q(\rho_1, \rho_1)Q(\rho_2, \rho_2) + 2Q^2(\rho_1, \rho_2). \quad (60)$$

5. TRAVEL TIMES AND ARRIVAL ANGLES OF CHAOTIC RAYS

Let us first consider a bundle of the trajectories with launch angles within a narrow interval with the center at a point χ_0. On long tracks ($r \gg \lambda$), these trajectories diverge in space and their identifiers may be noticeably different from the identifier of the unperturbed ray with launch angle χ_0. Therefore, the scatter of the arrival times of rays from this bundle is governed by the first term in Eq. (30), which is given by Eq. (31) with $\bar{I}$ corresponding to the launch angle χ_0. At $\Delta N \neq 0$, this term, as a rule, predominates. Let us approximate ΔN with a continuous random quantity $y/(2\pi)$ and use the approximate expression that follows from Eqs. (38) and (42) for the variance of y:

$$\langle y^2\rangle = B(\omega')^2\frac{r^3}{3}. \quad (61)$$

Using Eq. (31), we find the estimate of the rms scatter of arrival times for the rays from the bundle under consideration:

$$\Delta t = |\omega'(\bar{I})|(B/3)^{1/2}\bar{I}r^{3/2}/c_r. \quad (62)$$

From this expression, in particular, it follows that the quantity Δt increases in proportion with $r^{3/2}$. Such a dependence on the distance agrees well with the results of other authors [30]. In spite of the roughness of this estimate, a comparison with the results of numerical modeling shows that it adequately predicts the order of magnitude of Δt and its dependence on the parameters of the problem.

We now turn to the analysis of the scatter of arrival times of the rays forming the cluster. The arrival time difference between a ray involved in the formation of the cluster and the unperturbed ray (arriving at the receiver) with the same identifier is determined by

Eq. (30) with $\delta t_N = 0$. As was noted in Subsection 2.3, on short tracks (up to ~1000 km), the value of δt_I is relatively small and $\delta t \simeq \delta t_V$. The statistical characteristics of δt_V in a deep-water waveguide with sound velocity inhomogeneities due to the random field of internal waves are studied in detail in [6]. In spite of the fact that, in [6], the integral similar to that appearing in Eq. (32) is calculated along the unperturbed ray (we integrate along the perturbed path), the results obtained there can be used for estimating the variance of δt_V on the order of magnitude.

We concentrate on the term δt_I, which usually predominates on long tracks. Its mean value determines the cluster shift with respect to the arrival time of the unperturbed ray, and the variance characterizes the cluster width. When averaging formula (33), it is necessary to take into account the limitations imposed by inequality (46) on the action fluctuation statistics. Using the results of Section 4, we obtain

$$\langle \delta t_I \rangle = \frac{\omega'(\bar{I})}{2c_r}\int_0^r Q(\rho, \rho)d\rho = \frac{\omega'(\bar{I})}{12c_r}Br^2. \qquad (63)$$

Note that the sign of the cluster shift is determined by the sign of the derivative ω'. In actual deep-water waveguides, the ray length cycle, as a rule, increases with the ray launch angle and, therefore, this derivative is negative. Thus, the sound pulses traveling along the perturbed trajectories arrive earlier (at least, on average) than the pulses traveling along the unperturbed rays with the same identifier.

The rms spread of δt_I is determined by the formula

$$\tau = \sqrt{\langle \delta t_I^2 \rangle - \langle \delta t_I \rangle^2}, \qquad (64)$$

and we estimate it using Eqs. (60) and (63). According to Eq. (60), we have

$$\begin{aligned}\langle \delta t_I^2 \rangle &= \left(\frac{\omega'(\bar{I})}{2c_r}\right)^2 \int_0^r\int_0^r d\rho_1 d\rho_2 \\ &\times [Q(\rho_1, \rho_1)Q(\rho_2, \rho_2) + 2Q^2(\rho_1, \rho_2)] \\ &= \left(\frac{\omega'(\bar{I})}{2c_r}\right)^2 \frac{B^2 r^4}{20}.\end{aligned} \qquad (65)$$

Then, we obtain

$$\tau = \frac{|\omega'(\bar{I})|}{c_r}\frac{Br^2}{6\sqrt{5}} = 0.9|\langle \delta t_I \rangle|. \qquad (66)$$

Thus, for $\delta t \simeq \delta t_I$, the shift of the cluster and its width are approximately equal.

Finally, we estimate the width $\Delta\chi$ of the interval of grazing angles of the cluster-forming rays at the reception point located on the waveguide axis (at the minimum of $c_0(z)$). The center of this interval is close to the arrival angle $\bar{\chi}$ of the unperturbed ray with the action variable $\bar{I}$. According to Eq. (59), the rms scatter of the action variable for the cluster-forming rays at a distance r can be estimated as $\sqrt{Br/3}$. In the case when $\Delta\chi$ is small compared to $\bar{\chi}$, the following approximate expression is valid:

$$\sqrt{Br/3} = \left.\frac{\partial I}{\partial H_0}\frac{\partial H_0}{\partial \chi}\right|_{\chi = \bar{\chi}} \Delta\chi. \qquad (67)$$

With allowance for Eq. (10) and the relation between H and χ (see Eq. (5)), we obtain

$$\Delta\chi = \frac{\sqrt{Br/3}\omega}{n|\sin\bar{\chi}|}. \qquad (68)$$

For our model of the waveguide, at the distance r = 3000 km and for the clusters with $\Delta\chi$ within 5°–15°, the value of $\bar{\chi}$ varies from 1.4° to 0.4°.

6. NUMERICAL MODELING

To illustrate and test the formulas obtained, we construct so-called *t*–*z* diagrams (time fronts) for a 3000-km-long distance. They are shown in Fig. 2. Each point in the diagram represents the ray arrival on the time–depth plane. In the upper plot (the unperturbed waveguide), the points form two piecewise-continuous broken lines, one of which is formed by the rays launched from the source upwards, and the other, by the rays launched downwards. The dependence of the arrival time of a ray on its vertical coordinate in the perturbed waveguide (the lower plot) is also expressed as a continuous function. However, under the ray chaos conditions, the relation between *t* and *z* on long tracks becomes so complicated that the fan of the rays proves to be insufficiently dense for a visualization of this continuity. The random scatter of the points in a *t*–*z* diagram is an indicator of the ray chaos.

The diagrams in Fig. 2 are constructed on the basis of the numerically calculated trajectories of 48000 rays in the perturbed waveguide and 16000 rays in the unperturbed waveguide. In both cases, the rays are launched from a point source located at a depth of z_0 = –0.78 km. The initial momenta p_0 of these rays are uniformly distributed over the interval corresponding to the launch angles within ±12°.

Each segment of the *t*–*z* diagram in the unperturbed waveguide is formed by rays with the same identifier. In the perturbed waveguide, the rays have the same property, forming the slightly spread but, nevertheless, clearly distinguishable segments observed in the initial part of the diagram. In Fig. 2, the values of the identifiers (selectively) are indicated near the corresponding segments. As is seen, the initial parts of *t*–*z* diagrams, which are formed by steep rays, are almost similar for the perturbed and unperturbed waveguides. In the presence of a perturbation, the segments of the *t*–*z* diagram that are seen at the left are weakly spread and do not

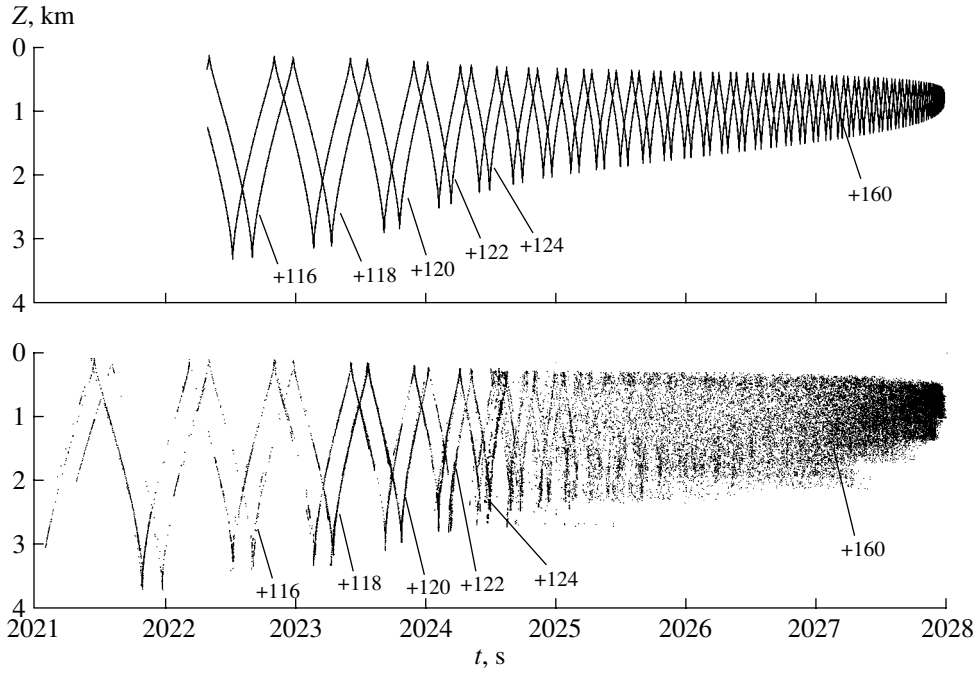

Fig. 2. Ray arrivals on the time–depth plane (t–z diagrams) at a distance of 3000 km in the unperturbed (upper plot) and perturbed (lower plot) waveguides. The point sound source is located at a depth of 0.78 km. Near several segments of the diagrams, the identifiers of the rays forming these segments are indicated.

overlap. This fact reflecting the stability of the initial part of the received signal is well known and has been observed in both numerical and field experiments [1, 10, 17].

When a signal is recorded by a point receiver located at a depth z_r, the ray arrival times are determined by the intersection of the t–z diagram with the horizontal line $z = z_r$. In the unperturbed waveguide, the intersection of this line with each segment of the diagram gives a single ray. In the presence of the perturbation, the segments are spread and, instead of individual unperturbed times, we obtain clusters of such times.

Under the ray chaos conditions, the trajectories are very sensitive to variations in the initial conditions, and, therefore, the numerical calculation of rays arriving at a given point at a distance $r \gg \lambda$ is very complicated from a technical point of view. However, the width and the shift of the cluster can be numerically estimated without solving this problem. One should expect that the characteristics of the cluster on long tracks vary rather weakly with small variations in the receiver depth. Therefore, one only needs to calculate the fan of a large number of trajectories and choose the trajectories that fall within some interval of depths with a width Δz and its center at the point z_r. The value of Δz must not necessarily be very small. However, it must not exceed the typical scale of variation of the ray arrival density with depth. Numerical estimates of the shift $\langle \delta t \rangle$ and the width τ of the cluster at the point z_r can be obtained by analyzing the arrival times of the rays that fall within the interval Δz and have the corresponding identifier.

Figure 3 compares the shifts $\langle \delta t \rangle$ and the broadening τ of the clusters that were predicted by Eqs. (63) and (66) with the numerical calculation carried out in the above-mentioned way for $z_r = -0.78$ km and $\Delta z = 100$ m. As is seen, for most clusters, our estimates give a correct result (at least, in the order of magnitude). At a distance of 3000 km, the shift and the broadening of the cluster formed by the flat (steep) rays are equal to 0.1 s (0.01 s) in order of magnitude.

Note that, in the Wiener process approximation, the action variable fluctuations are more or less the same for all rays. Therefore, the difference in the variances δt_I for the steep and flat rays is mainly determined by the factor ω' (see Eq. (33)). The dependence of the action I and the derivative ω' on the ray grazing angle at the waveguide axis is shown in Fig. 4. In our model, the value of $|\omega'|$ is very small for steep rays, which have smaller numbers of turning points M, as compared to the flat rays. For the steepest rays, the terms δt_I and δt_V are of the same order of magnitude even at a distance of 3000 km. For such rays, the relative error of predictions made for $\langle \delta t \rangle$ and τ without considering δt_V can be significant. This is evident from Fig. 3 for rays with small values of M.

Thus, the quantity $|\omega'|$, as well as the cluster width, decreases as the grazing angle χ increases. On the other hand, the action variable I and the time interval between adjacent clusters, which is given by the first term on the

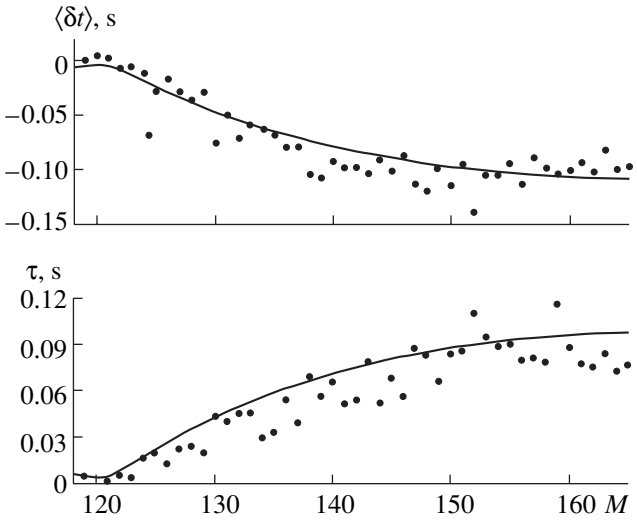

Fig. 3. Shift (upper plot) and width (lower plot) of a cluster formed by rays with identifiers equal to $+M$ with respect to the arrival time of the unperturbed ray with the same identifier. The source and the receiver are located at a depth of 0.78 km. The circles show the results of the numerical calculation of the ray trajectories for one of the realizations of inhomogeneities, and the solid lines represent the theoretical estimates by formulas (63) and (66).

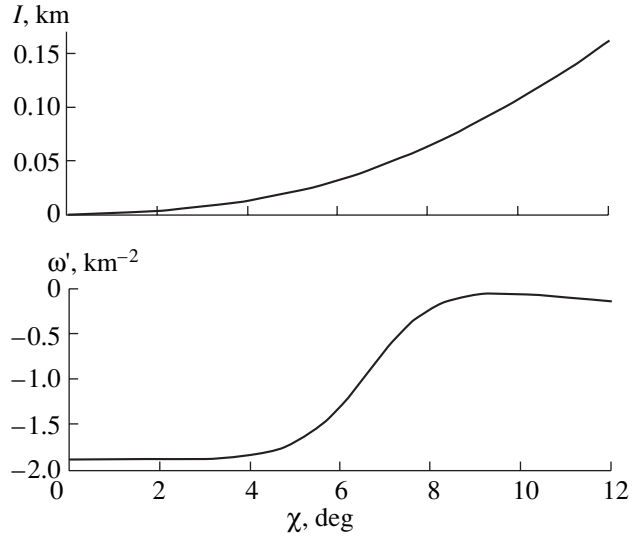

Fig.4. Dependence of the action variable I (upper plot) and the derivative ω' (lower plot) on the grazing angle of a ray at the waveguide axis (at a depth of 0.78 km).

right-hand side of Eq. (30), rapidly increase as χ grows (see Fig. 4). Owing to these two factors, clusters formed by steep rays are resolved even on very long tracks.

7. CONCLUSIONS

This paper presents a method for an approximate description of the fluctuations of ray arrival times in a realistic model of an underwater sound channel with inhomogeneities due to the random field of internal waves. It is shown that the analysis of the chaotic dynamics of rays is considerably simplified with the use of the Hamiltonian formalism expressed in terms of the action–angle canonical variables. The presence of a small parameter in problem (28) allows one to approximate the Hamiltonian equations (ray equations) by the Langevin linear stochastic equations (37) and (41). In this approximation, the action variable fluctuations are modeled by the Wiener process, whose basic statistical characteristics are well known and expressed by the simple formulas [23, 24]. This approach, which was formulated in [21] and [31], is used in this paper to analyze the properties of ray arrival times. The simplicity of the formulas obtained is the consequence of a series of approximations, whose domain of validity requires some refinement. Nevertheless, the results of our numerical modeling, as well as the calculations carried out in [30], confirm the validity of the approach under discussion for describing the chaotic ray structure of the sound field in a deep sea.

A rough estimate is obtained for the scatter of arrival times of rays launched from a point source under grazing angles within a fixed narrow interval. According to this estimate, the ray arrival times at a distance r occupy an interval whose average width increases in proportion with $r^{3/2}$. Such a dependence on distance agrees well with the results reported by other authors [30].

The most attention was given to a quantitative description of the effect of clustering of the ray arrival times. Here, the consideration was based on formulas (30)–(33) that were first obtained in [19, 21] (see also [20]). It is found that, on short and long tracks, two different mechanisms of cluster broadening manifest themselves. On short tracks (roughly speaking, up to 1000 km), the ray trajectories forming the cluster only slightly deviate from the unperturbed ray trajectory and the arrival time variations are determined by the sound velocity fluctuations along the trajectories. In this case, $\delta t \simeq \delta t_V$ and the cluster width grows with distance as $r^{1/2}$ [6]. On tracks longer than 1000 km, another mechanism comes into play. It is related to the fact that, despite the coincidence of the identifiers (similarity of topologies) of the rays forming the cluster, their trajectories considerably diverge in space. For most of the rays, $\delta t \simeq \delta t_I$, and, according to Eq. (63), the width of the cluster grows in proportion with r^2.

The sign of the cluster shift with respect to the arrival time of the unperturbed ray is determined by the dependence of the path cycle length on the launch angle at the source. In a typical deep-sea acoustic waveguide in which steep rays have longer cycles than flat rays, this shift is directed towards early times. However, theoretically, one can imagine a waveguide where the shift has the opposite sign.

The formulas obtained for the width and shift of the cluster give quantitative estimates that characterize the

stability of the initial part of the signal received at long-range sound propagation in the ocean. At the same time, it is necessary to note that the relation between the ray arrival times and the ray amplitudes was not investigated. This problem may be very important. As was shown (numerically) in [2], the difference in the arrival times of the rays with maximum amplitudes (playing the main role in the formation of the signal peak corresponding to the given cluster) may be much smaller than the total cluster width.

There are a number of problems related to the long-range sound propagation in the ocean and calling for further investigation. Among them, the problems taking into account the diffraction effects and describing the mode structure of the field of a pulsed signal at distances of the order of several thousands of kilometers seem to be of special interest [33].

ACKNOWLEDGMENTS

I am grateful to I.P. Smirnov, the author of the computer code used for the ray trajectory calculations. This work was supported by the Russian Foundation for Basic Research (project no. 03-02-17246) and a grant in Support of the Leading Scientific Schools (grant no. NSh-838.2003.2).

REFERENCES

1. P. F. Worcester, B. D. Cornuelle, M. A. Dzieciuch, *et al.*, J. Acoust. Soc. Am. **105**, 3185 (1999).
2. F. J. Beron-Vera, M. G. Brown, J. A. Colosi, *et al.*, J. Acoust. Soc. Am. **114**, 1226 (2003).
3. B. D. Dushaw, B. M. Howe, J. A. Mercer, *et al.*, IEEE J. Ocean. Eng. **24** (2), 202 (1999).
4. L. M. Brekhovskikh and Yu. P. Lysanov, *Fundamentals of Ocean Acoustics* (Gidrometeoizdat, Leningrad, 1982; Springer, New York, 1991).
5. W. Munk and C. Wunsch, Deep-Sea Res. **26**, 123 (1979).
6. *Sound Transmission through a Fluctuating Ocean*, Ed. by S. M. Flatte (Cambridge Univ. Press, Cambridge, 1979; Mir, Moscow, 1982).
7. S. S. Abdullaev and G. M. Zaslavskiĭ, Usp. Fiz. Nauk **161** (8), 1 (1991) [Sov. Phys. Usp. **34**, 645 (1991)].
8. D. R. Palmer, M. G. Brown, F. D. Tappert, and H. F. Bezdek, Geophys. Res. Lett. **15**, 569 (1988).
9. F. D. Tappert and X. Tang, J. Acoust. Soc. Am. **99**, 185 (1996).
10. J. Simmen, S. M. Flatte, and G.-Y. Wan, J. Acoust. Soc. Am. **102**, 239 (1997).
11. G. M. Zaslavskiĭ, *Chaos in Dynamical Systems* (Nauka, Moscow, 1984; Harwood, Chur, 1985).
12. K. B. Smith, M. G. Brown, and F. D. Tappert, J. Acoust. Soc. Am. **91**, 1939 (1992).
13. S. S. Abdullaev, *Chaos and Dynamics of Rays in Waveguide Media*, Ed. by G. Zaslavsky (Gordon and Breach, New York, 1993).
14. M. G. Brown, J. A. Colosi, S. Tomsovic, *et al.*, J. Acoust. Soc. Am. **113**, 2533 (2003).
15. I. P. Smirnov, A. L. Virovlyansky, and G. M. Zaslavsky, Phys. Rev. E **64**, 036221 (2001).
16. I. P. Smirnov, A. L. Virovlyansky, and G. M. Zaslavsky, Chaos **12**, 617 (2002).
17. M. G. Brown and J. Viechnicki, J. Acoust. Soc. Am. **104**, 2090 (1998).
18. J. A. Colosi and M. G. Brown, J. Acoust. Soc. Am. **103**, 2232 (1998).
19. A. L. Virovlyansky, J. Acoust. Soc. Am. **113**, 2523 (2003).
20. A. L. Virovlyansky, Izv. Vyssh. Uchebn. Zaved., Radiofiz. **46**, 555 (2003).
21. A. L. Virovlyansky, nlin.CD/0012015.
22. L. D. Landau and E. M. Lifshitz, *Course of Theoretical Physics*, Vol. 1: *Mechanics*, 3rd ed. (Nauka, Moscow, 1973; Pergamon, Oxford, 1976).
23. V. I. Tikhonov and M. A. Mironov, *The Markov Processes* (Sovetskoe Radio, Moscow, 1977) [in Russian].
24. C. W. Gardiner, *Handbook of Stochastic Methods for Physics, Chemistry, and the Natural Sciences* (Springer, Berlin, 1985; Mir, Moscow, 1986).
25. M. Born and E. Wolf, *Principles of Optics*, 4th ed. (Pergamon, Oxford, 1969; Nauka, Moscow, 1973).
26. F. B. Jensen, W. A. Kuperman, M. B. Porter, and H. Schmidt, *Computational Ocean Acoustics* (American Inst. of Physics, New York, 1994).
27. A. L. Virovlyanskiĭ, Akust. Zh. **31**, 664 (1985) [Sov. Phys. Acoust. **31**, 399 (1985)].
28. W. Munk and C. Wunsch, Rev. Geophys. Space Phys. **21**, 1 (1983).
29. A. L. Virovlyansky, J. Acoust. Soc. Am. **97**, 3180 (1995).
30. F. J. Beron-Vera and M. G. Brown, J. Acoust. Soc. Am. **115**, 1068 (2004).
31. A. L. Virovlyanskiĭ, Akust. Zh. **51**, 90 (2005) [Acoust. Phys. **51**, 71 (2005)].
32. S. M. Rytov, *Introduction to Statistical Radio Physics* (Nauka, Moscow, 1966), Part 1 [in Russian].
33. K. E. Wage, A. B. Baggeroer, and J. C. Preisig, J. Acoust. Soc. Am. **113**, 801 (2003).

Translated by Yu. Lysanov

Acoustical Physics, Vol. 51, No. 3, 2005, pp. 282–291. Translated from Akusticheskiĭ Zhurnal, Vol. 51, No. 3, 2005, pp. 342–351.

Energy Characteristics of the Sound Fields in the Barents Sea

O. P. Galkin and L. V. Shvachko

Andreev Acoustics Institute, Russian Academy of Sciences, ul. Shvernika 4, Moscow, 117036 Russia

e-mail: bvp@akin.ru

Received December 23, 2003

Abstract—Experimental studies of the intensity structure of the sound field in the Barents Sea were carried out. The signal propagation path was ~80 km in length, and the sea depth was ~220–250 m. Pseudonoise signals generated in one-third-octave frequency bands with central frequencies of 1.25 and 3.15 kHz were used. The sound source was positioned at two different points: in the subsurface layer at a depth of 10 m and under the discontinuity layer at a depth of 100 m. The reception depths were 15, 100, and 200 m. The experimental results were compared with the results of ray calculations taking into account the wind waves and the parameters of the ground at the bottom. The latter parameters were obtained by classifying the data available from the literature. As a result of the analysis, a fundamental possibility was demonstrated to predict the intensity characteristics of the field structure in a shallow sea with allowance for the depth dependence of sound velocity and the parameters of the waveguide boundaries. © *2005 Pleiades Publishing, Inc.*

The purpose of experimental studies of the sound field structure usually is not only the determination of the specific parameters of the field but also the determination of the extent to which they agree with the computational model in order to develop a foundation for predicting the sound field characteristics in different regions of the ocean. For a deep ocean, where the field is mainly formed by water-path signals propagating over rays that are not reflected from the waveguide boundaries, the intensity structure of the field formed by signals of the kilohertz frequency band agrees well with the results of ray and wave calculations [1–4]. In the case of a shallow sea, the problem becomes more complicated, because signals reflected from the surface and the bottom of the waveguide play a significant role in the sound field formation. Therefore, the calculations should take into account not only the variations in the sound velocity profile along the propagation path but also the characteristics of the agitated wavy surface and the parameters of the bottom sediments [5–7].

Experimental studies of the intensity structure of the sound field and its correlation with the computational model were the purpose of measurements carried out in the Barents Sea. The sound field was studied in the southern deep-water part of the sea. Figure 1a shows a map of the region where the experiments were carried out and the location of a path of signal propagation ~80 km in length. The sea depth along the path varied only slightly within 220–250 m.

The measurements were carried out in the first half of September and, because of adverse weather conditions (wind up to 12 m/s and sea state up to V), were performed in three stages with small intervals between them. Figure 1b shows the sound velocity profiles $C(z)$ characterizing the conditions at these three stages. The first two stages and the beginning of the third stage occurred in virtually identical conditions corresponding to the three profiles $C(z)$ shown at the left of Fig. 1b. In the near-bottom water layers, beginning from a depth of 200 m, a small increase in the sound velocity was observed. Although this varying gradient was rather unstable in time and space, it could play a certain role, leading to a decrease or increase in the ray grazing angle near the bottom and, hence, to a certain variation in the bottom reflection coefficient.

Within the last part of the propagation path, approximately beginning from a distance of 55 km, the hydrographic conditions noticeably differed from those described above and corresponded to the profile $C(z)$ shown in the right-hand part of Fig. 1b. The difference was caused by the influence of the warm Gulf Stream current. Since this influence manifested itself within the last portion of the path, the conditions of sound propagation along the main part of the path could be considered to be invariable.

1063-7710/05/5103-0282$26.00

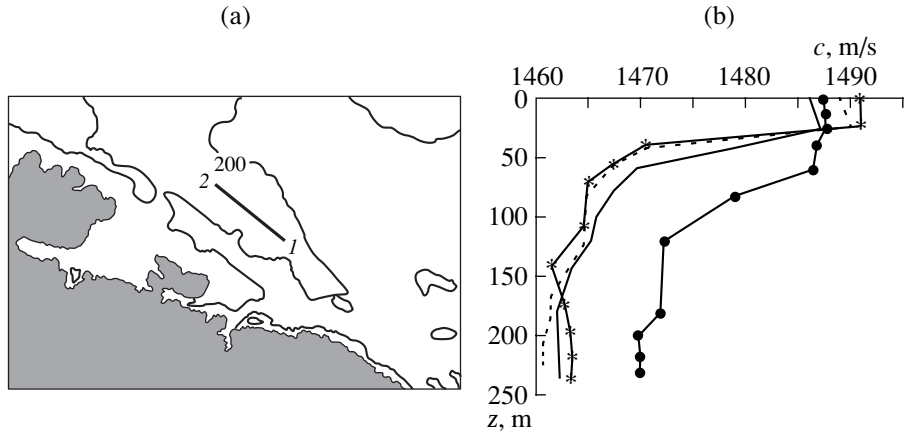

Fig. 1. Region of experiments in the Barents Sea: (a) position of the (*1*–*2*) path of propagation and (b) sound velocity profiles $C(z)$ for different stages of the experiments.

Two research vessels from the Acoustics Institute participated in the experiments. One of them, the transmitting vessel, moved along the path from point *1* to point *2* (Fig. 1a). At certain distances from the receiving vessel, which was drifting during the whole experiment, the transmitting vessel began drifting as well and emitted sound signals. The latter were noise signals emitted in turn by two sources in one-third-octave frequency bands with the central frequencies f_c = 1.25 and 3.15 kHz. The width of the main lobe of the directional pattern at a level of 0.7 of the maximum was ±18° and ±9°, respectively. The signal duration was 2–3 min, and the maximum of the directional pattern of the source was always directed at zero angle to the horizon. The experiments were performed with two different source positions: in the subsurface layer at a depth of 10 m and under the discontinuity layer at a depth of 100 m. The other vessel, the receiving one, which was located near point *1*, received the signals by omnidirectional hydrophones at three different depths simultaneously: in the near-surface channel at a depth of 15 m, under the discontinuity layer at a depth of 100 m coincident with one of the source depths, and near the bottom at a depth of 200 m. It should be noted that, during the time of measurements at a given distance, the transmitting vessel maintained a constant distance between the vessels by using a special mode of operation of its propellers (the so-called electric motion regime).

The sound field formed at the point of reception as a result of a relatively long (2–3 min) transmission represented a sum of all signals arriving over different rays. Therefore, the received noise signals were characterized by an envelope slowly varying in time and determined by both interference effects and fluctuations of individual signal levels due to the variability of the waveguide parameters. The received signals were subjected to computer processing by a special program with allowance for the interfering noise level, which was recorded each time before and after the reception of the transmitted signals.

Experiments studying the dependence of the intensity structure of the field on the source depth were carried out for two different types of the sound field: in the first case, both corresponding points were in the subsurface layer; in the second case, at least one of them was under the discontinuity layer. In the first case, the presence of a weak positive gradient of sound velocity in the upper 25-m-thick layer determined the sound propagation in the subsurface channel. Although the angular range captured by this channel was small and did not exceed 1.5°–2.0°, its effect on the formation of the total sound field was considerable. In the second case, the main role in the sound field formation was played by the rather strong discontinuity layer lying at depths of about 25 to 50 m. In this case, the field was formed by bottom-reflected signals and, partially, by signals reflected from both boundaries of the waveguide. Therefore, the level and the structure of the sound field were strongly affected by the reflection coefficients of the bottom and the wavy surface of the sea within the whole path of signal propagation.

To compare the experimental results with the theoretical estimates of the sound field characteristics, calculations were carried out with the use of Vagin's computer code [8] subjected to some modification. To take into account the effect of the lower boundary of the waveguide, the absolute value of the bottom reflection coefficient $|V|$ was determined by the formula

Table 1

Type of sediment	Minimal values of $V(\chi)$			Maximal values of $V(\chi)$			Mean values of $V(\chi)$		
	m	n	η	m	n	η	m	n	η
Sand	1.8	0.98	0.0078	2.1	0.83	0.03	1.9	0.9	0.019
Silty sand	1.6	0.98	0.0066	1.97	0.83	0.024	1.8	0.9	0.015
Sandy silt	1.4	0.985	0.003	1.9	0.87	0.03	1.66	0.93	0.015
Silt	1.2	1.02	0.001	1.65	0.94	0.026	1.44	0.98	0.014
Clay silt	1.2	1.03	0.0006	1.69	0.95	0.018	1.47	0.99	0.01

$$|V| = \left(\frac{\left(m\sin\chi - \left(\frac{(a^2+b^2)^{\frac{1}{2}} + a}{2} \right)^{\frac{1}{2}} \right)^2 + \frac{(a^2+b^2)^{\frac{1}{2}} - a}{2}}{\left(m\sin\chi + \left(\frac{(a^2+b^2)^{\frac{1}{2}} + a}{2} \right)^{\frac{1}{2}} \right)^2 + \frac{(a^2+b^2)^{\frac{1}{2}} - a}{2}} \right)^{\frac{1}{2}},$$

where $a = n^2(1 - \eta^2) - \cos^2\chi$, $b = 2\eta n^2$, χ is the grazing angle of a ray at the bottom, $m = \rho_{gr}/\rho_w$ is the ground-to-water density ratio, $n = c_w/c_{gr}$ is the ratio of sound velocities in water and in the ground, and η is the loss factor.

This formula is applicable to ground where the contribution of transverse waves to the reflection coefficient can be neglected, which in most cases is true for the upper sediment layer. For the bottom model under consideration (an absorbing fluid half-space), when estimating the reflection coefficient, it is necessary to know the parameters m, n, and η. These parameters are given in Table 1 for five types of bottom sediments. The data were taken from the results of ~900 measurements reported in the literature by different authors [9].

The use of the aforementioned bottom model is expedient in estimating the sound field characteristics for regions with a relatively flat bottom and for sufficiently high frequencies. The experimental studies under discussion were performed under such conditions.

One can also use the generalized data shown in Fig. 2, which illustrate the relation between the afore-

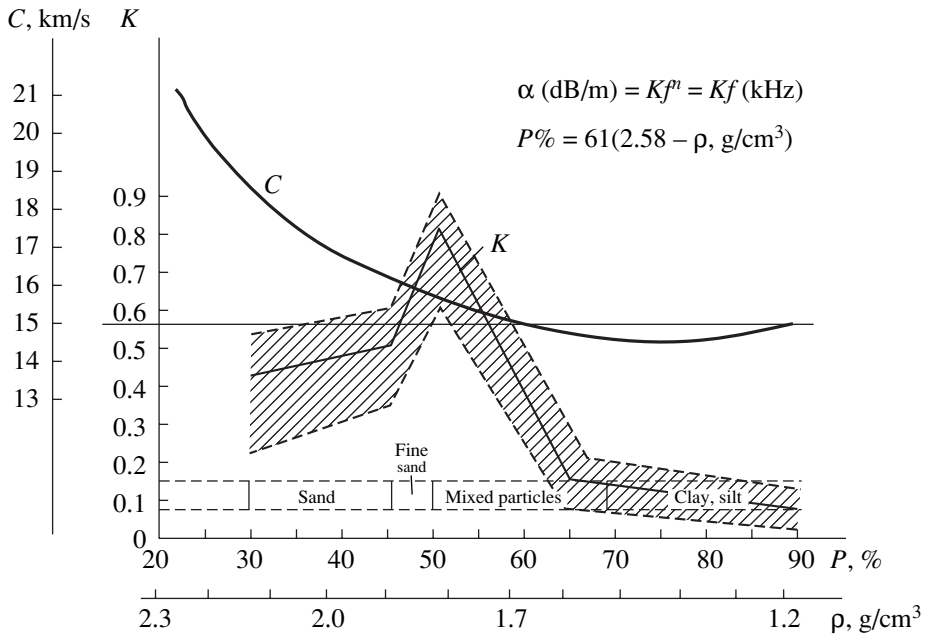

Fig. 2. Relation of the acoustic parameters of the ground (the longitudinal wave velocity C and the coefficient K determining the attenuation coefficient α) to the composition of the ground, its porosity P, and its density ρ.

Table 2

Wind, Beaufort scale	3	4		5		6			7		8		
Wind, knots / Waves, m/s	10	12	14	16	18	20	22	24	26	28	30	32	34
	5.1	6.2	7.2	8.2	9.3	10.4	11.4	12.5	13.5	14.5	15.6	16.6	17.6
Variance σ^2	0.01	0.03	0.06	0.12	0.21	0.36	0.58	0.89	1.34	1.93	2.74	3.76	5.12
Rms deviation, m	0.10	0.17	0.24	0.34	0.46	0.60	0.76	0.94	1.16	1.40	1.66	1.94	2.26
Rms height of waves, m	0.30	0.47	0.69	0.97	1.34	1.69	2.16	2.7	3.3	3.9	4.7	5.5	6.4
Height of waves $h_{3\%}$, m (3% of waves may be higher)	0.55	0.89	1.26	1.79	2.42	3.16	4.0	4.94	6.11	7.37	8.74	10.2	11.9
Mean height $\bar{h}$, m	0.11	0.17	0.25	0.34	0.46	0.59	0.77	0.96	1.16	1.40	1.68	1.95	2.27
Sea state	II	III		IV		V			VI		VII		

mentioned characteristics of the ground and the acoustic parameters of the bottom. They allow one to correlate different characteristics of the upper layer of bottom sediments (the type of sediments, the density ρ (g/cm^3), and the porosity P (%)) with such acoustic parameters of the bottom as the longitudinal wave velocity c (km/s), the attenuation coefficient α (dB/m), and the coefficient K. Note that the attenuation coefficient α is related to the sound frequency f (kHz) as $\alpha = Kf^n \approx Kf$, because $n \approx 1$–$1.2 \cong 1$, while the loss factor is $\eta \approx 0.018Kc$.

The absolute value of the coefficient of coherent reflection from the wavy surface $|V|$ was estimated by the formula

$$|V| = e^{\frac{P^2}{2}},$$

where $P = 2k\sigma\sin\chi$ is the Rayleigh parameter, $k = \frac{2\pi}{\lambda}$ is the sound wave number, λ is the sound wavelength, σ is the root-mean-square (rms) deviation of the surface, and χ is the grazing angle with respect to the flat surface.

Table 2 shows the parameters of surface waves that are necessary for calculations in the case of a sea state from II to VII.

The results of measuring the intensity structure of the field for signals of both frequency bands and for different source and reception depths are represented by closed circles in Figs. 3–7. The thin lines in these figures represent their calculated sound field characteristics for the experimental conditions. The calculations were performed for three values of the wind speed: 0 (no wind waves, calm), 7 (sea state III), and 11.4 m/s (sea state V). In Figs. 3, 4, and 6, these values refer to the upper, intermediate, and lower curves, respectively. The single calculated curves shown in Figs. 5 and 7 refer to any of the sea states. The parameters of the ground were taken for sandy silt and silt, because its density varied within 1.4–1.6 g/cm^3 along the propagation path.

In all of the plots, the ordinate axis represents the field intensity I (dB), and the abscissa axis, the distance r (km). The thick and thin monotone dependences issuing from the point $I = 0$ at $r = 1$ km represent the spherical and cylindrical decay laws. The dashed line parallel to the abscissa axis (at bottom right) shows the level of interfering noise recorded before and after the reception of the transmitted signals. In the analysis, for a more accurate comparison of experimental and calculated levels of $I(r)$, it is necessary to take into account the attenuation of sound in water. For a frequency $f_c = 1.25$ kHz, this quantity, determined as $\beta = 0.028f^{3/2}$ (dB/km), was small ($\beta = 0.04$ dB/km), and, even at the maximal distance of 76 km, it did not exceed 3 dB. Therefore, we ignored this correction in our calculations.

However, for signals with $f_c = 3.15$ kHz, the attenuation is considerable: $\beta = 0.16$ dB/km. Therefore, in Figs. 3b, 6, and 7, the cylindrical and spherical decay laws are represented with allowance made for the spatial attenuation.

As was mentioned above, the experiments were performed for two types of conditions of the sound field

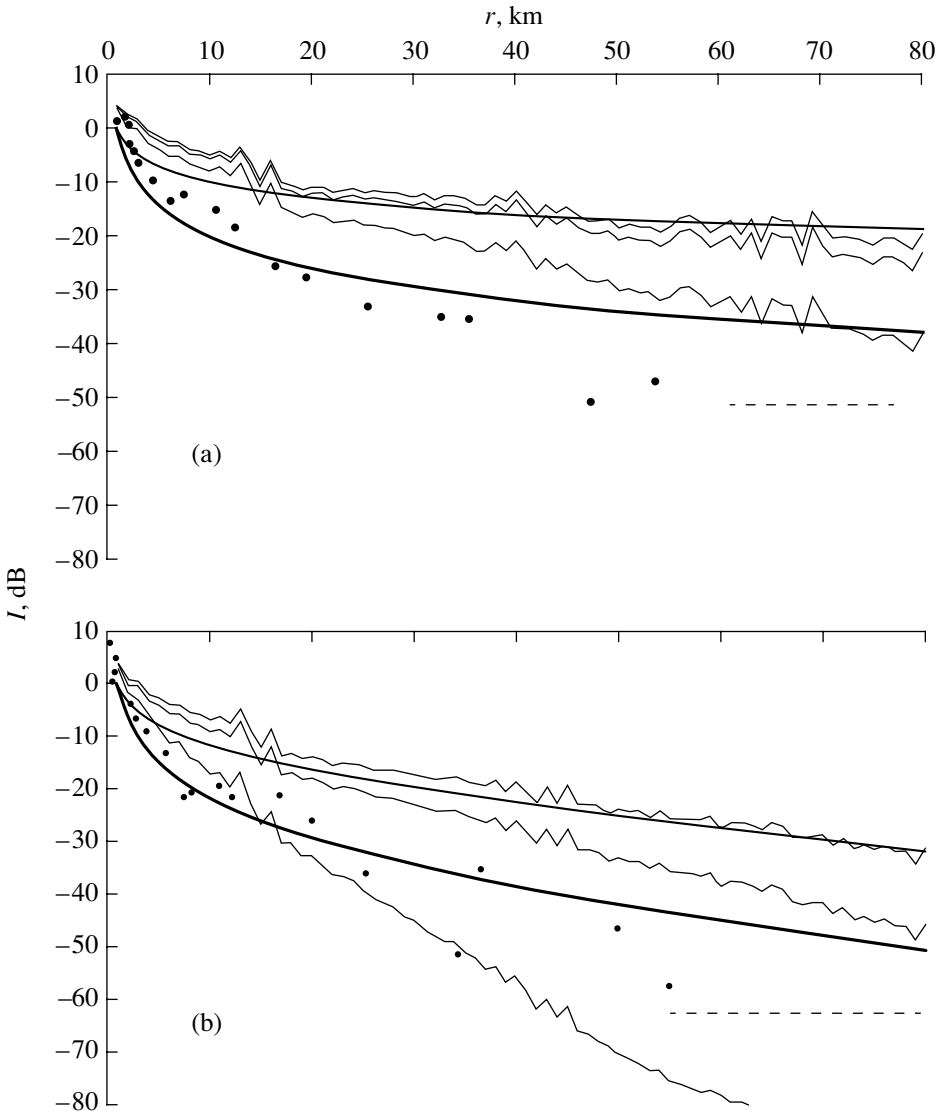

Fig. 3. Experimental (closed circles) and calculated dependences of the sound intensity I on distance r with a source depth of 10 m, a reception depth of 15 m, and f_c = (a) 1.25 and (b) 3.15 kHz.

formation. In the first case, both corresponding points lay near the sea surface, specifically, at depths of 10–15 m. In this case, the effect of the upper boundary on the received signal level was predominant, while the bottom characteristics virtually did not affect the field intensity. The experimental data and the results of calculations for this situation are shown in Figs. 3a and 3b for signals with central frequencies of 1.25 and 3.15 kHz, respectively. One can see that, for both experimental dependences $I(r)$, the points belonging to the initial part of the path (up to $r \cong 15$–20 km) lie below the line representing the cylindrical decay law and above the line representing the spherical law. Thus, within these distances, the experimental dependences of the sound field intensity on distance, $I(r)$, were characterized by positive levels of the propagation anomaly A for both frequencies. The maximal values of A did not exceed +(6–8) dB. As the distance increased, the value of the propagation anomaly rapidly decreased, and, near the end of the propagation path (at distances of 50–60 km), the quantity A reached its minimum: $A \cong$ –(15–18) dB. The experimental points lay either near the theoretical curves for sea states III and V (Fig. 3b, f_c = 3.15 kHz) or considerably lower (Fig. 3a, f_c = 1.25 kHz), which was related to the considerable energy leakage from the weak range-dependent thin subsurface channel under severe wind–wave conditions.

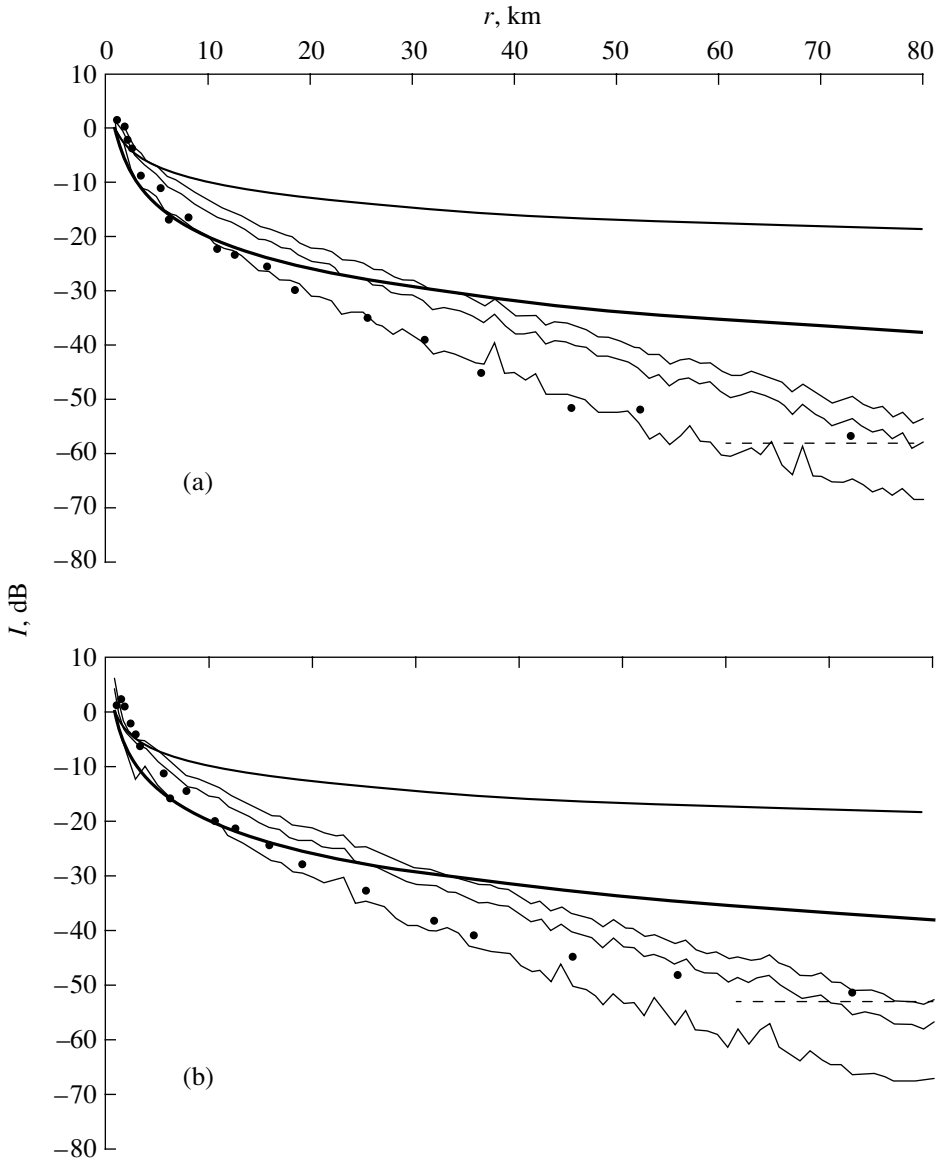

Fig. 4. Same as in Fig. 3 with a source depth of 10 m, f_c = 1.25 kHz, and a reception depth of (a) 100 and (b) 200 m.

Most of the experimental results were obtained for the case of the sound field formation with the participation of both the surface and the bottom of the sea and also for the case of a predominant contribution of the lower waveguide boundary. The comparison of the experimental and calculated dependences $I(r)$ obtained for the signals with f_c = 1.25 kHz at reception depths of 100 and 200 m are shown in Figs. 4 and 5 for source depths of 10 and 100 m, respectively. Similar data for signals with f_c = 3.15 kHz are shown in Figs. 6 and 7.

Let us first consider the results obtained for signals of both frequency bands with a source depth of 10 m and reception depths of 100 and 200 m lying below the discontinuity layer. In this case, both boundaries contribute to the formation of the sound field. From Figs. 4 and 6, one can see that, for both frequency bands, the experimental points lie below the cylindrical-law line for all distances under study; for f_c = 1.25 kHz and distances greater than 10–15 km, as well as for f_c = 3.15 kHz and distances greater than 5 km, the experimental points lie still lower, below the spherical-law line. The value of the propagation anomaly at the smallest distances is close to zero for f_c = 3.15 kHz and does not exceed +(5–8) dB for f_c = 1.25 kHz. At large distances, the minimal values of

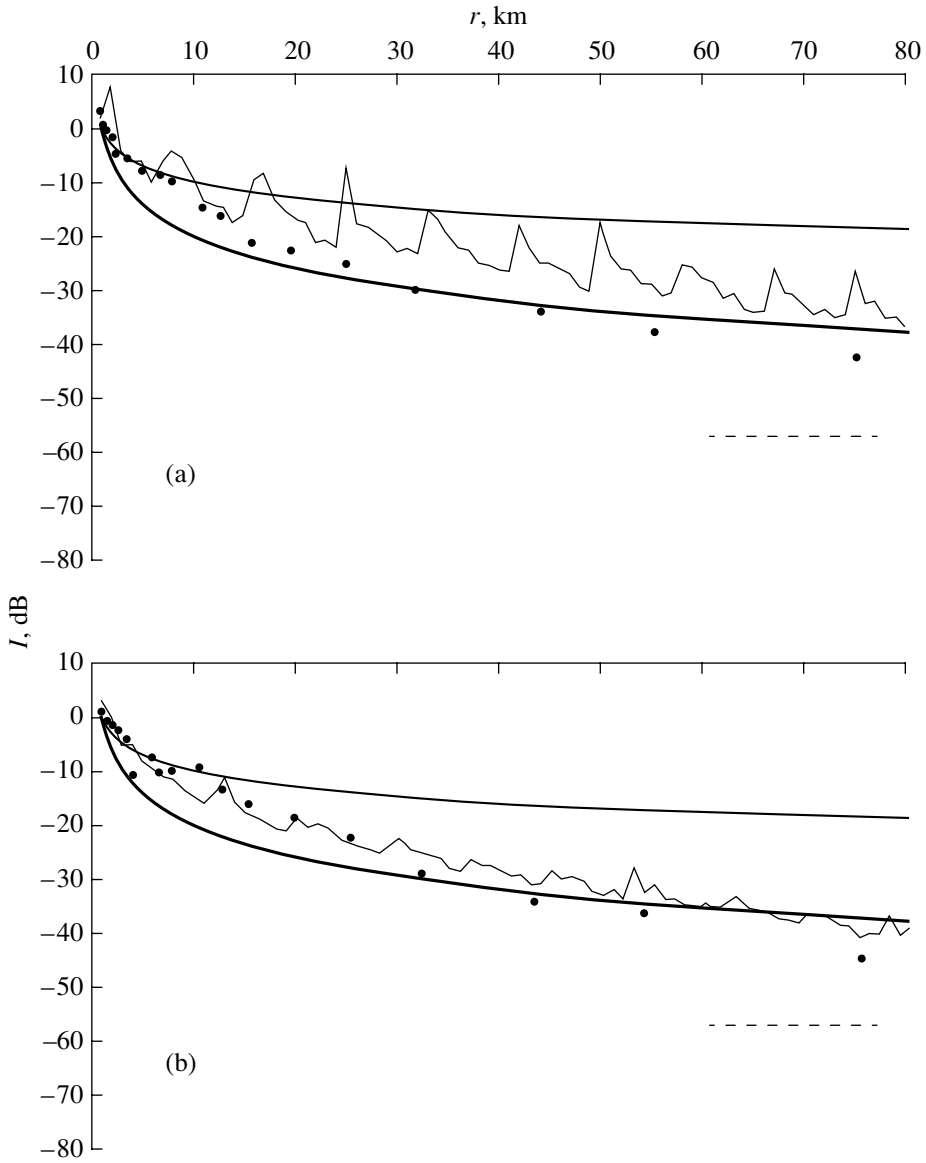

Fig. 5. Same as in Fig. 3 with a source depth of 100 m, f_c = 1.25 kHz, and a reception depth of (a) 100 and (b) 200 m.

the anomaly are about –(18–20) dB for both frequency bands.

From the data of Figs. 4 and 6, one can clearly see the relation between the sound field characteristics and the sea state. When at least one of the corresponding points lies near the surface, the dependence $I(r)$ is necessarily formed with its participation. The experimental points obtained for distances up to 40–50 km lie near the calculated curve $I(r)$ obtained for the sea state V, which approximately coincides with the experimental conditions. At the end of the path, a slight increase in the signal level is observed for both frequency bands, which is related to the changes in the experimental conditions at the last stage due to the warm Gulf Stream current (the right-hand plot in Fig. 1b).

Now, we analyze the results obtained for signals of the two frequency bands with both the source depth (100 m) and the reception depths (100 and 200 m) lying below the discontinuity layer (Figs. 5 and 7). In this case, the surface waves do not affect the sound field structure, which is confirmed by the plots in Figs. 5 and 7, and the governing role is played by the dependence of the field intensity on the coefficient of reflection from the lower boundary of the waveguide. As follows from the data presented, experimental points obtained for f_c = 1.25 kHz at virtually all distances lie near the line representing the spherical

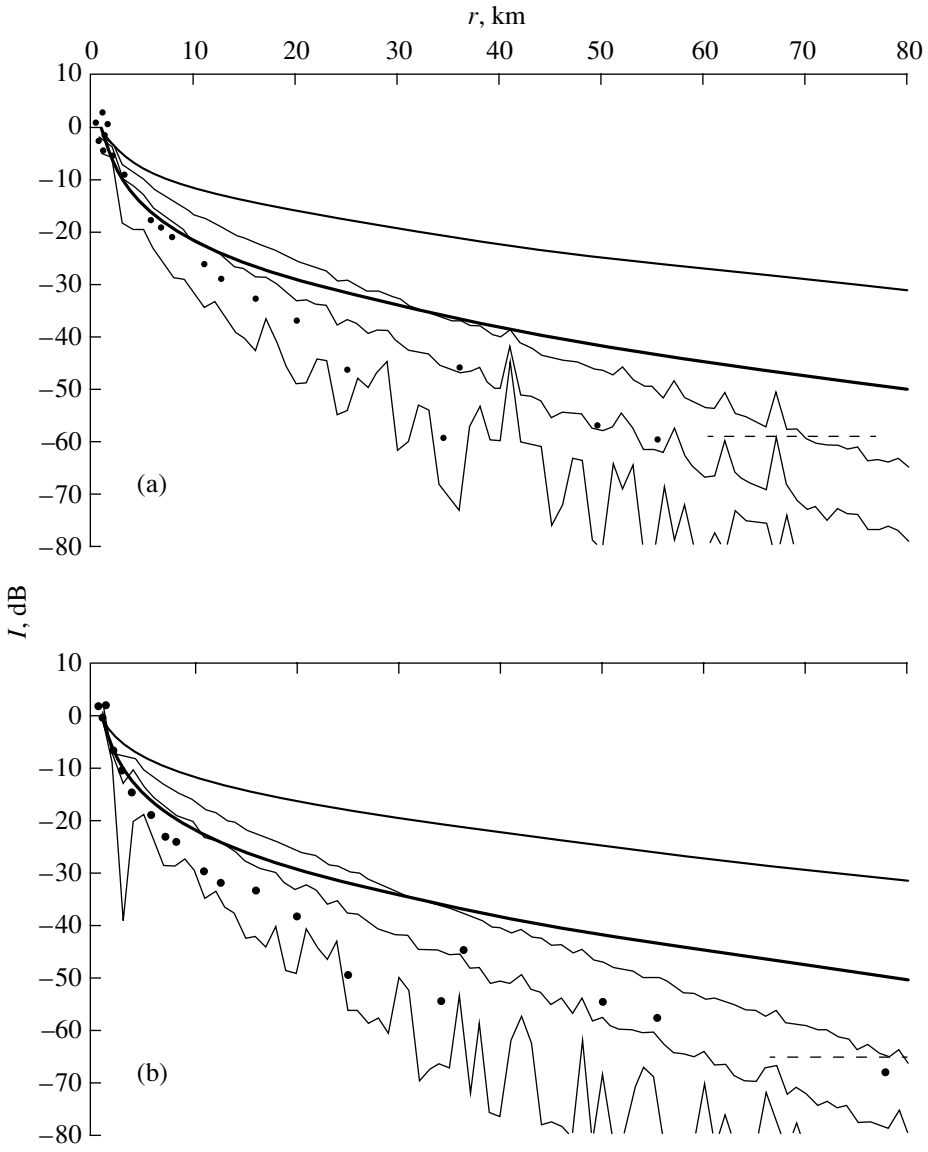

Fig. 6. Same as in Fig. 3 with a source depth of 10 m, f_c = 3.15 kHz, and a reception depth of (a) 100 and (b) 200 m.

decay law with maximal levels of propagation anomaly A no higher than +(8–10) dB at distances of up to 30 km and minimal values of about –(5–8) dB at the end of the path. In this case, for all distances under study, a better agreement between experimental data and calculated dependences $I(r)$ is observed for the reception depth of 200 m, as compared to the reception depth of 100 m. The experimental dependence $I(r)$ for the frequency band with f_c = 3.15 kHz is characterized by positive values of the propagation anomaly (no greater than +10 dB) at distances of up to 20 km and by minimal levels of about –20 dB at the end of the path.

From the analysis of the experimental dependences $I(r)$ obtained for both frequency bands (f_c = 1.25 and 3.15 kHz) with different positions of the corresponding points, we conclude that these dependences are in fairly good agreement with calculations despite the adverse weather conditions and complex hydrographic data in the region of the experiments. The results of this study demonstrate a fundamental possibility of predicting the sound field characteristics in such a complex medium as the Barents Sea.

Thus, there are reasons to believe that, for broadband signals, the intensity structure of the sound field in a shallow sea (provided that the ray theory applica-

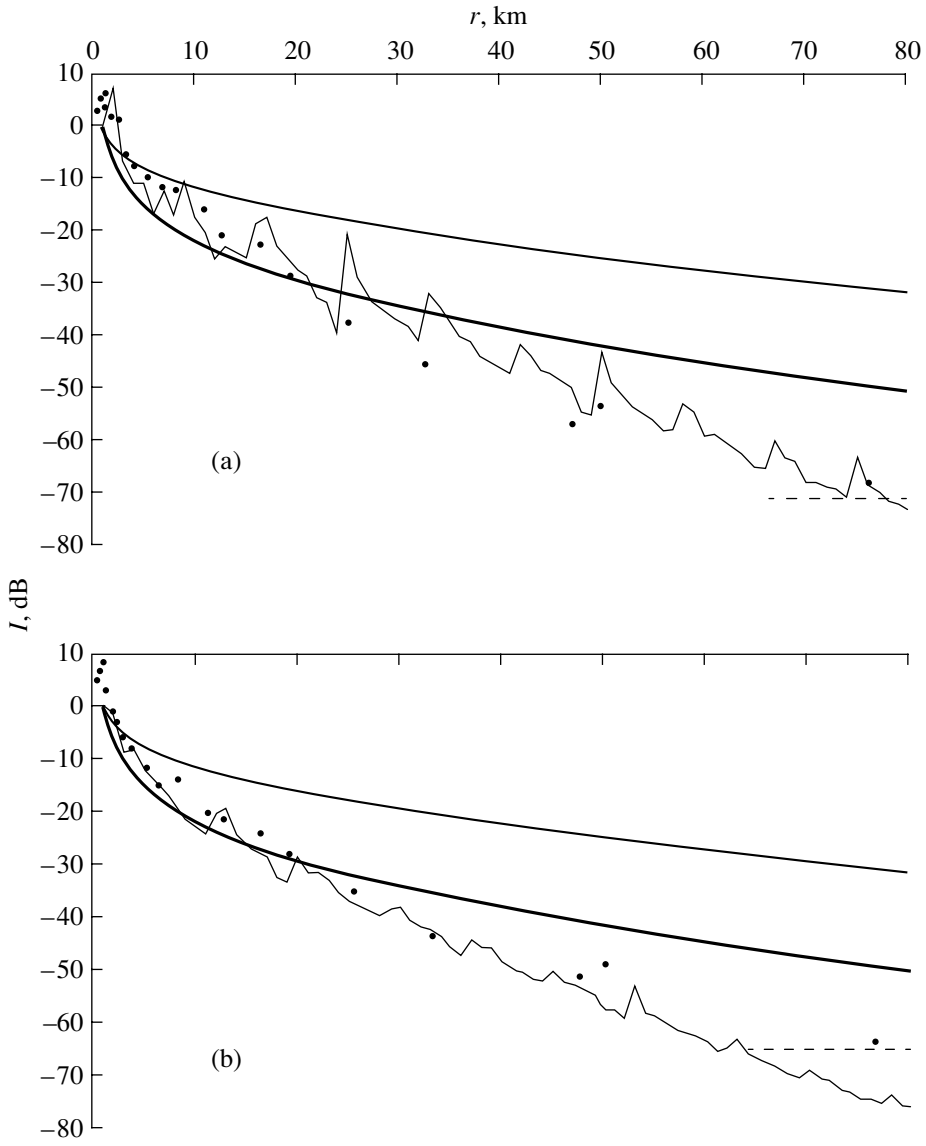

Fig. 7. Same as in Fig. 3 with a source depth of 100 m, f_c = 3.15 kHz, and a reception depth of (a) 100 and (b) 200 m.

bility conditions are satisfied) can be adequately estimated on the basis of the generalized data on the granulometric parameters of the bottom and the state of the sea surface in the region of interest. The necessary data on these characteristics for different regions of the ocean can be found in the literature (see, e.g., [10–12]). Evidently, for each chosen region, one has to take into account both seasonal and spatial variability of the sound velocity field, as well as the variation of the waveguide thickness along the chosen propagation path.

ACKNOWLEDGMENTS

This work was supported by the Russian Foundation for Basic Research (project no. 03-02-16565) and the Ministry of Industry and Science (grant no. NSh-1277.2003.5).

REFERENCES

1. O. P. Galkin, in *Acoustics of the Ocean: State of the Art*, Ed. by L. M. Brekhovskikh and I. B. Andreeva (Nauka, Moscow, 1982), pp. 92–106 [in Russian].
2. O. P. Galkin, L. V. Shvachko, E. A. Kharchenko, *et al.*, in *Acoustics in the Ocean* (Nauka, Moscow, 1992), pp. 114–127 [in Russian].
3. K. V. Avilov, O. P. Galkin, A. E. Lenets, *et al.*, in *Acoustics of the Ocean: Proceedings of 9th School–Seminar of Academician L.M. Brekhovskikh* (GEOS, Moscow, 2002), pp. 37–40.

4. D. M. Fromm, M. D. Collins, and G. V. Norton, J. Acoust. Soc. Am. **108**, 2562A (2000).
5. L. M. Brekhovskikh, in *Acoustics of the Ocean*, Ed. by L. M. Brekhovskikh (Nauka, Moscow, 1974), pp. 150–154 [in Russian].
6. N. S. Ageeva, V. D. Krupin, V. P. Perelygin, and N. V. Studenichnik, Akust. Zh. **40**, 181 (1994) [Acoust. Phys. **40**, 159 (1994)].
7. M. Snellen, D. G. Simons, M. Siderius, *et al.*, J. Acoust. Soc. Am. **109**, 514 (2001).
8. A. V. Vagin, *A Report of Institute of Acoustics, USSR Acad. Sci.* (Moscow, 1974).
9. N. K. Abakumova and O. P. Galkin, Vopr. Sudostr., Ser. Akust., No. 14, 90 (1980).
10. P. L. Bezrukov and I. O. Murdmaa, in *History of the World Ocean* (Nauka, Moscow, 1971) [in Russian].
11. A. V. Il'in, *Geomorphology of the Bottom in the Atlantic Ocean* (Nauka, Moscow, 1976) [in Russian].
12. *Winds and Waves in Oceans and Seas: Reference Data* (Transport, Leningrad, 1974) [in Russian].

Translated by E. Golyamina

Acoustical Physics, Vol. 51, No. 3, 2005, pp. 292–299. Translated from Akusticheskiĭ Zhurnal, Vol. 51, No. 3, 2005, pp. 352–359.

Field Focusing Control in Multimode Plane-Layered Waveguides

V. A. Grigor'ev* and V. M. Kuz'kin**

** Voronezh State University, Universitetskaya pl. 1, Voronezh, 394693 Russia*
e-mail: grig@box.vsi.ru
*** Wave Research Center, Prokhorov General Physics Institute, Russian Academy of Sciences, ul. Vavilova 38, Moscow, 119991 Russia*
e-mail: kuzkin@orc.ru

Received January 22, 2004

Abstract—The possibility of controlling localized fields in multimode regular waveguides on the basis of the interference invariant principle is studied by numerical simulation. It is demonstrated that, by tuning the radiation frequency of an array without changing the initial field distribution at the aperture, it is possible to perform the scanning by a focal spot in a waveguide. Estimates of the efficiency of this method depending on the size of a vertical linear array are presented. © *2005 Pleiades Publishing, Inc.*

INTRODUCTION

The practical needs of remote sensing of inhomogeneities in oceanic media lead to the problem of controlling the focusing (localization) of sound fields in multimode plane-layered waveguides. The problems of field localization at a preset point of a regular waveguide on the basis of the phase-conjugation principle were discussed in [1, 2]. The implementation of this idea in the field conditions was successfully demonstrated in [3, 4]. The problems of the formation of acoustic fields with a preset structure in multimode waveguides were considered most extensively in [5, 6]. The use of the conventional approach to scanning by a focal spot, which is connected with retuning of the field distribution at the aperture, leads to complications and rising costs of field experiments. This situation makes it necessary to study and test fundamentally new approaches to solving this problem that are realistic from an experimental point of view.

The interference invariant principle [7–9] is suitable for this purpose. The basis of this principle is the idea of the possibility of leveling the phase variations of a group of one-type modes due to the variations of the observation conditions by shifting the radiation frequency. The theory of the interference invariant was developed and confirmed by multiple experiments for the case of a point source. Its generalization to the case of an extended vertical array, where one-type groups of modes are excited in different ways at different depths, is not obvious and deserves a detailed investigation. In this paper, which is a further development of the ideas formulated in [7–9], the results of numerical simulation of controlling localized wave fields by tuning the radiation frequency without changing the initial field distribution over the aperture are given. Estimates of the efficiency of this method depending on the array size are presented.

STATEMENT OF THE PROBLEM

Let us introduce a cylindrical coordinate system (r, z, φ) and consider an axially symmetric waveguide with the profile of sound velocity $c(z)$. The water layer in the waveguide is bounded from above by the free surface $z = 0$ and from below by an impedance bottom $z = H(r)$. Omnidirectional sources are located at the coordinate origin $r = 0$ at the depths z_i, $i = 1, 2, \ldots, I$, where I is the number of elements of a vertical linear array. The array radiates a monochromatic signal with the acoustic power W_0. The localization of the array field at the frequency f_0 at the reference point $Q_0(r_0, z_0)$ is formed on the basis of the phase-conjugation principle. In the case of moving to the point $Q_j(r_j, z_j)$, a destruction (spreading) of the focal spot occurs because of the mode misphasing produced by the change in the observation conditions. Leveling of the phase variations of the modes, i.e., recovery of the field focusing, is performed by tuning the radiation frequency (the tuning frequency f_j and the frequency shift $\delta f_j = f_j - f_0$) without changing the distribution of sources. At the point Q_j, the field maximum $|u(Q_j)|$ is attained at the frequency f_j. In other words, at all other frequencies different from f_j (in the range δf_j), the field magnitude at the point Q_j takes on smaller values.

We evaluate the localization quality by the focusing factor q_j, the bandwidth Δf_j, and the dimensions Δr_j (longitudinal) and Δz_j (transverse) of the focal spot. We determine the bandwidth and the dimensions of the focal spot, which characterize its spreading, at the level of 0.7 of the field maximum in the vicinity of the point Q_j. The dimensions Δr_j and Δz_j refer to the horizontal and vertical directions, respectively. We evaluate the focusing factor characterizing the excess of the field

level in the localization region over the average (background) level in two different ways:

$$q_j' = \frac{|u(r_j, z_j, f_j)|}{|u_{\text{mid}}|}, \tag{1}$$

$$q_j'' = \frac{\frac{1}{\Delta z_j}\int_{\frac{\Delta z_j}{H}} |u(r_j, z, f_j)|^2 dz}{\frac{1}{H}\int_0^H |u(r_j, z, f_j)|^2 dz}, \tag{2}$$

where

$$|u_{\text{mid}}| = \frac{1}{H}\int_0^H |u(r_j, z, f_j)| dz. \tag{3}$$

The quantity $|u_{\text{mid}}|$ (Eq. (3)) determines the average field level over the waveguide thickness in the vicinity of the horizontal distance f_j at the frequency r_j. The parameter q_j' (Eq. (1)) characterizes the contrast of the focal spot with respect to the field, and the quantity q_j'' (Eq. (2)), the contrast of the localization region with respect to the average energy density.

Let us describe the distribution of sources in the case of focusing the array field at the reference point Q_0. We represent the vertical field distribution at the frequency f_0 at the coordinate origin, which is produced by a point source located at the point Q_0, in the form of a finite sum of the normal modes of a discrete spectrum:

$$w_0(0, z) = \sum_{m=1}^{M} w_m(0, z), \tag{4}$$

where

$$w_m(0, z) = \sqrt{\rho_0 c_0}\frac{\psi_m(r_0, z_0)\psi_m(0, z)}{\sqrt{\xi_m(0) r_0}} \times \exp(i\pi/4)\exp\left[i\int_0^{r_0} \xi_m(r_0 - r')dr'\right]. \tag{5}$$

Here, $\rho_0 = \rho(r_0, z_0)$ and $c_0 = c(r_0, z_0)$ are the water density and the sound velocity at the distance r_0 and depth z_0, $\psi_m(r, z)$ and $\xi_m(r)$ are the eigenfunction and the propagation factor of the mth mode, and M is the number of effectively propagating modes. In Eq. (5), the source power is assumed to be equal to unity. The principle of phase conjugation presumes that the distribution of particle velocities at the surface of the ith source of the array is phase-conjugate with the field $w_0(0, z_i)$ (Eq. (4)); i.e., the radiation power is

$$W_i = \eta_0 |w_0(0, z_i)|^2 W_0. \tag{6}$$

In the absence of interaction of the array elements, from the normalization condition $\sum_{i=1}^{I} W_i = W_0$, according to Eq. (6), we obtain an expression for the proportionality coefficient η_0:

$$\eta_0 = \left[\sum_{i=1}^{I} |w_0(0, z_i)|^2\right]^{-1}. \tag{7}$$

Such a phase distribution of sources produces a conjugate field, i.e., a field converging to the point Q_0. Let us sum up the fields of point sources. In this case, using Eqs. (6) and (7), the radiation field of the array $u(r, z)$ can be reduced to the form

$$u(r, z) = \sum_{m=1}^{M} u_m(r, z), \tag{8}$$

where

$$u_m(r, z) = a_m \frac{\psi_m(r, z)}{\sqrt{\xi_m(r) r}} \exp\left[i\int_0^r \xi_m(r')dr'\right]. \tag{9}$$

Here,

$$a_m = \sqrt{\eta_0 W_0}\exp(i\pi/4)\sum_{i=1}^{I} \sqrt{\rho_i c_i} w_0^*(0, z_i)\psi_m(0, z_i) \tag{10}$$

is the excitation coefficient of the mth mode.

NUMERICAL SIMULATION

We consider a regular plane-layered waveguide with depth $H = 120$ m and the profile of sound velocity $c(z)$ given in Fig. 1. The parameters of the absorbing liquid bottom are the ratio of the soil and water densities $\rho = 1.9$ g/cm^3 and the complex refraction index $n = 0.84(1 + i0.03)$. We consider three equidistant linear vertical arrays D_μ ($\mu = 1, 2, 3$) with period $d = 3$ m and radiation power $W_0 = 2$ kW. The frequency is $f_0 = 230$ Hz. The lower sources of the arrays are located at the bottom. The number of elements of the array D_1 is $I_1 = 41$ (the array crosses the whole waveguide); the number of elements of the array D_2 is $I_2 = 31$ (the array crosses three-quarters of the waveguide thickness); and the number of elements of the array D_3 is $I_3 = 21$ (the array crosses one-half of the waveguide thickness). The relative bandwidth of frequency tuning does not exceed 15%: $0.85f_0 \le f_j \le 1.15f_0$. The coordinates of the reference point Q_0 are $r_0 = 40$ km and $z_0 = 60$ m. The coordinates of the points Q_j ($j = 1, 2, \ldots, 6$), where the field is scanned on the basis of the interference invariant principle, are $r_1 = 30$ km, $z_1 = 60$ m; $r_2 = 35$ km, $z_2 = 60$ m; $r_3 = 45$ km, $z_3 = 60$ m; $r_4 = 50$ km, $z_4 = 60$ m; $r_5 = 40$ km, $z_5 = 90$ m; and $r_6 = 40$ km, $z_6 = 30$ m.

The results of numerical calculations are given in the table and partially presented in Figs. 2–8. In these figures, the dependences of the field magnitude (ampli-

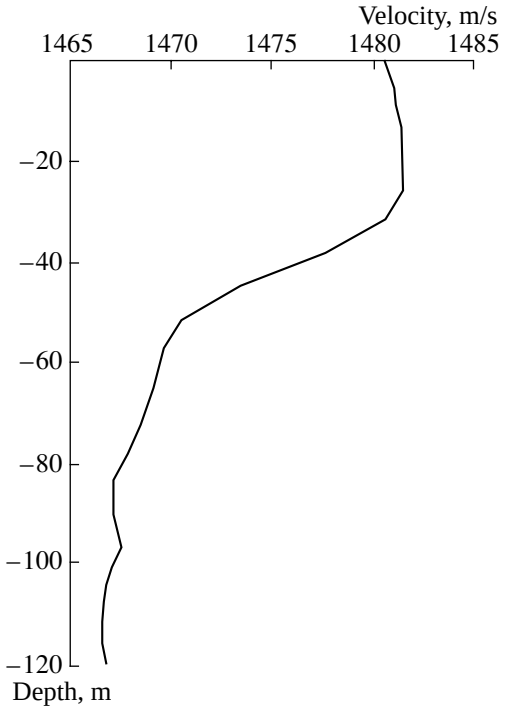

Fig. 1. Dependence of the sound velocity on depth.

tude) on frequency at different dimensions of the radiating array D_μ, $\mu = 1, 2, 3$, are shown at the points Q_j ($j = 0, 1, \ldots, 6$). From these dependences, the values of the tuning frequency f_j (and the bandwidth Δf_j) and the position of the maximum of the field amplitude $|u(r_j, z_j, f_j)|$ were determined. A calculation of the field amplitude at the frequency f_j as a function of horizontal and vertical displacements with respect to the point Q_j was conducted to determine the dimensions Δr_j and Δz_j of the focal spots. The dependences $|u(r, z_j, f_j)|$, r = var and $|u(r_j, z, f_j)|$, z = var are not presented in this paper for the sake of brevity. The bandwidth $\Delta f_{5,6}$ for the points $Q_{5,6}$ is not indicated, since the tuning frequency f_j goes beyond the lower boundary of the values $0.85f_0$. In the vicinity of the point Q_6, the field is weaker in comparison with the background level ($q_6' < 1$) because of its concentration near the lower boundary. This prevents the determination of the transverse dimension Δz_6 of the focal spot and the focusing factor q_6''. For the cases where two pronounced field maxima at different frequencies are observed at the points, the table gives the focusing parameters at each frequency. As one can see, the definition given by Eq. (1) yields smaller values of the focusing factor in comparison with the definition given by Eq. (2): $q_j'' > q_j'$.

At the reference point Q_0, where the field focusing is considered on the basis of the principle of phase conjugation, the longitudinal dimension Δr_0 of a focal spot is inversely proportional to the array length, while the transverse dimension Δz_0 and the focusing factor q_0' (or q_0'') almost do not depend on its length. In the case of

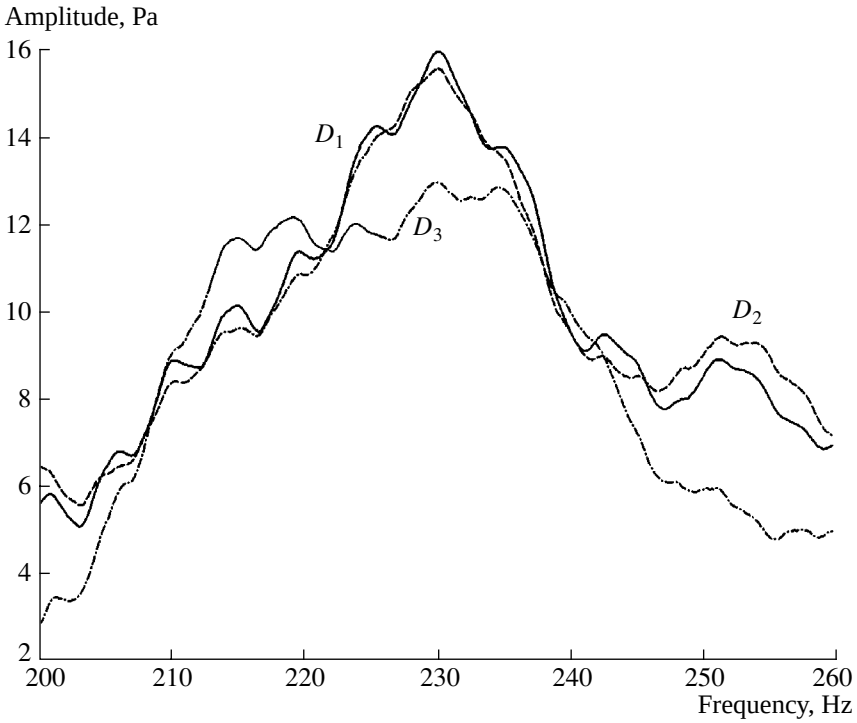

Fig. 2. Dependence of the acoustic field amplitude of an array on frequency at the point Q_0, $r_0 = 40$ km and $z_0 = 60$ m, for arrays D_1 (solid line), D_2 (dashed line), and D_3 (dash–dot line).

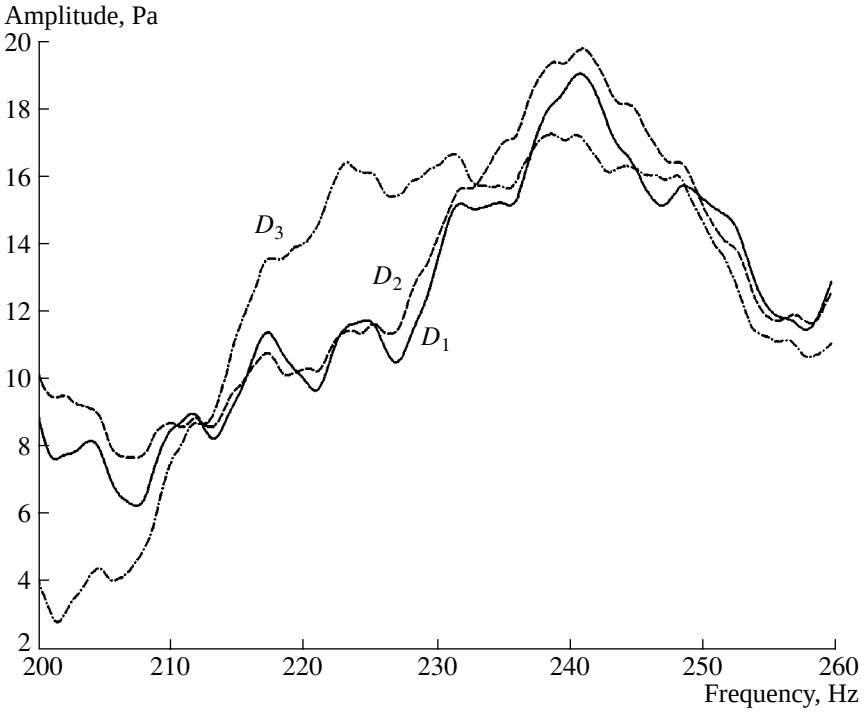

Fig. 3. Dependence of the acoustic field amplitude of an array on frequency at the point Q_1, r_1 = 30 km and z_1 = 60 m, for arrays D_1 (solid line), D_2 (dashed line), and D_3 (dash–dot line).

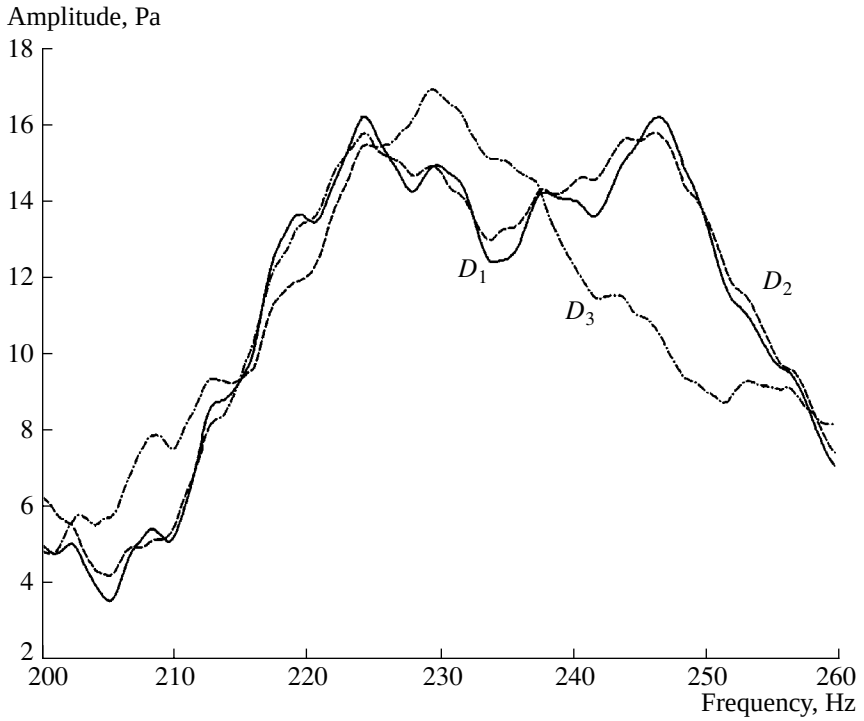

Fig. 4. Dependence of the acoustic field amplitude of an array on frequency at the point Q_2, r_2 = 35 km and z_2 = 60 m, for arrays D_1 (solid line), D_2 (dashed line), and D_3 (dash–dot line).

shifting the observation point by frequency tuning, the field focusing partially recovers (in comparison with the reference point). The tuning frequency does not depend on the array dimensions and decreases with increasing distance. The latter assumes a simple explanation [7]. At the same time, for example, at the points $Q_{2,3}$,

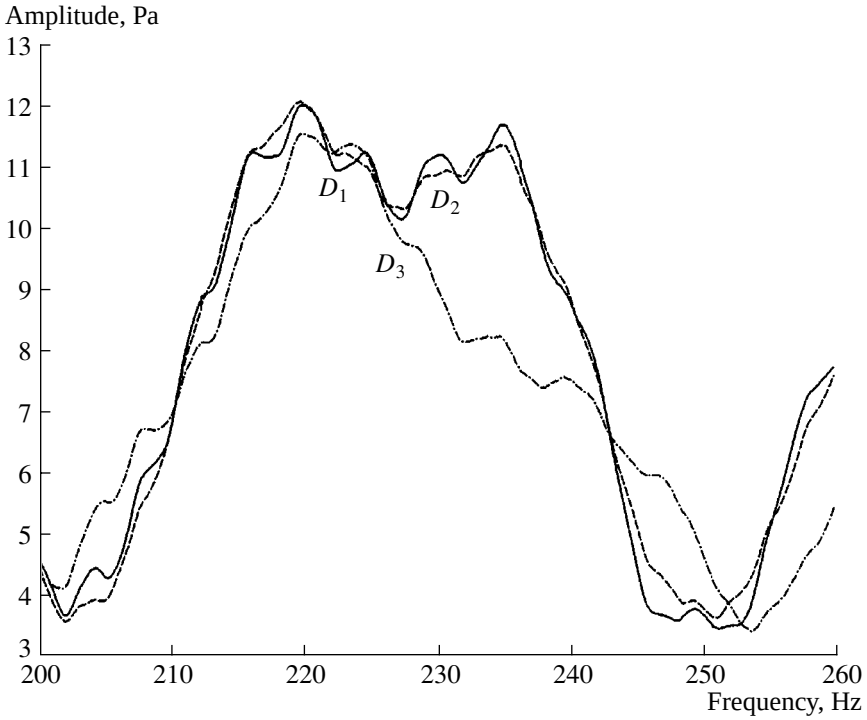

Fig. 5. Dependence of the acoustic field amplitude of an array on frequency at the point Q_3, r_3 = 45 km and z_3 = 60 m, for arrays D_1 (solid line), D_2 (dashed line), and D_3 (dash–dot line).

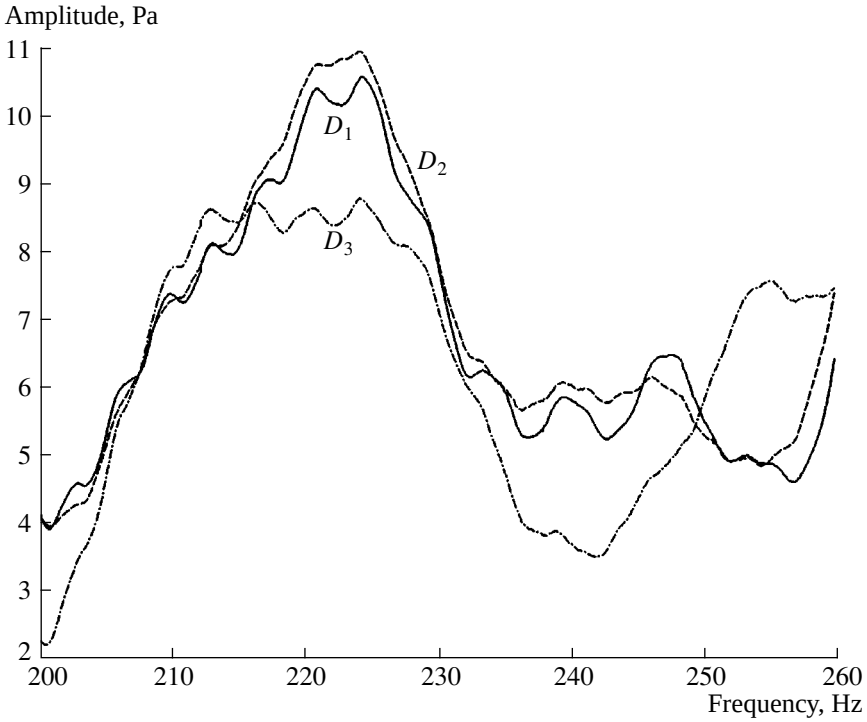

Fig. 6. Dependence of the acoustic field amplitude of an array on frequency at the point Q_4, r_4 = 50 km and z_4 = 60 m, for arrays D_1 (solid line), D_2 (dashed line), and D_3 (dash–dot line).

the localization of the field with close parameters of focusing occurs not at a single frequency but at two frequencies. Their average value is close to the frequency value obtained by the interpolation of the tuning frequencies over the pairs of points $Q_{0,1}$ and $Q_{0,4}$, respectively. This is apparently connected with the existence

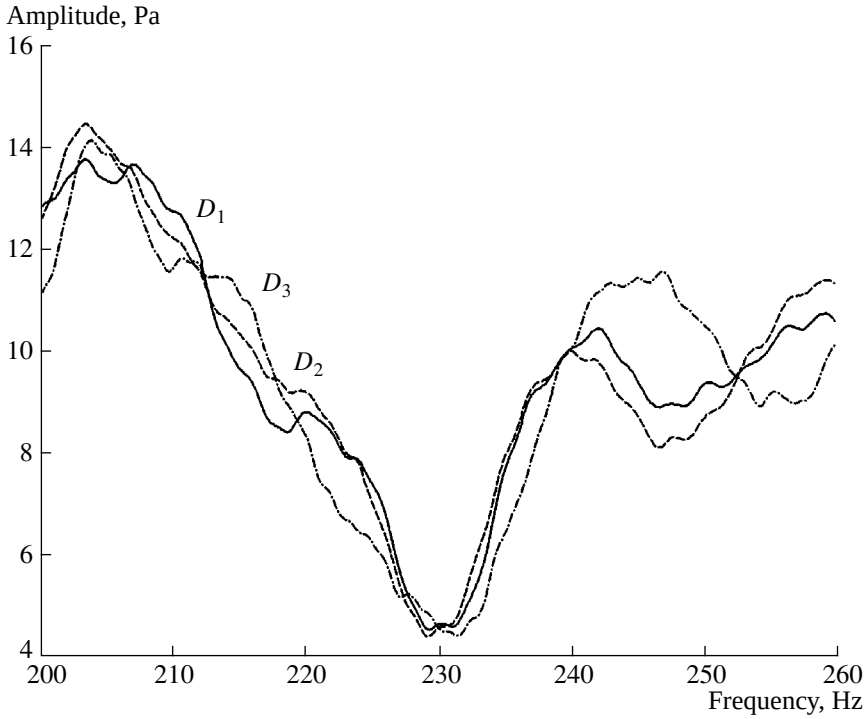

Fig. 7. Dependence of the acoustic field amplitude of an array on frequency at the point Q_5, r_5 = 40 km and z_5 = 90 m, for arrays D_1 (solid line), D_2 (dashed line), and D_3 (dash–dot line).

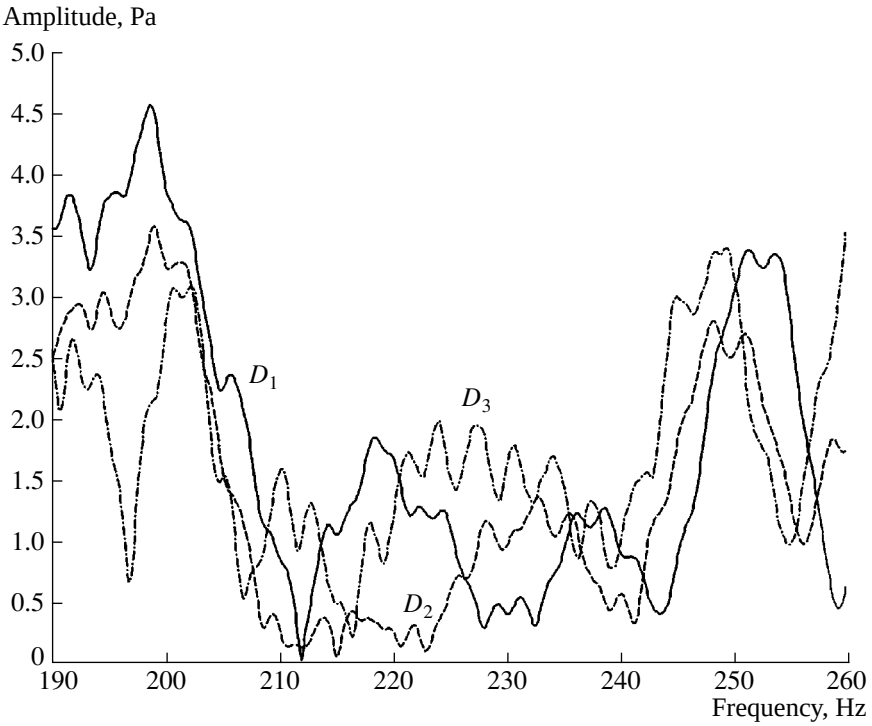

Fig. 8. Dependence of the acoustic field amplitude of an array on frequency at the point Q_6, r_6 = 40 km and z_6 = 30 m, for arrays D_1 (solid line), D_2 (dashed line), and D_3 (dash–dot line).

(at single points in the waveguide space) of strongly misphased groups of one-type modes. The manifestation of this effect becomes stronger with an increase in the array size. Except for the cases of more than one maximum at different frequencies, the quality of restored focusing does not noticeably depend on the

Parameters of the focal spots at observation points Q_j

j		0	1	2	3	4	5	6
r_j, m		40000	30000	35000	45000	50000	40000	40000
z_j, m		60	60	60	60	60	90	30
f_j, Hz	D_1	230.0	240.7	224.3	219.7	224.2	203.4	198.8
				246.3	234.7		241.8	250.9
	D_2	230.0	240.8	224.3	219.5	224.0	203.4	199.0
				245.9	234.5		239.7	247.8
	D_3	230.0	238.5	229.4	219.6	224.0	203.8	202.2
							246.5	248.9
Δf_j, Hz	D_1	19.4	24.3	35.8	29.6	19.2	–	–
	D_2	18.5	23.1	37.5	28.9	18.9	–	–
	D_3	32.7	37.7	22.6	23.8	24.6	–	–
Δr_j, m	D_1	700	1180	1370	1380	1210	1080	550
				1190	1410		1440	430
	D_2	930	1180	1730	1510	1220	1040	610
				1160	1540		1680	370
	D_3	1390	1290	630	820	1440	1610	1470
							1700	630
Δz_j, m	D_1	24.1	27.1	22.2	26.3	29.2	25.4	–
				23.4	23.2		54.2	
	D_2	26.6	27.8	24.9	29.1	31.6	24.7	–
				28.6	25.4		30.9	
	D_3	22.8	35.6	23.9	39.7	43.8	23.5	–
							29.7	
q'_j	D_1	3.1	2.3	2.3	2.2	2.2	2.3	0.7
				2.3	2.2		1.8	0.5
	D_2	2.9	2.5	2.2	2.2	2.3	2.4	0.5
				2.2	2.1		1.7	0.4
	D_3	2.4	2.2	2.6	2.3	1.8	2.6	0.6
							1.9	0.6
q''_j	D_1	3.7	3.0	2.9	3.0	2.9	3.3	–
				2.9	2.7		2.6	
	D_2	3.5	3.0	2.6	2.7	2.9	3.4	–
				2.7	2.6		2.7	
	D_3	3.9	2.7	3.6	2.5	2.0	3.8	–
							2.6	

size of the arrays $D_{1,2}$ or on the horizontal distance to the reference point. In the case of a further decrease in the aperture size (the array D_3), deterioration of the focusing quality is observed. The longitudinal dimension of the focal spot increases with respect to the reference point on average by a factor of 1.6, and the focusing factor decreases approximately by a factor of 0.7. In the case of a change in the detection depth, the focusing efficiency is determined by the sound velocity profile. Physically, this corresponds to a displacement of the focal spot mainly in the horizontal plane.

It is clear that these results are not connected with the choice of the method of focusing of the array field at the reference point. The only significant fact is that, by tuning the radiation frequency of an extended source, it is possible to level the phase variations of modes due to the displacements of the observation point. This confirms the possibility of transferring the

concept of interference invariance to the fields formed by vertically extended arrays.

CONCLUSIONS

Thus, by numerical simulation, we tested a new method of scanning by a focal spot in a multimode system with exactly known parameters on the basis of the interference invariant principle. The possibility of controlling localized fields on the basis of tuning the radiation frequency of an array without changing the distribution of the initial field over the aperture is demonstrated. Estimates of the efficiency of this method depending on the dimensions of a vertical linear array are given.

ACKNOWLEDGMENTS

This work was supported under the program "Coherent Acoustic Fields and Signals" of the Division of Physical Sciences, Russian Academy of Sciences, and by the grant "Scientific Schools," no. NSh-1553.2003.2.

REFERENCES

1. M. M. Dargeĭko, Yu. A. Kravtsov, V. G. Petnikov, *et al.*, Izv. Vyssh. Uchebn. Zaved. **27** (6), 746 (1984).
2. V. Ya. Danilov, Yu. A. Kravtsov, and A. G. Nakonechnyĭ, in *Formation of Acoustic Fields in Oceanic Waveguides*, Ed. by V. A. Zverev (Inst. Prikl. Fiz., Akad. Nauk SSSR, Gorki, 1991), pp. 32–54 [in Russian].
3. W. A. Kuperman, W. S. Hodgkiss, H. C. Song, *et al.*, J. Acoust. Soc. Am. **103**, 25 (1998).
4. W. S. Hodgkiss, H. C. Song, W. A. Kuperman, *et al.*, J. Acoust. Soc. Am. **105**, 1597 (1999).
5. V. I. Talanov, Izv. Vyssh. Uchebn. Zaved., Radiofiz. **28** (7), 872 (1985).
6. E. Yu. Gorodetskaya, A. I. Malekhanov, and V. I. Talanov, in *Formation of Acoustic Fields in Oceanic Waveguides: Reconstruction of Inhomogeneities*, Ed. by V. A. Zverev (Inst. Prikl. Fiz., Ross. Akad. Nauk, Nizhni Novgorod, 1994), pp. 9–43 [in Russian].
7. S. D. Chuprov, in *Acoustics of the Ocean: The Modern State*, Ed. by L. M. Brekhovskikh and I. B. Andreeva (Nauka, Moscow, 1982), pp. 71–91 [in Russian].
8. E. F. Orlov, in *Problems in the Ocean Acoustics*, Ed. by L. M. Brekhovskikh and I. B. Andreeva (Nauka, Moscow, 1984), pp. 85–93 [in Russian].
9. V. M. Kuz'kin, Akust. Zh. **41**, 344 (1995) [Acoust. Phys. **41**, 300 (1995)].

Translated by M. Lyamshev

Acoustical Physics, Vol. 51, No. 3, 2005, pp. 300–305. Translated from Akusticheskiĭ Zhurnal, Vol. 51, No. 3, 2005, pp. 360–365.

Analysis of the Sound Transmission Loss of Panels with Resonant Systems on the Basis of Equivalent Representations

B. M. Efimtsov and L. A. Lazarev

Zhukovskii Central Aerohydrodynamic Institute, Moscow Branch, ul. Radio 17, Moscow, 107005 Russia

e-mail: efimtsov@prob-lab.ru

Received December 30, 2003

Abstract—Effects of increasing the sound transmission loss of panels with the help of resonant systems on the basis of equivalent representations are analyzed. Emphasis is placed on the least-studied resonant systems, the inertial bodies of which simultaneously interact with media on each side of the panels. A universal expression for the sound transmission loss of panels with an arbitrary system of resonant elements with one degree of freedom is presented. It includes the parameters common to all types of resonators (the total mass, compressibility, quality factor, and characteristic frequencies). The expression can be directly used to compare the efficiency of different types of resonant systems mounted on a panel and to determine their optimum parameters. © *2005 Pleiades Publishing, Inc.*

In recent years, considerable attention has been devoted to studying resonant systems mounted on panels, with the aim to reduce their acoustic radiation and increase the sound transmission loss [1–7]. Nevertheless, as far as can be inferred from the publications, only one paper [5] is devoted to the purposeful investigation of physical phenomena determining the effects of increasing the transmission loss of panels by using various types of resonant systems and to their generalized description. It was found that these effects are determined by one of three phenomena: soft reflection, hard reflection, and acoustic compensation. The first phenomenon is determined by a sharp decrease in the input impedance of a panel after mounting resonant systems on it. The second phenomenon is connected with a sharp increase in the input impedance, and the third phenomenon is related to the reduction of the impedance to an almost purely imaginary value, which results in the compensation of the sound pressure or volume velocity. In this connection, an arbitrary system used for increasing the sound transmission loss can be ascribed to one of the three types: soft reflectors (SR), hard reflectors (HR), or acoustic compensators (AC).

In [5], we considered only resonant systems mounted on one side of a solid panel. These systems can be conventionally called one-sided systems. In the present paper, we generalize the results of [5] and extend them to arbitrary systems of resonant elements with one degree of freedom. Emphasis is placed on the resonant systems that are mounted in holes in a panel, so that their inertial bodies interact with media on both sides of the panel. These resonant systems will be conventionally called two-sided.

The analysis of the acoustic characteristics of panels with resonant systems and the generalization of the results are performed on the basis of the equivalent representation method. The essence of this method consists in determining acoustically equivalent systems. Its application enables us to combine different resonant systems into one of three types and to use unified relations for evaluating their acoustic characteristics.

We consider a system of two-sided compressible resonators schematically shown in Fig. 1. Resonators whose vibrations are accompanied by a change in their volume will be called compressible. The axis of vibration of resonators, in the general case, may deviate from the normal to the panel surface (the case of tilted resonators). Such a resonant system on a panel is characterized by the following parameters: the total surface mass of the resonant elements and the panel (M); the mass of inertial bodies of resonant elements per unit area (m); the stiffness per unit area (k) by which they are connected and which includes the stiffness of the air volume and the stiffness of mounting; the quality factor of a resonator Q; the relative areas of interaction with the medium on both sides of the panel (σ_1, σ_2); and the slope angle of the axis of vibration with respect to the normal to the panel (α) for tilted resonators.

Each of the resonant systems analyzed below can be considered as a particular case of two-sided compressible resonators. One-sided compensators (Fig. 2a) are a particular case of two-sided compensators in which one of the interacting areas is equal to zero ($\sigma_1 = 0$ or $\sigma_2 = 0$). Incompressible two-sided resonators (Fig. 2b) can be considered as a limiting case of compressible resonators when their areas of interaction are equal ($\sigma_1 = \sigma_2$). A panel with dynamic vibration absorbers (Fig. 2c) can be considered as a limiting case of the absence of direct interaction with the medium ($\sigma_1 = \sigma_2 = 0$). Helmholtz resonators (Fig. 2d) can be considered as a particular

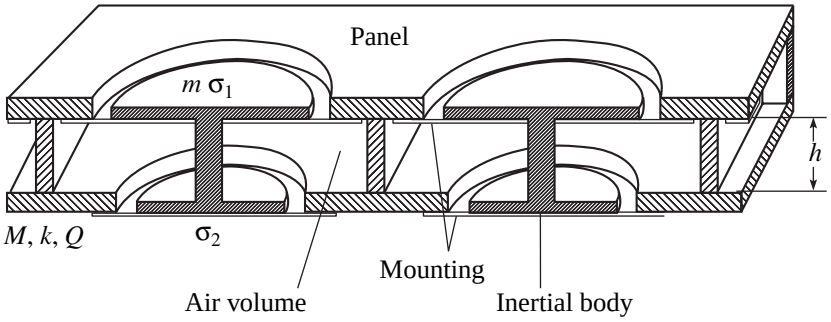

Fig. 1. Schematic diagram of a two-sided compressible resonator.

case of one-sided compensators with a small area of interaction ($\sigma \ll 1$) and a very small mass of their inertial bodies.

Therefore, the relations describing the behavior of two-sided compressible resonators (Fig. 1) should be valid for arbitrary systems of resonant elements with one degree of freedom.

Here, as in [5], we use the simplest mathematical model describing the transmission of normally incident sound waves through an infinite homogeneous purely inertial panel with a regular system of similar resonators whose parameters are assumed to be known. The resonator dimensions and the distances between them are assumed to be small (compared to the sound wavelength).

The transfer matrix for two-sided compressible resonators (AC2, Fig. 1), both direct and tilted, can be written in one of two forms:

$$A_{AC2} = \begin{pmatrix} 1 - M_2\omega^2/k_h\Omega_t & i\omega M\Omega_{12}/\Omega_t \\ i\omega/k_h\Omega_t & 1 - M_1\omega^2/k_h\Omega_t \end{pmatrix}; \quad (1)$$

$$A_{AC2} = \begin{pmatrix} 1 & i\omega M_2 \\ 0 & 1 \end{pmatrix}\begin{pmatrix} 1 & 0 \\ i\omega/k_h\Omega_t & 1 \end{pmatrix}\begin{pmatrix} 1 & i\omega M_1 \\ 0 & 1 \end{pmatrix}; \quad (2)$$

$$\Omega_t = 1 - (\omega/\omega_t)^2 + i\omega/\omega_t Q_t;$$

$$\Omega_{12} = 1 - (\omega/\omega_{12})^2 + i\omega/\omega_t Q_t;$$

$$M_1 + M_2 = M, \quad M_1 M_2 = k_h M(\omega_{12}^{-2} - \omega_t^{-2}).$$

Transfer matrices (1) and (2), accurate to a permutation of M_1 and M_2 (which corresponds to turning over the system), are expressed in terms of following the five parameters: the total surface mass of the system (M); the static stiffness of the system (k_h), determined by the change in its volume with a change in pressure; the tuning frequency of the system (ω_t) corresponding to the maximum of the transmission loss of the panel with resonators with a sufficiently high quality factor; the mass–elasticity–mass resonance frequency (ω_{12}), at which a dip in the transmission loss is observed; and the equivalent quality factor ($Q_t = Q\sqrt{k/m}/\omega_t$).

For two-sided compressible direct resonators (Fig. 1), the quantities involved in Eqs. (1) and (2) are determined by the expressions

$$k_h = \frac{k}{(\sigma_1 - \sigma_2)^2};$$

$$M_1 = \frac{m - M\sigma_2}{\sigma_1 - \sigma_2}; \quad (3)$$

$$\omega_t^2 = \frac{k}{M\sigma_1\sigma_2 + m(1 - \sigma_1 - \sigma_2)}.$$

The expressions for two-sided compressible tilted resonators coincide with the corresponding expressions for direct ones if we make the substitutions

$$m' = m\cos^2\alpha, \quad k' = k\cos^2\alpha, \quad \sigma_1' = \sigma_1\cos\alpha,$$
$$\sigma_2' = \sigma_2\cos\alpha, \quad M' = M + m\sin^2\alpha. \quad (4)$$

Consequently, tilted resonators are equivalent to direct resonators if their parameters satisfy Eqs. (4). Here, the primes designate the parameters of equivalent direct resonators. The mass–elasticity–mass resonance frequency for direct resonators of any type has the form

$$\omega_{12} = \sqrt{kM/((M-m)m)}, \quad (5)$$

and, for tilted resonators, it has the form

$$\omega_{12} = \sqrt{kM/((M - m\cos^2\alpha)m\cos^2\alpha)}. \quad (6)$$

For direct one-sided compensators ($\sigma_2 = 0$), Eqs. (3) take the form

$$k_h = k/\sigma^2; \quad M_1 = m/\sigma; \quad \omega_t^2 = k/(m(1-\sigma)); \quad (7)$$

and, for tilted one-sided compensators,

$$M_1 = m\cos\alpha/\sigma; \quad \omega_t^2 = k/(m(1 - \sigma\cos\alpha)). \quad (8)$$

For direct one-sided compensators (AC) mounted on side 1 (Fig. 2a), the value of M_1 coincides with the sur-

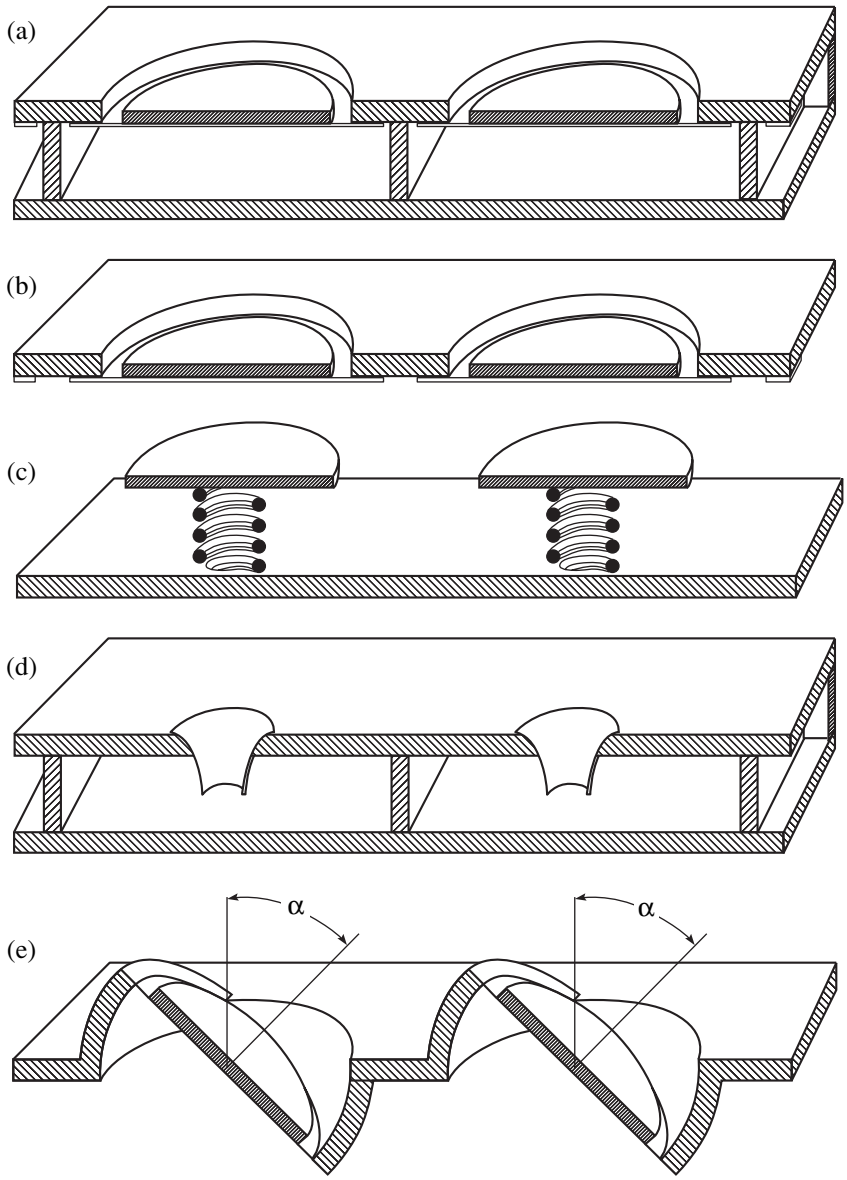

Fig. 2. Panels with resonant systems: (a) one-sided acoustic compensators, (b) two-sided incompressible resonators, (c) dynamic vibration absorbers, (d) Helmholtz resonators, and (e) tilted two-sided incompressible resonators.

face mass of the material of which their inertial bodies are made.

For an incompressible two-sided direct (HR, Fig. 2b) or tilted (HR2, Fig. 2e) resonator and for a panel with dynamic vibration absorbers (DVA, Fig. 2c), the transfer matrices have the same form:

$$A_{HR} = A_{HR2} = A_{DVA} = \begin{pmatrix} 1 & i\omega M\Omega_{12}/\Omega_t \\ 0 & 1 \end{pmatrix}; \quad (9)$$

$$\Omega_t = 1 - (\omega/\omega_t)^2 + i\omega/\omega_t Q_t;$$

$$\Omega_{12} = 1 - (\omega/\omega_{12})^2 + i\omega/\omega_t Q_t.$$

Here, the tuning frequency for a panel with dynamic vibration absorbers corresponds to their resonance frequency $\omega_t = \sqrt{k/m}$. For two-sided incompressible direct resonators, this frequency is determined from the expression

$$\omega_t^2 = k(M\sigma^2 + m(1-2\sigma))^{-1}, \quad (10)$$

and, for tilted two-sided incompressible resonators, from

$$\omega_t^2 = k(M\sigma^2 + m(1-2\sigma\cos\alpha))^{-1}. \quad (11)$$

For a panel with Helmholtz resonators ($\sigma_2 = 0, \sigma_1 \ll 1$), the direct interaction of which with the panel is

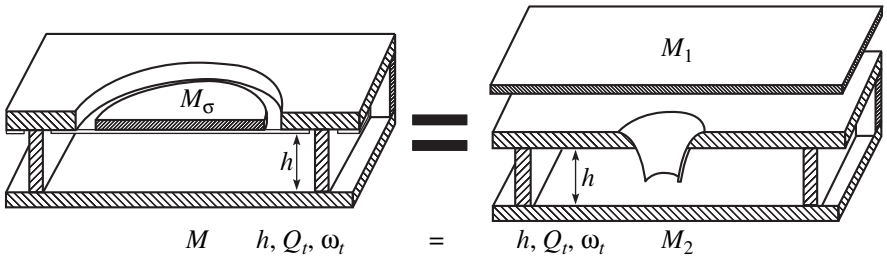

Fig. 3. Equivalence of a panel with acoustic compensators and a system consisting of two panels with Helmholtz resonators between them; $M_1 = m/\sigma$, $M_2 = M - m/\sigma$, M is the total surface mass, m is the mass of inertial bodies per unit area, and σ is the relative area of resonators.

neglected, the tuning frequency of the system is equal to the resonance frequency and its transfer matrix can be written as

$$A_{SR} = \begin{pmatrix} 1 & i\omega M \\ 0 & 1 \end{pmatrix}\begin{pmatrix} 1 & 0 \\ i\omega/k_h\Omega_t & 1 \end{pmatrix}, \qquad (12)$$

$$k_h = \rho c^2/h,$$

where h is the averaged thickness of the air cavities of resonators. Below, we use the more convenient dimensionless quantity $\bar{h} = h\omega_t/c$, which represents the wave thickness. By analogy with the Helmholtz resonators, for other types of compressible resonators, we use the equivalent wave thickness $\overline{h_e} = \rho c\omega_t/k_h$.

Thus, the transfer matrix of any of the systems under consideration can be expressed in terms of the same parameters (M, k_h, ω_t, ω_{12}, and Q_t). Therefore, if, for two systems, the values of these parameters are the same, these systems, with a properly chosen orientation, are equivalent to each other; that is, they are indistinguishable from the acoustical point of view.

The following systems with properly selected parameters are acoustically equivalent to each other: panels with Helmholtz resonators and one-sided compressible resonators tilted by 90°; a panel with dynamic vibration absorbers and a panel with two-sided incompressible direct or tilted resonators; one-sided compensators and two-sided compressible resonators, both of which can be direct or tilted.

Thus, any resonant system on a panel can be assigned to one of the three classes of systems: soft reflectors, hard reflectors, or acoustic compensators. Resonant systems belonging to one class may be acoustically equivalent. Therefore, two-sided incompressible (Figs. 2b, 2e) and compressible (Fig. 1) resonators can also be called two-sided hard reflectors and two-sided acoustic compensators, respectively.

Two systems are equivalent, accurate to orientation, if their total masses, tuning frequencies, and equivalent quality factors coincide and, in addition, if the equivalent wave thicknesses are equal for soft reflectors, the mass–elasticity–mass resonance frequencies are equal for hard reflectors, and both the equivalent wave thicknesses and mass–elasticity–mass resonance frequencies are equal for compensators.

According to the representation of the transfer matrix of compensators in form (2), a panel with compensators (one- and two-sided) is equivalent to a system consisting of two panels with surface masses M_1 and M_2 and Helmholtz resonators between them with the same tuning frequency, equivalent quality factor, and equivalent thickness (Fig. 3). Note that the masses M_1 and M_2 may take negative values. Therefore, it is convenient to use the equality of the parameters M_1 and M_2 as a criterion of the equivalence of compensators. In particular, from this equivalent representation for compensators, it is seen that a one-sided acoustic compensator is equivalent to a panel with soft reflectors (Helmholtz resonators), provided that the surface mass of the material of the inertial body of the compensator is equal to the total surface mass ($M_1 = M$ or $M_2 = M$).

The sound transmission loss of panels with compensators is described by the equality

$$TL = 20\log\left|\frac{1}{2}\left(\frac{a_{12}}{\rho c} + a_{11} + a_{22} + a_{21}\rho c\right)\right| = 20\log\left|1 + i\frac{(\bar{h} + M\omega(\Omega_{12} + i\bar{h})/\rho c)}{2\Omega_c}\right|. \qquad (13)$$

At the tuning frequency, the sound transmission loss is approximately determined as

$$TL(\omega_t) \approx 20\log(M\omega_t/2\rho c) + 20\log\left|(1 - \omega_t^2/\omega_{12}^2 + i\bar{h})Q_t\right|. \qquad (14)$$

Since all types of resonators are special cases of compensators, Eqs. (13), (14) are valid for any resonator.

We introduce the efficiency parameter Θ for resonators of any type as a quality-factor-independent coefficient by which the increase in the transmission loss after mounting the resonators can be found from the approximate expression

$$\Delta TL(\omega_t) \approx 20\log(\Theta Q_t), \quad Q_t \gg 1. \qquad (15)$$

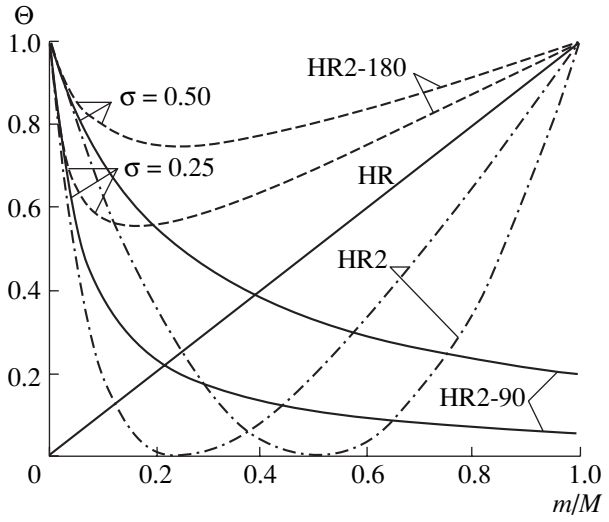

Fig. 4. Efficiency parameter of hard reflectors: dynamic vibration absorbers (HR), direct two-sided hard reflectors (HR2), and tilted by 90° (HR2-90) and turned-over (HR2-180) two-sided hard reflectors.

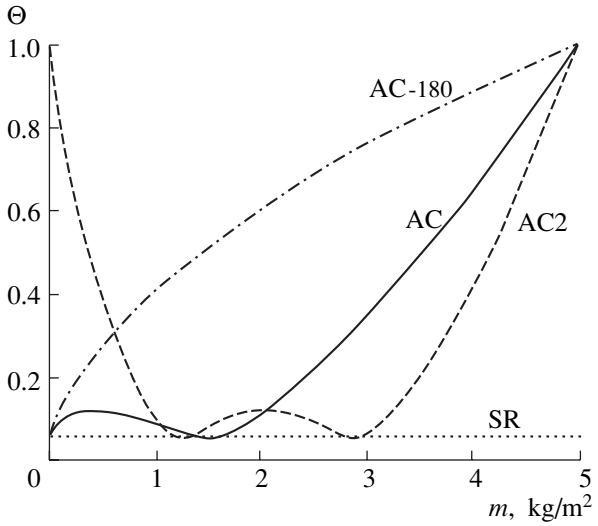

Fig. 5. Efficiency parameter of acoustic compensators: one-sided compensator (AC), direct two-sided compensator (AC2), turned-over one-sided compensator (AC-180), and soft reflector (SR); M = 5 kg/m^2, h = 0.03 m, f_t = 100 Hz, σ_1 = 0.25, and σ_2 for AC2 depends on m and varies from 0.5 to 0.6.

From Eq. (14) it follows that the efficiency parameter for resonators mounted on a single panel with fixed total mass equals

$$\Theta = \left|1 - \omega_t^2/\omega_{12}^2 + i\bar{h}\right|. \quad (16)$$

In particular, for hard reflectors, $\bar{h} = 0$ and $\Theta_{HR} = |1 - \omega_t^2/\omega_{12}^2|$, and, for soft reflectors, $\omega_t = \omega_{12}$ and $\Theta_{SR} = \bar{h}$. For hard reflectors, it may be convenient to express the efficiency parameter in terms of the mass of equivalent dynamic vibration absorbers m_1 as $\Theta_{HR} = m_1/M$. For two-sided hard reflectors, the mass of equivalent dynamic vibration absorbers is determined by the equality $m_1 = (m - M\sigma)^2/(M\sigma^2 + m(1 - 2\sigma))$. For compensators, the efficiency parameter is also conveniently expressed in terms of the panel masses M_1 and M_2 in the equivalent representation

$$\Theta_{AC} = \bar{h}\left|M_1 M_2 \omega_t/(M\rho c) - i\right|. \quad (17)$$

Let us consider the dependence of the efficiency parameter on the resonator mass for various types of resonators. Figure 4 shows the dependence of the efficiency parameter of various types of hard reflectors on the share of mass corresponding to inertial bodies (m/M). It should be noted that, for hard reflectors, the efficiency parameter does not depend on frequency and does not exceed unity. For direct two-sided hard resonators (HR2), the efficiency parameter becomes equal to zero when the surface masses of the panel material and resonators coincide ($m = M\sigma$) and approaches unity when the mass of resonators or the mass of the panel tends to zero. Figure 4 shows that, by turning the axis of vibration of resonators, it is possible to increase the value of the efficiency parameter at a constant mass of resonators.

Figure 5 displays the dependence of the efficiency parameter on the mass of inertial bodies for compensators. The parameter of efficiency has a minimum corresponding to soft reflectors (Helmholtz resonators) of the same equivalent thickness when the tuning frequency is equal to the mass–elasticity–mass resonance frequency. For turned-over (tilted at 180 degrees) one-sided compensators, the efficiency parameter is considerably greater than for direct compensators. For small masses of the inertial bodies of resonators, two-sided compensators have large values of the efficiency parameter. The value of the efficiency parameter of compensators that corresponds to its local maximum does not depend on the scheme of the compensator and equals $\Theta = \bar{h}\,|i - M\omega_t/4\rho c|$, because, in this case, the compensators are equivalent to a system consisting of two panels with equal masses ($M_1 = M_2 = M/2$) with Helmholtz resonators between them.

Thus, the acoustic properties of panels with a wide class of systems of resonant elements with one degree of freedom were investigated. Acoustic equivalence is established for various schemes of resonators: the equivalence of panels with dynamic vibration absorbers and panels with two-sided incompressible resonators; panels with acoustic compensators and panels with two-sided compressible resonators, as well as their equivalence to two panels with Helmholtz resonators between them; and the equivalence of tilted and direct resonant systems were all established. Resonant systems are classified on the basis of equivalent represen-

tations. A universal relationship is derived for evaluating the effect of an increase in the transmission loss of a single panel after mounting any type of resonators on it and also for determining the optimal parameters of the resonant systems.

REFERENCES

1. L. D. Pope, R. A. Prydz, L. S. Wirt, and H. L. Kuntz, J. Acoust. Soc. Am. **87**, 1597 (1990).
2. Zhaohui Sun, Jincai Sun, Chong Wang, and Yang Dai, Appl. Acoust. **48** (4), 311 (1996).
3. V. B. Stepanov, Akust. Zh. **44**, 532 (1998) [Acoust. Phys. **44**, 456 (1998)].
4. V. B. Stepanov, Akust. Zh. **46**, 259 (2000) [Acoust. Phys. **46**, 214 (2000)].
5. B. M. Efimtsov and L. A. Lazarev, Akust. Zh. **47**, 346 (2001) [Acoust. Phys. **47**, 291 (2001)].
6. W. Maysenholder, in *Forum Acusticum 2002: Conference Proceedings* (Sevilla, 2002).
7. B. M. Efimtsov and L. A. Lazarev, in *Proceedings of Conference on Internoise* (Hague, Netherlands, 2001).

Translated by A. Svechnikov

Acoustical Physics, Vol. 51, No. 3, 2005, pp. 306–312. Translated from Akusticheskiĭ Zhurnal, Vol. 51, No. 3, 2005, pp. 366–373.

Structure of the Focal Region at a Focusing with a Time Reversal of Waves in an Inhomogeneous Medium

V. A. Zverev

Institute of Applied Physics, Russian Academy of Sciences, ul. Ul'yanova 46, Nizhni Novgorod, 603995 Russia

e-mail: zverev@hydro.appl.sci-nnov.ru

Received June 6, 2003

Abstract—A focusing array with a time reversal of waves in an inhomogeneous medium is considered. It is shown that, at the focus of such an array, an oscillation trap can be formed. In a homogeneous medium, a wave first travels to the array focus, is focused, and then travels away from the focus, whereas, in an inhomogeneous medium, the wave does not travel at all. In the oscillation trap, an intense oscillation is formed, which arrives from nowhere and escapes to nowhere. The size of the oscillation trap is much smaller than that of the focal spot of the array in free space. The physical nature of this phenomenon and the possible areas of its practical application are discussed. © *2005 Pleiades Publishing, Inc.*

Many problems of acoustics can be solved by using focused antenna arrays [1, 2]. However, the use of the arrays considered in [1, 2] implies monochromatic transmitted signals and, more importantly, the absence of strong inhomogeneities in the medium (i.e., inhomogeneities that can affect the array performance). The implementation of a broadband focused array in a multipath inhomogeneous medium encounters fundamental difficulties caused by the fact that the inhomogeneities of the medium cannot be a priori compensated for. The purpose of this work is to consider the possibilities offered by the compensation for statical irregular inhomogeneities via the use of the time reversal of waves (TRW) [3, 4]. A focused array tuned using the TRW is not only protected from the influence of inhomogeneities and multipath propagation in the medium but also has a higher spatial resolution because of the formation of a volume aperture due to wave scattering from inhomogeneities. A specific feature of such an antenna array is that, with the use of the TRW procedure, the oscillations emitted by the array elements can be filtered and phased so as to produce a trap for the oscillations at the array focus. This term can be used to denote the place where intense oscillations are localized in a small spatial region and emit nothing into the medium in the absence of scatterers in the trap itself. The size of the region of oscillation localization can be much smaller than the size of the focal spot of the same array in a homogeneous medium. With the use of the TRW, in an inhomogeneous medium, an array can be created that features electronic scanning and has a number of spatial channels higher than the number of the array elements. The spatial resolution of such an array may exceed the ratio λ/D, where λ is the wavelength and D is the array aperture.

To clarify the specificity of focusing an array using the TRW, let us consider an example of an array in an inhomogeneous medium. Our consideration will be based on numerical models of the array and the medium. Let us consider an array consisting of N receiving–transmitting elements placed along a horizontal line and separated by n units of length. Such an array configuration simplifies the calculations, although, generally, the array may have an arbitrary shape. Let the focal point O be at a distance R from the array, on the line perpendicular to the line of the elements at the array midpoint. For our purpose, which consists in revealing the specificity of the focused array, it is sufficient to consider the focusing in the plane containing the array. Let us use a Cartesian coordinate system with the origin at point O, the y axis directed from O to the array center, and the x axis crossing this line at a right angle. Thus, y and x are the longitudinal and transverse coordinates, respectively. Let the signals received by the array have a continuous uniform spectrum. The sources of the signals can be both at point O and in its vicinity. We must know the distances from each array element to each possible transmitting point. These distances are given by the formula

$$W(k, x, y) = \sqrt{(R-y)^2 + ((k-0.5N)n-x)^2}. \quad (1)$$

Here, k is the ordinal number of the receiving–transmitting array element, starting from the edge of the array, and x and y are the distances measured from the point O in its vicinity.

1063-7710/05/5103-0306$26.00

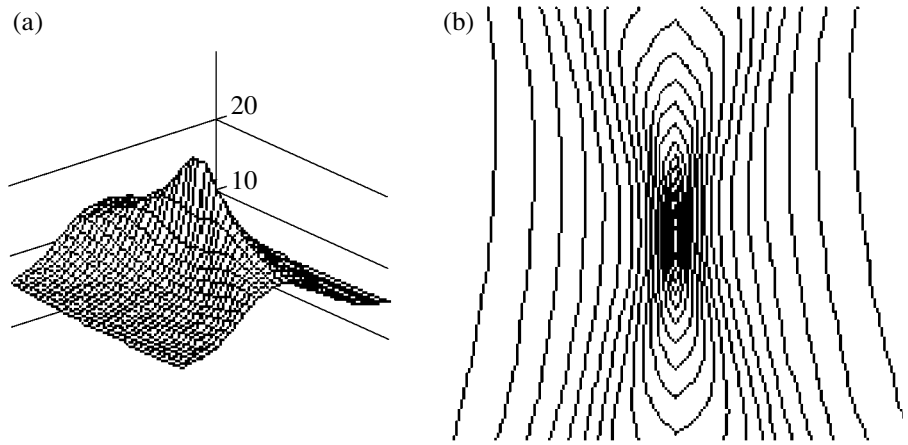

Fig. 1. Directivity pattern of a broadband focusing array. The amplitude is shown (a) as a function of coordinates (x, y) and (b) in the form of isolines. The array parameters appearing in Eq. (1) are as follows: $N = 32$; $R = 100$; and $n = 4$.

To focus the array at point O in a homogeneous medium, one must sum the signals of all array receivers in view of the fact that the signals arrive with different delays as determined by Eq. (1) at $x = 0$ and $y = 0$. The result of such a summation is referred to as the array output. Because the delays are known for an arbitrary point O, they can be a priori compensated for in such a way that the signals leaving point O arrive at each receiver simultaneously. To do so, the delays of the arriving signals should be decreased by the known values $W(k, 0, 0)$. Now, if the signals of all receivers are summed, one obtains the array focused at point O. The signal transmitted from point O with instantaneous amplitude equal to unity will have instantaneous amplitude equal to N at the array output. The signals transmitted from other points will arrive at each receiver with delays that are also known. These delays are

$$W_O(k, x, y) = W(k, x, y) - W(k, 0, 0). \quad (2)$$

Now, the array output is a function of frequency for each point (x, y). The frequency response of the channel has the following form [5]:

$$Q(m, x, y) = \sum_k \exp\left(i\frac{2\pi}{M}mW_O(k, x, y)\right). \quad (3)$$

Here, m is the frequency expressed as the number of the frequency samples that are separated by $2\pi/M$, where M is the number of samples in the time-domain Fourier transform. With such a definition of the frequency, which is especially advantageous for numerical calculations, the frequency in hertz is mF, where F is the frequency of sampling the signal in time [5].

The signal at the array output is determined by the inverse Fourier transform of the product of the signal spectrum and frequency response of the array output (3):

$$U(t, x, y) = \frac{1}{2\pi M}\sum_m Q(m, x, y)H(m)\exp\left(i\frac{2\pi}{M}mt\right). \quad (4)$$

Here, $H(m)$ is the time-domain Fourier spectrum of the signal and t is time. To obtain the array response for the signal at a point (x, y), one should know the shape of the signal or its Fourier spectrum $H(m)$.

Let us define the directivity pattern $G(x, y)$ of the array as the time-averaged array response to a noise signal with a uniform time-domain spectrum. Such a signal is produced by using a random sequence of numbers generated by a computer. In this case, the directivity pattern is given by the formula

$$G(x, y) = \frac{1}{M}\int_0^T |UN(t, x, y)|dt. \quad (5)$$

Here, $UN(t, x, y)$ is determined by Eq. (4) for $H(m)$ equal to the Fourier spectrum of the computer-generated random sequence with length M.

Figure 1 shows the directivity pattern of the focused array for $N = 32$, $R = 100$, $n = 4$, and $M = 128$. This type of directivity pattern is peculiar to a focused array in a homogeneous medium.

Let us consider how the result of focusing will change in a medium with strong inhomogeneities that substantially influence the array performance. Suppose that the inhomogeneities lead to random changes in the delays between points (x, y) and the receiving array elements. Let these changes vary within several units, with an interval of spatial correlation that is shorter than the distance between the array elements. Such a physical model of the medium coincides with that considered in [6, 7] (in [7], see pp. 195–197). With the problem at hand, one should not calculate or estimate the parameters of the random wave field, as in [6, 7]. It is quite suf-

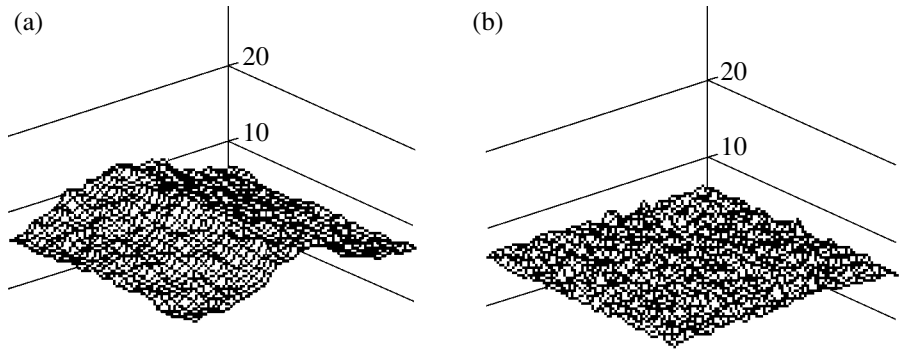

Fig. 2. Directivity patterns of a focused array in an inhomogeneous medium for examples (a) A and (b) B.

ficient to specify the values of fluctuations for the delays at the receiving elements. To do so, let us describe the inhomogeneous medium in a way that allows one to determine the process of wave propagation not only from point O but also from points (x, y). For every such point, an individual dependence of the delays in the wave propagation to the array elements takes place. The shape of this dependence is determined by the parameters appearing in the model of the inhomogeneous medium. Here, we consider two examples of the medium that differ in the parameters of correlation functions. In example A, the changes in delays at points (x, y) correlate with each other, while, in example B, they do not correlate.

Example A is obtained from example B by narrowing the two-dimensional spectrum of the spatial frequencies of delays by a factor of eight compared to the spectrum of example B. As a result, in example A, the delays between points (x, y) and the array elements vary smoothly.

Let us try to focus the array in the inhomogeneous medium in a manner that is used in a homogeneous medium, that is, by compensating only for the regular delays given by Eq. (1) with no changes in the irregular ones. Figure 2 shows the calculated directivity patterns of the focused array for the case when changes in the delays are added to the function $W(k, x, y)$ appearing in Eq. (3); all other parameters are the same. According to Fig. 2, the directivity pattern has drastically changed in comparison with Fig. 1. In such a situation, one usually says that the directivity pattern has "failed." In view of the fact that many acoustic media are inhomogeneous, the failure of the pattern is a serious obstacle to the use of focused arrays in acoustics. Note that the effect of the failure is more pronounced for arrays with higher numbers N of the receivers, that is, for more efficient arrays.

Let us use the results obtained to determine which inhomogeneities can be treated as strong. The inhomogeneities should be considered as strong if they substantially influence the array directivity pattern that is formed in the same way as in a homogeneous medium. A comparison of Figs. 1 and 2 shows that the inhomogeneities used in the computations are strong.

To avoid the failure of the directivity pattern, it is advantageous to use the time reversal of waves (TRW) [3, 4]. The TRW process consists of two steps [3]. At the first step, a short pulse is transmitted from the point of probable array focus (point O in our case). This pulse propagates in the inhomogeneous medium. With the aforementioned model of the medium, the wave transmitted from point O will arrive at the receiving elements with the following distribution of the arrival times:

$$W_{OF}(k, 0, 0) = W(k, 0, 0) + F(k), \tag{6}$$

where k is the ordinal number of the array element and $F(k)$ are random increments of the delays caused by the inhomogeneities of the medium.

Signal (6) received by each array element is stored, which is necessary to proceed to the next step. The second step consists in that the stored signals received by all array elements are reversed in time and transmitted from the same points at which they were received. The signals are sent to the same medium that is supposed to be frozen for the time of the first and second steps. Hence, the second step yields the time-reversed signals with opposite signs of the delays. The delays that increased the propagation time will now decrease this time, and vice versa. In the backward propagation of the signals, the delays remain the same as in the direct propagation, because the distribution of the delays is independent of the propagation direction. It is useful to consider the delays not only for point O but also for all points (x, y) that can be reached by the signal transmitted at the second step. Thus, in view of the first and second steps, the delay between points (x, y) and each receiving array element takes the form

$$\begin{aligned} W_{OF}(k, x, y) &= W(k, x, y) \\ &+ F(k, x, y) - W(k, 0, 0) - F(k, 0, 0). \end{aligned} \tag{7}$$

Here, $F(k, x, y)$ are the medium-caused changes in the delays from points (x, y) to each of the k array elements.

According to Eq. (7), the pulse transmitted from point O ($x = 0$, $y = 0$) into the inhomogeneous medium at the first step will arrive at the same point O at the second step simultaneously for all k array elements. The time-domain shape of the received pulse will be completely identical to that of the transmitted pulse [4]. This is the main idea of the TRW. However, the TRW procedure allows one to focus an array in an inhomogeneous medium not only to receive its own signal but also to receive an arbitrary broadband signal whose shape is known in advance.

The spectrum of the signal received at the first step (which consists of transmitting the known signal into the medium) has the following form at the kth array element:

$$S_1(\omega, k) = B(\omega)z(\omega, k). \quad (8)$$

Here, $B(\omega)$ is the Fourier spectrum of the pulse transmitted at the first step. This function is known. Therefore, Eq. (8) allows one to find the frequency response $z(\omega, k)$ of the channel from point O to the kth receiver. To avoid problems in solving Eq. (8) for the frequencies at which the absolute value of $B(\omega)$ is equal to zero or too small, one should use the technique proposed in [8]. Its essence consists in that one in advance changes the absolute values equal or close to zero in the spectrum of the function chosen to represent $B(\omega)$ to finite absolute values while retaining the argument. According to [8], such a procedure eliminates the difficulties of solving an equation of type (8). Upon finding the function $z(\omega, k)$, one can focus the array so as to receive an arbitrary broadband signal emitted from point O. It will be an array that uses the TRW procedure, although the wave is not time-reversed but rather focused for the reception of the signal arriving from point O.

For such focusing, one should multiply the spectrum of an arbitrary signal received by an array element by a function $z^*(\omega, k)$ that is complex-conjugate to the function found in the TRW procedure. After that, the Fourier spectrum of the signal transmitted from point O and received by the kth array element takes the form

$$S_N(\omega, k) = B_N(\omega)z(\omega, k)z^*(\omega, k), \quad (9)$$

where $B_N(\omega)$ is the spectrum of the arbitrary signal at point O.

Formula (9) can be treated as the result of filtering the signal, whose spectrum is $B_N(\omega)$, by the filter, whose frequency response is the squared absolute value of $z(\omega, k)$. Being the absolute value squared, such a frequency response has a constant component. Because of the frequency-independent component, the filter given by Eq. (9) lets all frequencies pass without distortions and makes all N signals received by the array elements be in phase. As a result of this processing of the signal, the array becomes focused at point O.

With an arbitrary medium, the squared absolute value of the frequency response can have both constant and variable components. The correlation noise can exist in this case [8]. In our case, when only signal delays are random, the squared frequency response appearing in Eq. (9) is equal to unity, and no correlation noise is observed.

The signals arriving at the array elements from points (x, y) will pass through the filter whose frequency response differs from $z(\omega, k)$ if the signal origins do not coincide with the point O. In this case, Eq. (9) transforms to the expression

$$S_N(\omega, k, x, y) = B_N(\omega)z(\omega, k, x, y)z^*(\omega, k, 0, 0). \quad (10)$$

By using Eq. (10), one can calculate the directivity pattern of the array. To do so, one can use the same method as in calculating the free-space directivity pattern (see above). The function $B_N(\omega)$ must be defined as the Fourier spectrum of a random sequence to use Eq. (5) at the terminal step of calculations. The frequency responses appearing in Eq. (10) are determined by the delays introduced earlier [5]:

$$z(\omega, k, x, y) = \exp\left(i\frac{2\pi}{M}m[W(k, x, y) + F(k, x, y)]\right). \quad (11)$$

To obtain the array response as a function of time and coordinates, as in Eq. (4), it is sufficient to substitute Eq. (11) into Eq. (9), to apply the inverse Fourier transform with respect to frequency m, and to sum the result over all k.

Figure 3 shows the calculated directivity patterns for the focused array. These patterns are obtained by using the TRW with the same parameters as in Fig. 1 for the two examples of the medium, A and B. The heights of the peaks at the centers of all curves are the same and are exactly equal to the height of the central peak in Fig. 1. Hence, no failure of the array directivity pattern occurs if the TRW procedure is used. On the contrary, the directivity pattern sharpens.

It should be noted that both directivity patterns shown in Fig. 3 are much narrower than the directivity pattern shown in Fig. 1 for the ideal case of a free medium. The possibility for the directivity pattern to be noticeably narrowed in an inhomogeneous medium was considered in [3], where an experimentally discovered tapering of the directivity pattern was reported. In explaining this effect in [3] and other papers, the authors emphasized the increase in the array aperture due to the signal scattering. In our case, such an explanation is insufficient. Here, the effect of wave scattering in the volume of the medium is used: a one-dimensional antenna array transforms to a volume one because of the inhomogeneities of the medium.

In a strongly inhomogeneous medium, the directivity of the array is governed by the statistical properties of the medium [4]. In turn, these statistical properties are determined by the specificity of the wave propaga-

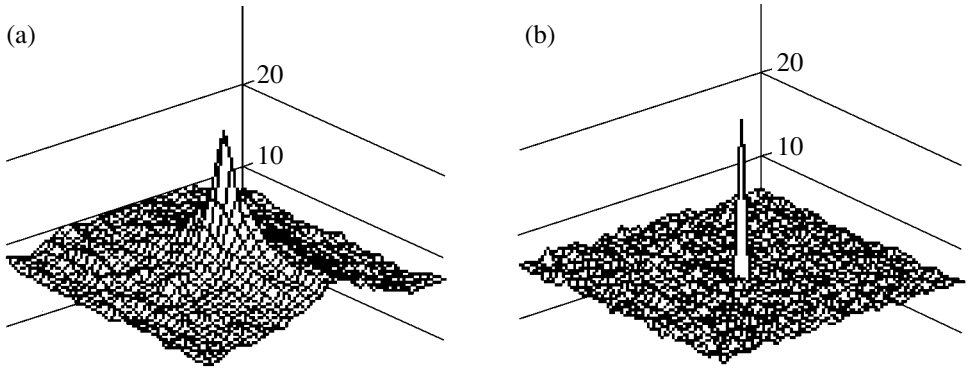

Fig. 3. Directivity pattern of a focused array with the TRW in an inhomogeneous medium for examples A and B.

tion in the volume of the inhomogeneous medium. Volume scattering forms the statistical properties of the wave field. To determine the directivity, it is necessary and sufficient to know frequency response (11) without knowing how and at which angles the waves are scattered in the medium. The possibility to ignore the details of wave propagation in the medium in determining the array directivity pattern can give an impression that such concepts as the aperture and diffraction do not contribute to the array directivity at all. This is not true. The complex character of wave propagation in the medium volume is the only factor that allows one to obtain the frequency response depending on coordinates (x, y) as in examples A and B. It is very important that the frequency responses of the propagation channels between points (x, y) and individual array elements substantially differ from each other. Such an effect can be produced by nothing but the wave fields scattered in the volume of the medium.

The aforementioned method serves to focus the array at point O. To focus the array at another point, it is sufficient to emit a short pulse from this point, to receive it at N elements of the array, and to determine the frequency responses for each element, just as in the aforementioned processing procedure. The frequency responses obtained in this way allow one to focus the array for signal reception from the point from which the short pulse was sent at the first step. With such a technique, the array can be tuned for simultaneously receiving signals from an arbitrary number of points. Here, the number of independent points of the array focusing is not limited by the number of array elements.

All the aforementioned considerations are valid for a medium whose parameters are constant in time. If the parameters vary to an extent that can influence the quality of focusing, the procedure of tuning the array with a pulsed signal sent from all reception points of interest should be repeated.

The array with the TRW also has a number of interesting features if it is used for signal transmission. In an inhomogeneous medium, such an array can produce a trap for the oscillations (OT), which is characterized by a local increase in the oscillation intensity and has a rather small size in comparison with that produced by the diffraction of waves by the array aperture. The OT is not the source of waves emitted into the medium. The properties of the OT can be found from Eq. (4). This expression is a function of time. To obtain the time dependence of the array output, one should specify the time dependence for the signal sent to the medium at the first step of the TRW. This dependence appears in Eq. (4) in the form of the Fourier spectrum, $H(m)$. Let us suppose that this function does not depend on m and is equal to unity for all m. This means that the signal is a pulse with a duration of one sample of time, which is emitted at the time equal to zero. Then, quantity (4) can be calculated. Function (4), the array output, will also be a pulsed signal with its maximum at the zero time. This is the result of substituting Eq. (3) into Eq. (4) if $H(m) = 1$. Figure 4 shows the array response to such a pulse in a homogeneous medium at three instants of time. The three responses are shown in an amplitude form as the curves of equal intensities of the oscillations. The signal successively takes the values shown from right to left. These curves correspond to the wave travelling to the focus, passing the focal point, and then travelling away from it. In an inhomogeneous medium, the situation is different: there is no travelling wave. If one plots Fig. 4 for an inhomogeneous medium, the only maximum will be at the center with noise of an approximately constant level to the left and to the right of it.

The situation is illustrated in Fig. 5. Here, the amplitude distributions are shown for the field at the array both for the instant of the exact focusing and for the previous and subsequent two instants of time. In Fig. 5a, corresponding to a homogeneous medium, the wave travels through the focal point of the array. Figure 5b corresponds to a strongly inhomogeneous medium of type B. This wave travels nowhere. It appears at the instant of focusing, but there is no increase in its amplitude at the previous and subsequent instants that correspond to approaching the focus and travelling away from it. This means that, in the inhomogeneous medium, the oscillation produced by the TRW at the

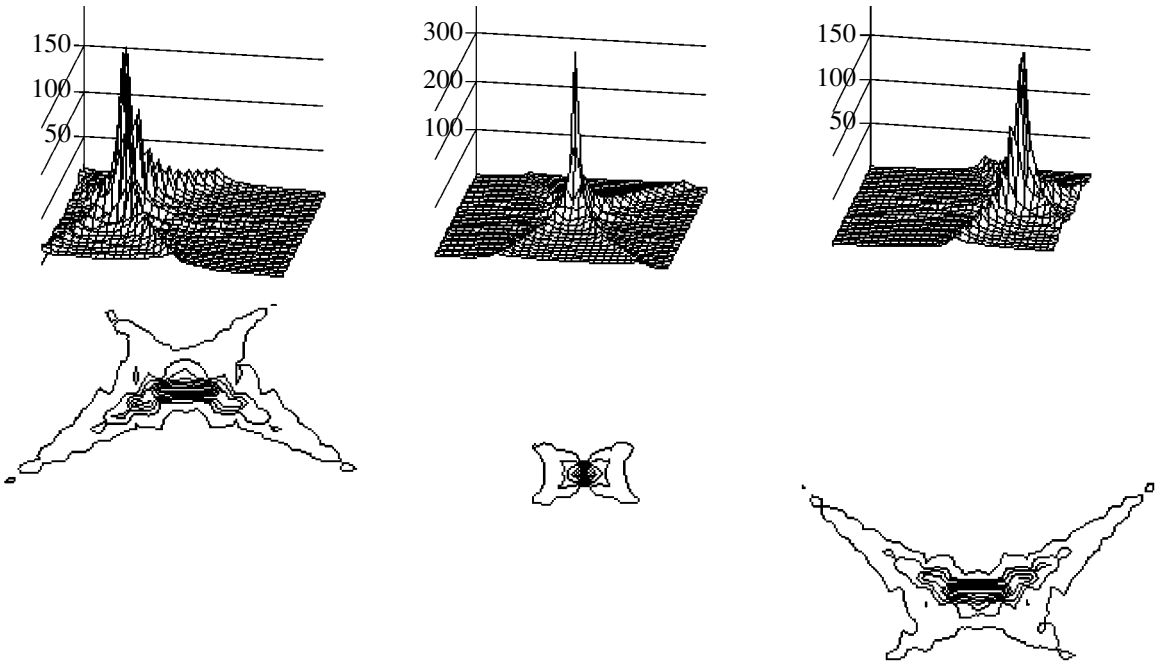

Fig. 4. Responses of the focused array to a short pulse for three instants of time. The instants correspond to the following time samples measured from the instant of focusing: –8, 0, and +8. The responses are represented in forms of amplitudes (upper plots) and isolines (lower plots).

focus radiates nothing in any direction. One can closely approach the OT without detecting it unless one enters the focusing point itself. Such an oscillation trap cannot be obtained by controlling the array transmission from a single plane in free space. Here, the interference and diffraction of waves in the volume of the medium are essential, although the array itself can be linear in this case.

The oscillation trap can be used in measurements. One can also form a set of OTs with a given configuration in space. Such an opportunity can be useful for solving a number of physical problems. For instance, an OT does not radiate by itself but, if a scatterer falls in the trap, this scatterer under the influence of intense oscillations begins to radiate waves, which can be observed at a long distance from the OT. This is an ideal dark-field method.

An OT can be used for nondestructive testing to monitor the formation of cracks in structures. To do so, one should create an OT in the probable region of cracking. If no cracks are present, the OT will not manifest itself, but, if the crack exists, a scattered signal will be generated that can be detected by a sensor.

Let us consider the intensity of oscillations in an OT. Let the pulse that is sent to form the OT have an amplitude a. The signals received by the array elements will have amplitudes a/v, where v is the amplitude attenuation due to the natural propagation loss. Let each array element emit a pulse with an amplitude Sa to produce the OT. Then, the amplitude within the OT will be

$$A = NSa/v.$$

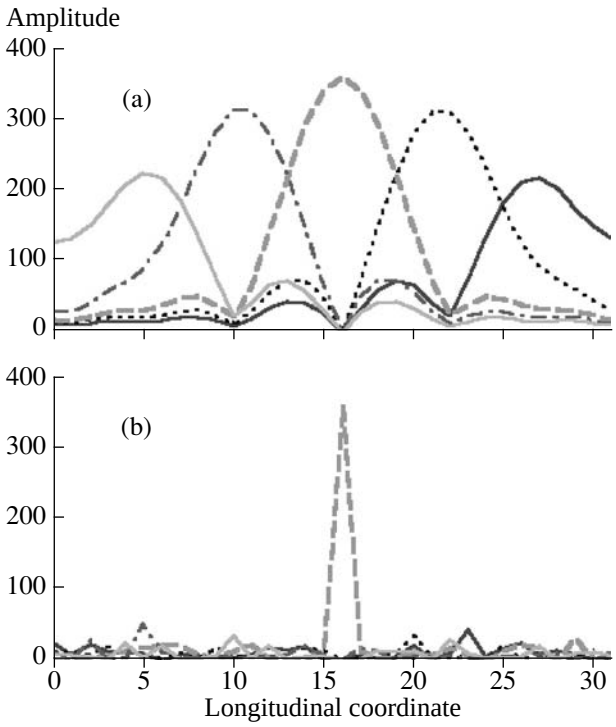

Fig. 5. The array outputs versus the longitudinal coordinate at five progressive instants of time: the first instant corresponds to the solid curve; the second, to the dash–dot curve; the third (the exact focusing), to long thick dashes; the fourth, to the dotted curve; and the fifth, to another solid curve. The outputs are calculated for (a) a homogeneous medium and (b) an inhomogeneous medium of type B.

Thus, the signal amplitude in the OT compared to the amplitude of the initial pulse is determined by the ratio NS/V. With a large number N of array elements, one can make the signal amplitude in the OT much higher than that of the initial pulse.

It is known [9] that an acoustic transmitter placed in an oil well causes an increase in the well production. In the recent years, the geological conditions of oil mining have become more complicated. Resources that are hard to extract represent the major part of the oil deposits in operation, and this part tends to increase [9]. That is why an improvement in the technology of oil production is urgent. One of the promising methods for intensifying oil extraction is acoustic action on the well, which is realized by placing a transducer into it. It is known that the efficiency of the acoustic effect on the well increases when the intensity of the sound field increases. Moreover, experimental data [9] show that the acoustic effect on the physical and chemical processes that leads to an increase in oil production is based on mechanisms of a threshold nature in sound intensity. It is difficult to insert a high-power transducer into the well. However, the intensity of acoustic vibrations in the well can increased almost without limit by focusing the radiation from the surface or from other places close to the well. In this case, the radiator in the well only serves to focus the radiation of high-power transducers at the required point of the inhomogeneous medium. It is advantageous to use the OT for this purpose. One can emit intense radiation from the ground, and this radiation can be focused simultaneously or in turn at a number of points that are planned in advance for the OTs.

With the aforementioned phenomenon, one can create efficient acoustic lenses by simple means. To obtain a lens, it is sufficient to put (glue) together a number of layers with rough surfaces and different sound speeds. If such a layered structure is thick enough, it can form a volume lens. This lens should be excited by N acoustic transducers. To tune the lens to a given focal distance, one can use the TRW procedure. The focal spot of such a lens can be smaller in size and have sharper boundaries than an ordinary lens with the same transverse dimension.

ACKNOWLEDGMENTS

This work was supported by the Russian Foundation for Basic Research, project nos. 00-15-96741 and 02-02-17056.

REFERENCES

1. V. A. Zverev, A. L. Matveev, M. M. Slavinskiĭ, and A. A. Stromkov, Akust. Zh. **43**, 429 (1997) [Acoust. Phys. **43**, 429 (1997)].
2. V. A. Zverev, Akust. Zh. **48**, 211 (2002) [Acoust. Phys. **48**, 176 (2002)].
3. M. Fink, D. Cassereau, A. Derode, *et al.*, Rep. Prog. Phys. **63**, 1933 (2000).
4. V. A. Zverev, Akust. Zh. **50** (6), 792 (2004) [Acoust. Phys. **50** (6), 685 (2004)].
5. V. A. Zverev and A. A. Stromkov, *Extraction of Signals from Noise by Numerical Methods* (Inst. Prikl. Fiz., Ross. Akad. Nauk, Nizhni Novgorod, 2001) [in Russian].
6. V. I. Klyatskin and V. I. Tatarskiĭ, Izv. Vyssh. Uchebn. Zaved., Radiofiz. **14** (5), 706 (1971).
7. S. M. Rytov, *Introduction to Statistical Radiophysics*, Part 1: *Random Processes*, 2nd ed. (Nauka, Moscow, 1976) [in Russian].
8. V. A. Zverev, Akust. Zh. **50** (5), 614 (2004) [Acoust. Phys. **50**, 523 (2004)].
9. D. A. Kas'yanov and G. M. Shalashov, Izv. Vyssh. Uchebn. Zaved., Radiofiz. **45** (2), 170 (2002).

Translated by E. Kopyl

Acoustical Physics, Vol. 51, No. 3, 2005, pp. 313–320. Translated from Akusticheskiĭ Zhurnal, Vol. 51, No. 3, 2005, pp. 374–382.

Application of the WKB Method to Calculating the Group Velocities and Attenuation Coefficients of Normal Waves in the Arctic Underwater Waveguide

V. D. Krupin

Andreev Acoustics Institute, Russian Academy of Sciences, ul. Shvernika 4, Moscow, 117036 Russia

e-mail: bvp@akin.ru

Received November 22, 2003

Abstract—Algorithms based on the WKB approximation are proposed for the fast and accurate calculation of the group time delays and effective attenuation coefficients of normal waves in the deep-water sound channel of the Arctic Ocean. These characteristics of the modes are determined in the adiabatic approximation by integrating the local group velocity and attenuation coefficient over the horizontal distance between the ends of the propagation path. According to the WKB method, the local group velocity is the ratio of two quantities. The first one is the sum of the length of the ray corresponding to the mode and the side displacement of the ray at the reflection by the ice cover. The second one is the sum of the travel time of the sound signal along the ray cycle and the time delay caused by the side displacement. The grazing angle of the ray is determined from the condition of quantization for the phase integral. According to the WKB method, the local attenuation coefficient of the mode is specified as the ratio of the squared modulus of the coherent reflection coefficient at the lower boundary of the ice cover and the sum of the cycle length and the side displacement of the ray. Simple recurrent relations are proposed to estimate, with fair accuracy and short calculating time, the phase integral, the integral that describes the cycle length, and the related local group velocities and attenuation coefficients. The capacity and efficiency of the algorithms are confirmed by the comparison of the aforementioned mode characteristics calculated by using the proposed relations and the precise computer code. The calculations are performed with the sound speed profiles obtained from the temperature and salinity measurements during the SEVER and SCICEX-1995 expeditions. © *2005 Pleiades Publishing, Inc.*

To numerically model the ocean monitoring methods based on acoustic tomography [1–3], matched-field processing [4–7] in the adiabatic approximation, and mode filtering [8, 9], one needs rather fast, robust, and accurate algorithms for calculating the characteristics of normal waves (modes). Such characteristics include the local wave numbers of modes, their phase and group velocities, the attenuation coefficients, and the corresponding integral quantities, namely, the phases, the group time delays (GTD), and the effective (averaged over the propagation path) attenuation coefficients (EAC) of normal waves. In the adiabatic approximation, the GTD of a mode is determined by integrating the local group velocity over the distance along the path. The corresponding EAC is given by integrally averaging the local attenuation coefficient of the mode. The aforementioned integral characteristics of the modes can be found by the numerical retrieval of the local complex eigenfunctions and eigenvalues of the modes for a number of vertical sound speed profiles along the path. For this purpose, computer programs can be used (e.g., [10, 11]). However, such a procedure implies multiply executing these programs for a broad frequency band with a large number of values of the waveguide parameters that depend on distance. Thus, the computational expenses may be high. The use of the WKB method in numerically determining the mode characteristics can substantially reduce the calculation time and increase the efficiency of the algorithms for estimating the waveguide parameters from the data of experiments studying the sound fields in the ocean.

In this paper, universal iterative algorithms based on the WKB method are presented. These algorithms provide fast, robust, and accurate calculations of the local group velocities, the local attenuation coefficient, the GTD, and the EAC for normal waves in deep-water regions of the Arctic Ocean. In deriving the formulas used in these algorithms, the under-ice medium is modeled as a stratified one, and the local profile of the sound field at a fixed distance is approximated by a continuous piecewise linear function that increases with depth. The number of nodes in the local profile is arbitrary but sufficient to fully describe the specificity of the spatial structure of the sound speed in deep-water Arctic regions.

According to the WKB method, the local group velocity of an individual mode is given by the ratio of two quantities. The first quantity is the sum of the

1063-7710/05/5103-0313$26.00

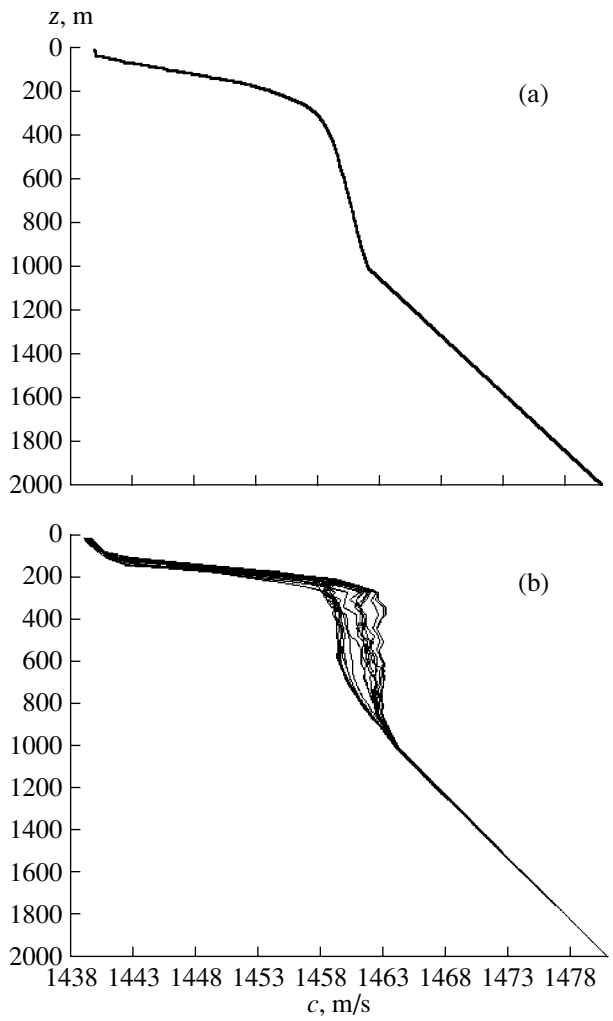

Fig. 1. Sound speed profiles calculated by using the data on the thermohaline structure measured in the oceanographic surveys on the paths (a) from Spitsbergen Island to Point Barrow (the SEVER expedition) and (b) from the Nansen basin to the Beaufort Sea (the SCICEX cruise, 1995).

length of the ray cycle corresponding to this mode and the side displacement of this ray at reflection from the ice cover. The second one is the sum of the travel time along this ray within a single cycle and the delay caused by the aforementioned displacement of the ray. The grazing angle of the ray is determined from the known condition of quantization for the phase integral. The values of the side displacement and the corresponding time delay are the partial derivatives of the phase in the coherent reflection coefficient at the water–ice interface with respect to the grazing angle and the frequency. With the WKB formalism, the local attenuation coefficient of an individual mode is specified as the ratio (in decibels) of the squared modulus of the coherent reflection coefficient at the lower ice surface and the sum of the length of the aforementioned ray cycle and its side displacement.

The length of the ray cycle and the cyclic travel time are the integrals over depth, in which the integrands have singularities at the ends of the integration interval (at the turning points). For this reason, standard quadrature formulas are hardly applicable to the calculation. With the accepted piecewise linear approximation of the local sound speed profile, the integrals can be calculated for each layer by simple recurrent relations that involve elementary functions. These relations provide a sufficiently high accuracy in determining the local group velocity and the local attenuation coefficient and lead to a substantial decrease in the calculation time in comparison with exact computer codes based on the modal representation of the sound field. The proposed algorithm also allows one to rapidly calculate the GTD and the EAC with both an accuracy and calculation time nearly independent of frequency.

To confirm the working capacity and calculating efficiency of the aforementioned algorithms, the calculated dependences of the group velocity, the local attenuation coefficient, the GTD, and the EAC on the mode number are calculated for the modeled arctic waveguides with the natural sound speed profiles presented in Fig. 1. It is shown that these calculations fit the results obtained by using the mode computer code [11] to a high accuracy.

In what follows, the guided modes of lower numbers $n = 1, 2, \ldots, N$ are considered. Such modes correspond to the rays refracted upwards and reflected only by the ice surface. In accordance with the WKB method [12, 13], the local group velocity v_n of an individual mode with number n is given by the ratio

$$v_n = (D_n + \Delta_n)/(t_n + \tau_n). \quad (1)$$

Here, D_n is the cycle length for a ray with a grazing angle $\chi_n = \arccos[(\mathrm{Re}\xi_n)/k]$ at the water–ice interface (this length is equal to the distance between two successive reflection points at the lower ice surface); ξ_n is the complex horizontal wave number of the nth mode; $k = 2\pi/c_0$ is the wave number in water; $c_0 = c(0) = 2$ is the sound speed in water near the ice surface; Δ_n is the horizontal displacement of the ray bundle at reflection by the ice surface; t_n is the travel time along the ray within a single cycle; and τ_n is the time delay associated with this displacement. The values of D_n and t_n are determined as $D_n = D(\chi_n)$ and $t_n = T(\chi_n)$, where, for an arbitrary grazing angle χ at the water–ice interface, the functions $D(\chi)$ and $T(\chi)$ are given by the integrals

$$D(\chi) = 2\cos\chi\int_0^{z_t}[c_0^2/c(z)^2 - \cos^2\chi]^{-1/2}dz, \quad (2)$$

$$T(\chi) = 2c_0\int_0^{z_t}c^{-2}(z)[c_0^2/c(z)^2 - \cos^2\chi]^{-1/2}dz. \quad (3)$$

The grazing angles χ_n are found from the equation of quantization for the phase integral:

$$kJ(\chi) + \varphi_s(\chi, kl)/2 = (n + 1/4)\pi, \quad (n = 1, 2\ldots N), \quad (4)$$

$$J(\chi) = \int_0^{z_t} \sqrt{c_0^2/c(z)^2 - \cos^2\chi}\, dz. \quad (5)$$

In Eqs. (2)–(4), the following notations are used: l is the thickness of the ice cover; $z_t \equiv z_t(\chi)$ is the depth of the turning point of the ray with the grazing angle χ (this turning point is the only solution to the equation $c_0/c(z_t) - \cos\chi = 0$); and φ_s is the phase of the coherent reflection coefficient at the interface between water and the ice layer. The aforementioned relations are valid for all modes with numbers $n = 1, 2, \ldots, N$ and grazing angles $\chi_n \le \chi_b$, where $\chi_b = \arccos[c_0/c(H)]$ is the grazing angle of the ray touching the bottom. According to [12, 13], quantities Δ_n and τ_n are determined by the expressions $\Delta_n = -\left(\frac{\partial\varphi_s}{\partial\xi}\right)_{\chi=\chi_n}$ and $\tau_n = -\left(\frac{\partial\varphi_s}{\partial\omega}\right)_{\chi=\chi_n}$, where $\xi = k\cos\chi$ is the real part of the horizontal wave number corresponding to an arbitrary grazing angle χ of the ray at the water–ice interface and ω is the cyclic frequency. According to Eqs. (1)–(5), the group velocity of the nth mode can be expressed as follows:

$$v_n = (D_n + \Delta_n)/[(2/c_0)J_n + (\cos\chi_n/c_0)D_n + \tau_n], \quad (6)$$

$$J_n = J(\chi_n). \quad (7)$$

In addition, according to Eqs. (2) and (5), the integrals D and J are related by a simple expression:

$$D = -\frac{2}{\sin\chi}\frac{\partial J}{\partial\chi}. \quad (8)$$

Thus, to determine the group velocity, one should calculate the integral $J(\chi)$, its derivative with respect to the grazing angle, and the simple roots of Eq. (4).

The integrands in the expressions for J and D have singularities at the ends of the integration interval, which are the turning points of the ray with the grazing angle χ. Hence, the standard quadrature formulas are hardly applicable. However, with our approximation of the local sound speed profiles in the form of piecewise functions of depth, the integrals J and D can be calculated layer by layer with the use of rather simple recurrent relations expressed in terms of elementary functions. Within each individual layer, the function $c(z)$ is supposed to have the form

$$c(z) = c_l + g_l(z - z_l) \text{ for } z_l \le z \le z_{l+1}, \quad l = (1, 2, \ldots L), \quad (9)$$

where c_l is the sound speed at the interfaces $z = z_l = \sum_{j=1}^{l} h_j$ of the aforementioned water layers with thickness h_l, $g_l = (c_{l+1} - c_l)/h_l$ are positive vertical gradients of the sound speed in these layers, and L is the maximal number of water layers.

Let us now consider the recurrent procedure of calculating the integral J as a function of the grazing angle χ in more detail. Suppose that the grazing angle χ of the ray corresponds to the turning depth $z_t = z_{t,l+1}$ within the $(l+1)$th layer, that is, within $z_{l+1} \le z_{t,l+1} \le z_{l+2}$. Hence, the grazing angle χ falls within the interval $\bar\chi_{l+1} \le \chi \le \bar\chi_{l+2}$, where $\bar\chi_{l+1} = \arccos(c_0/c_{l+2})$ and $\bar\chi_{l+2} = \arccos(c_0/c_{l+2})$. Denote the corresponding integral $J = J(\chi)$ as $J = J_{l+1}$. Then,

$$J_{l+1} = \sum_{j=1}^{l-1}\int_{z_j}^{z_{j+1}} f_j(z,\chi)\,dz + \int_{z_l}^{z_{l+1}} f_l(z,\chi)\,dz + \int_{z_{l+1}}^{z_{t,l+1}} f_{l+1}(z,\chi)\,dz, \quad (10)$$

where

$$f_j(z,\chi) = \sqrt{c_0^2/[c_j + g_j(z - z_j)]^2 - \cos^2\chi}, \quad j = 1, 2\ldots L+1. \quad (11)$$

If the turning depth $z_t = z_{t,l}$ of the ray with the grazing angle χ is within the lth layer (within the interval $z_l \le z_{t,l} \le z_{l+1}$) or $\bar\chi_l \le \chi \le \bar\chi_{l+1}$, where $\bar\chi_l = \arccos(c_0/c_{l+1})$ and $\bar\chi_{l+1} = \arccos(c_0/c_{l+1})$, the integral $J = J_l$ can be expressed as follows:

$$J_l = \sum_{j=1}^{l-1}\int_{z_j}^{z_{j+1}} f_j(z,\chi)\,dz + \int_{z_l}^{z_{t,l}} f_l(z,\chi)\,dz, \quad (12)$$

where the functions $f_j(z, \chi_n)$ are given by Eq. (11). By explicitly calculating the integrals following the first summands on the right-hand sides of Eqs. (10) and (12), the following expressions can be derived:

$$\int_{z_l}^{z_{l+1}} f_l(z,\chi)\,dz = \frac{c_0}{g_l}(u_{l+1} - u_l) - \frac{c_0}{2g_l}\ln\left[\frac{(1+u_{l+1})(1-u_l)}{(1-u_{l+1})(1+u_l)}\right],$$

$$\int_{z_{l+1}}^{z_{t,l+1}} f_{l+1}(z,\chi)dz$$

$$= \frac{c_0}{g_{l+1}}(u_{t,l+1}-u_{l+1}) - \frac{c_0}{2g_{l+1}}\ln\left[\frac{(1+u_{t,l+1})(1-u_{l+1})}{(1-u_{t,l+1})(1+u_{l+1})}\right],$$

$$\int_{z_l}^{z_{t,l}} f_l(z,\chi)dz$$

$$= \frac{c_0}{g_l}(u_{t,l}-u_l) - \frac{c_0}{2g_l}\ln\left[\frac{(1+u_{t,l})(1-u_l)}{(1-u_{t,l})(1+u_l)}\right],$$

where

$$u_l = \sqrt{1-\chi_l^2}, \quad u_{l+1} = \sqrt{1-x_{l+1}^2},$$

$$u_{t,l} = \sqrt{1-x_{t,l}^2}, \quad u_{t,l+1} = \sqrt{1-x_{t,l+1}^2},$$

$$x_l = \cos\chi\frac{c_l}{c_0}, \quad x_{l+1} = \cos\chi\frac{c_{l+1}}{c_0},$$

$$x_{t,l} = \cos\chi\frac{c_l}{c_0}\left[1+\frac{g_l}{c_l}(z_{t,l}-z_l)\right],$$

$$x_{t,l+1} = \cos\chi\frac{c_{l+1}}{c_0}\left[1+\frac{g_{l+1}}{c_{l+1}}(z_{t,l+1}-z_{l+1})\right].$$

Then, in view of the formulas for the aforementioned integrals and the equalities $u_{t,l} = 0$ and $u_{t,l+1} = 0$, which are the consequences of the vanishing functions $f_l(z_{t,l}, \chi)$ and $f_j(z_{t,l+1}, \chi)$ at the turning points, Eqs. (12) and (10) can be reduced to the form

$$J_l(\chi) = S_{l-1} + \left(-\frac{c_0}{g_l}u_l + \frac{c_0}{2g_l}\ln\frac{1+u_l}{1-u_l}\right), \tag{13}$$

$$J_{l+1}(\chi) = S_{l-1} + \frac{c_0}{g_l}(u_{l+1}-u_l)$$

$$-\frac{c_0}{2g_l}\ln\frac{(1+u_{l+1})(1-u_l)}{(1-u_{l+1})(1+u_l)} \tag{14}$$

$$+\left(-\frac{c_0}{g_{l+1}}u_{l+1} + \frac{c_0}{2g_{l+1}}\ln\frac{1+u_{l+1}}{1-u_{l+1}}\right).$$

The quantity S_{l-1} in Eqs. (13) and (14) defines the first summand of Eqs. (10) and (12), these formulas being valid for the grazing angles $\bar{\chi}_l \le \chi \le \bar{\chi}_{l+1}$ and $\bar{\chi}_{l+1} \le \chi \le \bar{\chi}_{l+2}$, respectively. Thus, according to Eqs. (13) and (14), the integral $J(\chi)$ can be calculated by using the recurrent expression

$$J(\chi) = \begin{cases} J_1(\chi) = -\dfrac{c_0}{g_1}\left(u_1 - \dfrac{1}{2}\ln\dfrac{1+u_1}{1-u_1}\right), \\ \text{if} \quad \chi \le \bar{\chi}_1 = \arccos\left(\dfrac{c_0}{c_2}\right), \\ J_2(\chi) = \dfrac{c_0}{g_1}(u_2-u_1) \\ -\dfrac{c_0}{2g_1}\ln\dfrac{(1+u_2)(1-u_1)}{(1-u_2)(1+u_1)} \\ -\dfrac{c_0}{g_2}\left(u_2 - \dfrac{1}{2}\ln\dfrac{1+u_2}{1-u_2}\right), \\ \text{if} \quad \bar{\chi}_1 \le \chi \le \bar{\chi}_2, \\ J_{l+1} = J_l + c_0(g_l^{-1} - g_{l+1}^{-1}) \\ \times\left(u_{l+1} - \dfrac{1}{2}\ln\dfrac{1+u_{l+1}}{1-u_{l+1}}\right), \\ \text{if} \quad \bar{\chi}_{l+1} \le \chi \le \bar{\chi}_{l+2}, \quad l = 2, 3, \ldots L-1 \end{cases} \tag{15}$$

where

$$u_1 = \sin\chi, \quad u_2 = \sqrt{1-(c_3/c_0)^2\cos^2\chi},$$

$$u_{l+1} = \sqrt{1-(c_{l+1}/c_0)^2\cos^2\chi}, \quad \bar{\chi}_{l+1} = \arccos(c_0/c_{l+2}).$$

In view of Eq. (8), the differentiation of Eqs. (15) and simple transformations lead to the following recurrent relations for the function $D(\chi)$:

$$D(\chi) = \begin{cases} D_1(\chi) = 2\dfrac{c_0}{g_1}\tan\chi, \\ \text{if} \quad \chi \le \bar{\chi}_1 = \arccos\left(\dfrac{c_0}{c_2}\right), \\ D_2(\chi) = 2\dfrac{c_0}{g_1}\dfrac{\sin\chi - u_2}{\cos\chi} + 2\dfrac{c_0}{g_2}\dfrac{u_2}{\cos\chi}, \\ \text{if} \quad \bar{\chi}_1 \le \chi \le \bar{\chi}_2, \\ D_{l+1} = D_l \\ +2c_0(g_{l+1}^{-1} - g_l^{-1})\sqrt{\tan^2\chi - \left(\dfrac{c_{l+1}^2}{c_0^2} - 1\right)}, \\ \text{if} \quad \bar{\chi}_{l+1} \le \chi \le \bar{\chi}_{l+2}, \quad l = 2, 3, \ldots L-1. \end{cases} \tag{16}$$

To find the roots $\chi = \chi_n$ ($n = 1, 2, \ldots, N$) of Eq. (4), a standard procedure can be used (the method of interval bisection or the secant method, for instance). These procedures require multiple calculations of both the phase integral $J(\chi)$ with the use of recurrent formulas (15) and the phase $\varphi_s(\chi, kl)$ of the coherent reflection coefficient. The local group velocities $\{v_n, n = 1, 2, \ldots, N\}$

can be found according to Eqs. (6) and (7), where the quantities J_n and D_n are given by recurrent relations (15) and (16) at $\chi = \chi_n$, $n = 1, 2, \ldots, N$. In turn, the resulting quantities J_n and D_n can be used to rapidly calculate the local attenuation coefficients of the modes under the influence of the volume absorption of elastic waves in the ice cover and the scattering of the elastic and sound waves by the rough surface of the ice. For the normal waves captured by the under-ice sound channel, the local attenuation coefficients denoted as $\{\beta_n$ (dB/km), $n = 1, 2, \ldots, N\}$ are determined by the WKB method [13] as follows:

$$\beta_n = -20\log_{10}|V_s(\chi_n)| \times 10^3/[\Delta_n(\chi_n) + D_n(\chi_n)], \quad (17)$$

where $|V_s(\chi_n)|$ is the modulus of the coherent reflection coefficient of the mode at the water–ice interface.

Let us consider the results of the test computations. Such results include the dependences of the modal group velocities, the attenuation coefficients, the GTD, and the EAC on the mode number. In Figs. 2–4, these results are presented for two deep-water arctic waveguides with an ice cover. The latter was modeled as a uniform absorbing elastic layer with the mean thickness $l = 3.5$ m and the following parameters [14]: $c_p = 3832.7$ m/s (the velocity of longitudinal waves); $c_s = 1903.5$ m/s (the velocity of shear waves); $\delta_p = 0.058$ dB/m/kHz (the attenuation of the longitudinal waves); $\delta_s = 0.348$ dB/m/kHz (the attenuation of shear waves); and $\rho = 0.91$ g/cm^3 (the ice density). The sea floor was modeled as a uniform liquid absorbing half-space with a velocity of longitudinal waves $c_b = 1600$ m/s, a density of 1.8 g/cm^3, and an attenuation of 0.1 dB/m/kHz. The choice of the model for the sea floor is not important, because we consider normal waves that do not interact with the bottom.

Figures 2a and 2b correspond to the aforementioned model of the arctic waveguide with an ice cover in the form of a homogeneous absorbing elastic layer of constant thickness $l = 3.5$ m and with the range-independent $c(z)$ profile shown in Fig. 1a. This profile was obtained by averaging the profiles at the intermediate points of the European part of the oceanographic survey, namely, from Spitsbergen Island to Point Barrow. The length of the survey was 2000 km, and the mean sea depth was $H = 3000$ m. The sound speed profiles were calculated from the temperature and salinity profiles measured in the SEVER experiment [15]. Figure 2a compares the modal group velocities $\{v_n, n = 1, 2, \ldots, 20\}$ calculated according to Eqs. (4)–(6), (15), and (16) in the WKB approximation with the group velocities calculated, using the modified mode computer code found in [11], by the formula

$$v_n = \left[\frac{\partial \mathrm{Re}(\xi_n)}{\partial\omega}\right]^{-1} = \mathrm{Re}\left\{\frac{\xi_n}{\omega}\left[\int_0^H \frac{w_n^2}{c(z)^2}dz - \frac{\partial G_b}{\partial(\omega^2)}w_n(H)^2 + \frac{\partial G_s}{\partial(\omega^2)}w_n(0)^2\right]^{-1}\right\}. \quad (18)$$

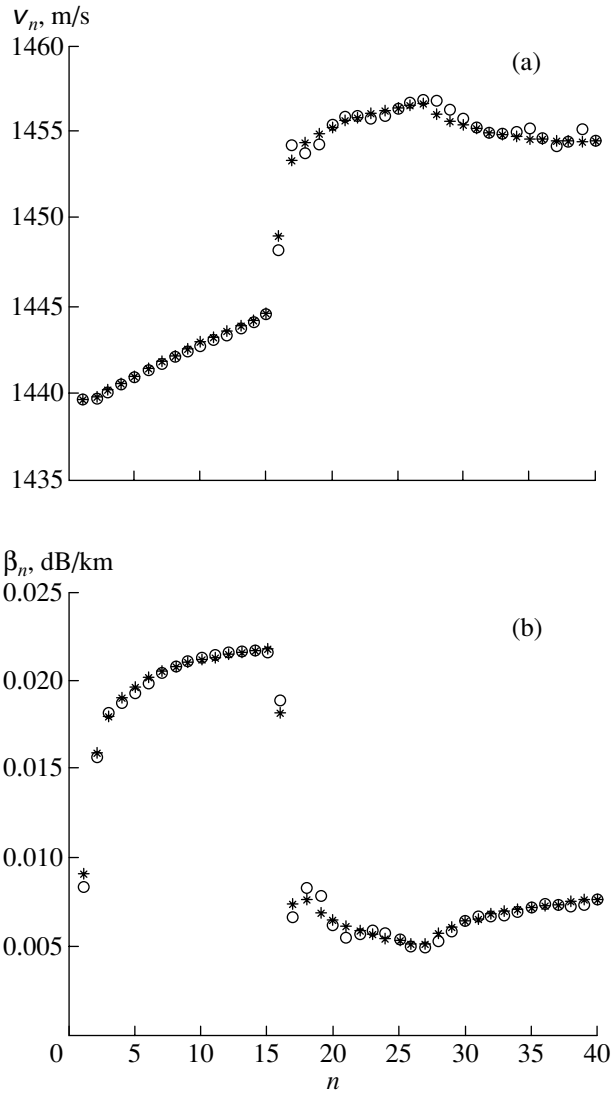

Fig. 2. Dependences of (a) the group velocity v_n (m/s) and (b) the attenuation coefficient β_n (dB/km) at a frequency of 250 Hz for the modeled horizontally uniform arctic waveguide with an ice cover of constant thickness (3.5 m): (°) the precise mode computer code and (*) the WKB method.

Here, the quantities $w_n(z)$ and $\lambda_n = \xi_n^2$ (the squared complex horizontal wave number for the nth mode) are the normalized eigenfunction and the nth eigenvalue, respectively, for the following spectral boundary problem:

$$\frac{d^2w}{dz^2} + \left[\frac{\omega^2}{c^2(z)} - \lambda\right]w = 0, \quad (19)$$

$$\left[\frac{dw}{dz} + G_s(\lambda)w\right]_{z=0} = \left[\frac{dw}{dz} + G_b(\lambda)w\right]_{z=H} = 0. \quad (20)$$

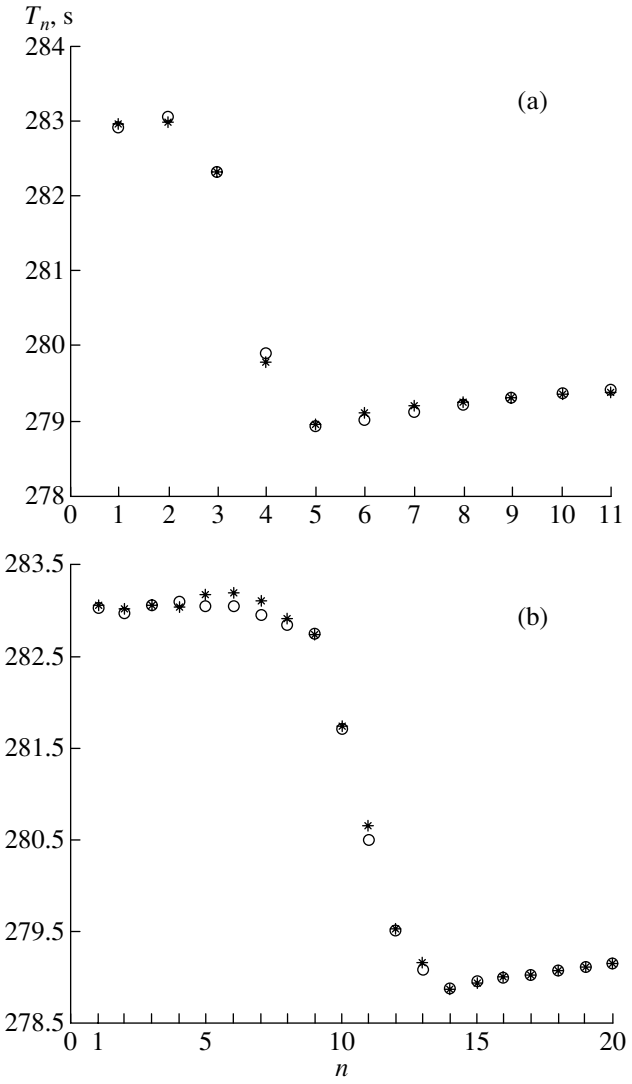

Fig. 3. Dependences of the GTD (T_n, s) on the mode number for the modeled arctic waveguide with range-dependent characteristics and a stochastically rough ice cover at frequencies of (a) 80 and (b) 250 Hz: (°) the precise mode computer code and (*) the WKB method.

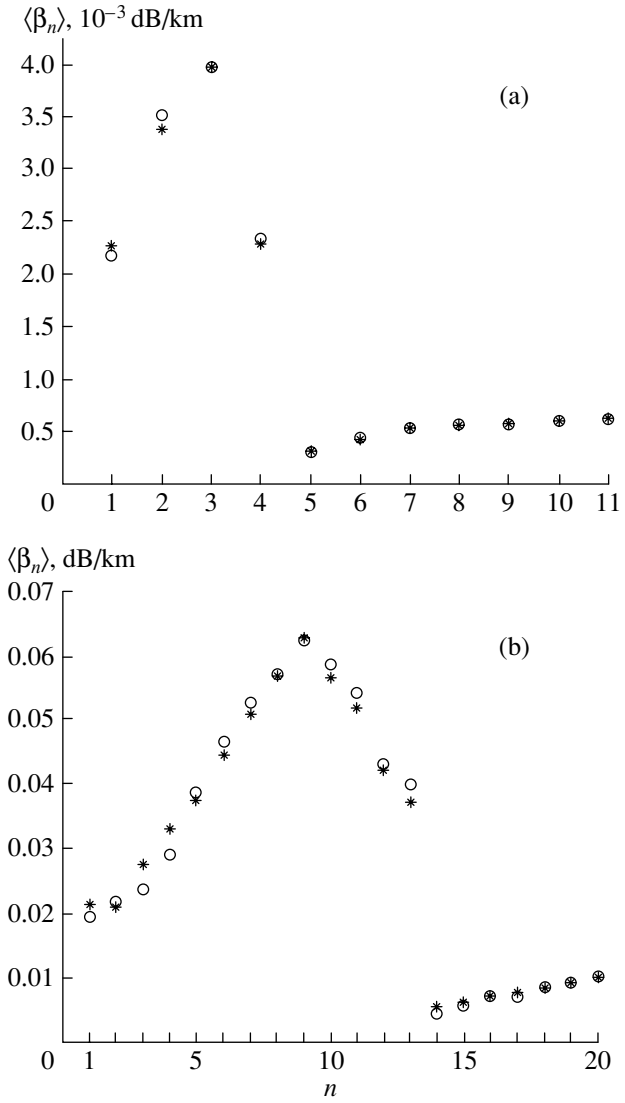

Fig. 4. Dependences of the EAC ($\langle\beta_n\rangle$, dB/km) on the mode number for the modeled arctic waveguide with range-dependent characteristics and a stochastically rough ice cover at frequencies of (a) 80 and (b) 250 Hz: (°) the precise mode computer code and (*) the WKB method.

In these equations, $\lambda = \xi^2$ is the spectral parameter, ξ is the horizontal wave number, H is the thickness of the water layer, $c(z)$ is the sound speed in the water layer, and G_s and G_b are the input admittances of the uniform ice layer and the bottom at the boundaries $z = 0$ and $z = H$, respectively. Formula (18) is obtained in a way similar to that used in [16] to derive the expression describing the group velocity in an oceanic waveguide with a free upper boundary. However, first boundary condition (20) at the water–ice interface was now used instead of the condition $w = 0$ at the free boundary $z = 0$. The eigenfunctions w_n appearing in Eq. (18) satisfy the normalization condition

$$\int_0^H w_n^2 dz + \left[\frac{\partial G_b(\omega, \lambda)}{\partial\lambda} w_n(H)^2 - \frac{\partial G_s(\omega, \lambda)}{\partial\lambda} w_n(0)^2\right]_{\lambda = \lambda_n} = 1. \quad (21)$$

The aforementioned admittances are calculated as

$$G_s = ik\sin\chi\frac{V_s(\chi) - 1}{V_s(\chi) + 1} \text{ and } G_b = \frac{\sqrt{\xi^2 - k_b^2}}{m_b}, \quad (22)$$

where $\chi = \arccos(\xi/k)$ is the grazing angle of the plane wave incident from the water on the ice cover; V_s is the

complex reflection coefficient for the plane wave at the water–ice interface, which is determined according to Brekhovskikh formula [17]; k_b is the wave number for longitudinal waves in the sea floor (in view of the absorption); and m is the ratio of the densities of the bottom material and water. The final expression for G_s as a function of ξ can be found in [7].

The data presented in Figs. 3 and 4 correspond to the modeled deep-water arctic waveguide with a stochastically rough ice cover and with the spatial distribution of the sound field shown in Fig. 1b. In the latter figure, the sound speed profiles $c(z, r)$ are presented for the initial 19 equidistant points of the initial part of the propagation path, with the distances $0 \le r = R = 500$ km. The path passes along the oceanographic survey from the Nansen basin to the Beaufort Sea, between the points (85° N, 46° E) and (73.6° N, 156.45° W). The parameters of the ice cover were as above. At each distance r, the sound speed profiles were calculated according to the empirical formula of Chen, Millero, and Lee with the temperature and salinity profiles [18] measured from the ice surface to the bottom at 10-m increments. These data were obtained in the SCICEX transarctic cruise of an American submarine in 1995.

Figures 3 and 4 show the dependences of the GTD (that is, the times of mode propagation along the paths) $\{T_n, n = 1, 2, \ldots, 20\}$ and the EAC (that is, the attenuation coefficients averaged over the path) $\{\langle\beta\rangle_n$ (dB/km), $n = 1, 2, \ldots, 20\}$ on the mode number. These quantities are calculated in the adiabatic approximation by integrating the inverse local modal group slownesses $s_n = v_n(r)^{-1}$ and the local modal attenuation coefficients over distance:

$$T_n = \int_0^R v_n(r)^{-1} dr, \tag{23}$$

$$\langle\beta_n\rangle = \frac{1}{R}\int_0^R \beta_n(r) dr. \tag{24}$$

Here, R is the path length and $n = 1, 2, \ldots, N$. To precisely calculate the aforementioned integral characteristics with Eqs. (23) and (24), multiple executions of rather complicated procedures are required. These procedures include solving the spectral boundary problem given by Eqs. (19), (20), and (22) to find the local complex eigenfunctions $w_n(z, r)$ and wave numbers $\xi_n(r)$ of the modes for the sequence of the $c(z, r)$ profiles along the path. For this purpose, one should use the coherent reflection coefficient at the water–ice interface as the function $V_s(\chi)$ appearing in Eq. (22) for the admittance G_s in boundary condition (20). Upon numerically determining the values of $\{\xi_n(r)$ and $w_n(r), n = 1, 2, \ldots, N\}$, the local modal group velocities $\{v_n(r), n = 1, 2, \ldots, N\}$ were determined by Eq. (18) and the local modal attenuation coefficients $\{\beta_n, n = 1, 2, \ldots, N\}$ were calculated as $\beta_n = 20(\log_{10} e)\mathrm{Im}(\xi_n) \times 10^3$ dB/km.

The dependences of the quantities T_n and $\langle\beta_n\rangle$, which are shown in Figs. 3 and 4, were obtained by both numerically solving spectral problem (19), (20), (22) with the use of the precise mode computer code [11] and using the WKB approximation according to Eqs. (4)–(6) and (15)–(17). The coherent reflection coefficient $V_s(\chi)$ appearing in Eqs. (17) and (22) was calculated according to Kudryashov's formulas [19] with the material and statistical geometrical parameters of arctic ice. The formulas by Kudryashov imply that the autocorrelation functions of the roughness at the two boundaries of the ice cover are the same and follow the exponential law $R(d) = \exp(-d/l_c)$, where d is the separation of two points of the ice cover, the correlation length l_c being large compared to the sound wavelength in water. The geometrical parameters of the ice cover were specified as follows: the mean ice thickness $l = 3.5$ m; the standard deviations of the lower and upper boundaries of the ice cover $\sigma_1 = 2.3$ m and $\sigma_2 = 0.6$ m; $l_c = 40$ m; and the cross-correlation coefficient of the two boundaries of the ice cover $K = 0.7$.

According to Figs. 2–4, the WKB-calculated (by Eqs. (4)–(6) and (15)–(17)) dependences of the group velocities $\{v_n, n = 1, 2, \ldots, N\}$, the attenuation coefficients $\{\beta_n, n = 1, 2, \ldots, N\}$, and the integral characteristics $\{T_n, n = 1, 2, \ldots, N\}$ and $\{\langle\beta_n\rangle, n = 1, 2, \ldots, N\}$ coincide with those obtained by numerically calculating the complex eigenvalues and eigenfunctions of the spectral boundary problem given by Eqs. (19), (20), (22) to a high accuracy. However, the WKB-based calculations of the aforementioned characteristics take a much shorter time (by a factor of several tens) than the time required for the calculations based on the mode computer code, irrespective of frequency.

One can expect that the WKB-based algorithms for calculating the group velocities and the attenuation coefficients of modes are most useful in the following situations: (i) in calculating the dependences of the mode characteristics on the parameters of the thermohaline structure of the under-ice medium in the arctic waveguide (on the thickness and the salinity of the desalinated and haloclinic layers or the layer of Atlantic water masses, for instance); (ii) in calculating the dependences of the mode characteristics on various parameters of the ice cover and on the sound frequency; (iii) in calculating the travel times of the modes in the under-ice sound channel on long propagation paths with range-dependent temperature and salinity profiles; and (iv) in calculating the time–frequency dispersion curves and many other characteristics of the modes.

The calculated values of the GTD and the EAC can be quite useful for selecting the optimal central frequency and the bandwidth of the probing signal, for choosing the length of the propagation path, and for determining the group of most informative modes with high intensities in implementing acoustic methods of

monitoring the thermohaline structure [20, 21] and the ice cover [4, 7].

ACKNOWLEDGMENTS

This work was supported by the Russian Foundation for Basic Research (project no. 01-02-16636) and the US Civilian Research & Development Foundation (project no. RG2-2407-MO-02).

REFERENCES

1. W. H. Munk and C. Wunsch, Rev. Geophys. Space Phys. **21**, 777 (1983).
2. E. C. Shang, J. Acoust. Soc. Am. **85**, 1531 (1989).
3. P. Sutton, W. M. Moravitz, B. D. Cornuelle, *et al.*, J. Geophys. Res. **99**, 12487 (1994).
4. E. Livingston and O. Diachok, J. Acoust. Soc. Am. **86**, 1909 (1989).
5. A. Tolstoy and O. Diachock, J. Acoust. Soc. Am. **89**, 1119 (1991).
6. L. M. Brekhovskikh, A. N. Gavrilov, V. V. Goncharov, *et al.*, Izv. Ross. Akad. Nauk, Fiz. Atmos. Okeana **38**, 726 (2002) [Izv., Acad. Sci., Atmos. Oceanic Phys. **38**, 642 (2002)].
7. V. D. Krupin, Akust. Zh. **48**, 788 (2002) [Acoust. Phys. **48**, 697 (2002)].
8. A. G. Voronovich, V. V. Goncharov, A. Yu. Nikol'tsev, and Yu. A. Chepurin, Akust. Zh. **38**, 661 (1992) [Sov. Phys. Acoust. **38**, 365 (1992)].
9. Yu. A. Chepurin and A. N. Gavrilov, in *Acoustics of the Ocean: Proceedings of IX School–Seminar of Academician L. M. Brekhovskikh* (GEOS, Moscow, 2002), pp. 182–187.
10. M. B. Porter and E. L. Reiss, J. Acoust. Soc. Am. **77**, 1760 (1985).
11. V. D. Krupin, Sudostr. Prom-st, Ser. Akust., No. 2, 82 (1989).
12. K. M. Guthrie, J. Sound Vibr. **34**, 289 (1974).
13. C. T. Tindle and D. E. Weston, J. Acoust. Soc. Am. **67**, 1614 (1980).
14. D. F. McCammon and S. T. McDaniel, J. Acoust. Soc. Am. **77**, 499 (1985).
15. I. V. Polyakov and L. A. Timokhov, Meteorol. Gidrol., No. 7, 68 (1994).
16. D. M. F. Chapman and D. D. Ellis, J. Acoust. Soc. Am. **74**, 973 (1983).
17. L. M. Brekhovskikh, *Waves in Layered Media* (Akad. Nauk SSSR, Moscow, 1957; Academic, New York, 1980).
18. *Environmental Working Group (EWG), Joint U.S.–Russia Atlas of the Arctic Ocean [CD-ROM]* (National Snow and Ice Data Center, Boulder, CO, 1998).
19. V. M. Kudryashov, Akust. Zh. **42**, 247 (1996) [Acoust. Phys. **42**, 215 (1996)].
20. G. I. Kozubskaya, V. M. Kudryashov, and K. D. Sabinin, Akust. Zh. **45**, 250 (1999) [Acoust. Phys. **45**, 217 (1999)].
21. V. D. Krupin, in *Acoustics of the Ocean. Atmospheric Acoustics: Proceedings of XIII Session of the Russian Acoustic Society* (GEOS, Moscow, 2003), Vol. 4, pp. 44–47.

Translated by E. Kopyl

Acoustical Physics, Vol. 51, No. 3, 2005, pp. 321–327. Translated from Akusticheskiĭ Zhurnal, Vol. 51, No. 3, 2005, pp. 383–390.

Fracture Localization in Space as a Cause of Variations in the Amplitude Distribution of Acoustic Emission Signals

A. V. Lavrov

Moscow State Mining University, Leninskiĭ pr. 6, Moscow, 119991 Russia

e-mail: avlavrov@mail.ru

Received October 7, 2003

Abstract—The change in the spatial distribution of acoustic emission sources in the course of the deformation and fracture of samples of materials and rocks is accompanied by changes in the amplitude distribution of the received signals because of the geometric spread of the elastic wave front. It is customary to characterize the amplitude distributions of acoustic emission signals in terms of the *b* value (the slope of the differential amplitude distribution). In particular, the localization of the sources may cause a decrease in the *b* value, which is usually interpreted as a precursor of macrofracture. A correct interpretation of the decrease in the *b* value is only possible if the location of the sources in space is accomplished and a correction for the spread and attenuation of elastic waves is introduced. © *2005 Pleiades Publishing, Inc.*

1. INTRODUCTION

1.1 Amplitude Distribution of Acoustic Emission Signals

Deformation and fracture of rocks and materials is accompanied by mobilization of defects of different types and sizes. One of the manifestations of the defect formation process is acoustic emission (AE), i.e., the emission of elastic waves due to irreversible or partially reversible structural changes. Among the AE mechanisms are, for example, the twinning or outcrop of dislocations or their clusters to boundaries of mineral grains, growth of microcracks and macrocracks, pore closure, etc. [1–7].

Modern instruments are capable of measuring the parameters of individual AE signals (the arrival time, amplitude, duration, and spectrum), as well as the parameters of the AE flux (number of signals per unit time, time gap between the signals, and others). If the measurements use several receiving channels, the AE source can be localized; i.e., the coordinates of the defect that produced the signal can be found. The localization on a plane requires at least three channels, and localization in space, four. The high cost of the receiving channel, which contains a receiving transducer, a preamplifier, filters, and analog-to-digital converter, impels researchers to limit their AE measurements to an available number of channels, which is not always capable of providing the localization. The AE measurements, in a laboratory and under field conditions alike, are often performed with single-channel equipment (see, e.g., [8]).

The amplitude distribution of the received AE signals and its variation in the course of loading characterizes the evolution of the fracture process in time. For instance, the amplitude analysis can reveal specific stages of the rock fracture and, in particular, the transition of the fracture from one hierarchical level to another [9].

Amplitude distributions of AE signals are usually represented in logarithmic coordinates with the abscissa axis representing the logarithm of the amplitude or the amplitude in decibels and the ordinate axis, the logarithm of the number of events whose amplitude is higher than that specified on the abscissa axis. We will conventionally refer to the plot obtained in this manner as the *cumulative plot*. We will use the term *differential plot* to refer to the plot if its ordinate axis shows the logarithm of the number of events whose amplitudes fall into a given range. An example of the cumulative amplitude distribution of the AE signals produced by the diametric compression of a disk-shaped sample of crinoid limestone is shown in Fig. 1 [10]. The threshold recording level was chosen in the experiment to be 40 dB, i.e., higher than the level of laboratory and circuit noise.

The cumulative plot in Fig. 1 can be approximated by the straight line

$$\log N = a - b\log A, \tag{1}$$

where A is the amplitude in volts; N is the number of signals whose amplitude is higher than A; and the b value, which enters into expression (1), characterizes the slope of the amplitude distribution. In Fig. 1, $b = 1.33$.

Expression (1) has the same form as the Gutenberg–Richter law known in seismology. Gutenberg–Richter's law is usually regarded as evidence of the self-similarity of the geological medium. Expression (1) plays a

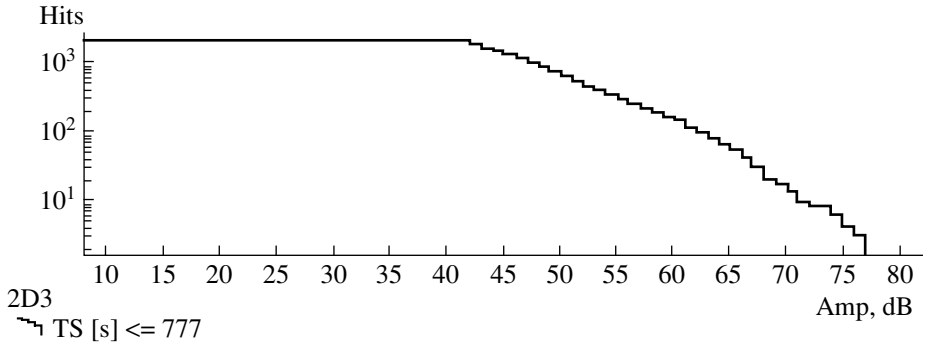

Fig. 1. Cumulative amplitude distribution of AE signals produced by the diametric compression of a disk-shaped limestone sample [10].

key role in the substantiation of the self-organized criticality concept in the physics of earthquakes [11, 12].

The differential amplitude distribution corresponding to Eq. (1) is described by the expression [13]

$$n(A)dA = kA^{-m}dA, \quad (2)$$

where $n(A)dA$ is the number of signals whose amplitude is in the range from A to $(A + dA)$. The dimensionless exponent m characterizes the slope of the differential amplitude distribution. A comparison of expressions (1) and (2) shows that

$$b = m - 1. \quad (3)$$

The logarithmic differential distribution often differs from the linear function described by Eq. (2). The deviation of the curve at small $\log A$ (near the AE measurement threshold) is due to the incompleteness of the AE measurements. The deviation of the curve on its right side is due to the small size of the statistics of high-amplitude events [9, 13]. The m parameter is usually estimated by processing the central linear part of the plot.

The perfect linear shape of the amplitude distribution described by Eqs. (1) and (2) corresponds to the linear energy distribution in logarithmic coordinates, $\log n = f(\log E)$, where E is the energy of the received AE signal. Deviations in the amplitude distribution in its leftmost and rightmost parts cause similar deviations from the linear behavior of the energy distribution. The actual shape of the energy distribution can be approximated by the expression [14]

$$n(E)dE = \frac{1}{d\sqrt{2\pi}}\frac{1}{E}\exp[-(\ln E - k)^2/(2d^2)], \quad (4)$$

where d and k are constant numbers.

Experiments show that the parameter b depends on the type of the rock and on the conditions of the experiment. In the process of loading the rock samples, a reduction in the b value is often observed as macrofracture is approached. For example, in the course of loading a dolerite sample, the b value decreases from 0.3–0.9 at the beginning of the experiment to 0.0–0.3 when the sample approaches its ultimate stress [13]. The decrease in the b value when approaching the ultimate stress is usually treated as a possible precursor of a macrofracture. In fact, the decrease in the b value means a relative increase in the contribution of high-amplitude events to the net AE emission. High-amplitude AE signals are produced by large cracks; therefore, a decrease in the b value may be regarded as a result of crack fusion, development of higher rank cracks, and transition of the fracture process to a higher hierarchical level followed by macrofracture.

This study demonstrates that the decrease in the b value may be caused not by the growth of defects generating the AE signal but by their localization in space. If the signal amplitude is measured neglecting the spread of the wave front, the localization of the fracture causes a decrease in the b value very similar to that observed in the experiments. Such a major mistake in processing and interpreting the AE measurement data obtained in the experiments on rock deformation occurs in all cases when the location of the source in space is impossible (for example, when the AE equipment used offers less then four channels).

1.2. Effect of Elastic Wave Attenuation on the Amplitude Distribution of AE Signals

Unander [15] has theoretically shown that the attenuation of elastic waves in the course of their propagation from the AE source (defect) to the receiver affects the amplitude distribution of AE signals. As an example, he considered a uniform distribution of sources in a hemisphere centered at the receiver. The amplitude distribution of received signals was calculated for the case when the sources have the same intensity. It was found that the amplitude distribution of the received signals differs from the linear function and the b value depends on amplitude and ranges from 0.0 to 3.0. A nonuniform source intensity distribution was also

analyzed, and the *b* value was found to depend on amplitude and to lie within 0.0 to 3.0 as well [15].

The amplitude distribution and *b* values are affected by the source intensity and the attenuation coefficient. It was shown that an increase in the attenuation coefficient shifts the amplitude distribution to the right, i.e., reduces *b*. A similar decrease in the *b* value is observed if the source intensity increases at a nonzero attenuation coefficient (i.e., the geometric spread is accompanied by a dissipation loss) [15]. Unander has thus shown that the *b* value decrease may be caused by an increase in the energy of events, as well as by the growth of the attenuation coefficient of elastic waves due to the increase in the number of defects when approaching fracture.

Weiss [16] corroborated the conclusions drawn in [15] by using a different theoretical method. He has shown that, if the amplitudes of the emitted signals are equal and no attenuation takes place, the cumulative distribution of the received signals in the logarithmic coordinates is a linear function with a slope of $b = 3.0$. A nonzero attenuation coefficient causes the distribution to be nonlinear. Like Unander, Weiss only considered the sources uniformly distributed in a sphere of radius *R* centered at the AE receiver.

1.3. Fracture Localization

The effect of the spread and attenuation of elastic waves on the observed amplitude distribution of AE signals was studied in [15, 16] for a particular arrangement of sources in space, namely, for the uniform distribution in a sphere centered at the AE receiver. In real experiments, the sources may be irregularly distributed over the space occupied by the sample, i.e., the sources may be localized. The localization of the AE sources originates from a number of causes. Among these are the initial inhomogeneity of the medium, a nonuniform distribution of relatively weaker sources, a layered structure, cracks, etc. For example, experiments [17] in which AE sources were located by eight-channel equipment have shown that the uniaxial loading of layered sandstone creates a fracture localization zone as early as at initial stages of loading (at a stress lower than $0.3\sigma_{compr}$, where σ_{compr} is the rock's ultimate uniaxial compression strength). This zone is subparallel to the layers, which are in turn perpendicular to the loading direction.

Along with the localization due to the initial inhomogeneity of rock, the fracture localization in macrocracks is observed at the final deformation stage. In particular, granite and sandstone samples were subjected to triaxial compression at a constant lateral pressure of 50 MPa [18]. The AE was measured with a six-channel system, which was capable of locating the sources in three dimensions. In the experiment, a feedback in the AE activity was provided, which allowed one to extend the time taken by the fracture stage near the sample's ultimate stress and also beyond it.

In granite, which is a relatively homogeneous fine-grained rock, the transition from the formation of sparse microcracks to localization of the sources in a macrofracture occurred abruptly after the peak axial stress was left behind.

The time between the passing of the peak stress and the formation of the macrofracture was several tenths of a second. The *b* value remained approximately constant and equal to ≈3.0 until the sample reached its ultimate stress. At the ultimate stress, a few tenths of a second before the macrofracture, the *b* value began to decrease. By the time the macrocrack was formed, the *b* value decreased to 1.0–1.5. The fractal dimension *D* of the spatial source distribution in the same sample did not exhibit such a precursor variation and remained equal to ≈2.7 until the macrofracture was initiated when *D* fell to 1.7–1.8 [18]. In another granite sample, no precursor decrease in the *b* value was observed.

In limestone, which is characterized by a relatively high inhomogeneity, the localization scenario was somewhat different [18]. Similar to experimental results reported in [17], clustering of AE sources was observed long before the stress reached its maximum value. Beginning with the moment when the stress reached its peak, the *b* value gradually decreased from 3.0–3.5 to ≈2.5. The formation of macrofracture was accompanied by a further and faster decrease in the *b* value from 2.5 to 1.5–2.0. The gradual decrease in the *b* value in limestone was accompanied by a gradual decrease in the fractal dimension of the spatial source distribution from $D \approx 2.5$ at the peak stress to $D \approx 1.5$ at the moment when the macrofracture was formed [18].

A detailed study of fracture localization and of shear band microstructure was reported in [19], where it was noted that the beginning of inhomogeneous deformation corresponds to the ultimate stress stage, while the final formation of the shear bands corresponds to the post-ultimate-stress stage. The number of shear bands depends on the lateral pressure σ_3 and grows with σ_3. The shear bands were clearly seen after the experiment was completed and the samples were taken out of the chamber.

Summarizing the above brief review of experimental studies of the fracture localization observed in the course of the deformation of rock samples, the following should be noted. The formation of microfractures is preceded by clustering of defects in space, which can be revealed by the location of AE sources, as well as by deformation measurements. The uniform defect distribution over the sample volume is followed by a more complex distribution, which clearly exhibits irregularly

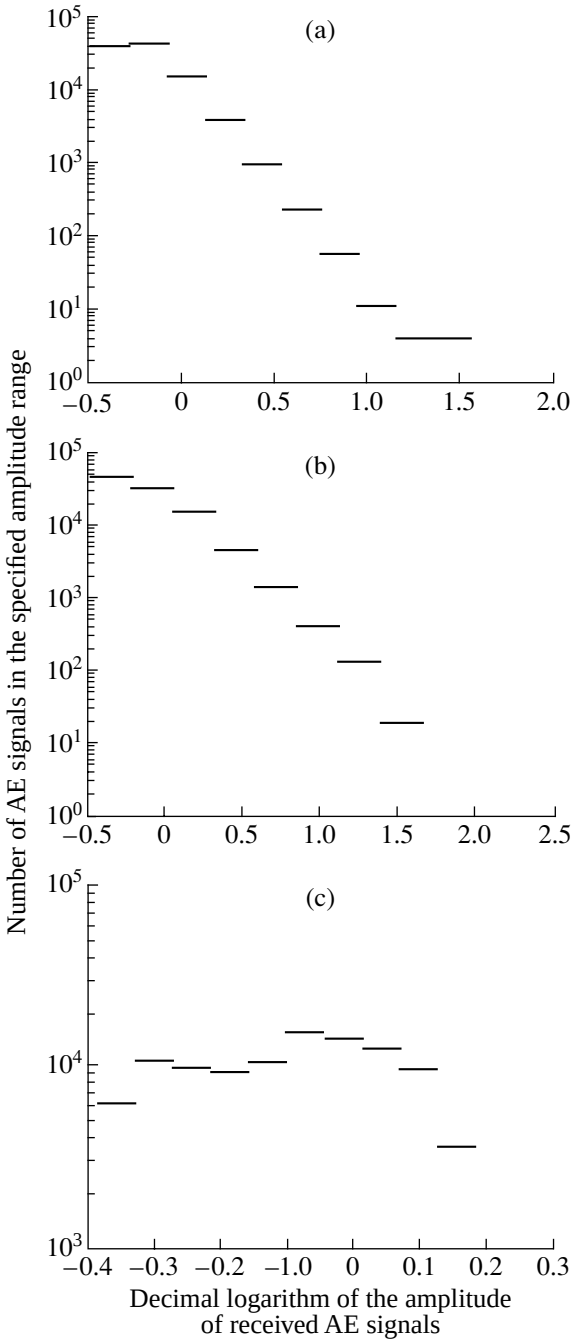

Fig. 2. Simulated amplitude distributions of received AE signals: (a) basic case (the sources are uniformly distributed over the sample); (b) the sources are distributed over the shear band, and the AE receiver is at the intersection of the shear band and sample's lateral surface; and (c) localization of the sources in the shear band, where the AE receiver is at the center of sample's lateral face.

shaped clusters usually resembling half-disks, disks, ellipsoids, etc. As the next section shows, such a qualitative redistribution of AE sources over the sample may change the *b* value of the amplitude distribution of the received signals if it is calculated neglecting the source location.

2. SIMULATION OF THE *b*-VALUE VARIATIONS DUE TO FRACTURE LOCALIZATION

Below, we study the effect of the geometric spread of elastic waves on the amplitude distribution of received AE signals. The loss is absent, and reflection from the sample boundaries is neglected. Amplitudes of all emitted signals are equal. Amplitudes of the received signals are $A = 1/r$, where r is the distance from the AE source to the receiver.

2.1. Uniform Source Distribution over a Prism Sample

First, consider the uniform distribution of 10^5 sources over a sample in the form of a rectangular parallelepiped with a height-to-base side ratio of 2 : 1 (the base is square). This is the basic geometry. It describes the source distribution typical of the initial stage of loading of the prism sample. The AE receiver is placed at the center of sample's lateral face. The amplitude distribution of received AE signals for this configuration is shown in Fig. 2a. The abscissa axis represents the decimal logarithm of the received signal amplitude, $\log A$. The $\log A$ values are divided into ten categories, the number of signals in each category is calculated, and these numbers are plotted on the ordinate axis on the logarithmic (base ten) scale. It can be shown that the slope of this histogram equals *b*. In Fig. 2a, $b = 3.0$, which is in a good agreement with the values obtained experimentally [18].

One should note the plateaus of the histogram in the rightmost and leftmost parts of Fig. 2a. This behavior resembles real experimental observations.

2.2. Fracture Localization in Shear Bands

Figure 3a illustrates the situation in which a fracture localization zone in the form of an oblique shear band is formed and the AE receiver resides at the intersection of this zone and the sample's lateral face. The localization zone is inclined to the sample axis at an angle of 45°. The ratio of the sample height to its base side is 2 : 1. The localization zone thickness is 1/20 of the base side, which agrees well with experimental results reported in [19]. The number of sources uniformly distributed over the localization zone is 10^5.

The amplitude distribution of the received AE sources is shown in Fig. 2b. The slope of the histogram in its central part yields $b = 2.0$. In the left and right parts, deviations from the linear behavior are observed. The value of $b = 2.0$ is typical of the uniform source distribution over a plane (if the receiver itself lies in the same plane). Thus, changing from the source distribution over the sample volume to the distribution over a narrow localization layer that passes through the location of the AE receiver reduces the *b* value from 3.0 to 2.0. This reduction is caused by the change in the fracture zone geometry alone rather than in the amplitude distribution of the source.

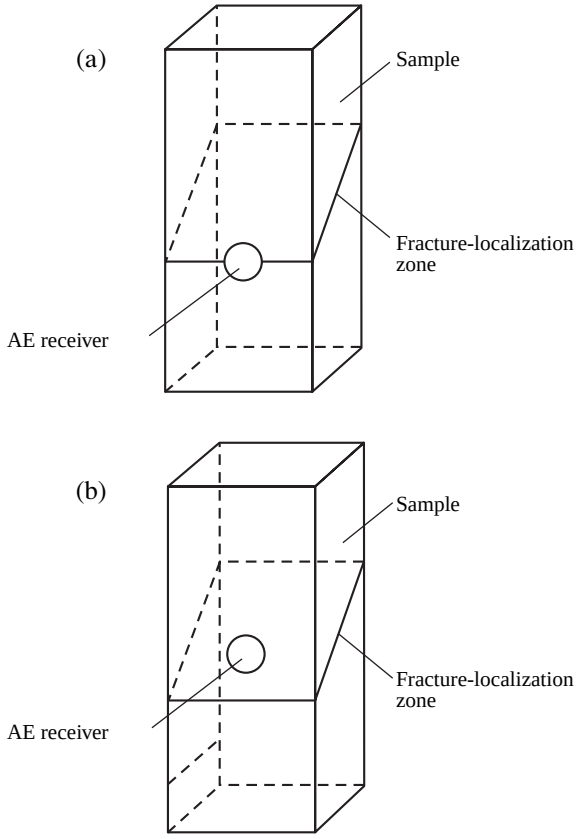

Fig. 3. Rock sample with the AE receiver mounted on it.

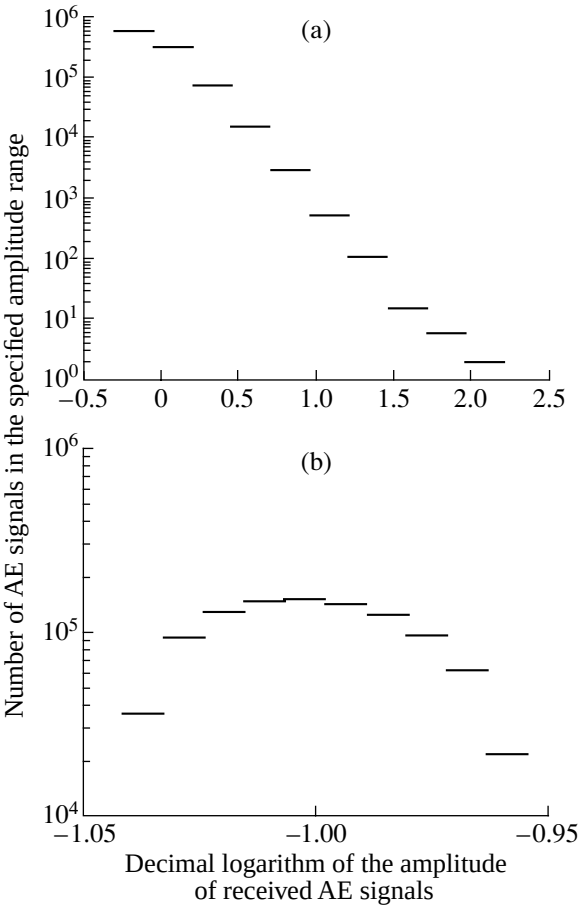

Fig. 4. Simulated amplitude distributions of received AE signals for the sources localized in a sphere and the AE receiver placed (a) at the sphere boundary and (b) at a distance of 10*R* from the center of the sphere.

Even more dramatic changes in the amplitude distribution of the received signals are observed when the receiver is at the center of the sample's lateral face (Fig. 3b) rather than at the intersection of the localization zone and the lateral face. The localization zone passes through the sample center at an angle of 45° to the longitudinal axis, and its thickness is 1/20 of the base side length. The sample height-to-base edge ratio is 2 : 1, as above.

The amplitude distribution corresponding to the configuration of Fig. 3b is shown in Fig. 2c. A typical feature of this distribution is its strong nonlinearity. Except for the rightmost part of the histogram, the slope is characterized by $b < 2.0$. In the central part of the distribution, regions with $b = 0.0$ and even $b < 0.0$ are present.

In real samples, several localization zones are often observed. This effect must lead to even more complex amplitude distributions of the received AE signals and to a decrease in the *b* value relative to that at the scattered microcrack accumulation stage (compare Figs. 2a and 2c).

2.3. Source Localization in a Sphere

Experiments on the sample deformation in which the sources were located show that, due to the inhomogeneity of rock, a localization in the form of irregular and often isometric clusters may already be observed at the early stages (Section 1.3). Without aiming at imitating clusters of the real geometry, let us consider the amplitude distribution of the received signals produced by sources uniformly distributed over a sphere for various receiver positions relative to the sphere center. The sphere radius *R* equals 1.0; the total number of sources is 10^6. When the receiver resides at the center of the sphere, the amplitude distribution of the received signals proves to be linear, with $b = 3.0$. This result coincides with the *b* value obtained for a similar configuration in [15, 16].

When the receiver is at the boundary of the sphere (i.e., at a distance of 1.0 from its center), the distribution of the received signals remains mainly linear, with a certain flattening in its leftmost and rightmost parts (Fig. 4a). In the central part of the distribution, the *b* value is 3.0.

When the receiver is placed outside of the clusterization region at a distance of twice the sphere's radius, the distribution becomes nonlinear with a negative slope ($b < 0.0$) in its leftmost part. Note that real exper-

iments detect only those AE signals whose amplitude is above a certain threshold level. Therefore, the region with the negative slope, typical of low amplitudes, may be absent. In some experiments (for example, in [13]), $b < 0.0$ was observed.

Moving the receiver further away from the center of the sphere makes the left part of the distribution with a slope of $b < 0.0$ even more pronounced, and the distribution becomes actually symmetric. As an example, Fig. 4b shows the amplitude distribution for the receiver placed at a distance of $10R$ from the center of the sphere.

For the sake of comparison, consider the clustering of the sources in a cube of length 2.0 on the edge. When the receiver is at a distance of 10.0 from the cube's center, on the perpendicular constructed at the center of the cube face, the amplitude distribution is actually uniform with $b = 0.0$. A similar behavior is observed when the receiver is at a distance of 100.0 from the cube's center. Simulations performed for the receiver placed at the center of the cube provide a linear distribution with $b = 3.0$ and a weak flattening in its rightmost and leftmost parts, similar to the situation illustrated in Fig. 4a. This again shows that the clustering may reduce the b value from 3.0 to 0.0 solely because of the geometric spread of the elastic wave rather than a change in the amplitude distribution of the emitted signals.

CONCLUSIONS

Fracture localization in the shear planes changes the amplitude distribution of the received AE signals and the b value because of the spread of the elastic waves as they propagate from the source to the AE receiver. A change in the geometry of the fracture zone from three-dimensional (a uniform source distribution over the sample volume) to two-dimensional (a shear band with the receiver located in its plane) reduces b from 3.0 to 2.0. In real experiments, this reduction can erroneously be interpreted as evidence of a change in the energy distribution of the sources, i.e., an increase in the relative contribution of higher energy events. Such changes are usually regarded as precursors of macrofracture. To a certain extent, the decrease in b due to the localization can be regarded as the precursor, because it is an indication of the rearrangement of microcracks before macrofracture.

The fracture localization into three-dimensional clusters (sphere, cube) distorts the amplitude distribution and makes it nonlinear, decreasing the b value to 0.0 and even to negative values. The spread of the elastic waves flattens the amplitude distribution of the received signals in its leftmost and rightmost parts, which agrees well with actual observations.

The results of our study show that experimental measurements of the AE signal amplitude distribution that do not allow for the amplitude decrease due to the spread of the waves ($1/r$) cannot be regarded as correct. In particular, all measurements of the b value made by one-, two-, or three-channel AE systems should be considered incorrect. To retrieve correct amplitude distributions, the system must locate the sources and allow for the spread and attenuation of waves. An example of correct AE spectra measurements with allowance for the elastic wave attenuation in the course of propagation can be found, e.g., in [20], where the fracture of wood and fiberglass composite materials under mechanical loading is studied.

Using one receiver, one can correctly measure the distribution of time intervals between sequentially received AE signals. These intervals, as well as the amplitudes, are distributed according to the power scaling law (in certain cases at least). Such measurements were performed, for example, in [8]. In addition, qualitative changes in the character of the fracture process are accompanied by changes in the AE frequency spectra. These spectra provide information on the parameters of propagating cracks [21]. An efficient method for analyzing the AE signals, which has become rather popular in the recent years, is the wavelet analysis [22, 23].

ACKNOWLEDGMENTS

This work was supported by the Russian Foundation for Basic Research, project no. 01-05-64105, and the Program for Supporting the Leading Scientific Schools, project no. NSh-1467.2003.5.

REFERENCES

1. V. A. Greshnikov and Yu. V. Drobot, *Acoustic Emission: Application to Testing Materials and Products* (Izd. Standartov, Moscow, 1976) [in Russian].
2. D. Lockner, Int. J. Rock Mech. Min. Sci. Geomech. Abstr. **30** (7), 883 (1993).
3. A. S. Voznesenskiĭ, Yu. V. Demchishin, E. M. Shafarenko, *et al.*, in *Proceedings of X Session of the Russian Acoustical Society* (GEOS, Moscow, 2000), Vol. 2.
4. X. Lei, K. Masuda, O. Nishizawa, *et al.*, J. Struct. Geology **26** (2), 247 (2004).
5. V. A. Robsman, Akust. Zh. **38**, 129 (1992) [Sov. Phys. Acoust. **38**, 66 (1992)].
6. V. V. Rzhevskiĭ, V. S. Yamshchikov, V. V. Shkuratnik, *et al.*, Dokl. Akad. Nauk SSSR **273**, 1094 (1983).
7. V. S. Kuksenko, I. E. Inzhevatkin, B. Ts. Manzhikov, *et al.*, in *Physical and Engineering Problems in Mineral Resource Mining* (1987), No. 1.
8. P. Diodati, P. Bak, and F. Marchesoni, Earth Planet. Sci. Lett. **182**, 253 (2000).
9. N. G. Tomilin and V. S. Kuksenko, in *Science of the Earth: Physics and Mechanics of Geomaterials*, Ed. by A. V. Lavrov (Vuzovskaya Kniga, Moscow, 2002), pp. 116–135 [in Russian].
10. A. V. Lavrov, in *Proceedings of XI Session of the Russian Acoustical Society* (GEOS, Moscow, 2001), Vol. 2, p. 99.
11. P. Bak and C. Tang, J. Geophys. Res. **94** (11B), 15635 (1989).

12. K. Ito and M. Matsuzaki, J. Geophys. Res. **95** (5B), 6853 (1990).
13. G. M. Fonseka, S. A. F. Murrell, and P. Barnes, Int. J. Rock Mech. Min. Sci. Geomech. Abstr. **22** (5), 273 (1985).
14. V. Rudajev, J. Vilhelm, J. Kozák, and T. Lokajíček, Int. J. Rock Mech. Min. Sci. Geomech. Abstr. **33** (7), 743 (1996).
15. T. E. Unander, Int. J. Rock Mech. Min. Sci. Geomech. Abstr. **30** (7), 947 (1993).
16. J. Weiss, Bull. Seismol. Soc. Am. **87** (5), 1362 (1997).
17. M. Seto, M. Utagawa, and K. Katsuyama, in *Proceedings of 8th International Congress on Rock Mechanics*, Ed. by T. Fujii (Balkema, Rotterdam, 1995), Vol. 1, p. 201.
18. D. A. Lockner and J. D. Byerlee, in *Proceedings of 5th Conference on AE/MA in Geologic Structures and Materials* (Trans. Tech., Clausthal-Zellerfeld, 1995), p. 45.
19. P. Bésuelle, J. Desrues, and S. Raynaud, Int. J. Rock Mech. Min. Sci. Geomech. Abstr. **37** (8), 1223 (2000).
20. A. Guarino, A. Garcimartín, and S. Ciliberto, Eur. Phys. J. B: Condens. Matter **6** (1), 13 (1998).
21. V. V. Krylov, P. S. Landa, and V. A. Robsman, Akust. Zh. **39**, 108 (1993) [Acoust. Phys. **39**, 55 (1993)].
22. C. U. Grosse, F. Finck, J. H. Kurz, and H. W. Reinhardt, Constr. Building Mater. **18**, 203 (2004).
23. A. Lavrov, M. Wevers, and A. Vervoort, J. Acoust. Emiss. **20**, 292 (2002).

Translated by A. Khzmalyan

Acoustical Physics, Vol. 51, No. 3, 2005, pp. 328–337. Translated from Akusticheskiĭ Zhurnal, Vol. 51, No. 3, 2005, pp. 391–401.

Regularization of Boundary Integral Equations in the Problems of Wave Field Diffraction by Curved Boundaries

G. A. Maximov and D. N. Lesonen

Moscow Engineering Physics Institute (State University), Kashirskoe sh. 31, Moscow, 115409 Russia

e-mail: maximov@dpt39.mephi.ru

Received March 25, 2004

Abstract—A regularization of the exact Fredholm integral equations for the field or its derivative on a scattering surface is proposed. This approach allows one to calculate the scattering or diffraction of pulsed wave fields by curved surfaces of arbitrary geometry. Mathematically, the method is based on the replacement of the exact Fredholm integral equations by their truncated analogs, in which the contributions of the geometrically shadowed regions are cancelled. This approach has a clear physical meaning and provides stable solutions even when the direct numerical solution of mathematically exact initial integral equations leads to unstable results. The method is mathematically substantiated and tested using the problem of plane-wave scattering by a cylinder as an example. © *2005 Pleiades Publishing, Inc.*

One of the most powerful methods for solving the problems of acoustic, electromagnetic, or seismic wave diffraction by curved boundaries is the integral equation method [1–3]. In the framework of the latter, a problem is reduced to solving exact Fredholm integral equations of the first or second kind for the field or for its normal derivative at a scattering boundary. For pulsed wave fields characterized by a broad spectrum of wavelengths, this method is only one to provide solutions for diffraction by a surface of an arbitrary shape in both the long and short wave regions, as well as in the intermediate resonance region.

According to Green's theorem [4], the scalar field $U(\mathbf{r})$ at the internal points of a medium can be expressed through its value and the value of its normal derivative at an arbitrary boundary $\mathbf{r} = \mathbf{r}_s$:

$$U(\mathbf{r}) = U_0(\mathbf{r}) + \int_S dS\left\{U(\mathbf{r}_S)\frac{\partial}{\partial n_s}G(\mathbf{r}, \mathbf{r}_s) - G(\mathbf{r}, \mathbf{r}_s)\frac{\partial}{\partial n_s}U(\mathbf{r}_s)\right\}, \quad (1)$$

where $U_0(\mathbf{r})$ is the direct field of the sources and $G(\mathbf{r}, \mathbf{r}_s)$ is the Green function of free space.

For the Dirichlet and Neumann boundary conditions, assuming that the internal point in Eq. (1) tends to the boundary of the region $\mathbf{r} \longrightarrow \mathbf{r}_s$ and separating the singular part from the Green function, we obtain a Fredholm equation of the second kind for the field or for its normal derivative at the curved boundary of the medium. For example, in the case of the Dirichlet boundary condition ($U(\mathbf{r}_s) = 0$), we have the following equation for the normal derivative $V(\mathbf{r}_s) = \partial U(\mathbf{r}_s)/\partial n_s$:

$$V(\mathbf{r}) = 2V_0(\mathbf{r}) - 2\int_S dS' V(\mathbf{r}')\frac{\partial}{\partial n}G(\mathbf{r}, \mathbf{r}'). \quad (2a)$$

In the case of the Neumann boundary condition, a similar equation is obtained for the field at the surface $U(\mathbf{r}_s)$:

$$U(\mathbf{r}) = 2U_0(\mathbf{r}) - 2\int_S dS' U(\mathbf{r}')\frac{\partial}{\partial n'}G(\mathbf{r}, \mathbf{r}'). \quad (2b)$$

We note the symmetry of boundary conditions (2a) and (2b) for the problems with Dirichlet and Neumann boundary conditions. If we ignore the fact that $U(\mathbf{r}_s)$ is the field at the boundary and $V(\mathbf{r}_s)$ is its derivative, the only difference between Eqs. (2a) and (2b) is the difference in the signs of the integrals and normal derivatives taken with respect to different arguments of the Green function.

Thus, the problem of the wave field diffraction by an arbitrary boundary is initially reduced to solving Eq. (2). Then, substituting the resulting value of the field or its normal derivative at the boundary in Eq. (1), we can calculate the wave field at any point of the region with a curved boundary under consideration. Note that the classical Kirchhoff approximation for the field on the illuminated part of the surface corresponds to the first terms in Eqs. (2).

Naturally, in the case of an arbitrary scattering surface, this approach can be efficient only with the use of numerical methods. A numerical solution of Eq. (2) is

1063-7710/05/5103-0328$26.00

possible by the iteration method or on the basis of the grid approximation, namely, by replacing the Fredholm integral equation of the second kind (Eq. (2)) with a set of linear algebraic equations for the values of the field or its normal derivative at the nodes of a certain grid at the boundary.

However, a direct numerical solution of the Fredholm integral equations in diffraction problems allows one to obtain stable solutions when the slopes and curvatures of the surface are relatively small, whereas, in the case of steep slopes and great curvatures, the numerical methods become unstable, leading to ill-posed matrices in the grid approximation or to divergent solutions in the iteration method [1, 2].

This occurs because, when the surface is characterized by steep slopes and large heights of the surface roughness, the contribution of multiply reflected waves becomes dominant. It also includes the contribution of mutually shadowed points of the surface. According to [5], this contribution is cancelled in different orders of the series expansion in terms of the scattering multiplicity, which leads to divergent iterations. Let us consider the problem of a plane wave

$$U_0(\mathbf{r}) = \exp(i\mathbf{k}_0\mathbf{r})$$

scattered by an arbitrary boundary with the Dirichlet condition. With allowance for the fact that the Green function of free space has the form

$$G(\mathbf{r}, \mathbf{r}') = \frac{1}{4\pi}\frac{\exp(ik|\mathbf{r}-\mathbf{r}'|)}{|\mathbf{r}-\mathbf{r}'|},$$

we can represent Eq. (2) as

$$V(\mathbf{r}_1) = 2i(\mathbf{k}_0\mathbf{n}_1)U_0(\mathbf{r}_1)$$
$$-2\int_S dS_2 V(\mathbf{r}_2)(\mathbf{n}_1\mathbf{e}_{12})\left(ik_0 - \frac{1}{|\mathbf{r}_1-\mathbf{r}_2|}\right)G(\mathbf{r}_1-\mathbf{r}_2), \quad (3)$$

where $\mathbf{n}_1$ is the normal vector to the surface at the point $\mathbf{r}_1$ and $\mathbf{e}_{12}$ is the unit vector in the direction of $\mathbf{r}_1 - \mathbf{r}_2$. If we solve Eq. (3) by the iteration method, the first correction to the zero iteration,

$$V^0(\mathbf{r}_1) = 2i(\mathbf{k}_0\mathbf{n}_1)\exp(i\mathbf{k}_0\mathbf{r}_1) = V_0(\mathbf{r}_1),$$

can be represented as

$$V^1(\mathbf{r}_1) = -2\int_S dS_2 2i(\mathbf{k}_0\mathbf{n}_2)\exp(i\mathbf{k}_0\mathbf{r}_2)(\mathbf{n}_1\mathbf{e}_{12})$$
$$\times\left(ik_0 - \frac{1}{|\mathbf{r}_1-\mathbf{r}_2|}\right)\frac{1}{4\pi}\frac{\exp(ik_0|\mathbf{r}_1-\mathbf{r}_2|)}{|\mathbf{r}_1-\mathbf{r}_2|}. \quad (4)$$

In the geometrical optics limit $k_0|\mathbf{r}_1 - \mathbf{r}_2| \gg 1$, the main contribution to integral (4) is made by the vicinities of the stationary points $\mathbf{r}_2 = \mathbf{r}_s$ of the phase function

$$h(\mathbf{r}_2) = \mathbf{k}_0\mathbf{r}_2 + k_0|\mathbf{r}_1 - \mathbf{r}_2|, \quad (5)$$

which are determined from the condition

$$(\boldsymbol{\tau}_s\nabla_s)h(\mathbf{r}_s) = 0,$$

where $\boldsymbol{\tau}_s$ is the tangential vector at the point $\mathbf{r}_s$. Thus, at stationary points, the following condition should be met:

$$(\mathbf{k}_0\boldsymbol{\tau}_s) + k_0(\mathbf{e}_{1s}\boldsymbol{\tau}_s) = 0. \quad (6)$$

Introducing the unit vector $\mathbf{e}_{k_0}$ along the wave number of the incident wave as $\mathbf{k}_0 = k_0\mathbf{e}_{k_0}$, we represent condition (6) in the form

$$(\mathbf{e}_{k_0} + \mathbf{e}_{1s})\boldsymbol{\tau}_s = 0. \quad (7)$$

This condition can be satisfied in two ways [5]:

$$\mathbf{e}_{1s}\boldsymbol{\tau}_s = -\mathbf{e}_{k_0}\boldsymbol{\tau}_s$$

or

$$\mathbf{e}_{1s} = -\mathbf{e}_{k_0}. \quad (8)$$

According to [5], the first of these conditions corresponds to specularly reflecting points, and the second, to shadowing points.

An estimate of integral (4) in the geometrical optics limit can be obtained by the stationary phase method. For this purpose, we expand the phase function in the vicinity of a stationary point by using the surface curvature lines as a local coordinate system (ξ, η) [6]:

$$h(\mathbf{r}_2 \approx \mathbf{r}_s) = h(\mathbf{r}_s)$$
$$+\frac{1}{2}\left(\frac{\partial^2 h(\mathbf{r}_s)}{\partial\xi^2}\Delta\xi^2 + 2\frac{\partial^2 h(\mathbf{r}_s)}{\partial\xi\partial\eta}\Delta\xi\Delta\eta + \frac{\partial^2 h(\mathbf{r}_s)}{\partial\eta^2}\Delta\eta^2\right). \quad (9)$$

The expansion coefficients in formula (9) can be calculated by taking into account that the derivatives along the surface curvature lines correspond to the tangential unit vectors along the curvature lines, $\partial\mathbf{r}/\partial\xi = \boldsymbol{\tau}_\xi$ and $\partial\mathbf{r}/\partial\eta = \boldsymbol{\tau}_\eta$, and that, along the curvature lines, the Frene formulas for plane curves are valid [6]:

$$\begin{cases}\partial\boldsymbol{\tau}_\xi/\partial\xi = K_\xi\mathbf{n}\\ \partial\mathbf{n}/\partial\xi = -K_\xi\boldsymbol{\tau}_\xi,\end{cases} \quad (10)$$

where $K_\xi = 1/R_\xi$ is one of the two principal curvatures of the surface at a nonsingular point (R_ξ is the curvature radius).

Using relations (10) for the first derivatives of function (5), it is easy to obtain a relation equivalent to Eq. (7):

$$\partial h/\partial\xi = (\boldsymbol{\tau}_\xi, (\mathbf{e}_{k_0} + \mathbf{e}_{21})).$$

For the second derivatives, we obtain the expressions

$$\frac{\partial^2 h}{\partial\xi^2} = K_\xi(\mathbf{n}, (\mathbf{e}_{k_0} + \mathbf{e}_{21})) + \frac{1-(\boldsymbol{\tau}_\xi\mathbf{e}_{21})^2}{|\mathbf{r}_{12}|},$$

$$\frac{\partial^2 h}{\partial\eta\partial\xi} = \left(\frac{\partial^2\mathbf{r}_{12}}{\partial\eta\partial\xi}, (\mathbf{e}_{k_0} + \mathbf{e}_{21})\right) - \frac{(\boldsymbol{\tau}_\xi\mathbf{e}_{21})(\boldsymbol{\tau}_\eta\mathbf{e}_{21})}{|\mathbf{r}_{12}|}.$$

Thus, for the shadowed points satisfying condition (8), the expansion of the phase function in their vicinity can be represented in the form

$$h(\mathbf{r}_2 \approx \mathbf{r}_s) = h(\mathbf{r}_s) + \frac{1}{2|\mathbf{r}_{12}|}((1-(\boldsymbol{\tau}_\xi \mathbf{e}_{21})^2)\Delta\xi^2$$
$$-2(\boldsymbol{\tau}_\xi \mathbf{e}_{21})(\boldsymbol{\tau}_\eta \mathbf{e}_{21})\Delta\xi\Delta\eta + (1-(\boldsymbol{\tau}_\eta \mathbf{e}_{21})^2)\Delta\eta^2).$$

Substituting this expression into integral (4) and performing the integration, we obtain

$$V^1(\mathbf{r}_1)$$
$$= \frac{k_0(\mathbf{k}_0\mathbf{n}_s)(\mathbf{n}_1\mathbf{e}_{1s})}{\pi|\mathbf{r}_{1s}|}\exp(ik_0h(\mathbf{r}_s))\frac{2\pi i}{k_0}\frac{|\mathbf{r}_{1s}|}{\sqrt{(\mathbf{n}_s\mathbf{e}_{s1})^2}}. \quad (11)$$

Replacing $\mathbf{e}_{s1}$ with $\mathbf{e}_{k_0}$ according to Eq. (8) ($\mathbf{e}_{s1} = -\mathbf{e}_{1s}$), we represent Eq. (11) in the form

$$V^1(\mathbf{r}_1) = -2i(\mathbf{n}_1\mathbf{e}_{k_0})\exp(i\mathbf{k}_0\mathbf{r}_1)\frac{(\mathbf{n}_s\mathbf{e}_{k_0})}{\sqrt{(\mathbf{n}_s\mathbf{e}_{k_0})^2}} \quad (12)$$
$$= -V^0(\mathbf{r}_1)\mathrm{sgn}(\mathbf{n}_s\mathbf{e}_{k_0}).$$

Thus, one can see that the contribution of the shadowing stationary points is equal (correct to the sign) to the field value at the shadowing point and can differ from it in sign if the projection of the normal to the surface at the shadowing point onto the vector of the incident wave is positive. This occurs, for example, for the singly shadowed points of the surface.

The situation described above explains the origin of the difference between the physical picture of the wavefield propagation, which occurs without penetration of the field through a scattering surface with perfect boundary conditions, and exact boundary integral equations (2), which do contain such a contribution. This contribution proves to be completely cancelled in the exact solution of integral equation (2). The mechanism of this cancellation is evident from the aforementioned geometrical optics estimate of the contribution made by the shadowing points. However, in the numerical calculations, because of the finite accuracy of the approximations used, the contribution of the field propagating beyond the reflecting boundary ceases to be completely cancelled, which leads to unstable and even divergent solutions.

Thus, it becomes necessary to apply the regularization of the initial integral equations to eliminate the contribution made by the mutually shadowed points of the surface. Mathematically, such a regularization can be constructed as follows [7–13]. For simplicity, we consider the case of a convex body, so that, when a plane wave is incident on it, only singly shadowed points of its surface are present.

Let us represent Eqs. (2) in the operator form

$$V = 2V_0 + LV, \quad (2c)$$

where L is the integral operator, V_0 is the field produced by the external source on the surface under consideration, and V is the desired field or its normal derivative on the surface.

We formally divide the field of the surface source generated by the plane wave in two parts in such a way that V_0^+ is equal to the field of the incident wave on the illuminated part of the surface and to zero on the shadowed part of the surface, while V_0^- is equal to the field of the incident wave on the shadowed part of the surface and to zero on the illuminated part. In this case, the following relation is evidently valid:

$$2V_0 = 2V_0^+ + 2V_0^-. \quad (13)$$

First, we show how, in the geometrical optics approximation, from Eq. (2c) we obtain a physically evident result: the field on the shadowed part of the surface is equal to zero.

Substituting Eq. (13) in Eq. (2c) and performing a single integration, we obtain

$$V = 2V_0^+ + 2V_0^- + L2V_0^+ + L2V_0^- + L^2V. \quad (13a)$$

Using the geometrical optics relation (17), which, in terms of the new notation, takes the form

$$L2V_0^+ = -2V_0^-, \quad (14)$$

we represent Eq. (13a) as

$$V = 2V_0^+ + L(2V_0^- + LV).$$

The subsequent iterations of this equation can be easily performed, because, at each iteration, the contributions of the shadowed and shadowing points are cancelled, and, after the nth iteration, we obtain

$$V = 2V_0^+ + L^n(2V_0^- + LV).$$

Assuming that the operator L is a compression operator (to a small extent at least), we find that the following relation is valid in the limit $n \longrightarrow \infty$:

$$V = 2V_0^+,$$

which corresponds to the conventional Kirchhoff approximation in the geometrical optics approximation.

Now, from the integral operator L, we formally separate the part $\bar{L}$ corresponding to the geometrical optics contribution over the illuminated region: $L = \tilde{L} + \bar{L}$, where $\tilde{L}$ is the operator associated with the diffraction. Then, at the first iteration with respect to the scattering multiplicity, we have

$$V = 2V_0^+ + 2V_0^- + \bar{L}2V_0^+ + \tilde{L}2V_0^+ + L2V_0^- + L^2V. \quad (15)$$

Since the contribution of the shadowing points and the geometrical-optics contribution of the incident field in the shadowed region cancel each other [5], we obtain

$$\bar{L}2V_0^+ = -2V_0^-. \tag{16}$$

Simplifying Eq. (21), we represent it in the form

$$V = 2V_0^+ + \tilde{L}2V_0^+ + L(2V_0^- + LV).$$

Integrating this equation once again, we obtain

$$\begin{aligned} V = {} & 2V_0^+ + \tilde{L}2V_0^+ + L(2V_0^- + L2V_0^+) \\ & + L^2\tilde{L}2V_0^+ + L^2(2V_0^- + LV). \end{aligned} \tag{17}$$

Taking into account that, according to condition (22), we have

$$2V_0^- + L2V_0^+ = \tilde{L}2V_0^+,$$

we reduce Eq. (23) to the form

$$V = 2V_0^+ + \sum_{i=0}^{n} L^i\tilde{L}2V_0^+ + L^n(2V_0^- + LV),$$

which is valid for an arbitrary nth iteration. Again assuming that the operator L is a compression operator, for an infinite number of iterations we obtain

$$V = 2V_0^+ + \sum_{i=0}^{\infty} L^i\tilde{L}2V_0^+. \tag{18}$$

Thus, according to Eq. (18), the solution to initial problem (2c) can be represented as the sum

$$V = 2V_0^+ + V_1, \tag{19}$$

where V_1 denotes the sum of an infinite series. This sum itself can be obtained as a formal solution to the integral equation

$$V_1 = \tilde{L}2V_0^+ + LV_1, \tag{20}$$

which differs from initial equation (2c) in only the form of the inhomogeneous term, in which the field incident on the illuminated part of the surface is integrated by the diffraction operator $\tilde{L}$ and which, therefore, has a certain smallness compared to the initial incident field V_0^+.

Then, using the similarity of Eqs. (2c) and (20) and taking into account that the operators L and $\tilde{L}$ are linear, the solution to Eq. (20) can be sought in a form analogous to that of the source, namely,

$$V_1 = \tilde{L}\tilde{V}_1.$$

If we assume that the operators L and $\tilde{L}$ commute, Eq. (20) can be reduced to initial equation (2c) for the function $\tilde{V}_1$, and this equation, in its turn, can also be regularized. Thus, by repeatedly applying the regularization described above, solution (19) can be represented in the form of a series:

$$\begin{aligned} V &= 2V_0^+ + \tilde{L}2V_0^+ + \tilde{L}^2 2V_0^+ + \tilde{L}^3 2V_0^+ + \ldots \\ &= 2V_0^+ + \sum_{n=1}^{\infty} \tilde{L}^n 2V_0^+, \end{aligned}$$

which is a formal solution to the integral equation

$$V = 2V_0^+ + \tilde{L}V. \tag{21}$$

Hence, we have shown that initial equation (2c) containing the geometrical optics contribution of the mutually shadowed points of the surface can be transformed by the mathematically exact regularization procedure into a form that completely excludes the geometrical optics contribution of the mutually shadowed points. In this case, in the zero approximation, the solution to this equation is equivalent to the Kirchhoff approximation.

The only considerable disadvantage of regularized representation (19)–(21) is the insufficiently clear definition of the diffraction operator $\tilde{L}$: it is determined as the part that remains after the subtraction of the geometrical optics contribution. This definition allows no constructive approach to solving Eq. (21).

To find a constructive approach to the regularization of Eq. (2c) on the basis of geometrical optics relation (14), we transfer the definiteness in the field separation to the operator. For this purpose, we separate the integral operator L into two parts corresponding to the illuminated L_0^+ and shadowed L_0^- parts of the surface: $L = L_0^+ + L_0^-$. We also represent the field incident on the surface from the external source $2V_0$ as a sum of two fields, $2V_0 = 2V_0^+ + 2V_0^-$, in such a way that the geometrical optics condition of type (14) or (16) is satisfied:

$$L_0^+ 2V_0^+ = -2V_0^-. \tag{22}$$

This condition now serves for the determination of the functions $2V_0^+$ and $2V_0^-$ by the quite clearly defined operator L_0^+. Evidently, in the geometrical optics limit, the functions $2V_0^+$ and $2V_0^-$ correspond to the incident field on the illuminated $2V_0^+$ and shadowed $2V_0^-$ parts of the surface. In the general case, relation (22) is equivalent to the integral equation with a stable clearly defined operator L_0^+:

$$2V_0^+ = 2V_0 + L_0^+ 2V_0^-. \tag{23}$$

We repeat the above regularization procedure with allowance for relation (22) and with the new under-

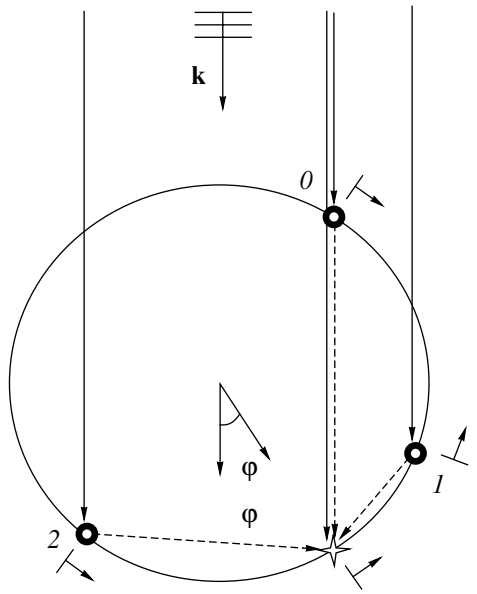

Fig. 1. Geometry of the problem for a circular cylinder. The numbered circles denote the points of stationary phase, which have the domains of existence (*0*) $\varphi \in [\pi/2, \pi]$, (*1*) $[\pi/3, \pi/2]$, and (*2*) $[5/3\pi, 2\pi]$. The arrows indicate the directions of their motion with the displacement of the point at which the field is considered.

standing of the functions $2V_0^+$ and $2V_0^-$. Integrating initial equation (2c), we obtain

$$V = 2V_0^+ + 2V_0^- + L_0^+ 2V_0^+ + L_0^- 2V_0^+ + L2V_0^- + L^2 V. \quad (24)$$

With allowance for relation (22), part of the terms in Eq. (24) are mutually cancelled, and Eq. (31) can be represented as

$$V = 2V_0^+ + L_0^- 2V_0^+ + L(2V_0^- + LV). \quad (25)$$

Continuing the iteration process in the same way as was done for Eq. (22), solution (25) can be represented in a form similar to Eq. (26):

$$V = 2V_0^+ + V^1, \quad (26)$$

where V^1 is the solution to the integral equation

$$V^1 = L_0^- 2V_0^+ + LV^1. \quad (27)$$

The set of integral equations (23), (26), and (27) is fully equivalent to initial equation (2c). Formally, Eq. (27) has the same form as Eq. (2c) and could be regularized in the same way as was done for Eq. (20). However, another form of the initial field for V^1, namely, $L_0^- 2V_0$, complicates the procedure because of the noncommutativity of the operators L and L_0^- and will not be discussed in this paper. Nevertheless, as will be shown below, the zero approximation $2V_0^+$ satisfying Eq. (23) already adequately approximates the exact solution to the problem. The next correction can be obtained by retaining the inhomogeneous term as the estimate of the solution to Eq. (27), $V^1 = L_0^- 2V_0^+$, so that the solution (26) is represented as

$$V = 2V_0^+ + L_0^- 2V_0^+.$$

To test the general regularization method, we used the problem of plane-wave scattering by a circular cylinder, for which an analytical solution exists in the form of a Rayleigh series [3]:

$$V(\varphi) = \sum_{n=-\infty}^{\infty} \frac{2(-i)^{n-1}}{\pi a} \frac{e^{-in\varphi}}{H_n^{(2)}(ka)} \quad (28a)$$

for the Dirichlet boundary condition and

$$U(\varphi) = -\sum_{n=-\infty}^{\infty} \frac{2(-i)^{n-1}}{\pi ka} \frac{e^{-in\varphi}}{H_n^{(2)'}(ka)} \quad (28b)$$

for the Neumann boundary condition.

In this case, Eqs. (2a) and (2b) have the form

$$V(\varphi) = 2V_0(\varphi) - \frac{i}{4}\int_0^{2\pi} d\varphi' V(\varphi') H_1^{(2)}(z) z, \quad (29a)$$

$$U(\varphi) = 2U_0(\varphi) + \frac{i}{4}\int_0^{2\pi} d\varphi' U(\varphi') H_1^{(2)}(z) z, \quad (29b)$$

where the initial fields are expressed as

$$U_0 = \exp(ika\cos\varphi), \quad V_0 = ik\cos\varphi\exp(ika\cos\varphi)$$

and the distance between two points of the surface is denoted as

$$z(\varphi', \varphi) = 2ka\left|\sin\left(\frac{\varphi' - \varphi}{2}\right)\right|.$$

The angles φ and φ' are conveniently measured starting from the center of the most shadowed point of the surface that is to the rear of the incident wave (Fig. 1). Note that, for a circular cylinder, three points of stationary phase are present (see Fig. 1): one shadowing point with the domain of existence $\varphi \in [\pi/2, \pi]$ and two reflecting points with the domains of existence $\varphi \in [\pi/3, \pi/2]$ and $\varphi \in [5/3\pi, 2\pi]$.

The truncated equations for $2V_0^+$ and $2U_0^+$ in terms of this notation have the form

$$V_0^+(\varphi) = 2V_0(\varphi) - \frac{i}{4}\int_{\pi/2}^{3\pi/2} d\varphi' V_0^+(\varphi') H_1^{(2)}(z) z, \quad (30a)$$

$$U_0^+(\varphi) = 2U_0(\varphi) + \frac{i}{4}\int_{\pi/2}^{3\pi/2} d\varphi' U_0^+(\varphi') H_1^{(2)}(z) z. \quad (30b)$$

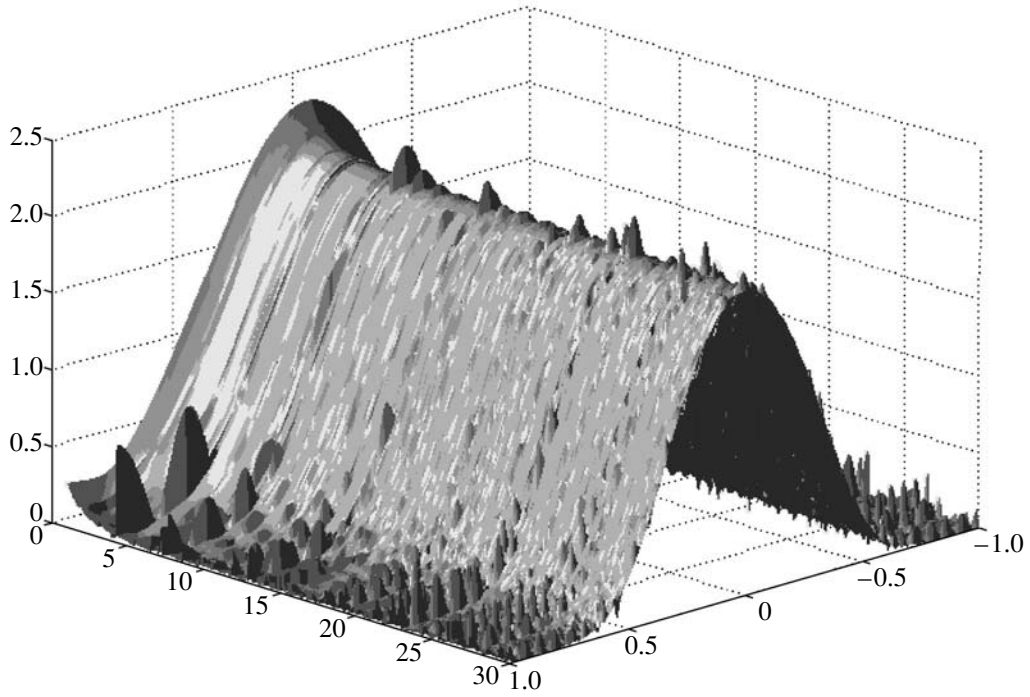

Fig. 2. Angular (in radians) distribution of the currents over the surface of a circular cylinder with the Dirichlet boundary condition for different wavelengths from the interval $ka \in (0.5, 30)$. The distribution is obtained by solving the nonregularized boundary integral equation with the number of discretization points $N = 300$.

Equations (29) and (30) were solved numerically by the finite-difference approximation of these equations, replacing the integral term by the corresponding integral sum over N points. The resulting set of algebraic equations with the dimensions $N \times N$ can be solved by, e.g., the Gauss method.

Figure 2 shows the solution to integral equation (29a) for the normal derivative of the field (below, for brevity, we consider the surface currents by analogy with the corresponding electromagnetic problem) in the problem of plane-wave diffraction by a circular cylinder with the Dirichlet boundary condition. The solution is calculated at $N = 300$, without using the regularization, for different values of the dimensionless wave number ka in the interval from 0.5 to 30.

One can see that, near the natural resonance frequencies of the cylinder, for the internal problem we have a set of wavelengths or frequencies near which the use of the initial nonregularized equation leads to considerable deviations of the numerical solution from the smooth exact solution represented by the Rayleigh series. If, on the basis of such numerical results, we try to calculate the diffraction of a pulsed field by the cylinder by taking the Fourier integral with respect to frequency, we arrive at a result far from reality. This occurs because Eq. (29a) contains the contribution of the resonance waves of the internal problem, which should be cancelled in the exact solution, while, in any numerical calculation, the parasitic contribution proves to be considerable because of the finite accuracy.

The regularization method was tested by the examples of problems, with the Dirichlet and Neumann boundary conditions, both near the resonances and away from them. For the Dirichlet condition, one of the resonances corresponds to $ka = 5.33$ and, as a close nonresonance value, we used $ka = 5.81$. For the Neumann condition, as a resonance value we chose $ka = 7.01$ and, as a close nonresonance value, $ka = 6.8$.

Figures 3a and 3b show the direct solution to Eq. (29a) and the approximation $2V_0^+$ obtained by solving truncated equation (30a) in comparison with the exact solution in the form of Rayleigh series (28a) (the dashed line) for the nonresonance wavelength $ka = 5.81$. In Fig. 3a, one can see a full coincidence of the solution to the initial equation with the Rayleigh series. The solution to truncated equation (30a) for $2V_0^+$ (Fig. 3b) does not exhibit such a good coincidence with the exact solution in the form of the Rayleigh series but still provides a quite acceptable approximation for the surface currents, especially in the light-shadow region.

Figures 4a and 4b show similar solutions for surface currents for the resonance case with a close wavelength $ka = 5.33$. In this case (as is seen from Fig. 4a), the solution to the initial integral equation qualitatively differs from the exact solution in the form of the Rayleigh series. Figure 4b shows the approximation $2V_0^+$, which,

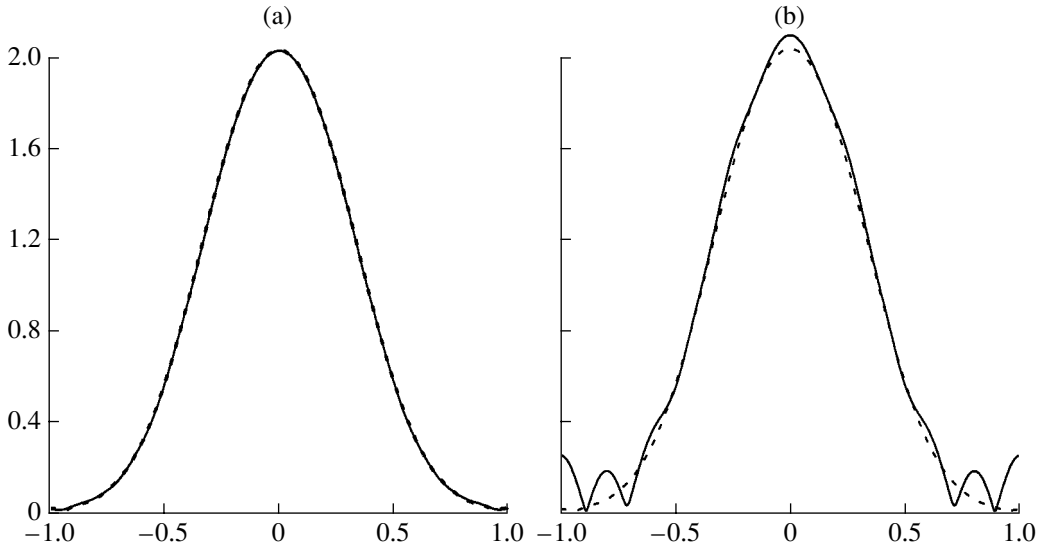

Fig. 3. Angular (in radians) distribution of the currents over the surface of a circular cylinder with the Dirichlet boundary condition when the currents are excited by a nonresonance plane incident wave with $ka = 5.81$. The dashed lines show the exact solution obtained by summation of Rayleigh series (28a). The solid lines show (a) the zero approximation $2V_0^+$ obtained by numerically solving regularized (truncated) integral equation (30a) and (b) the numerical solution to initial integral equation (29a).

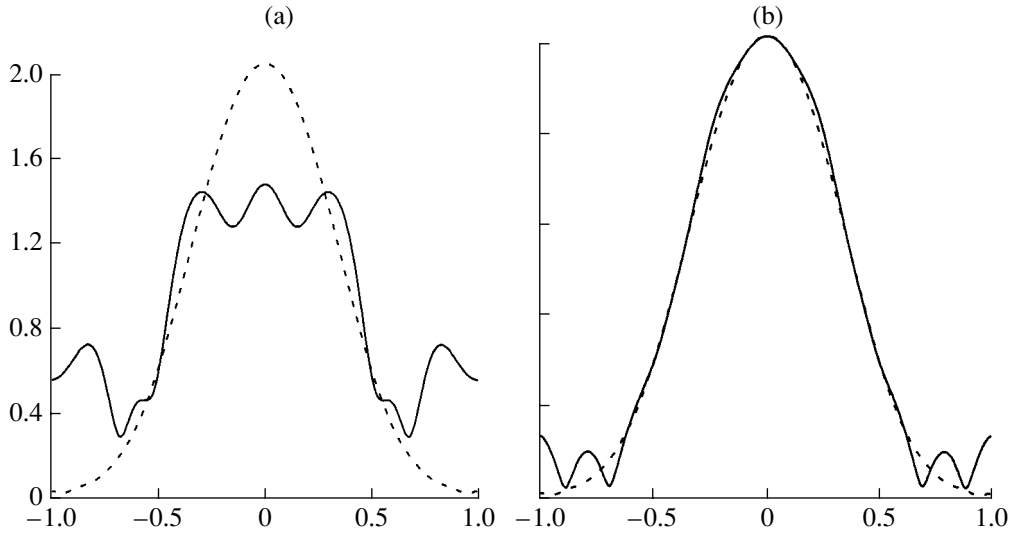

Fig. 4. The same as in Fig. 3 but for the resonance case $ka = 5.33$.

being the solution to truncated integral equation (30b), practically repeats the corresponding result obtained for the nonresonance case (see Fig. 3b).

Similar results for a cylinder with the Neumann boundary condition are shown in Figs. 5 and 6. Again, one can see that the solution to initial integral equation (29b) proves to be unstable in the vicinity of the internal resonance of the cylinder, while the zero approximation $2V_0^+$ of the regularized equation is stable to resonance and, in this sense, is a uniform approximation to the exact solution.

Note that, for the Neumann boundary condition, the accuracy of the zero approximation $2V_0^+$ proves to be somewhat inferior to that in the case of the Dirichlet boundary condition. This occurs because, at the boundary of the light-shadow region by which the initial integral operator L is truncated, the incident wave field tends to zero for the Dirichlet boundary condition and to a constant equal to two for the Neumann boundary condition. Therefore, with the truncation of the integral operator, a more considerable diffraction contribution from the boundary of the integration region is retained in the case of the Neumann boundary conditions.

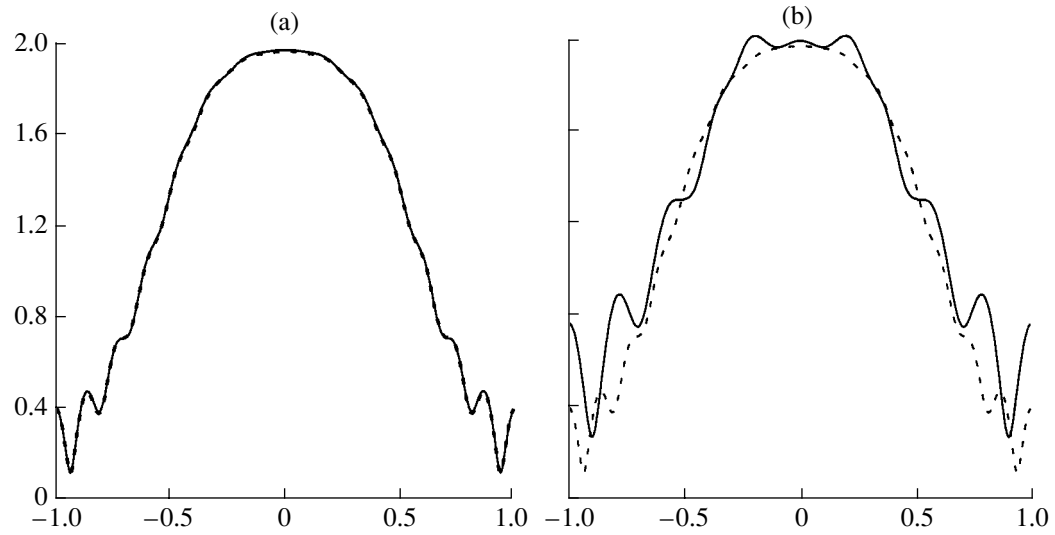

Fig. 5. Angular (in radians) distribution of the currents over the surface of a circular cylinder with the Neumann boundary condition when the currents are excited by a nonresonance plane incident wave with $ka = 6.8$. The dashed lines show the exact solution obtained by summation of Rayleigh series (28b). The solid lines show (a) the zero approximation $2V_0^+$ obtained by numerically solving regularized (truncated) integral equation (30b) and (b) the numerical solution to initial integral equation (29b).

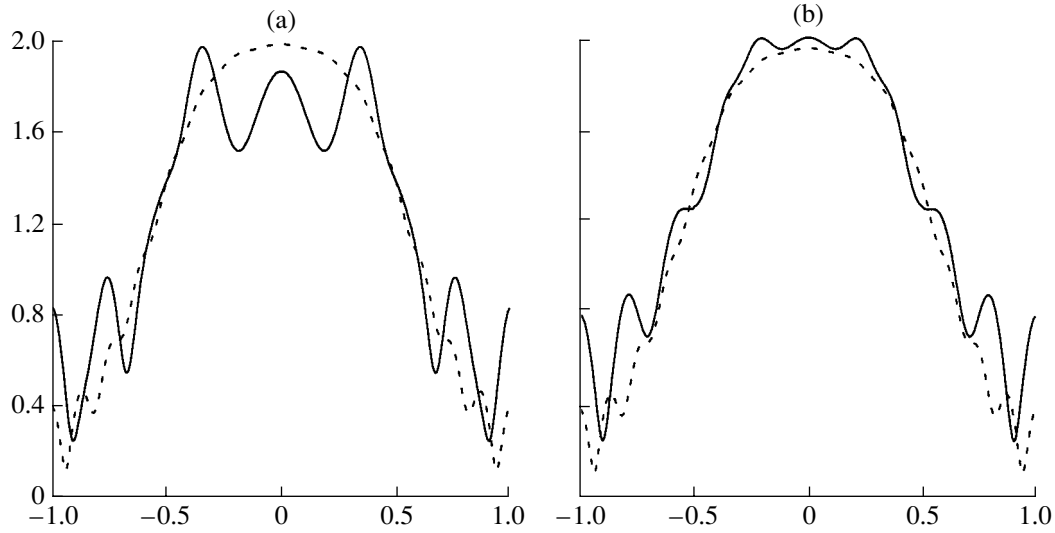

Fig. 6. The same as in Fig. 5 but for the resonance case $ka = 7.01$.

Now, let us show that the splitting of solution (26) is exact. For this purpose, we consider the numerical solution of remaining equation (27), which, for the cylinder, takes the form

$$V^1(\varphi) = \frac{i}{4}\int_{-\pi/2}^{\pi/2} d\varphi' 2V_0^+(\varphi')H_1^{(2)}(z)z - \frac{i}{4}\int_{\pi/2}^{3\pi/2} d\varphi' V^1(\varphi')H_1^{(2)}(z)z, \tag{31a}$$

$$V^1(\varphi) = \frac{i}{4}\int_{-\pi/2}^{\pi/2} d\varphi' 2U_0^+(\varphi')H_1^{(2)}(z)z + \frac{i}{4}\int_{\pi/2}^{3\pi/2} d\varphi' U^1(\varphi')H_1^{(2)}(z)z. \tag{31b}$$

In Figs. 7a and 7b, the dashed lines show the difference between the exact solution given by the Rayleigh series for the surface currents in the Dirichlet problem and the solution to the truncated equation for V_0^+ for the

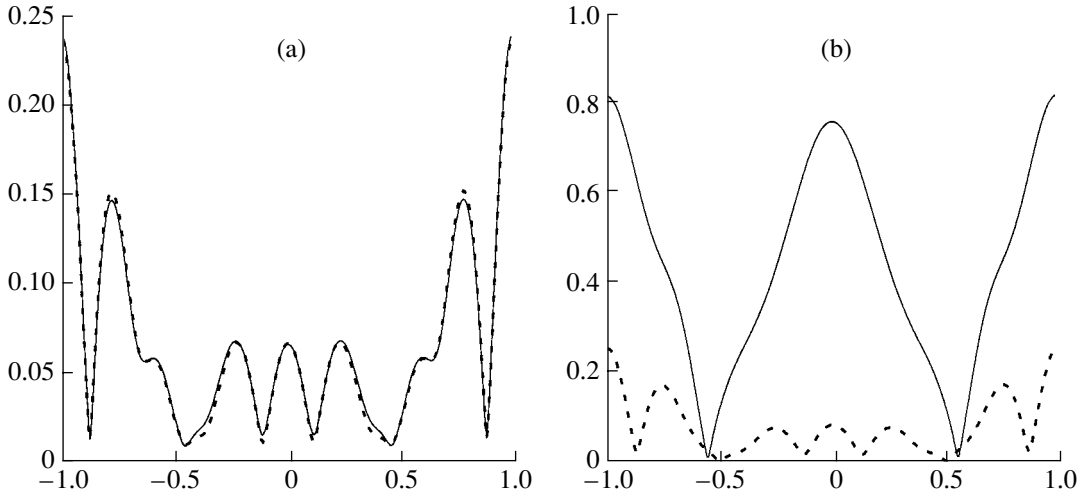

Fig. 7. Angular (in radians) distribution of the correction currents V^1 (Eq. (39a)) (solid line) over the surface of a circular cylinder with the Dirichlet boundary conditions under the excitation by the (a) nonresonance $ka = 5.81$ and (b) resonance $ka = 5.33$ plane incident waves. The dashed lines show the difference between the exact solution to the problem in the form of Rayleigh series (28a) and the regularized approximation $2V_0^+$ (Eq. (29a)) shown in Figs. 3b and 4b.

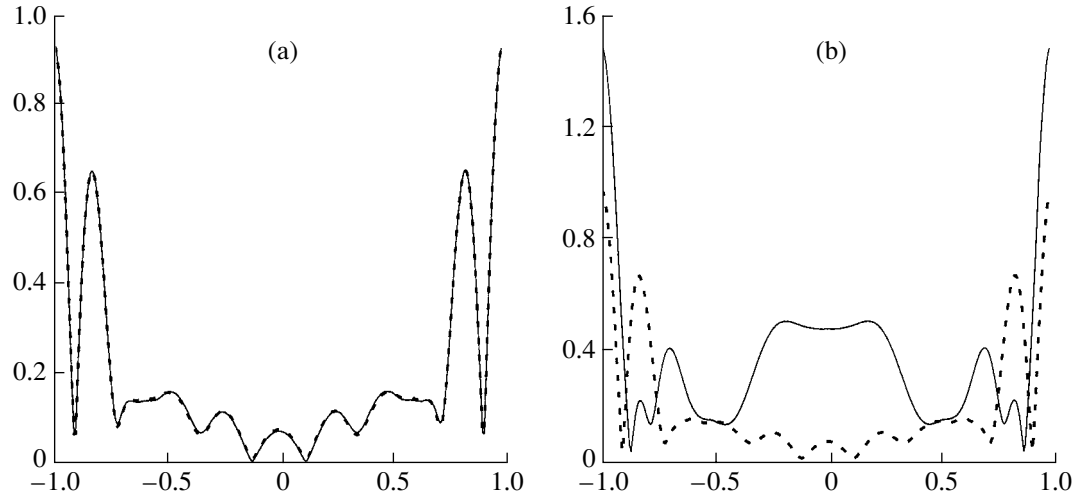

Fig. 8. Angular (in radians) distribution of the correction currents U^1 (Eq. (39b)) (solid line) over the surface of a circular cylinder with the Neumann boundary conditions under the excitation by the (a) nonresonance $ka = 6.80$ and (b) resonance $ka = 7.01$ plane incident waves. The dashed lines show the difference between the exact solution to the problem in the form of Rayleigh series (36b) and the regularized approximation $2U_0^+$ (Eq. (38b)) shown in Figs. 5b and 6b.

same values of the resonance and nonresonance wavelengths. The solid lines in these figures show the direct numerical solution to Eq. (39a).

Figures 8a and 8b show the corresponding results for the problem with the Neumann boundary condition.

From the figures presented in this paper, it follows that, in the nonresonance case, the solution to Eq. (31) for V^1 yields the correction that should be added to obtain the exact solution. In the resonance case, all factors related to the instability of the initial integral operator are retained, which leads to a considerable deviation of the numerical solution for V^1 from the exact solution. It should also be noted that, in all cases, the sum of the solutions, $V = 2V_0^+ + V^1$, reproduces with a machine accuracy the result of the direct numerical solution of initial integral equation (29).

Thus, in this paper, we have shown that when, in the presence of shadowed points of the surface, the numerical solution of the initial boundary integral equation proves to be unstable in the vicinity of the resonance wavelengths, it is possible, in the framework of exact mathematical procedures, to transform the initial inte-

gral equation into an equivalent set of two integral equations whose form is such that already the stable solution to one of them reproduces with fair accuracy the solution to the exact problem. The second of these equations structurally coincides with the initial one and can also be regularized. The details arising in this situation will be considered in a future paper.

REFERENCES

1. D. Colton and R. Kress, *Integral Equation Methods in Scattering Theory* (Wiley, New York, 1984; Mir, Moscow, 1987).
2. V. F. Apel'tsin and A. G. Kyurkchan, *Analytical Properties of Wave Fields* (Mosk. Gos. Univ., Moscow, 1990) [in Russian].
3. R. B. Vaganov and B. Z. Katsenelebaum, *Fundamentals of the Diffraction Theory* (Nauka, Moscow, 1982) [in Russian].
4. P. M. Morse and H. Feshbach, *Methods of Theoretical Physics* (McGraw-Hill, New York, 1953; Inostrannaya Literatura, Moscow, 1958 and 1959), Vols. 1 and 2.
5. E. G. Liszka and J. J. McCoy, J. Acoust. Soc. Am. **71**, 1093 (1982).
6. G. A. Korn and T. M. Korn, *Mathematical Handbook for Scientists and Engineers*, 2nd ed. (McGraw-Hill, New York, 1968; Nauka, Moscow, 1984).
7. G. A. Maksimov and D. N. Lesonen, in *Proceedings of Scientific Session MIFI-99* (Mosk. Inzh.–Fiz. Inst., Moscow, 1999), Vol. 1, p. 153.
8. G. A. Maksimov and D. N. Lesonen, in *Proceedings of XI Session of the Russian Acoustical Society* (GEOS, Moscow, 2001), Vol. 1, p. 189.
9. G. A. Maksimov and D. N. Lesonen, in *Proceedings of Scientific Session MIFI-2002* (Mosk. Inzh.–Fiz. Inst., Moscow, 2002), Vol. 5, p. 76.
10. G. A. Maksimov and D. N. Lesonen, in *Acoustics of the Ocean: Proceedings of IX Scientific School–Seminar of Academician L. M. Brekhovskikh Combined with XII Session of the Russian Acoustical Society* (GEOS, Moscow, 2002), p. 241.
11. G. A. Maximov and D. N. Lesonen, in *Official Publication of the Forum Acusticum Sevila 2002*, Special Issue of Rev. Acust. **33** (2002), NUM-08-002-IP. ISBN: 84-87985-07-6.
12. G. A. Maksimov and D. N. Lesonen, in *Proceedings of Scientific Session MIFI-2003* (Mosk. Inzh.–Fiz. Inst., Moscow, 2003), Vol. 5, p. 56.
13. G. A. Maximov and D. N. Lesonen, in *Proceedings of the Tenth International Congress on Sound and Vibration* (Int. Inst. of Acoustics and Vibration, Stockholm, 2003), CD, Vol. 4, P-150, p. 1961.

Translated by E. Golyamina

Acoustical Physics, Vol. 51, No. 3, 2005, pp. 338–346. Translated from Akusticheskiĭ Zhurnal, Vol. 51, No. 3, 2005, pp. 402–411.

Luminescence Induced by Spherically Focused Acoustic Pulses in Liquids

G. N. Sankin

Lavrent'ev Institute of Hydrodynamics, Siberian Division, Russian Academy of Sciences, pr. Akademika Lavrent'eva 15, Novosibirsk, 630090 Russia

e-mail: sankin@hydro.nsc.ru

Received May 15, 2003

Abstract—The determination of the phase of the bubble oscillation at the instant of light emission, which is a key issue for understanding the origin of cavitation luminescence of liquids, is discussed. The observation of luminescence in the course of the nucleation and growth of a bubble up to its collapse is performed in a bipolar wave consisting of a compression phase followed by a rarefaction phase in the regime of a two-fraction bubble cluster formation. The space–time distributions of the luminescence intensity and pressure and the dynamics of the cluster in water and a glycerin solution are investigated at the early stage of cavitation. A correlation between the maximal density of light flashes and the positive pressure pulses in the field of superposition of the initial and secondary cavitation compression waves is revealed. It is shown that the spherical focusing of acoustic pulses both away from the boundaries of the liquid and near its free surface makes it possible to compare the luminescence intensities for different rates of the pressure decrease. *© 2005 Pleiades Publishing, Inc.*

INTRODUCTION

Cavitation luminescence in liquids is the subject of numerous publications [1]. It is well known that, when the collapse occurs near a solid boundary or a free boundary of a liquid, the spherical shape of a bubble is distorted [2, 3] and its luminescence weakens or completely disappears [4, 5]. The boundaries complicate the pattern of the wave motion in the liquid, which affects the intensity of the luminescence. To eliminate the undesirable consequences of these factors, various focusing systems that form convergent pulses or quasi-stationary acoustic waves away from the boundaries of the liquid are used [6, 7].

Quasi-stationary tests do not make it possible to monitor the dynamics of sonoflashes in correlation with the bubble dynamics. Therefore, the issue of the phase of bubble oscillations and the moments of light emission remains open to discussion [1, 8]. This problem may be solved by using the excitation of luminescence of liquids in a pulse mode corresponding to the first period of an ultrasonic wave [9]. With this approach, it is possible to observe the whole dynamics of the cavitation process and the luminescence in the course of the nucleation, growth, and collapse of bubbles [10]. The position of the focus of negative pressure, at which, according to theoretical estimates, the coefficient of increase of the gas bubble radius reaches its maximum [11], is essential. From the results of previous studies [10, 12, 13], it follows that the beginning of luminescence of a liquid in an acoustic field correlates with the phase of rarefaction and with the process of cavitation rupture of the liquid.

At the reflection of a wave from a free surface, owing to the inversion of the wave amplitude, it is possible to use not only the energy of the rarefaction wave but also the energy of the compression pulse for producing cavitation, which in this case mainly occurs in the near-surface region. The rate of the pressure decrease at the reflection of a shock wave (SW) considerably increases compared to the case of focusing within the bulk of the liquid. The number of bubbles formed at such a cavitation is greater than that at the cavitation in the liquid bulk. At the reflection of an SW from a cylindrical or flat radiator, the formation of a highly disperse foamy medium is possible [14, 15].

In the case of an SW reflected from a free surface, the amplification of collective processes (including the luminescence) connected with cavitation is achieved [10], which, according to [16], may influence the intensity of the emission spectrum in the UV region. These preliminary studies showed that, at the reflection of an SW from a free surface, the detected amount of light is considerably greater than that in the case of the focusing within the bulk of the liquid.

In the present paper, the early stage of the luminescence of a liquid is investigated with an acoustic pulse produced by a radiator in the form of a spherical segment and focused at the region near the free surface of the liquid.

EXPERIMENTAL

The cavitation was produced by an electromagnetic generator of SWs [17] with a radiator mounted at the bottom of a container (Fig. 1). The radiator shaped like

1063-7710/05/5103-0338$26.00

a spherical segment had an aperture $D = 70$ mm and a focal length $F = 55$ mm. For studying the dynamics of the cavitation processes, high-speed filming was performed by an Imacon 468 camera (DRS Hadland Ltd, 8 frames, an exposure time of 10 ns) through glass windows of the container by the technique described in [18]. The design of the container excluded the light emission from the radiator and joints under the pulsed loading. The experiments were carried out at room temperature in distilled water and in a 10% glycerin solution, which exhibits a brighter cavitation luminescence [19].

The intrinsic luminescence of the cavitation zone was observed using an R5600U-06 photomultiplier tube (PMT) (Hamamatsu, with a spectral range of 260–530 nm, a time resolution of 5.8 ns in the output circuit, and a photocathode diameter of 8 mm). To measure the space–time distribution of luminescence of the region adjacent to the radiator axis (the z axis), the image formed in the focal area of the SW radiator was transferred with a magnification K_{opt} by using a 50-mm lens L_1 to a nontransparent screen with a rectangular opening of height D_v and width D_h, behind which the PMT was placed. The screen, together with the PMT, could be moved by a fine-adjustment screw along the z' coordinate parallel to the radiator axis. The size of the opening in the screen and the magnification of the optical system are given in Table 1. The coordinates of the point of observation z and z' are related as

$$z' = zK_{opt}. \quad (1)$$

Thus, the light flashes observed using the PMT refer to the part of the compression wave with the duration

$$\Delta\tau = D_v/(K_{opt}c) \quad (2)$$

(see Table 1), where c is the speed of sound in the liquid. The optical system was dimmed; the dark signal was equal to 3×10^3 pulses per second.

The time count was taken from the instant of the current discharge of the generator. For synchronization, we used the antenna signal induced by the electromagnetic field of the current in the coil. The triggering of the oscilloscope, flash lamp, and camera was performed by using a DG 535 trigger-pulse generator (Stanford Research Systems). The signals were recorded by TDS 784A digital oscilloscopes (Tektronix, an analog input of 1 GHz, a sampling frequency of 4 GS/s, 8 bit).

RESULTS AND DISCUSSION

Cavitation

To obtain a detailed picture, high-speed filming of the hydrodynamic processes was used. The case of focusing of the wave at the area near the free surface, which was perpendicular to the generator axis, was studied [20]. With the aforementioned geometry of the radiator, the focus of the rarefaction wave was 5 mm closer to the radiator than the focus of the compression wave [17]. For reducing the influence of the free surface on the cavitation cluster at the focus of the rarefaction wave, the free surface was spaced from the radiator at a distance equal to or greater than the focal length for the compression wave. At the early stage (<7 μs), this influence was excluded due to the finite velocity of sound propagation (~1.5 mm/μs), because, in this case, the distance between the liquid boundary and the center of the cluster exceeded 5 mm.

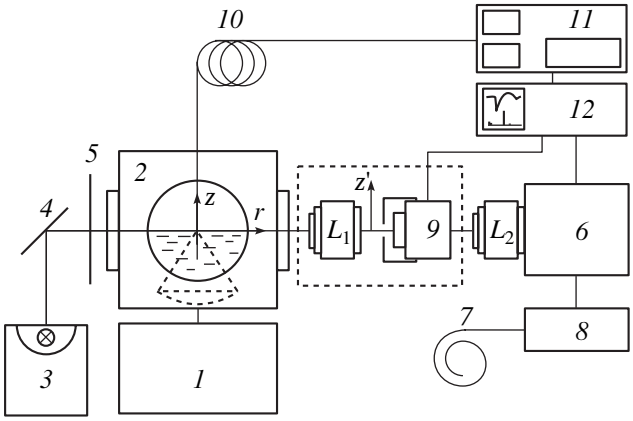

Fig. 1. Schematic diagram of the experiment (the part within the dashed line was installed when necessary): (*1*) generator of current pulses, (*2*) container, (*3*) flash lamp, (*4*) mirror, (*5*) depolished glass, (*6*) Imacon 468 camera, (*7*) antenna, (*8*) generator of delayed pulses, (*9*) photomultiplier tube with a diaphragm, (*10*) light guide, (*11*) FOPH 300 pressure gauge, (*12*) TDS 784A oscilloscope, and (L_1, L_2) lenses.

Figure 2 illustrates the overall picture of the cavitation phenomenon for the pressure at the radiator $p_s = 9.7$ MPa. In this experiment, the liquid surface was at the focal plane of the generator at $z = 0$ mm. The initial pulse produces the first cavitation cloud (*4*) extended along the axis (in the form of an ellipse). As is seen from the figure, the center of the cloud is 5–10 mm below the focus, which corresponds to the amplitude distribution of the negative pressure phase measured earlier [17]. For the case of cavitation far from the boundary of the liquid, the dynamics of the cluster (*4*), whose form mainly depends on the negative pressure component in the initial wave, was described in [21]. In the case under consideration, i.e., with a free surface, its dynamics is almost the same.

The cavitation of the liquid also occurs in the reflected wave, the pressure in which is inverted. The cavitation zone is located directly under the free surface

Table 1. Resolution of the optical system

No.	Liquid	K_{opt}	D_v, mm	D_h, mm	$\Delta\tau$, μs
1	Water	0.8	1.0	2.0	0.8
2	10% glycerin solution	0.9	1.2	1.3	0.9

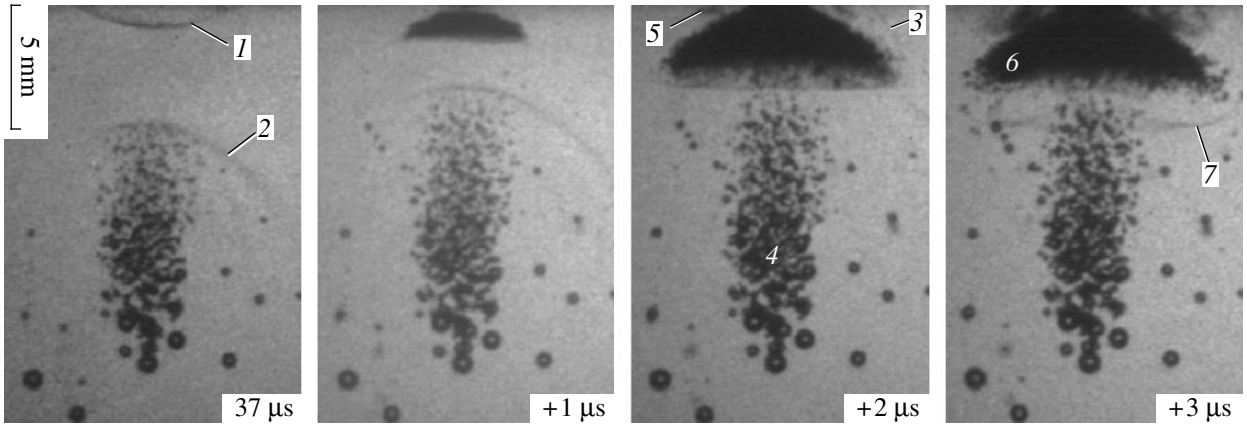

Fig. 2. Cavitation induced by a focused shock wave in water near the free surface ($z = 0$) for $p_s = 7.7$ MPa. The free surface coincides with the top edge of the frame. Numerical designations are explained in the text.

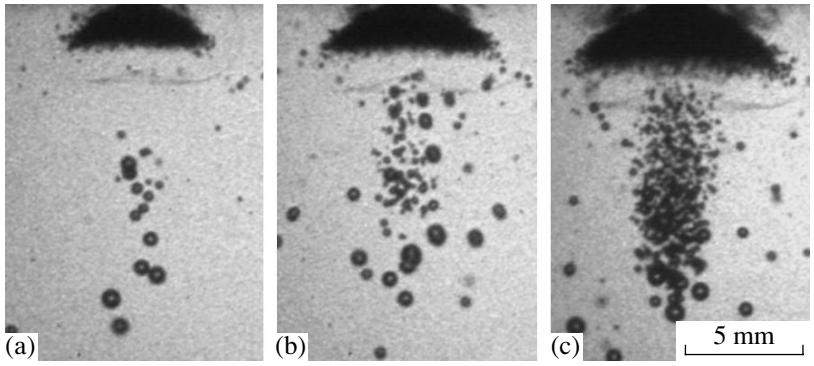

Fig. 3. Photographs of cavitation near the free surface ($z = 0$ mm) for different pressures at the radiator output: p_s = (a) 5.9, (b) 7.7, and (c) 9.7 MPa.

and has the form of a conic foglike cloud (*6*). The top of the cone is surrounded by a cavitation ring (*5*). The filmogram shows that the area occupied by the near-surface cloud varies with time, but no collapse to an unmeasurable size is observed [22].

The intense cavitation observed in the cloud (*6*) is the result of the combined action of the compression and rarefaction half-waves at their interference. Therefore, the height h of the cloud is approximately equal to the half-wavelength (see, e.g., [23]):

$$h = c(t_1 - t_2)/2, \quad (3)$$

where t_1 and t_2 are the times of arrival of fronts 1 and 2 at the focus.

It is established that the form of this almost conic cloud depends on both the pressure amplitude at the radiator output (Fig. 3) and the position of the free surface relative to the radiator (Fig. 4). As a rule, the maximal height h and angle 2Θ of the cone increase with the growth of the pressure amplitude at the radiator. The geometrical characteristics of the cavitation cloud under the free surface at $z = 0$ are given in Table 2.

One should also note the changes in the shape of the cloud for different depths of the radiator. As the radiator approaches the free surface, the cavitation cloud (*6*) separates into two clouds (Fig. 4a). Conversely, as the radiator moves away from the free surface, the lower cloud boundary becomes convex towards the radiator (Fig. 4c). The cause of the change in the form of the cavitation cloud is a pressure field that can be approximately evaluated by the measured pressure field in the absence of cavitation [17]. At the radiator axis, for $z = -10$ mm (below the focal point), the delay $t_1 - t_2$ between the compression wave and the rarefaction wave coming from the radiator periphery is greater than the corresponding delay at the focus. Therefore, after the reflection of the compression wave from the free surface, this wave interferes with the rarefaction wave according to Eq. (3) at a depth $h|_{z=-10\,\mathrm{mm}} > h|_{z=0}$. As a result, the pressure has two minima along the z axis,

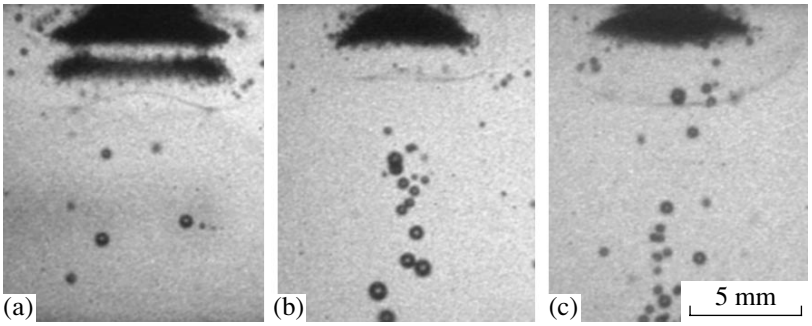

Fig. 4. Cavitation near the free surface 3 μs after the wave front has reached the free surface at p_s = 5.9 MPa for different positions of the free surface: z = (a) –10, (b) 0, and (c) + 10 mm.

and a cavitation region is formed in each of these minima, which is clearly seen in Fig. 4a.

Figure 5 shows the phase velocity of propagation of the lower edge of the cloud, v_l, which was measured from the filmogram within intervals of 100 ns. The time dependence of v_l begins from the value equal to the sound speed, then reaches its maximum (3.3 km/s for p_s = 7.7 MPa) and drops to zero, which corresponds to the terminal stage of the cluster growth. As follows from the Fig. 2, an acoustic wave whose front is clearly visible in the filmogram (*3* and *7*) propagates from the cluster (*6*).

In the process of propagation and reflection of the shock wave producing the cavitation, a considerable change in the pulse shape was observed. As in [21], we observed the so-called forced acoustic scattering waves (*2*) diverging from the elliptic cavitation cloud (*4*). The secondary acoustic compression waves (*3*, *7*) are also observed at the formation of the near-surface cluster (*6*) [24]. The source of the secondary cavitation waves (SCW) is found to be the intersection of normals to the SCW fronts and is located inside the cavitation cloud.

Luminescence

For determining the distribution of light flashes in time, the signal from the PMT was summed up. Figure 6 shows the signal of the PMT whose observation area was near the free surface. The signal was averaged over 32 frequent (of frequency 0.16 Hz) shots. Under these test conditions, the wave reached the free surface at t_0 = 35 μs. The result of addition shows that, at the early stage of luminescence, three groups of flashes with different typical intensities can statistically be distingushed within separate intervals of 34.7–35.4, 35.4–36.2, and 36.2–37.3 μs. The duration of every single flash was shorter than the time resolution of the output circuit of the PMT (5.8 ns).

The study of the dark current and the PMT operation at low illuminations suggests that the pulse intensities in the first and second groups correspond to the detection of single photons. The pulses belonging to the third group correspond to several photons reaching the PMT. The total number of photons for a flash of maximal intensity was on the order of 10^5.

In the next run of tests, the free surface of water was above the focus at z = 5 mm; i.e., a gap between the extended cloud and the conic cloud was present. In this gap, which was not distorted by cavitation, a film was shot and the pressure was measured. The results of the test are presented in Fig. 7 [20]. The filmogram (Fig. 7a) consists of two parts: the first part has eight frames and the second part has four frames.

For finding the space–time relation between the flashes and the compression waves, statistical data were collected for the time delay of every flash with every equidistant position of the slit center (D_h = 1.2 mm) corresponding to z from –5.2 to 4.4 mm; these data are presented in Fig. 7b. (Note that the true slit position z' can be computed by formula (1).) The number of the PMT pulses is presented in the form of histograms with a linear scale; the histograms are constructed on the basis of the time positions of the pulses. The time interval of the histograms is chosen to be equal to 100 ns, which is less than $\Delta\tau$ (Table 1). The pulse amplitude was not considered. For z = 4.4 mm, 78 pulses were counted. The traces of waves (*A*, *B*, and *B*') detected from filmograms and oscillograms are superimposed in the same figure for comparing the dynamics of luminescence with the pressure sign. The oscillogram of pressure measured at the focus for p_s = 5.9 MPa is shown in Fig. 7c.

As is seen, for $z > 0$, three groups of flashes are also present in the signal in this case.

The first group is presumably produced by the bubbles that remained from preceding tests, in which they

Table 2. Parameters of the near-surface cloud for z = 0

p_s, MPa	Θ	max h, mm	max v_l, m/s
3.0	65° ± 2°	1.52 ± 0.05	2270 ± 60
4.3	64° ± 2°	1.69 ± 0.05	2500 ± 60
5.9	67° ± 2°	1.96 ± 0.05	2950 ± 60
7.7	62° ± 2°	2.16 ± 0.05	3350 ± 60

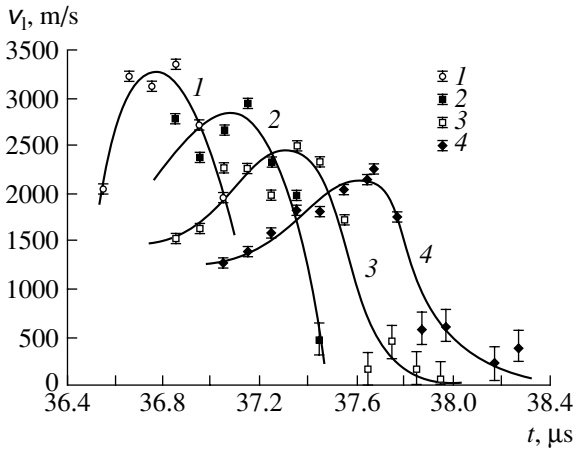

Fig. 5. Velocity of the lower edge of the near-surface cavitation cloud as a function of time for the pressure values p_s = (*1*) 7.7, (*2*) 5.9, (*3*) 4.3, and (*4*) 3.0 MPa.

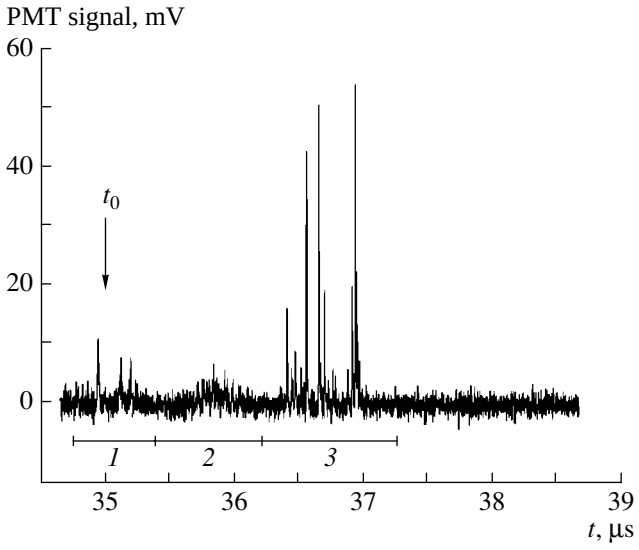

Fig. 6. Inverted signal of the photomultiplier tube averaged over 32 frequent shots (16 shots for each of the positions z = –0.6 mm and z = –1.8 mm) for p_s = 7.7 MPa in the 10% glycerin solution. Numbers *1*, *2*, and *3* indicate the group numbers, and t_0 is the time of the shock-wave front arrival at the free surface.

did not have enough time to rise to the surface or to dissolve, and that are compressed in the initial wave (*AB*). The intensity of this group of flashes, as will be seen below, increases with the decrease in the interval between tests. The second group is recorded at the moment of cavitation of the liquid. The third group of flashes corresponds to the collision of the SCW front (*B*') with the near-surface cloud. The light of this group is recorded only for several upper positions of the PMT slit because of the light reflection from the bubbles in the elliptic cavitation cloud. For the PMT positions corresponding to $z < –2.8$ mm, only two groups of flashes were detected: (i) from the remaining bubbles compressed in the *AB* wave and (ii) from the bubbles expanded in the rarefaction phase (*BB*') and compressed by the SCW (*B*').

In the next run of tests, a 10% glycerin solution was used. Figure 8 shows the histograms of luminescence for the case of focusing the shock wave at the free surface in the modes of rare (frequency f = 0.01–0.02 Hz, histograms 1–5) and frequent (f = 0.16 Hz, histogram 1') shots. The test results show that, for rare shots, the first group of flashes near the surface (with the center of the diaphragm at z = –0.6 mm) is practically absent.

Figure 8 also shows the isobars of the pressure at the axis that were calculated for a plane pressure pulse by using a model without cavitation. The pressure in the pulse was approximated by a formula from [25]:

$$p(t) = p_{atm} + 37(1 + \tanh(3 \times 10^7 t))\cos(1.6 \times 10^6 t) \times \exp(-0.7 \times 10^6 t).$$

Here, p is measured in megapascals, t in seconds, and p_{atm} = 0.1 MPa.

The excess of the duration of every phase (positive and negative) of the compression wave over the interval $\Delta\tau$ calculated with formula (2) made it possible to relate all flashes near the moments corresponding to maximum or minimum pressure to one sign of pressure. The analysis of histograms 4 and 5 showed that the luminescence of the liquid does not occur in the rarefaction phase (*BB*') during the expansion of bubbles. The flashes are observed behind the front *B*' in the compression wave. The arrival of the SCW at the area of near-surface cavitation is the cause of the third group of flashes observed in histograms 1–3 at the moments t = 36.5–37 μs. The cavitation-free model for this cavitation zone predicts the minimum of pressure at the time interval t = 35.5–36.5 μs. In the experiment, this time interval is characterized by positive pulses produced by the SCW (wave *A*' in Fig. 7), which explains the appearance of the second group of flashes.

As was mentioned above, the luminescence in the first group of flashes is caused by the collapse of gas bubbles. The luminescence in the near-surface cloud is determined by the bubbles caused by cavitation and, hence, filled mainly with vapor. They cannot be filled with the gas drawn from the atmosphere above the surface. From Table 2, it follows that, at the early stage of cavitation, this is impossible owing to the supersonic phase velocity v_l of the propagation of the lower boundary of the bubble cloud, which exceeds the mass velocity of the medium by more than 60 times. Therefore, during the time of observation of the cloud (≤7 μs), the depth of penetration of water with gas bubbles captured near the surface is much smaller than h. The comparison of results for different liquids shows that the number of luminescence pulses in the second group of flashes, when normalized by the number of shots and the area of the PMT slit, for the aforemen-

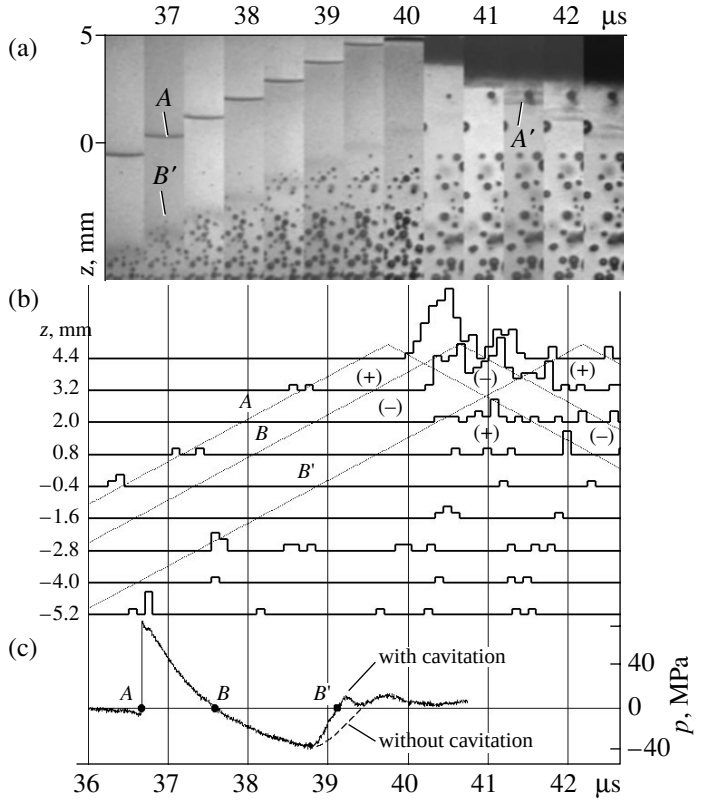

Fig. 7. The time correlation between the pressure in a bipolar wave, the bubble dynamics, and the luminescence in water; the free surface is at $z = 5$ mm. (a) Filmogram for $p_s = 7.7$ MPa (the frame width is 1.8 mm; the frame center coincides with the symmetry axis of the process). (b) Histograms of luminescence for $p_s = 7.7$ MPa, for equidistant values of z from –5.2 to 4.4 mm (32 rare-mode tests for every slit position), with the wave traces extracted from the filmogram (*A* is the front of the initial wave, *B* is the front of the rarefaction wave, and *A*', *B*' are the fronts of the SCWs). The plus and minus signs show the sign of pressure at the axis in the precavitation mode. (c) Pressure for $p_s = 5.9$ MPa, $r = z = 0$ mm (the focus); at the instants *A*, *B*, and *B*', the pressure is equal to zero. The dashed line corresponds to the pressure without cavitation (obtained by an approximation).

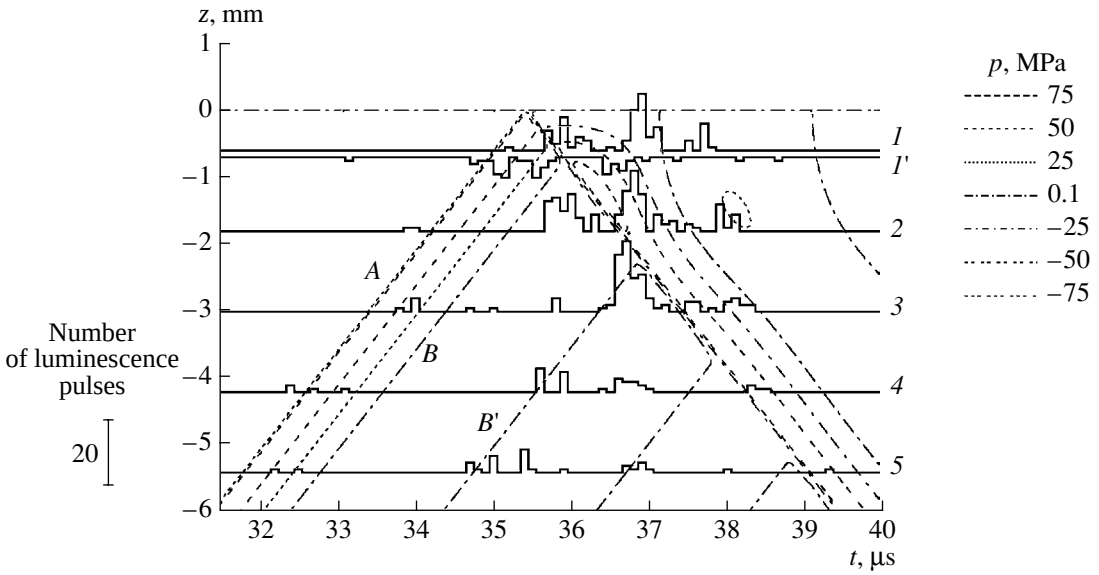

Fig. 8. Histograms of the luminescence pulses for $p_s = 7.7$ MPa in the 10% glycerin solution; each histogram is summed over 16 runs. Curves *1*–*5* correspond to rare shots for $z = -0.6$, –1.8, –3.0, –4.2, and –5.4 mm, respectively; curve *1*' corresponds to frequent shots for $z = -0.6$ mm (an inverted histogram). Isolines of pressure at the axis are superimposed; the isolines are calculated using the model without cavitation.

Table 3. Pressure amplitudes and the total number of light flashes accumulated in 16 shots

p_s, MPa	p_1^+, MPa $z = 0$ $r = 0$	p_1^-, MPa $z = 0$ $r = 0$	p_2^+, MPa $z = 3$ mm $r = 5$ mm	Luminescence $z = -0.6$ mm, $r = 0$		
				group 1	group 2	group 3
3.0	65 ± 5	–18 ± 3	0 ± 0.5	1	9	1
4.3	70 ± 5	–20 ± 3	1 ± 0.5	8	18	4
5.9	75 ± 5	–33 ± 3	4 ± 0.5	8	13	8
7.7	75 ± 5	–39 ± 3	6 ± 0.5	15	12	14
9.7	75 ± 5	–42 ± 3	8 ± 0.5	–	–	–

tioned glycerin solution is 2.8 times greater than the corresponding number for water. This agrees well with the data reported by other authors [19] and confirms the cavitation origin of the bubbles of the near-surface cloud.

The histograms of luminescence of the cloud (*6* in Fig. 2) were constructed for various pressures at the radiator output. The generator operated in the mode of frequent shots (the repetition frequency depends on the charging voltage and is given in [17]). Every histogram was summed over 16 runs. The results are presented in Fig. 9. For all operating modes, regardless of the pressure amplitude and the frequency of repetition of the runs, three groups of flashes are present in the figure. The number of flashes in every group, together with the values of pressure amplitudes in the compression phase p_1^+, in the rarefaction phase p_1^-, and in the SCW p_2^+, are presented in Table 3. The dependence of the shock wave velocity on pressure leads to the time shift of the second group of flashes. As a consequence, for a lower pressure, the wave from the generator reaches the free surface later. The time interval between the first and third group of flashes is $t_{13} = 1.7 \pm 0.4$ μs. It can be evaluated by the formula $t_{13} = t_1 - t_2 - h/c$. With allowance for Eq. (3), it is close to half the time interval between the initial (with front *A*) and secondary (with front *B*') compression pulses (Fig. 7c), which can be related to the first and third groups of flashes, respectively.

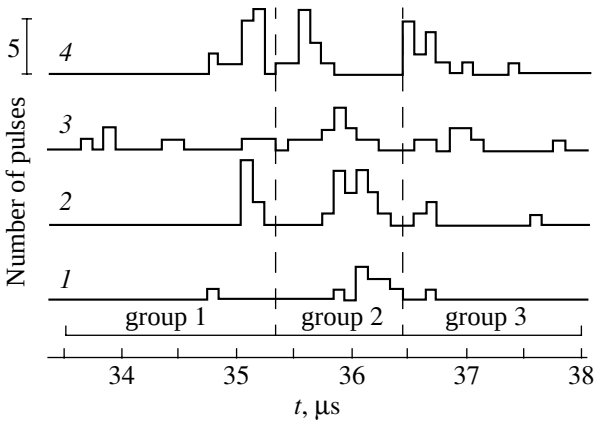

Fig. 9. Histograms of the luminescence signals in a 10% glycerin solution for p_s: (*1*) 3.0, (*2*) 4.3, (*3*) 5.9, and (*4*) 7.7 MPa; every histogram is averaged over 16 frequent shots. The free surface is at $z = 0$, and the center of the area of observation is at $z = -0.6$ mm.

CONCLUSIONS

The combined investigation, including the detection of the luminescence of liquid, the pressure measurement, and the high-speed filming in the course of the cavitation, has made it possible to determine the space–time correlation between the maximal density of flashes and the positive pressure pulses at the focusing of the compression and rarefaction waves. In the case of the focusing at a near-free-surface area, it is possible to distinguish three groups of flashes. Away from the liquid boundary, only two groups of flashes were observed. Every group of flashes corresponds to a positive peak of pressure in both the initial and the secondary compression waves:

(i) The first group of flashes is synchronized with the action of the compression phase of the initial wave (*AB*, Fig. 7) and is determined by the luminescence of the collapsing bubbles that remained from previous tests. The number of these bubbles depends on the pressure in the rarefaction phase of the initial wave, and, hence, the intensity of flashes of group 1 grows with the increase in the initial pressure at the radiator output. It also grows with the increase in the frequency of tests, i.e., with the decrease in the time that elapsed after the previous test, which reduces the possibility of the bubbles rising to the surface or dissolving.

(ii) The second group of flashes emitted by the elliptic cluster is produced by the bubbles expanded in the rarefaction phase of the initial wave (*BB*', Fig. 7) and compressed by the secondary cavitation wave (wave front *B*', Fig. 7). As is known from [26], the bubbles in a cavitation cluster at the focus of the rarefaction wave are kinematically divided into two fractions: expanding and collapsing bubbles. This process is accompanied by the transformation of the rarefaction wave into the compression wave [21] with which the second group of flashes correlates.

(iii) For the second group of flashes emitted by the near-surface cluster, it is possible to assume the same mechanism of luminescence as for the cluster formed in the rarefaction phase of the initial wave. In this case, the pressure in the near-surface layer also has a phase of compression and a phase of rarefaction after the reflection. The cavitation occurs in the compression pulse of the initial wave reflected from the free surface and is accompanied by the transformation of the rarefaction wave into the compression wave [24]. Hence, one can expect that the cavitation and the wave processes are similar to the processes that occur far from the liquid boundary in the case of a bipolar wave [26]. Unlike the luminescence of the elliptic cluster, the intensity of flashes in group 2 is smaller and the number of flashes is greater than, for instance, in group 3. The total number of flashes in group 2 is constant, because the volume of this cluster (see Table 2), as well as the pressure in the compression phase of the initial wave (Table 3), practically does not depend on the pressure at the radiator output.

(iv) The collapse of the bubbles of the near-surface cloud under the external action of the positive phase of pressure of the secondary cavitation wave arriving from the elliptic cloud is the source of light within the time interval corresponding to the third group of flashes. It explains the growth of the number of flashes with the increase in pressure in the secondary cavitation wave.

In the case of spherical focusing at the free surface, the decrease in the duration and increase in the amplitude of the rarefaction wave occurs. The concentration of cavitation bubbles in the cluster grows, and their maximal radius decreases. As was shown in [26], the expansion of bubbles after the first collapse is more isotropic (without formation of high-speed jets) than their expansion in the case of the pulsed compression of gas [27] or cavitation [28] cavities in an external SW, where the shape of bubbles is unstable. These results testify to a more spherical collapse of bubbles of the smaller size fraction in a two-fraction cluster under the action of the SCW. In addition, the decrease in the lifetime of a bubble reduces the diffusion of gas into the bubble and contributes to a deeper collapse [29]. Thus, one can expect an enhancement of the collapse and the luminescence intensity of a bubble in a two-fraction cluster compared to a monodisperse one.

ACKNOWLEDGMENTS

This work was supported by the German Service of Academic Exchange (grant DAAD no. A/00/01480), the Acoustical Society of America (grant CRDF no. 1210/1), and the Russian Foundation for Basic Research (grant nos. 00-02-17992, 03-02-17682, 01-02-06444-mas, 02-02-06838-mas, and 03-02-06212-mas).

I am grateful to V.S. Teslenko for formulating the problem; to W. Lauterborn and R. Mettin for their hospitality at the Third Physical Institute, University of Gottingen, Germany and for providing the possibility to use the diagnostic facilities; to T. Kurz and D. Krefting for their assistance in the automation of the experiment; and to M.E. Topchiyan and A.S. Zhdan for a careful reading of the paper and helpful remarks.

REFERENCES

1. M. A. Margulis, Usp. Fiz. Nauk **170**, 263 (2000) [Phys. Usp. **43**, 259 (2000)].
2. V. S. Teslenko, Prikl. Mekh. Tekh. Fiz., No. 4, 109 (1976).
3. V. S. Teslenko, Kvantovaya Élektron. (Moscow) **4**, 1732 (1977).
4. V. S. Teslenko, in *Proceedings of the First International Conference, Goettingen, Germany, 1979*, Ed. by W. Lauterborn (Springer, Berlin, 1980), p. 30.
5. C. D. Ohl, O. Lindau, and W. Lauterborn, Phys. Rev. Lett. **80**, 393 (1998).
6. W. Lauterborn, T. Kurz, R. Mettin, and C. D. Ohl, in *Advances in Chemical Physics*, Ed. by I. Prigogine and Stuart A. Rice (Wiley, New York, 1999), Vol. 110, pp. 295–379.
7. A. J. Coleman, M. J. Choi, J. E. Saunders, and T. G. Leighton, Ultrasound Med. Biol. **18** (3), 267 (1992).
8. S. Putterman, P. G. Evans, G. Vazquez, and K. Weninger, Nature **409**, 782 (2001).
9. V. S. Teslenko, Yu. É. Danilova, and V. P. Safonov, in *Dynamics of a Continuous Medium* (Inst. Gidrodin. Sib. Otd. Ross. Akad. Nauk, Novosibirsk, 1997), No. 112, pp. 235–241 [in Russian].
10. V. S. Teslenko, G. N. Sankin, and A. P. Drozhzhin, Fiz. Goreniya Vzryva **35** (6), 125 (1999).
11. A. J. Coleman, M. Whitlock, T. Leighton, and J. E. Saunders, Phys. Med. Biol. **38**, 1545 (1993).
12. V. S. Teslenko, G. N. Sankin, and A. P. Drozhzhin, in *Nonlinear Acoustics at the Turn of the Millennium: Proceedings of the 15th International Symposium on Nonlinear Acoustics, Göttingen, Germany, 1999*, Ed. by W. Lauterborn and T. Kurz; AIP Conf. Proc. **524**, 375 (2000).
13. T. J. Matula, P. R. Hilmo, M. R. Bailey, and L. A. Crum, Ultrasound Med. Biol. **28**, 1199 (2002).
14. S. V. Stebnovskiĭ, Prikl. Mekh. Tekh. Fiz. **174** (2), 126 (1989).
15. V. K. Kedrinskiĭ, A. S. Besov, and I. É. Gutnik, Dokl. Akad. Nauk **352**, 477 (1997) [Phys. Dokl. **42**, 87 (1997)].
16. D. F. Vona, M. W. Miller, H. D. Maillie, and C. H. Raeman, J. Acoust. Soc. Am. **98**, 706 (1995).
17. G. N. Sankin, Akust. Zh. **50**, 261 (2004) [Acoust. Phys. **50**, 212 (2004)].
18. D. V. Voronin, G. N. Sankin, V. S. Teslenko, *et al.*, Prikl. Mekh. Tekh. Fiz. **44** (1), 22 (2003).
19. P. I. Golubnichii, V. D. Goncharov, and Kh. V. Protopopov, Sov. Phys. Acoust. **16**, 323 (1971).
20. G. Sankin, R. Mettin, R. Geisler, *et al.*, in *Fortschritte der Akustik: DAGA 2001, Harburg–Hamburg, Germany*

(Otto von Estorff, DEGA Oldenburg, 2001), CDROM, ISBN 3-9804568-9-7.

21. V. S. Teslenko, Pis'ma Zh. Tekh. Fiz. **20** (5), 51 (1994) [Tech. Phys. Lett. **20**, 363 (1994)].
22. G. N. Sankin, Candidate's Dissertation in Physics and Mathematics (Novosibirsk, 2002).
23. G. N. Sankin, Prib. Tekh. Éksp. **46** (3), 145 (2003) [Instrum. Exp. Tech. **46**, 419 (2003)].
24. G. N. Sankin, R. Mettin, W. Lauterborn, and V. S. Teslenko, in *Proceedings of XI Session of the Russian Acoustical Society* (GEOS, Moscow, 2001), Vol. 1, p. 32.
25. C. C. Church, J. Acoust. Soc. Am. **86**, 215 (1989).
26. G. N. Sankin and V. S. Teslenko, Dokl. Akad. Nauk **393**, 762 (2003) [Dokl. Phys. **48**, 665 (2003)].
27. V. E. Dontsov and P. G. Markov, Prikl. Mekh. Tekh. Fiz., No. 1, 45 (1991).
28. D. V. Voronin, G. N. Sankin, V. S. Teslenko, *et al.*, in *Nonlinear Acoustics at the Beginning of the 21st Century: Proceedings of the 16th International Symposium on Nonlinear Acoustics (ISNA-16), Moscow, 2002*, Ed. by O. V. Rudenko and O. A. Sapozhnikov (Faculty of Physics, Moscow State Univ., Moscow, 2002), Vol. 2, pp. 931–934.
29. I. Akhatov, O. Lindau, A. Topolnikov, *et al.*, Phys. Fluids **13**, 2805 (2001).

Translated by A. Svechnikov

Acoustical Physics, Vol. 51, No. 3, 2005, pp. 347–353. Translated from Akusticheskiĭ Zhurnal, Vol. 51, No. 3, 2005, pp. 412–418.

Diffraction of a Convergent Sound Wave by an Elastic Cylindrical Shell with a Longitudinal Fixation

V. V. Tyutekin, A. I. Boĭko, and Yu. V. Tyutekin

Andreev Acoustics Institute, Russian Academy of Sciences, ul. Shvernika 4, Moscow, 117036 Russia

e-mail: Tyutekin@akin.ru

Received April 20, 2004

Abstract—The problem of the diffraction of a zero-order convergent cylindrical wave by a cylindrical shell with a longitudinal fixation along one of its generatrices is considered. The problem is solved on the basis of using the so-called helical waves, which are aperiodic eigensolutions to the equations of the shell motion. The diffraction field is represented in the form of a convergent series in cylindrical harmonics. The method of the solution allows for a generalization to several cases of longitudinal fixation with conditions of different forms. The calculation of the scattering amplitude of the diffraction field is carried out for various frequencies and shell parameters. © *2005 Pleiades Publishing, Inc.*

The diffraction of sound waves by elastic shells of different shapes is still of considerable theoretical and practical interest, which is confirmed by the large number of papers concerned with this subject (see, for example, [1–8]). These papers mainly consider homogeneous shells and shells with a periodic transverse fixation [2]. To solve such problems, it is possible to restrict consideration to solving the equations of shell oscillations by trying solutions periodic in angle. At the same time, the problem of sound diffraction by a shell with a longitudinal fixation of its surface can be of great practical interest. In this case, the solutions to the equations for shells should be sought in the class of aperiodic functions [9]. In this paper, we solve precisely this problem.

To simplify the process, we consider a convergent cylindrical wave coaxial with the shell as the field incident on the shell and a perfectly rigid fixation of the shell surface along the line $\theta = \text{const}$. The generalization of the problem to the case of, e.g., a plane wave or several longitudinal fixations of, e.g., an impedance form does not represent a major difficulty.

Since dependence on the coordinate z is absent in this problem, the shell oscillations can be described by the following set of two differential equations [10]:

$$L\mathbf{U} = \mathbf{f}, \tag{1}$$

where $\mathbf{U} = (v, w)^T$ is the vector of the shell displacement and L is the matrix differential operator of the form

$$L_{22} = \frac{1}{a^2}\frac{\partial^2}{\partial\theta^2} + k_p^2; \quad L_{23} = -L_{32} = -\frac{1}{a^2}\frac{\partial}{\partial\theta};$$

$$L_{33} = -\left(\frac{h^2}{12}\Delta^2 + \frac{1}{a^2} - k_p^2\right).$$

Here, θ is the polar angle, v is the displacement in angle θ, w is the displacement perpendicular to the shell surface, a is the shell radius, and h is the shell thickness. In addition, $k_p^2 = \frac{\rho\omega^2(1-\sigma^2)}{E} = \frac{\rho\omega^2}{E_1}$ is the square of the wave number for longitudinal waves in a plate, ρ is the density of the shell material, E is the Young modulus, σ is the Poisson ratio, and $\Delta = \frac{1}{a^2}\frac{\partial^2}{\partial\theta^2}$.

Vector $\mathbf{f}$ has the form

$$\mathbf{f} = (E_1 h)^{-1}(0, p(a))^T, \tag{2}$$

where $p(a)$ is the sound pressure on the outer surface of the shell. The quantity $p(r, \theta)$ satisfies the Helmholtz equation

$$\Delta p + k_0^2 p = 0, \tag{3}$$

where $\Delta = \frac{\partial^2}{\partial r^2} + \frac{1}{r}\frac{\partial}{\partial r} + \frac{1}{r^2}\frac{\partial^2}{\partial\theta^2}$, $k_0^2 = \left(\frac{\omega}{c}\right)^2$, ω is the circular frequency, and c is the sound velocity in the medium around the shell.

The solution to Eq. (3) can be represented in the form

$$p = p_0 + p_1, \tag{4}$$

where p_0 and p_1 are the sound pressures in the incident and scattered waves, respectively. In this case,

$$p_0 = H_0^{(2)}(k_0 r), \quad p_1 = \sum_{n=0}^{\infty} a_n H_n^{(1)}(k_0 r)\cos n\theta, \tag{5}$$

1063-7710/05/5103-0347$26.00 © 2005 Pleiades Publishing, Inc.

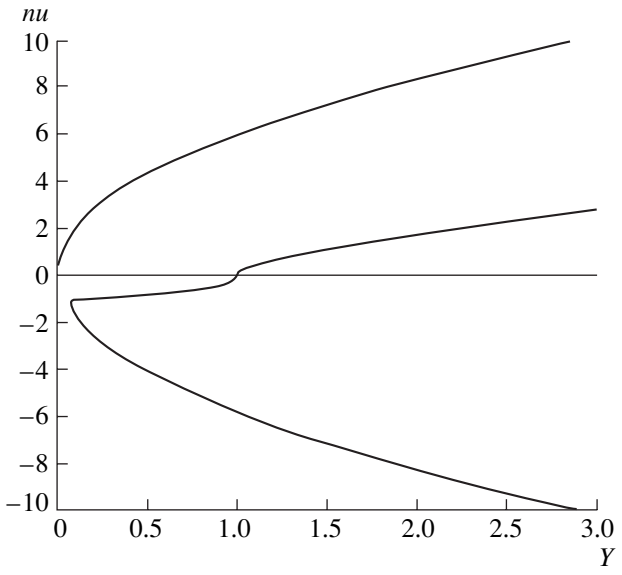

Fig. 1. Dispersion curves for the solution to Eq. (12) at $H = 0.1$.

where a_n are unknown coefficients and $H_0^{(2)}(k_0 r)$ and $H_n^{(1)}(k_0 r)$ are the Hankel cylindrical functions of the first and second kind.

The solutions to Eqs. (1) and (3) must satisfy the boundary conditions

$$w = -\frac{1}{\omega^2 \rho_0}\frac{\partial p}{\partial r} \quad \text{for } r = a, \tag{6}$$

$$\mathbf{u} = 0 \quad \text{for } \theta = \pi. \tag{7}$$

Here, ρ_0 is the density of the acoustic medium around the shell and $\mathbf{u} = (v, w, w'_\theta)$ is the vector of generalized displacements ($w'_\theta = \frac{\partial w}{\partial \theta}$). Equation (7) describes the conditions imposed on the components of the vector of shell displacements along the generatrix $\theta = \pi$.

Introducing new dimensionless parameters $Y = k_p a$, $y = k_0 a$, and $H = \frac{h}{a}$, the set of Eqs. (1) can be rewritten in the form

$$\frac{d^2 v}{d\theta^2} + Y^2 v - \frac{dw}{d\theta} = 0, \tag{8}$$

$$\frac{dv}{d\theta} - \frac{H^2}{12}\frac{d^4 w}{d\theta^4} - (1 - Y^2)w = \frac{a^2}{hE_1}\left[H_0^{(2)}(y) + \sum_{n=0}^{\infty} a_n H_n^{(1)}(y)\cos n\theta\right]. \tag{9}$$

We represent the solution to Eqs. (8) and (9) in the form of the sum of vectors

$$\mathbf{U} = \mathbf{U}_0 + \mathbf{U}_1. \tag{10}$$

Here, $\mathbf{U}_0$ is the eigensolution to Eqs. (8) and (9) (with the right-hand side equal to zero). We try the components of the vector $\mathbf{U}_0$, which is determined by Eq. (10), in the form

$$v_0 = B\sin\nu\theta, \quad w_0 = A\cos\nu\theta. \tag{11}$$

Here, A and B are some arbitrary constants.

Substituting Eqs. (10) and (11) into Eqs. (8) and (9), we obtain a homogeneous system of algebraic equations, which leads to a dispersion equation with respect to ν:

$$\Delta(\nu) = (\nu^2 - Y^2)\left(\frac{H^2}{12}\nu^4 + 1 - Y^2\right) - \nu^2 = 0. \tag{12}$$

The quantity $\Delta(\nu)$ is the third-order polynomial with respect to ν^2, and, therefore, the solution to Eq. (12) has three independent roots. This is confirmed by Fig. 1, where the solutions to this equation are given as the functions of the dimensionless parameter $Y = k_p a$. (The values of $\nu < 0$ correspond to imaginary values.) One can see that there is one real and two imaginary roots up to the values of $Y < 1$; at $Y > 1$, there are two real and one imaginary roots (the physical interpretation of this fact is given in [8]). Correspondingly, solutions (11) to Eq. (12) can be represented in the form of three components:

$$v_0 = \sum_{j=1}^{3} B_j \sin\nu_j\theta, \quad w_0 = \sum_{j=1}^{3} A_j \cos\nu_j\theta, \tag{13}$$

where A_j and B_j are unknown constants. From the first equation of the shell motion (Eq. (8)), it follows that

$$B_j = \frac{\nu_j}{\nu_j^2 - Y^2} A_j.$$

The vector $\mathbf{U}_1 = (v_1, w_1)^T$ in Eq. (10) is the forced solution to Eqs. (8) and (9). We try this solution in the form

$$v_1 = \sum_{n=0}^{\infty} b_n \sin n\theta, \quad w_1 = \sum_{n=0}^{\infty} c_n \cos n\theta. \tag{14}$$

To "connect" the solutions $\mathbf{U}_0$ and $\mathbf{U}_1$, we expand the functions v_0 and w_0 from Eqs. (13) on the interval $[-\pi, \pi]$ in the eigenfunctions (orthogonal to each other) of the solutions given by Eqs. (14). This yields

$$v_0 = \sum_{j=1}^{3} B_j \sum_{n=1}^{\infty} v_{jn} \sin n\theta,$$
$$w_0 = \sum_{j=1}^{3} A_j \sum_{n=0}^{\infty} w_{jn} \cos n\theta. \tag{15}$$

Here,

$$v_{jn} = \frac{2(-1)^n}{\delta_n \pi} \frac{n}{\nu_j^2 - n^2} \sin \nu_j \pi,$$
$$w_{jn} = \frac{2(-1)^n}{\delta_n \pi} \frac{\nu_j}{\nu_j^2 - n^2} \sin \nu_j \pi, \quad (16)$$

where $\delta_n = 2$ at $n = 0$ and $\delta_n = 1$ at $n > 0$.

If the relation $n^2 = \nu_j^2$ is valid at certain $n \neq 0$ and j, i.e., ν_j is equal to an integer number, then, evidently, $v_{jn} = w_{jn} = 1$ for this n. All other coefficients with this value of j are equal to zero.

Substituting Eqs. (13) and (16) into Eqs. (8) and (9), taking into account the boundary condition of Eq. (6), and eliminating the unknowns b_n, we obtain the following relationship between the coefficients a_n and c_n:

$$\alpha_1 z_n c_n - H_n^{(1)}(y) a_n = (\delta_n - 1) H_0^{(2)}(y),$$
$$c_n + \alpha_2 H_n^{(1)'}(y) a_n \quad (17)$$
$$= (1 - \delta_n) \alpha_2 H_0^{(2)'}(y) - \sum_{j=1}^{3} A_j w_{jn}; \quad n = 0, 1, 2, \ldots.$$

In Eq. (17), the following notations are introduced:

$$\alpha_1 = \frac{E_1 h}{a^2}, \quad \alpha_2 = \frac{k_0}{\omega^2 \rho_0},$$
$$z_n = \frac{n^2}{n^2 - Y^2} - \frac{H^2}{12} n^4 - 1 + Y^2.$$

Let us solve Eqs. (8) and (17) as a set of equations. Omitting intermediate mathematics, for the coefficients a_n, b_n, and c_n, we obtain

$$a_n = (\delta_n - 1) A(y) - \frac{\alpha_1}{D_n(y)} \sum_{j=1}^{3} A_j z_n w_{jn},$$
$$b_n = \frac{n}{n^2 - Y^2} c_n,$$
$$c_n = (1 - \delta_n) \alpha_2 C(y) - \frac{H_n^{(1)}(y)}{D_n(y)} \sum_{j=1}^{3} A_j w_{jn}; \quad (18)$$
$$n = 0, 1, 2, \ldots.$$

Here, the following notations are used:

$$D_n(y) = \frac{Z_m}{Y^2} z_n H_n^{(1)'}(y) + H_n^{(1)}(y), \quad Z_m = \frac{\rho \omega h}{\rho_0 c},$$
$$A(y) = \left[\frac{Z_m}{Y^2} z_0 H_1^{(2)}(y) - H_0^{(2)}(y) \right] \frac{1}{D_0(y)},$$
$$C(y) = \frac{H_0^{(1)}(y) H_1^{(2)}(y) - H_1^{(1)}(y) H_0^{(2)}(y)}{D_0(y)} = \frac{4i}{\pi y D_0(y)},$$

where Z_m is the modulus of the inertial impedance of a plate made of the shell material.

Thus, we determined solution (10), which describes the shell motion as a function of three arbitrary constants A_j. To determine these constants, we use the conditions given by Eqs. (7) at $\theta = \pi$. As a result, we obtain the following algebraic set of equations:

$$\sum_{j=1}^{3} A_j \frac{\nu_j \sin \nu_j \pi}{\nu_j^2 - Y^2} = 0,$$
$$\sum_{j=1}^{3} A_j [\cos \nu_j \pi + \Delta_j] = -\alpha_2 C(y), \quad (19)$$
$$\sum_{j=1}^{3} A_j \nu_j \sin \nu_j \pi = 0.$$

In Eqs. (19), we introduced the notation

$$\Delta_j = \sum_{n=0}^{\infty} (-1)^{n+1} \frac{H_n^{(1)}(y)}{D_n(y)} w_{jn}.$$

The solution to Eqs. (19) has the form

$$A_j = -\alpha_2 C(y) \Phi_j / \Phi_\nu, \quad (20)$$

where

$$\Phi_1 = \frac{Q_{23}}{\nu_1 \sin \nu_1 \pi}, \quad Q_{23} = \frac{1}{\nu_3^2 - Y^2} - \frac{1}{\nu_2^2 - Y^2},$$
$$\Phi_2 = \frac{Q_{13}}{\nu_2 \sin \nu_2 \pi}, \quad Q_{13} = \frac{1}{\nu_1^2 - Y^2} - \frac{1}{\nu_3^2 - Y^2},$$
$$\Phi_3 = \frac{Q_{12}}{\nu_3 \sin \nu_3 \pi}, \quad Q_{12} = \frac{1}{\nu_2^2 - Y^2} - \frac{1}{\nu_1^2 - Y^2},$$
$$\Phi_\nu = \left(\frac{\cot \nu_1 \pi}{\nu_1} + \frac{\Delta_1}{\nu_1 \sin \nu_1 \pi} \right) Q_{23}$$
$$+ \left(\frac{\cot \nu_2 \pi}{\nu_2} + \frac{\Delta_2}{\nu_2 \sin \nu_2 \pi} \right) Q_{13} + \left(\frac{\cot \nu_3 \pi}{\nu_3} + \frac{\Delta_3}{\nu_3 \sin \nu_3 \pi} \right) Q_{12}.$$

Let us substitute the coefficients A_j determined by Eq. (20) into Eqs. (18) and represent the amplitudes a_n of the cylindrical harmonics of the field scattered by the shell in the following final form:

$$a_n = (\delta_n - 1) A(y)$$
$$+ \frac{2(-1)^n}{\delta_n \pi \Phi_\nu} \frac{Z_m z_n C(y)}{Y^2 D_n(y)} \sum_{j=1}^{3} \Psi_{jn}, \quad (21)$$

where $n = 0, 1, 2, \ldots$, $\Psi_{1n} = \dfrac{Q_{23}}{\nu_1^2 - n^2}$, $\Psi_{2n} = \dfrac{Q_{13}}{\nu_2^2 - n^2}$, $\Psi_{3n} = \dfrac{Q_{12}}{\nu_3^2 - n^2}$.

The function Φ_ν involves quantities of the form

$$\frac{\Delta_j}{\nu_j \sin \nu_j \pi} = -\frac{2}{\pi} \sum_{n=0}^{\infty} \frac{1}{\delta_n (\nu_j^2 - n^2)} \frac{H_n^{(1)}(y)}{D_n(y)}. \qquad (22)$$

One can readily see that the series on the right-hand side of Eq. (22) is convergent, since, at large n, the common term of the series is majorized by the quantity equal to a certain constant divided by n^6.

From Eq. (21), it follows that, when $H \longrightarrow 0$ (the case of a thin-walled shell), we have $a_0 \longrightarrow -H_0^{(2)}(y)/H_0^{(1)}(y)$ and $a_n = 0$ at $n \neq 0$. Thus, the diffraction field p_1 has the character of the scattering of a convergent cylindrical wave by a perfectly soft cylinder. In another case, when $\rho/\rho_0 \longrightarrow \infty$, we have $a_0 \longrightarrow H_1^{(2)}(y)/H_1^{(1)}(y)$, $a_n = 0$ at $n \neq 0$, and the field p_1 is the field of diffraction of a convergent cylindrical wave by a perfectly rigid cylinder. If fixation conditions (7) are absent, Eq. (21) yields $a_0 = A(y)$ and $a_n = 0$ for $n \neq 0$, which corresponds to the case of diffraction of a convergent wave by a free shell.

It is necessary to make several remarks regarding set of equations (19). The function Φ_ν is the determinant of the system involving the quantities ν_j (see Fig. 1) and $y = \omega a/c$, which depend on the frequency ω of the incident field (a convergent cylindrical wave in our case). If the incident field is absent, the right-hand side of the system is equal to zero and the equation $\Phi_\nu = 0$ is the dispersion equation for the determination of the eigenfrequencies of oscillations for a shell with the fixation conditions along the generatrix $\theta = \pi$ and with an acoustic medium surrounding it. Since a sound radiation into the medium occurs in the case of the shell oscillations, the resonance frequencies of this system are complex. If the external medium is absent, all $\Delta_j = 0$ and the solutions to the equation $\Phi_\nu = 0$ describe the eigenfrequencies of shell oscillations in vacuum.

Note that Eq. (21) gives a complete analytical solution to the stated problem. A further investigation can be conducted only using numerical methods. Let us take the scattering amplitude of the field p_1 in the far wave zone as the quantity for calculation. For this purpose, we use the asymptotics of the Hankel functions

$$H_n^{(1)}(y) = \sqrt{\frac{2}{\pi y}} \exp\left[i\left(y - \frac{n\pi}{2} - \frac{\pi}{4}\right)\right]\left[1 + O\left(\frac{1}{y}\right)\right],$$

$$-\pi < \arg y < 2\pi,$$

for $y \longrightarrow \infty$. As the result, we obtain an expression for the scattering amplitude u of the field p_1:

$$u = \sum_{n=0}^{\infty} (-i)^n a_n \cos n\theta. \qquad (23)$$

The calculation of the value of $|u|$ by Eq. (23) was performed at various physical and wave parameters of the shell. This calculation shows that Parceval's energy identity is valid for the coefficients a_n; in our case, this identity has the form

$$0.5 \sum_{n=0}^{\infty} \delta_n |a_n|^2 = 1.$$

Calculation of the wave parameters for a shell that are close to its complex resonance frequencies are of special interest. Figure 2 presents the results of such a calculation for the relative thickness of the shell $H = 0.1$ and two of its wave dimensions namely, $Y = 0.7423$ (Fig. 2a) and $Y = 1.0753$ (Fig. 2b). It follows from the calculation that, in these cases, the scattering strongly depends on the angle θ, and the irregularity of the scattering pattern increases with frequency. To investigate the rib influence on the result of scattering, we calculated the values of $|u|$ at the same parameters without the complex amplitudes $A(y)$ that correspond to these frequencies, are involved in a_0, and describe the scattering of a convergent cylindrical wave by a free shell. From Figs. 3a and 3b, it follows that the influence of a rib at these resonance frequencies is essential and has the same order of magnitude as the total scattering amplitudes in Fig. 2.

To investigate the relative distribution of energy among the different-number modes of the scattering pattern, we performed the calculation for different physical and wave parameters of the shell. Figure 4 demonstrates the relative distribution of energy for the first eight modes at the parameter $H = 0.1$ and wave dimensions $Y = (1)$ 0.1, (2) 0.3, (3) 0.7423, and (4) 1.0753. One can see from the plot that the mode energies and, therefore, their amplitudes noticeably decrease with the number growth, which provides for a good convergence of the series given by Eq. (23). Moreover, the mode energies (except for the energy of the zero mode) rapidly decrease with the decrease in the wave dimension of the shell.

Figure 5 gives in more detail the relative distribution of energy over the modes of the scattered field amplitude for the cases $Y = (1)$ 0.7423 and (2) 1.0753. The mode numbers are plotted along the abscissa axis. In the first case, the resonance for the mode of number 3 arises, and in the second case, for the mode of number 4. The energy growth for the modes with these numbers occurs basically on account of the energy of the zero mode.

Together with the resonance cases, we considered the cases of the so-called antiresonance scattering,

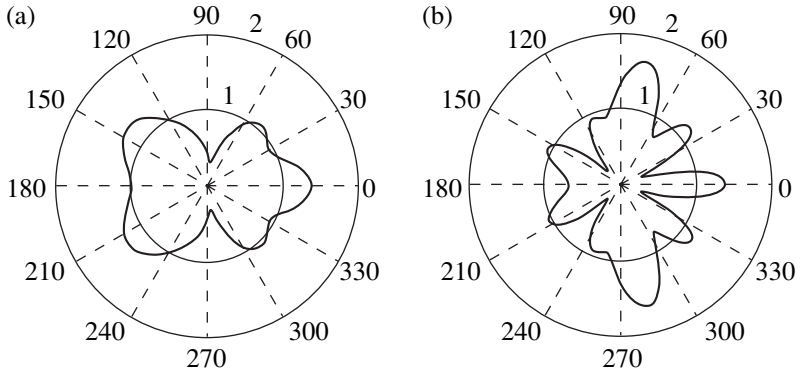

Fig. 2. Modulus of the scattering pattern for $H = 0.1$ and $Y =$ (a) 0.7423 and (b) 1.0753.

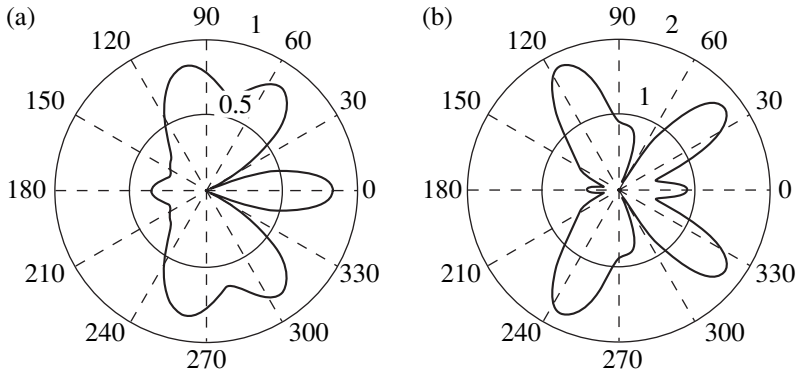

Fig. 3. Modulus of the scattering pattern due to influence of a rib of the shell for $H = 0.1$ and $Y =$ (a) 0.7423 and (b) 1.0753.

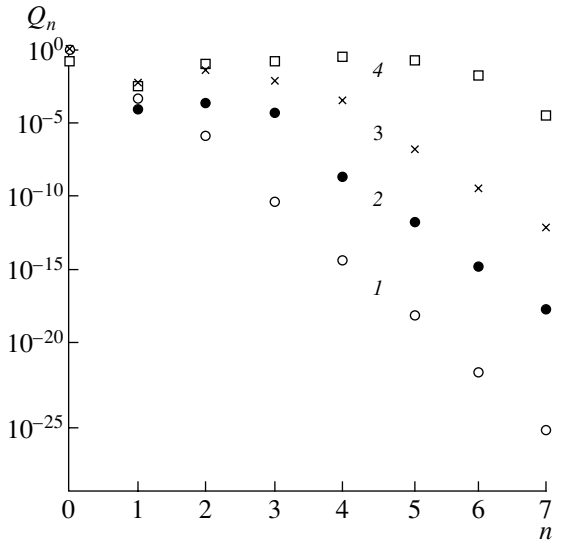

Fig. 4. Relative energy distribution for seven modes of shell oscillations for $H = 0.1$ at frequencies $Y =$ (*1*) 0.1, (*2*) 0.3, (*3*) 0.7423, and (*4*) 1.0753.

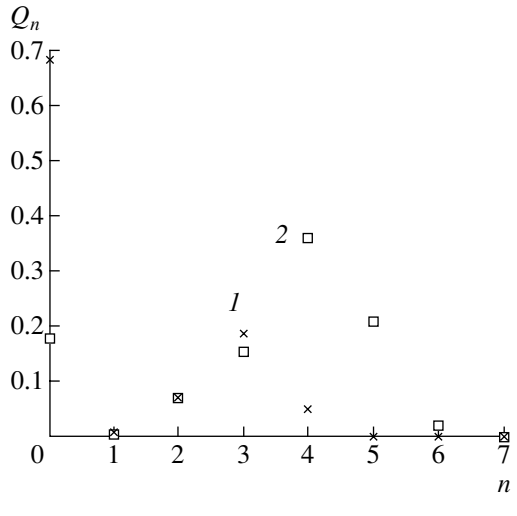

Fig. 5. Relative energy distribution among the zero mode and the first seven modes of shell oscillations for $H = 0.1$ at resonance frequencies $Y =$ (*1*) 0.7423 and (*2*) 1.0753.

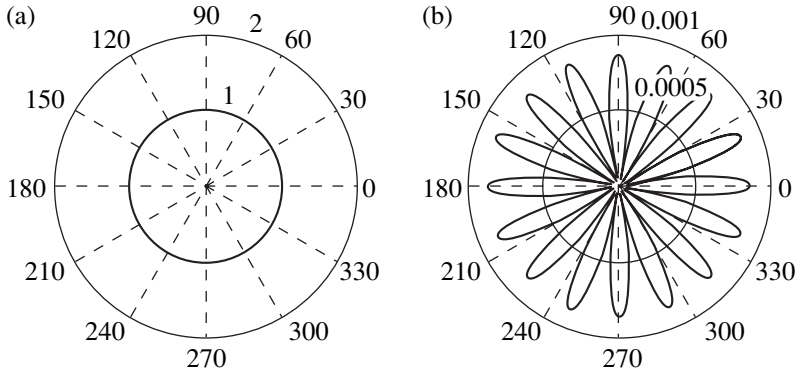

Fig. 6. (a) Modulus of the scattering pattern of the shell and (b) the influence of a rib of the shell on the scattering pattern for $H = 0.03$ and $Y = 0826955$.

where the modulus of the scattered field amplitude is of a circular character, i.e., is almost independent of the angle θ and is governed by the quantity $A(y)$ describing scattering by a ribless shell.

Figure 6a represents the total scattering amplitude that corresponds to the case $H = 0.03$ and $Y = 0.826955$. One can see from the plot that the modulus of the scattering amplitude is close to unity at all observation angles θ. The scattering amplitude without the quantity $A(y)$, which corresponds to the antiresonance frequency of the scattering pattern, is given in Fig. 6b. At this frequency, the relation

$$\mathrm{Im}D_n(y) = 0 \qquad (24)$$

is valid. In the calculation presented in the plot, $n = 8$. In the case where condition (24) is satisfied, the amplitude of the term of the corresponding number in series (22) substantially increases. This series is involved in the quantity Φ_v, whose value also considerably grows. The reason for this is the fact that the scattered field is practically determined by the function $A(y)$ alone. Thus, the antiresonance of the scattering pattern is an indispensable consequence of the resonance of some term of series (22).

Figure 7 gives the values of the scattering field amplitudes up to the number $n = 9$ inclusive. From the plot, it follows that, for the modes with nonzero numbers, number eight mode takes on the maximum value. The amplitude of this mode is at least three orders of magnitude higher than the amplitudes of all other modes, except for the zero mode. This means that, in this case, the rib influence on the amplitude of the scattering pattern is mainly determined by the eighth oscillation mode.

To investigate the resonance properties of the shell, we calculated the values of its resonance frequencies in the absence of the acoustic medium. Figure 8 presents the dependence of the number of resonances of a "dry"

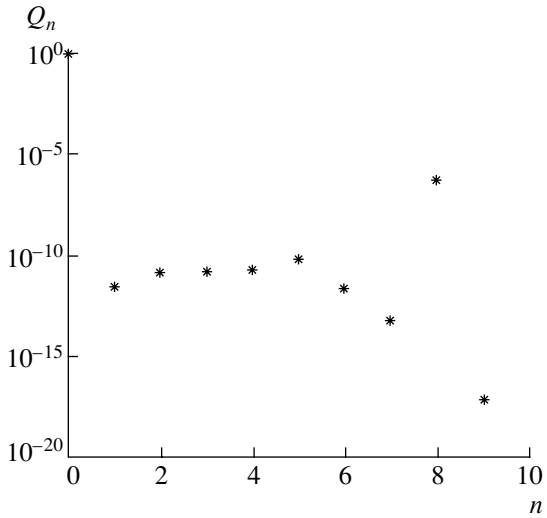

Fig. 7. Relative energy distribution among the first nine modes of shell oscillations for $H = 0.03$ and $Y = 0.826955$.

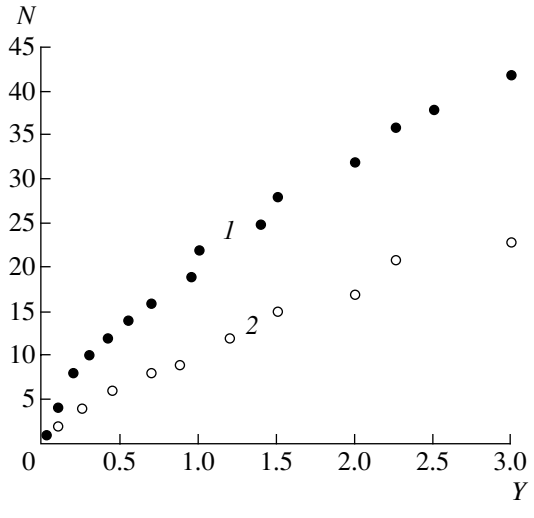

Fig. 8. Number of resonance frequencies for a "dry" shell as a function of its wave dimensions for $H =$ (*1*) 0.03 and (*2*) 0.1.

shell with longitudinal fixation as a function of its wave dimension *Y*. The calculation was performed for two values of its relative thickness: $H = (1)\ 0.03$ and $(2)\ 0.1$. This calculation gives a general idea of the number of such resonances and their distribution. From the plot, one can see that the number of resonances increases as the relative thickness of the shell decreases and that this number is very large in the frequency range under consideration.

REFERENCES

1. H. A. Schenck and G. W. Benthien, Akust. Zh. **41**, 828 (1995) [Acoust. Phys. **41**, 731 (1995)].
2. V. V. Muzychenko, *Sound Diffraction by Elastic Shells* (Nauka, Moscow, 1993) [in Russian].
3. J. F. M. Scott, J. Sound Vibr. **232** (125), 241 (1988).
4. M. C. Junger and D. Feit, *Sound, Structures, and Their Interaction*, 2nd ed. (MIT Press, Massachusetts, 1986).
5. L. Haumesser, D. Decultet, F. Leon, and G. Maze, J. Acoust. Soc. Am. **111**, 2034 (2002).
6. J. D. Kaplunov and M. V. Wilde, J. Acoust. Soc. Am. **111**, 2692 (2002).
7. K. Saijyou and S. Yoshikava, J. Acoust. Soc. Am. **112**, 2808 (2002).
8. V. V. Tyutekin, Akust. Zh. **49**, 843 (2003) [Acoust. Phys. **49**, 721 (2003)].
9. V. V. Tyutekin, Akust. Zh. **50**, 331 (2004) [Acoust. Phys. **50**, 273 (2004)].
10. S. P. Timoshenko and S. Woinowsky-Krieger, *Theory of Plates and Shells*, 2nd ed. (McGraw-Hill, New York, 1959; Nauka, Moscow, 1966).

Translated by M. Lyamshev

Acoustical Physics, Vol. 51, No. 3, 2005, pp. 354–361. From Akusticheskiĭ Zhurnal, Vol. 51, No. 3, 2005, pp. 419–427.

Acoustic Radiation from a Shell-Encapsulated Baffled Cylindrical Cap[1]

S. M. Hasheminejad and M. Azarpeyvand

Department of Mechanical Engineering, Iran University of Science and Technology, Narmak, Tehran, 16844 Iran

e-mail: hashemi@iust.ac.ir

Received February 20, 2004

Abstract—An exact study of radiation of an acoustic field due to radial/axial vibrations of a baffled cylindrical piston, eccentrically positioned within a fluid-filled thin cylindrical elastic shell, into an external fluid medium is presented. This configuration, which is a realistic idealization of a liquid-filled cylindrical acoustic lens with a focal point inside the lens when used as a sound projector, is of practical importance with a multitude of possible applications in underwater acoustics and ocean engineering. The formulation utilizes the appropriate wave field expansions along with the translational addition theorems for cylindrical wave functions to develop a closed-form solution in the form of an infinite series. Numerical results reveal the key effects of excitation frequency, cap angle, radiator position (eccentricity), dynamics of the elastic shell, and cap surface velocity distribution on sound radiation. © *2005 Pleiades Publishing, Inc.*

1. INTRODUCTION

Analytical solutions of interior or exterior boundary value problems in various fields such as potential theory, acoustics, and electromagnetism are strictly dependent on the shape of boundaries. In particular, when multiple objects are present in a sound field, there is an acoustical interaction between the objects due to cross scattering [1–12]. Many researchers have studied the mutual interaction between cylindrical objects subjected to a primary acoustic field. Acoustic interaction of two oscillating cylinders in an ideal fluid was considered in [1]. Scattering of acoustic waves from two parallel cylinders in a viscous fluid was analyzed in [2]. The acoustic field of an oscillating cylindrical body close to a rigid screen was investigated in [3]. The transient interaction of two thin-walled cylindrical piezoelectric ceramic underwater radiators (transducers) was studied in [4]. Just recently, the problem of acoustic radiation of a cylindrical radiator near a rigid/compliant flat boundary was considered in [5]. Scattering of a plane acoustic wave by an infinite penetrable (impenetrable) circular cylinder parallel to another one of acoustically small radius was examined in [6]. An exact solution based on the classical modal series method for the problem of radiation loading on a cylindrical source freely suspended in a fluid-filled cylindrical cavity with a permeable boundary has been developed in [7, 8].

A small cylindrical source freely suspended inside a fluid-filled cylindrical elastic shell, which is itself submerged in an unbounded acoustic field, may be regarded as a sensible model for a cylindrical acoustic lens when used as a sound projector rather than a receiver. A primitive model of a cylindrical acoustic lens was originally analyzed in [9], where the author studied acoustic radiation due to a time-harmonic pressure applied at the inner boundary of an acoustic fluid body composed of two parallel, nonconcentric circular cylinders using the Helmholtz integral equation formulation. Similarly, acoustic radiation from a shell-encapsulated concentric cylindrical source in an infinite acoustic medium is studied in [10, 11]. In a subsequent work, the latter analysis is extended to the cylindrical transducer immersed in an acoustic half-space [12]. Some recent applications of the cylindrical acoustic lens are discussed in [13–15]. Just recently, energy distribution and radiation loading of a cylindrical source suspended within a nonconcentric fluid cylinder was investigated in [16].

The acoustic radiation from pistons placed on baffles has been considered extensively in the literature for various piston and baffle geometries (i.e., planes, spheres, cylinders, and spheroids). The self-radiation impedance for the classic problem of a radially (axially) vibrating piston on a rigid sphere/cylinder is presented in [17, 18]. The mutual acoustic impedance of pistons on a sphere and a cylinder are analyzed in [19] and [20], respectively. The acoustic radiation impedance of curved vibrating caps and rings located on hard baffles of prolate and oblate spheroidal obstacles are formulated in [21, 22]. Likewise, the problem of self- and mutual radiation impedances for rectangular piston sources vibrating on a rigid prolate spheroidal baffle is investigated in [23]. Acoustic radiation from a radially

[1] This article was submitted by the authors in English.

1063-7710/05/5103-0354$26.00 © 2005 Pleiades Publishing, Inc.

vibrating spherical cap set on a spherical baffle near a rigid/soft flat boundary is studied in [24]. Just recently, the problem of sound radiation from a liquid-filled underwater spherical acoustic lens with an internal eccentric baffled spherical piston was considered in [25]. The principal objective of the current paper is to study the effect of cap angle (effective radiation area) on acoustic radiation from a fluid-filled cylindrical acoustic lens containing an internal eccentric baffled cylindrical piston. Therefore, the present work is in fact a realistic extension of the basic model presented in [16], for the case when the internal source is partially baffled (i.e., it is not wholly vibrating) and a thin elastic shell separates the inner and outer mediums. The proposed model is a realistic idealization for an internal focusing cylindrical acoustic lens.

2. FORMULATION

The problem considered here is that of computing acoustic radiation from a cylindrical elastic shell with an eccentric inner (baffled) cylindrical piston that is radially/axially vibrating with a time-harmonic and arbitrary velocity. The geometry and the coordinate systems used are depicted in Fig. 1. The origins O_1 and O_2 of the two cylindrical coordinate systems (r_1, θ_1) and (r_2, θ_2), which are at distance r_0 apart, are placed at the center of the source and the fluid cylinder, respectively. The direct distance between the center of the source and the receiver (field point) is r_1; the distance between the center of the fluid cylinder and the receiver is r_2. The fluid is assumed to be inviscid and ideally compressible. Thus, one may start with the familiar wave equation in an ideal compressible fluid [27]:

$$\frac{\partial^2 p}{\partial t^2} - c^2 \nabla^2 p = 0, \tag{1}$$

where p is the acoustic pressure, c is the ideal speed of sound evaluated at ambient conditions, and ∇^2 is the Laplacian operator. As the cylindrical source is assumed to undergo time-harmonic surface oscillations with frequency ω, we expect solutions of the form [27]

$$p(r, \theta, t) = Re[\bar{p}(r, \theta, \omega)e^{-i\omega t}], \tag{2}$$

where *Re* indicates the real part of a complex number and the quantity $\bar{p}(r, \theta, \omega)$ may be complex. Substitution of the above presumption into (1) yields a Helmholtz-type equation:

$$(\nabla^2 + k^2)p = 0, \tag{3}$$

where $k = \omega/c$ is the acoustic wave number, and we have assumed harmonic time variations throughout with the $e^{-i\omega t}$ dependence and the overbar notation suppressed for simplicity.

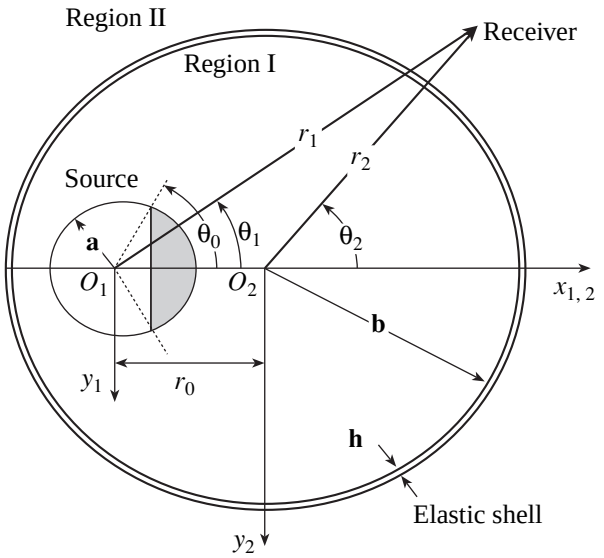

Fig. 1. Problem geometry.

The cylindrical source is supposed to be rigid except for a cap region ($-\theta_0 \le \theta \le \theta_0$), which vibrates radially (axially) with a prescribed velocity $U^{(0)}$ ($U^{(1)}$). The cap velocity can be expressed as a linear combination of cylindrical modes in the form of an infinite series [18]

$$\begin{aligned} u^{(0)}(\omega) &= \sum_{n=0}^{\infty} U_n^{(0)}(\omega)\cos n\theta_1 \\ &= \begin{cases} U^{(0)}(\omega), & -\theta_0 \le \theta_1 \le \theta_0, \\ 0, & \theta_0 \le \theta_1 \le 2\pi - \theta_0, \end{cases} \\ u^{(1)}(\omega) &= \sum_{n=0}^{\infty} U_n^{(1)}(\omega)\cos n\theta_1 \\ &= \begin{cases} U^{(1)}(\omega)\cos\theta_1, & -\theta_0 \le \theta_1 \le \theta_0, \\ 0, & \theta_0 \le \theta_1 \le 2\pi - \theta_0, \end{cases} \end{aligned} \tag{4}$$

where $U_n^{(0)}(\omega)$ and $U_n^{(1)}(\omega)$ are the modal coefficients of the radial and axial velocity distributions, respectively. These coefficients can readily be determined after multiplying both sides of (4) by $\cos m\theta_1$ ($m = 0, 1, 2, \ldots$), integrating over $d\theta_1$, and exploiting the orthogonality of the transcendental harmonics. As a result, we obtain [18]

$$U_n^{(0)}(\omega) = \frac{U^{(0)}(\omega)\int_{-\theta_0}^{\theta_0} \cos n\theta_1 d\theta_1}{\int_{-\pi}^{\pi} (\cos n\theta_1)^2 d\theta_1}$$

$$= \left(\frac{2\sin n\theta_0}{n\left(\pi + \dfrac{\sin 2n\pi}{2n}\right)}\right) U^{(0)}(\omega),$$

$$U_n^{(1)}(\omega) = \frac{U^{(1)}(\omega)\displaystyle\int_{-\theta_0}^{\theta_0} \cos n\theta_1 \cos\theta_1 d\theta_1}{\displaystyle\int_{-\pi}^{\pi} (\cos n\theta_1)^2 d\theta_1} \tag{5}$$

$$= \frac{1}{\pi}\left(\frac{\sin(n-1)\theta_0}{n-1} + \frac{\sin(n+1)\theta_0}{n+1}\right) U^{(1)}(\omega).$$

The fluid in the interior of the cylindrical shell is denoted region I, while the outer medium is denoted region II. In region I, the possibility of both incoming and outgoing (standing) waves exists, while, in region II, only outgoing waves are possible. The solution of the Helmholtz equation for the acoustic pressure inside the fluid-filled cylindrical shell may be represented by

$$p^{\mathrm{I}}(r, \theta_1, \omega) = \sum_{n=0}^{\infty} i^n \varepsilon_n [a_n H_n^{(1)}(k_1 r_1) + b_n H_n^{(2)}(k_1 r_1)] \cos n\theta_1, \tag{6}$$

where $\varepsilon_n = 1$ for $n = 0$ and $\varepsilon_n = 2$ for $n \geq 1$; $k_{\mathrm{I}} = \omega/c_{\mathrm{I}}$ is the acoustic wave number in fluid medium I; $H_n^{(1)}$ and $H_n^{(2)}$ are the cylindrical Hankel functions of the first and second kind, respectively [28]; and $a_n(\omega)$ and $b_n(\omega)$ are unknown modal coefficients. Similarly, noting that the external fluid medium is unbounded and keeping in mind the radiation condition, the solution in the outer region can be expressed as a linear combination of outgoing cylindrical waves as

$$p^{\mathrm{II}}(r_2, \theta_2, \omega) = \sum_{n=0}^{\infty} i^n \varepsilon_n c_n H_n^{(1)}(k_{\mathrm{II}} r_2) \cos n\theta_2, \tag{7}$$

where $k_{\mathrm{II}} = \omega/c_{\mathrm{II}}$ is the acoustic wave number in fluid medium II and $c_n(\omega)$ is an unknown modal coefficient.

The equations of motion for a closed cylindrical elastic shell, including both membrane (extensional) and flexural (inextensional) effects, are presented in [29]. The general displacements of the cylindrical shell are normally expressed in terms of the shell's midsurface deflections. Considering only the nontorsional axisymmetric motions, the midsurface radial $W(\theta_2, \omega)$ and tangential $V(\theta_2, \omega)$ displacements may be expanded in cylindrical harmonics as [29]

$$W(\theta_2, \omega) = \sum_{n=0}^{\infty} W_n(\omega) \cos n\theta_2,$$
$$V(\theta_2, \omega) = \sum_{n=0}^{\infty} V_n(\omega) \sin n\theta_2. \tag{8}$$

The equations of shell motion are satisfied if the modal coefficients $W_n(\omega)$ and $V_n(\omega)$ satisfy the equations [29]

$$[\Omega^2 - n^2]V_n - nW_n = 0,$$
$$-nV_n + [\Omega^2 - (1 + \beta^2 n^4)]W_n = -\frac{b^2(1-\nu^2)}{Eh}\Delta p_n, \tag{9}$$

where $\beta^2 = h^2/12b^2$, $\Omega = \omega b/c_p$ is a nondimensional frequency parameter, $c_p^2 = E/(1-\nu^2)\rho_s$ is the phase velocity of a compressional wave in the elastic shell, ρ_s is the solid material density, h is the shell thickness, E is the modulus of elasticity, ν is the Poisson ratio, and $\Delta p_n = p_n^{\mathrm{I}} - p_n^{\mathrm{II}}$ is the modal component of the pressure differential at the shell's surface, which will be determined in the next subsection.

Many radiation and scattering problems involve waves of one characteristic shape that are incident upon a boundary of some other shape. Thus, it is difficult to satisfy the boundary conditions on that surface. There exists, however, a class of mathematical relationships called wave transformations that circumvent this difficulty in many cases by allowing one to study the fields scattered by various bodies, all of which are referred to a common origin. Accordingly, in order to realize orthogonality in the current problem, which involves nonconcentric cylindrical boundaries, we can express the cylindrical wave functions of the (r_1, θ_1) coordinate system in terms of cylindrical wave functions of the (r_2, θ_2) coordinate system through application of the classical form of the translational addition theorem for bicylindrical coordinates [30]:

$$X_n(k_{\mathrm{I}} r_1) e^{in\theta_1} = \sum_{m=-\infty}^{\infty} X_m(k_{\mathrm{I}} r_2) J_{n-m}(k_{\mathrm{I}} r_0) e^{i(n-m)\theta_{12} + im\theta_2}, \tag{10}$$

where $X_n(\,)$ is one of the cylindrical Bessel functions of order n; since, in our problem, the eccentric cylinders have a common x axis, we set $\theta_{12} = 0$ or π. The above addition theorem may be put in a (computationally) more advantageous form [5]:

$$X_n(k_{\mathrm{I}} r_1)\cos n\theta_1 = \sum_{m=0}^{\infty} \delta_m X_m(k_{\mathrm{I}} r_2) R_{nm}(k_{\mathrm{I}} r_0) \cos m\theta_2, \tag{11}$$

where

$$R_{nm}(k_\mathrm{I} r_0) = J_{n-m}(k_\mathrm{I} r_0) e^{i(n-m)\theta_{12}} + (-1)^m J_{n+m}(k_\mathrm{I} r_0) e^{i(n+m)\theta_{12}}, \tag{12}$$

in which $\delta_n = 1/2$ for $n = 0$ and $\delta_n = 1$ for $n \geq 1$, and the following relation for the terms involving Bessel functions of negative order is employed:

$$X_{-m}(\,) = (-1)^m \mathrm{X}_m(\,). \tag{13}$$

Incorporation of (10) into (6) allows us to express the pressure differential at the shell surface as

$$\Delta p(r_2, \theta_2, \omega) = p^\mathrm{I}(r_2, \theta_2, \omega) - p^\mathrm{II}(r_2, \theta_2, \omega) = \sum_{n=0}^{\infty} \Delta p_n(r_2, \omega) \cos n\theta_2, \tag{14}$$

where

$$\Delta p_n(r_2, \omega) = \delta_n A_n H_n^{(1)}(k_\mathrm{I} r_2) + \delta_n B_n H_n^{(2)}(k_\mathrm{I} r_2) - i^n \varepsilon_n c_n H_n^{(1)}(k_\mathrm{II} r_2), \tag{15}$$

in which

$$A_n(\omega) = \sum_{m=0}^{\infty} \varepsilon_m i^m R_{mn}(k_\mathrm{I} r_0) a_m(\omega), \qquad B_n(\omega) = \sum_{m=0}^{\infty} \varepsilon_m i^m R_{mn}(k_\mathrm{I} r_0) b_m(\omega). \tag{16}$$

The unknown modal coefficients a_n, b_n, and c_n and modal components of the shell midsurface displacements W_n and V_n must be determined by imposing suitable boundary conditions. Correspondingly, the continuity of normal velocity at the surface of the radially/axially vibrating source requires that

$$u_r^\mathrm{I}(a, \theta_1, \omega) = \frac{1}{i\omega\rho_\mathrm{I}} \frac{\partial p^\mathrm{I}(r_1, \theta_1, \omega)}{\partial r_1}\Bigg]_{r_1 = a} = \sum_{n=0}^{\infty} \begin{Bmatrix} U_n^{(0)}(\omega) \\ U_n^{(1)}(\omega) \end{Bmatrix} \cos n\theta_1, \tag{17}$$

where ρ_I is the fluid density in the (inner) region I. Similarly, the continuity of normal velocities at the inner and outer surfaces of the shell demands that

$$-i\omega W(\theta_2, \omega) = \frac{1}{i\omega\rho_\mathrm{I}} \frac{\partial p^\mathrm{I}(r_2, \theta_2, \omega)}{\partial r_2}\Bigg]_{r_2 = b - \frac{h}{2}}, \qquad -i\omega W(\theta_2, \omega) = \frac{1}{i\omega\rho_\mathrm{II}} \frac{\partial p^\mathrm{II}(r_2, \theta_2, \omega)}{\partial r_2}\Bigg]_{r_2 = b + \frac{h}{2}}, \tag{18}$$

where ρ_II is the fluid density in the (outer) region II. The unknown modal coefficients can now be determined by incorporation of the translational addition theorem in the stated boundary conditions and the equations of shell motion. Therefore, employing (5), (6), and (10) in boundary conditions (17) and (18), we obtain, for the $n \geq 0$ modes,

$$\frac{i^{n+1}\varepsilon_n}{c_\mathrm{I}\rho_\mathrm{I}} [a_n H_n^{(1)'}(k_\mathrm{I} a) + b_n H_n^{(2)'}(k_\mathrm{I} a)] = \begin{cases} U_n^{(0)}(\omega), & \text{radial vibrations,} \\ U_n^{(1)}(\omega), & \text{axial vibrations,} \end{cases}$$

$$\delta_n [H_n^{(1)'}(k_\mathrm{I} b) A_n + H_n^{(2)'}(k_\mathrm{I} b) B_n] = \omega\rho_\mathrm{I} c_\mathrm{I} W_n, \qquad i^n \varepsilon_n H_n^{(1)'}(k_\mathrm{II} b) c_n = \omega\rho_\mathrm{II} c_\mathrm{II} W_n. \tag{19}$$

The unknown coefficients $a_n(\omega)$, $b_n(\omega)$, and $c_n(\omega)$ may readily be computed by solving the linear systems of equations (9) and (19). Subsequently, from (7), the on-axis forward radiated far-field pressure amplitude, $|p^\mathrm{II}(r_\infty, \theta_2 = 0, \omega)|$, may be promptly calculated. This completes the necessary background required for an exact acoustic analysis of the problem.

3. NUMERICAL RESULTS

In order to illustrate the nature and general behavior of the solution, we consider a numerical example in this section. With respect to the large number of parameters involved here, no attempt is made to exhaustively evaluate the effect of varying each of them. The intent of the collection of data presented here is merely to illustrate the kinds of results to be expected from some representative and physically realistic choices of values for these parameters. From these data, some trends are noted and general conclusions drawn about the relative importance of certain parameters. Correspondingly, noting the crowd of parameters that enter into the final expressions and keeping in view the availability of numerical data, we shall confine our attention to a particular model. The surrounding ambient fluid is assumed to be water at atmospheric pressure and 300 K. The elastic shell is taken to be a 3% stainless steel shell of radius $b = 100$ cm and thickness $h = 0.03b = 3$ cm. The piston is set on a rigid cylindrical baffle of radius $a = 0.01b = 1$ cm. The interior fluid is selected to be 3M Company Fluorinert chemical FC-72 [31]. The numerical values for the input parameters, which are used in the calculations, are summarized in the table. A MATLAB code was constructed to treat boundary conditions, to determine the unknown modal coefficients, and to compute the acoustic field quantities as functions of the distance parameter r_0/b and the nondimensional frequency $kb_e = \omega b_e/c$, where $b_e = b\sin(\theta_0/2)$ refers to the effective piston radius [18], for selected cap angles θ_0. Accurate computations for the derivatives of cylindrical Bessel functions were accomplished by utilizing (9.1.27) in [28]. The computations were

Input parameter values

Parameter	Numerical value	Parameter	Numerical value
Fluid properties		Elastic shell	
Pressure, bar	1.00	E, dyn/cm^2	2.15×10^{12}
Temperature, K	300	h, cm	0.3
c_I, cm/s	5.12×10^4	ν	0.283
ρ_I, g/cm^3	1.68	ρ_s, g/cm^3	7.8
c_{II}, cm/s	1.49×10^5	b, cm	10
ρ_{II}, g/cm^3	0.997	a, cm	0.1

performed on a Pentium IV personal computer with a truncation constant of $N = 30$ to assure convergence in the high-frequency range, and also in case of close proximity of the source to the shell boundary (high eccentricity).

Figure 2 displays the effects of the nondimensional frequency kb_e, cap angle θ_0, and source eccentricity r_0/b on the normalized far-field on-axis radiated pressure magnitude (i.e., $|p^{II}(r_\infty, \theta_2 = 0, \omega)|/\rho_{II} c_{II}^2$) for an axially vibrating shell-encapsulated baffled cylindrical piston. Here, due to the similarity of the numerical results, the plots associated with the radially vibrating cap are not displayed for brevity. The main observations are as follows. The greatest pressure amplitudes generally occur as the source is moved toward the cylindrical boundary of the lens. At a fixed excitation frequency, kb_e, source eccentricity has a relatively moderate effect on the far-field pressure for the fully vibrating cylinder $\theta_0 = 180°$. This effect noticeably increases as the cap angle is decreased to $\theta_0 = 30°$. The overall pressure magnitudes increase as the nondimensional frequency kb_e is raised. The highest on-axis far-field pressure amplitudes and, thus, the most efficient sound projection characteristics for the encapsulated lens are noted for the smallest cap angle (i.e., $\theta_0 = 30°$). The wholly oscillating source ($\theta_0 = 180°$) appears to be the least favorable situation, as it exhibits a very low far-

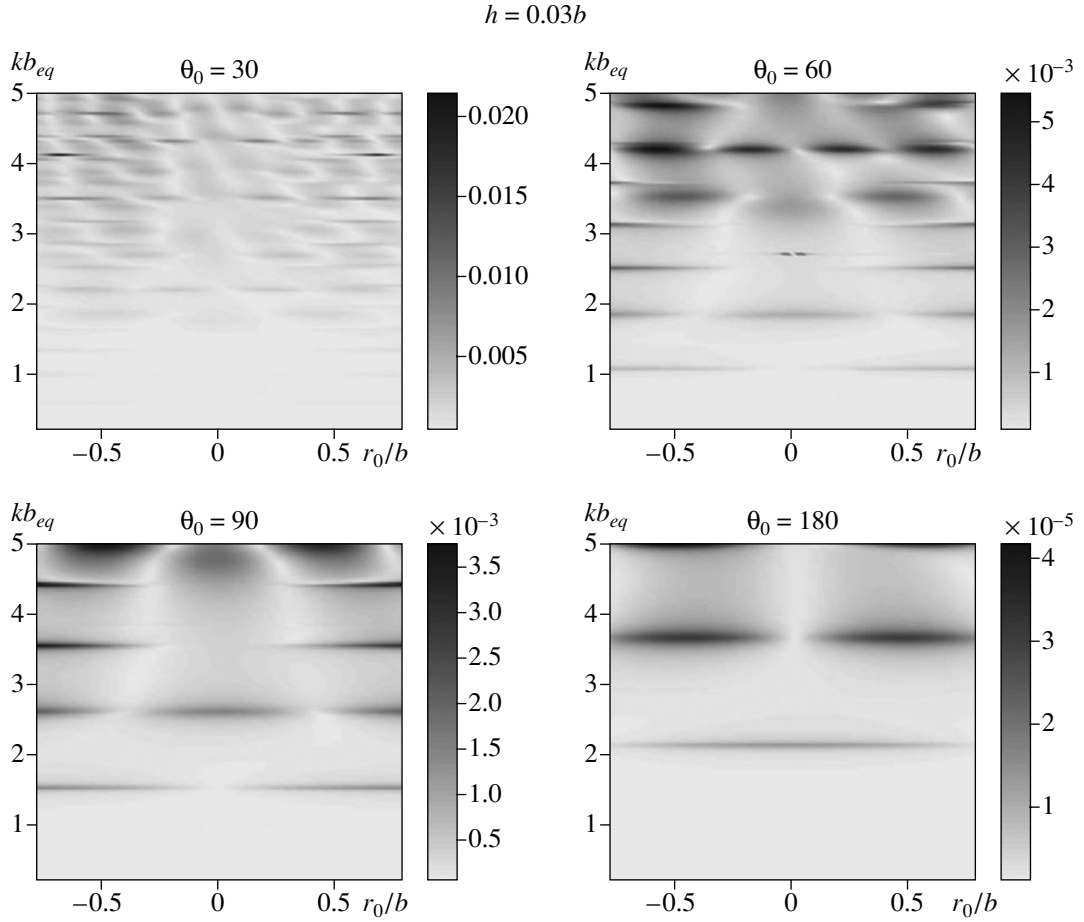

Fig. 2. The change in the normalized far-field on-axis radiated pressure magnitude for an axially vibrating shell-encapsulated baffled cylindrical piston with the nondimensional frequency and source eccentricity at selected cap angles.

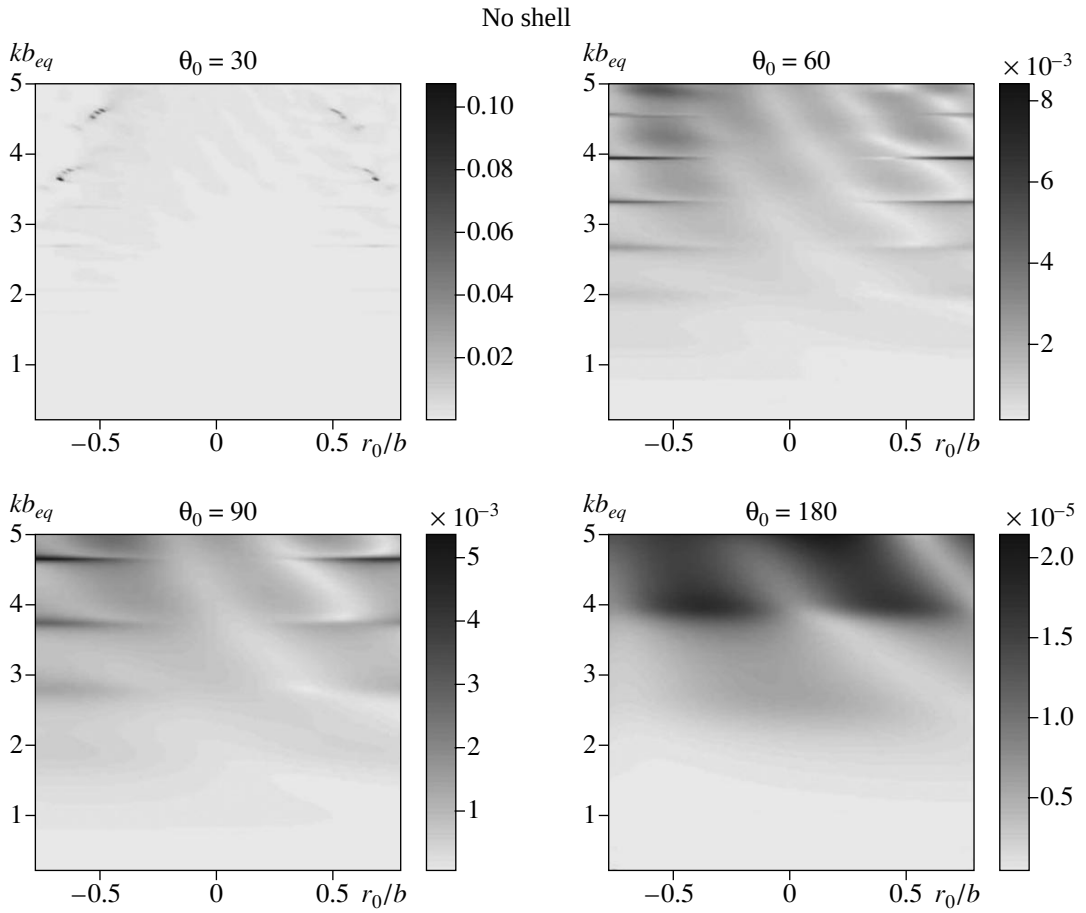

Fig. 3. The change in the normalized far-field on-axis radiated pressure magnitude for an axially vibrating baffled cylindrical piston suspended inside a fluid cylinder with the nondimensional frequency and source eccentricity at selected cap angles.

field pressure amplitude. Furthermore, to examine the shell dynamic interaction effects, we have presented the far-field pressure magnitudes in the absence of the cylindrical shell in Fig. 3. Comments similar to those in the above discussion can be made. The most important observation is the general increase in the pressure amplitudes for the partially vibrating pistons, especially for the cap angle $\theta_0 = 30°$. In contrast, encapsulating the wholly vibrating source by the elastic shell seems to cause a notable increase in the maximum amplitude of the resonant pressure oscillations that build up in the far field.

Finally, to check the overall validity of the work, we first used our code to compute the normalized radiation impedance load per unit area on the vibrating piston by taking advantage of Foldy's definition of radiated power [26] for the case of an eccentric baffled radially vibrating cylindrical cap suspended inside a water-filled ($\rho_s = \rho_I = \rho_{II} \approx 1$ g/cm^3) very light and thin ($h \approx 0.0001b$) cylindrical shell immersed in water; i.e., we utilized [18]

$$Z_r(\theta_0, \omega) = \frac{\int_{-\theta_0}^{\theta_0} p^I(r_1 = a, \theta_1, \omega)[u^{(0)}(\omega)]^* d\theta}{\int_{-\theta_0}^{\theta_0} [u^{(0)}(\omega)]^2 d\theta}, \quad (20)$$

where the asterisk denotes a complex conjugate quantity. The radiation impedance can readily be obtained after substituting the first expression of (4) and (6) into (20) and exploiting the orthogonality property of the transcendental harmonics. Figure 4 shows that the calculated (normalized) radiation resistance ($Re\{Z_r\}/\rho_I c_I$) and radiation reactance ($Im\{Z_r\}/\rho_I c_I$) components precisely reduce to the curves appearing in the figure in [18, p. 227]. Subsequently, further verifications were made for a wholly vibrating cylinder ($\theta_0 = 180°$) suspended inside a "very thin" shell filled with Fluorinert chemical FC-72 and immersed in water. The on-axis radiated far-field acoustic pressure corresponding to the radially/axially vibrating cylinders was confirmed to

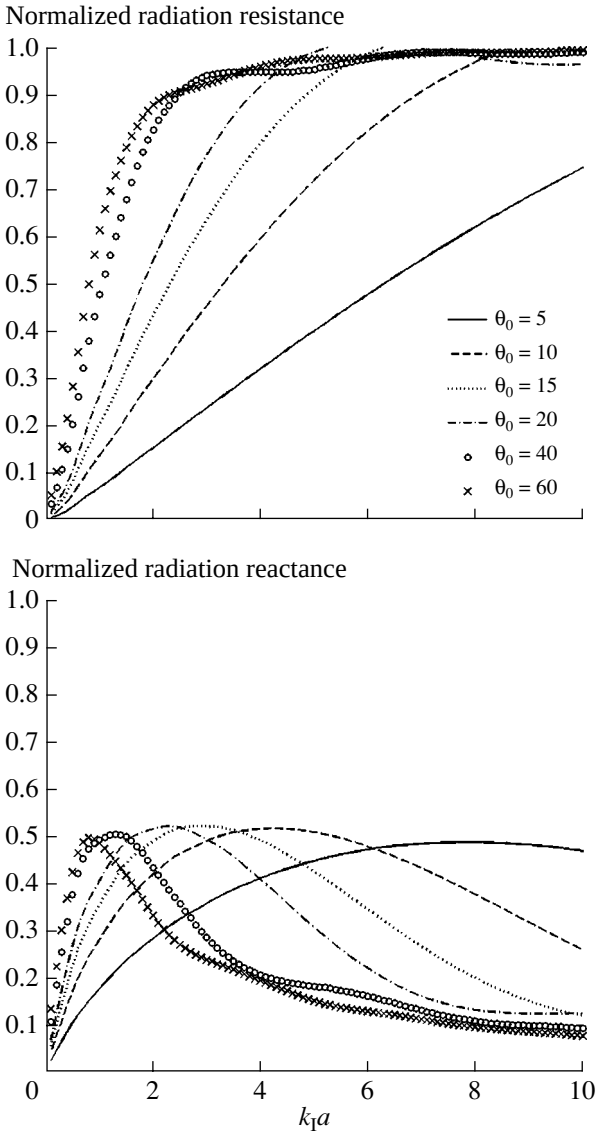

Fig. 4. The resistive and reactive components of the radiation impedance load per unit area on the radially vibrating cylindrical cap eccentrically suspended inside a water-filled very light and thin cylindrical shell immersed in water.

closely duplicate the numerical results for the wholly pulsating ($n = 0$)/oscillating ($n = 1$) modes presented in Figs. 6–8 in [16].

4. CONCLUSIONS

Acoustic radiation from a liquid-filled cylindrical lens with an eccentric inner cylindrical cap, undergoing time-harmonic radial/axial surface vibrations, is studied. An exact treatment of the fluid/structure interaction that involves utilization of the dynamic field equations, the pertinent boundary conditions, and the translational addition theorems for cylindrical wave functions is presented. Subsequently, the on-axis radiated far-field sound pressure is evaluated for representative values of the parameters characterizing the system. Numerical results reveal that source eccentricity generally improves the acoustic performance of the system. The highest pressure amplitudes and, thus, the most efficient sound projection are noted for the smallest cap angle considered. Encapsulating the partially vibrating (baffled) cylinder by the elastic shell causes a general decline in the pressure amplitudes. In contrast, encapsulating the wholly vibrating (unbaffled) cylinder by the elastic shell roughly doubles the maximum amplitude of the resonant pressure oscillations that are developed in the far field.

REFERENCES

1. D. N. Gorelov, Prikl. Mekh. **3**, 146 (1973).
2. A. P. Zhuk, Prikl. Mekh. **27**, 108 (1991).
3. Y. N. Ryabukha, Prikl. Mekh. **15**, 117 (1979).
4. A. E. Babaev, V. G. Savin, and A. A. Leiko, J. Acoust. Soc. Am. **108**, 157 (2000).
5. S. M. Hasheminejad and M. Azarpeyvand, Int. J. Eng. Sci. **41**, 2253 (2003).
6. J. A. Roumeliotis, A. P. Ziopoulos, and G. C. Kokkorakis, J. Acoust. Soc. Am. **109**, 870 (2001).
7. S. M. Hasheminejad and H. Hosseini, ASME Trans. J. Appl. Mech. **69**, 675 (2002).
8. S. M. Hasheminejad and H. Hosseini, Soil Dyn. Earthquake Eng. **22**, 441 (2002).
9. R. P. Shaw and G. J. Tai, J. Acoust. Soc. Am. **56**, 1437 (1974).
10. V. G. Savin, I. I. Chernushenko, and N. A. Shul'ga, Prikl. Mekh. **15**, 110 (1979).
11. E. L. Shenderov, *Wave Problems of Hydroacoustics* (Sudostroenie, Leningrad, 1972) [in Russian].
12. A. N. Guz, Y. N. Ryabukha, and N. A. Shul'ga, Prikl. Mekh. **17**, 21 (1981).
13. D. L. Folds and D. H. Brown, J. Acoust. Soc. Am. **43**, 10 (1968).
14. D. L. Folds, J. Acoust. Soc. Am. **49**, 435 (1971).
15. L. A. A. Warnes and C. R. Hood, Ultrasonics **20**, 123 (1982).
16. S. M. Hasheminejad and M. Azarpeyvand, Acta Mech. **164**, 15 (2003).
17. E. Skudrzyk, *The Foundations of Acoustics: Basic Mathematics and Basic Acoustics* (Springer, New York, 1971; Mir, Moscow, 1976).
18. F. P. Mechel, *Formulas of Acoustics* (Springer, Berlin, 2002).
19. C. H. Sherman, J. Acoust. Soc. Am. **31**, 947 (1959).
20. J. E. Greenspon and C. H. Sherman, J. Acoust. Soc. Am. **36**, 149 (1964).
21. A. L. Van Buren, J. Acoust. Soc. Am. **50**, 1343 (1971).
22. R. Baier, J. Acoust. Soc. Am. **51**, 1705 (1972).

23. J. E. Boisvert and A. L. Van Buren, J. Acoust. Soc. Am. **111**, 867 (2002).
24. S. M. Hasheminejad and M. Azarpeyvand, IEEE J. Ocean Eng. **31**, 1129 (2004).
25. S. M. Hasheminejad and M. Azarpeyvand, IEEE J. Ocean. Eng. **29**, 110 (2004).
26. W. Thompson, Jr., J. Acoust. Soc. Am. **54**, 1694 (1973).
27. A. D. Pierce, *Acoustics: An Introduction to Its Physical Principles and Applications* (American Inst. of Physics, New York, 1991).
28. M. Abramowitz and I. A. Stegun, *Handbook of Mathematical Functions* (National Bureau of Standards, Washington, 1965; Nauka, Moscow, 1979).
29. M. C. Junger and D. Feit, *Sound, Structures, and Their Interaction*, 2nd ed. (MIT Press, Massachusetts, 1986).
30. Y. A. Ivanov, *Diffraction of Electromagnetic Waves on Two Bodies* (Nauka i Tekhnika, Minsk, 1968; NASA Nech. Transl., Washington, 1970).
31. *On the Acoustic Properties for 3M FC*, http://www.mmm.com.

Acoustical Physics, Vol. 51, No. 3, 2005, pp. 362–364. Translated from Akusticheskiĭ Zhurnal, Vol. 51, No. 3, 2005, pp. 428–430.

Sound Absorption by Monopole–Dipole Resonators in a Multimode Waveguide

A. D. Lapin

Andreev Acoustics Institute, Russian Academy of Sciences, ul. Shvernika 4, Moscow, 117036 Russia

e-mail: mironov@akin.ru

Received April 8, 2004

The scattering and absorption of sound by a monopole–dipole resonator in a narrow pipe has been studied earlier [1]. A resonator of this kind has the form of a spherical cavity that has a neck (a Helmholtz resonator) and is fastened by a small bar to the pipe wall. The radius of the spherical cavity and the length of the bar are assumed to be small compared to the wavelength of sound. In fact, this resonator is a combination of monopole and dipole resonators positioned at the same point. The monopole and dipole scattered fields produced by the resonator are orthogonal. The cited publication shows that, at a certain friction (when the friction resistance is equal to the radiation resistance), a single monopole–dipole resonator completely absorbs resonance-frequency sound in a narrow pipe. Note that, at the optimal friction, a single monopole resonator (a fixed Helmholtz resonator [2, 3]) and a single dipole resonator (a rigid sphere fastened by a small bar to the pipe wall [4]) absorb no more than half the energy of the incident wave.

It is of interest to study the problem of sound absorption by monopole–dipole resonators in a wide pipe (a multimode waveguide). Below, it is shown that, using such resonators, it is possible to completely absorb the zero-order mode in a multimode waveguide. The number of resonators required for this purpose can be minimized by choosing their optimal positions in the waveguide cross section. These conclusions are made on the basis of solving an auxiliary problem on the scattering of a plane sound wave from an unbounded array of monopole–dipole resonators with friction. Let the array lie in the plane $z = 0$ and the scatterers (Helmholtz resonators mounted on small bars) be positioned at the points with the coordinates $x = qL$, $y = sl$, where L and l are the array periods along the x and y axes, respectively; the periods satisfy the conditions $L < \lambda$ and $l < \lambda$, where λ is the sound wavelength; and q and s are arbitrary integers. Let a plane harmonic wave with a pressure $p_0(z) = \exp(ikz)$, where k is the wave number (the time factor $\exp(-i\omega t)$ is omitted) be incident on the array from the half-space $z < 0$. Under the effect of this wave, the scatterers perform volume oscillations and vibrations and produce monopole (p_1) and dipole (p_2) scattered fields. The monopole and dipole fields of the array are determined by the formulas [5]

$$p_1(x, y, z) = \frac{\rho c V}{2Ll}\left\{\exp(ik|z|)\right.$$
$$\left. - i\sum_{m,n}\frac{k}{\alpha_z^{mn}}\exp[i(k_x^m x + k_y^n y) - \alpha_z^{mn}|z|]\right\}, \quad (1)$$

$$p_2(x, y, z) = -\mathrm{sgn}z\frac{ik\rho c M}{2Ll}\left\{\exp(ik|z|)\right.$$
$$\left. + \sum_{m,n}\exp[i(k_x^m x + k_y^n y) - \alpha_z^{mn}|z|]\right\}, \quad (2)$$

where $k_x^m = m2\pi/L$, $k_y^n = n2\pi/l$, $\alpha_z^{mn} = \sqrt{(k_x^m)^2 + (k_y^n)^2 - k^2}$, V is the volume velocity of a monopole (a Helmholtz resonator), M is the dipole moment of a vibrating sphere, the dipole axis coincides with the z axis, ρ and c are the density of the medium and the sound velocity in it, $\mathrm{sgn}z = +1$ for $z > 0$, $\mathrm{sgn}z = -1$ for $z < 0$, and the summation is performed over all integral values of m and n except for $m = n = 0$. If the array periods are smaller than the sound wavelength, the scattered fields p_1 and p_2 consist of a single homogeneous plane wave and an infinite number of inhomogeneous plane waves. The total field is equal to $p = p_0 + p_1 + p_2$.

The volume velocity of a monopole and the dipole moment of a sphere can be obtained from the equations of motion (volume oscillations and vibrations) of the resonator positioned at the origin of coordinates (all resonators are in phase). The equation of forced volume oscillations has the form

$$m_1\ddot{\xi}_1 + r_1\dot{\xi}_1 + \kappa_1\xi_1 = [f_0 + f_1 + f_2]\exp(-i\omega t), \quad (3)$$

where m_1 is the air mass in the resonator neck; $\xi_1(t)$ is the displacement of this mass; κ_1 is the coefficient of

1063-7710/05/5103-0362$26.00

elasticity; and f_0, f_1, and f_2 are the complex amplitudes of the resultant forces that arise due to the effect produced on the resonator neck by the sound fields p_0, p_1, and p_2, respectively. For a small (compared to the sound wavelength) resonator, these force amplitudes are expressed as

$$f_0 = -\sigma_1 p_0(0) = -\sigma_1,$$

$$f_1 = -\sigma_1 \frac{\rho c V}{2Ll}\left\{1 - i\sum_{m,n}\frac{k}{\alpha_z^{mn}}\exp(-\alpha_z^{mn}a)\right\}, \quad f_2 = 0,$$

where σ_1 is the cross-sectional area of the neck and a is the radius of the spherical cavity. The volume velocity of the monopole is $V = \sigma_1 v_1$, where $v_1 = \dot{\xi}_1(t)\exp(+i\omega t)$ is the complex amplitude of the particle velocity.

The equation describing the forced vibrations of a resonator mounted on a small bar under the effect of the sound field has the form

$$m_2\ddot{\xi}_2 + r_2\dot{\xi}_2 + \kappa_2\xi_2 = [F_0 + F_1 + F_2]\exp(-i\omega t), \quad (4)$$

where m_2 is the mass of the spherical cavity; $\xi_2(t)$ is the displacement of this mass; r_2 is the friction factor; κ_2 is the coefficient of elasticity; and F_0, F_1, and F_2 are the complex amplitudes of the resultant forces due to the effect produced on the rigid sphere by the sound fields p_0, p_1, and p_2, respectively [6]. For a small (compared to the sound wavelength) sphere, these amplitudes are approximately calculated as

$$F_0 = -i\frac{ka}{3}\sigma_1, \quad F_1 = 0,$$

$$F_2 = -ka\frac{\rho c\sigma_2^2}{12Ll}\left\{ka - i\left[1 + \sum_{m,n}\exp(-\alpha_z^{mn}a)\right]\right\}v_2,$$

where $\sigma_2 = 4\pi a^2$ is the surface area of the sphere and $v_2 = \dot{\xi}_2(t)\exp(i\omega t)$ is the complex amplitude of the particle velocity. The dipole moment of a vibrating sphere is $M = 4\pi a^3 v_2$.

From Eqs. (3) and (4), we obtain the complex amplitudes of particle velocities:

$v_1 = f_0/Z_1 = -\sigma_1/Z_1$, $v_2 = F_0/Z_2 = -i(ka/3)\sigma_2/Z_2$, where

$$Z_1 = \left\{(r_1 + R_1) + i\left[\frac{\kappa_1}{\omega} - \omega(m_1 + m_1')\right]\right\},$$

$$Z_2 = \left\{(r_2 + R_2) + \left[\frac{\kappa_2}{\omega} - \omega(m_2 + m_2')\right]\right\},$$

$R_1 = -\mathrm{Re}\dfrac{f_1}{v_1} = \dfrac{\rho c\sigma_1^2}{2Ll}$ is the monopole radiation resistance,

$m_1' = \dfrac{1}{\omega}\mathrm{Im}\dfrac{f_1}{v_1} = \dfrac{\rho c\sigma_1^2}{2Ll\omega}\sum_{m,n}\dfrac{k}{\alpha_z^{mn}}\exp(-\alpha_z^{mn}a)$ is the associated mass of the monopole,

$R_2 = -\mathrm{Re}\dfrac{F_2}{v_2} = (ka)^2\dfrac{\rho c\sigma_2^1}{12Ll}$ is the dipole radiation resistance, and

$m_2' = \dfrac{1}{\omega}\mathrm{Im}\dfrac{F_2}{v_2} = \dfrac{\rho c\sigma_2^2 ka}{12Ll\omega}\left[1 + \sum_{m,n}\exp(-\alpha_z^{mn}a)\right]$ is the associated mass of the dipole.

The total field is determined as

$$p = \exp(ikz) - \left[\frac{R_1}{Z_1} + \frac{R_2}{Z_2}\mathrm{sgn}z\right]\exp(ik|z|) + \sum_{m,n}\left[\frac{k}{\alpha_z^{mn}}\frac{R_1}{Z_1} - \frac{R_2}{Z_2}\mathrm{sgn}z\right]\exp[i(k_x^m x + k_y^n y) - \alpha_z^{mn}|z|]. \quad (5)$$

The monopole and dipole scattered fields produced by the resonator array are orthogonal. The eigenfrequencies of the resonators are $\omega_1 = \sqrt{\kappa_1/(m_1 + m_1')}$ and $\omega_2 = \sqrt{\kappa_2/(m_2 + m_2')}$ for volume oscillations and vibrations, respectively. Note that the acoustic coupling of two closely spaced Helmholtz resonators in a free medium was studied in [7].

Let us set $r_1 = R_1$, $r_2 = R_2$, and $\omega_1 = \omega_2$. This means that, for volume oscillations and vibrations, the friction resistance is equal to the radiation resistance and the eigenfrequencies ω_1 and ω_2 coincide. Then, we obtain $\left[\dfrac{R_1}{Z_1} + \dfrac{R_2}{Z_2}\mathrm{sgn}z\right] = \dfrac{1}{2}[1 + \mathrm{sgn}z]$ and the total field given by Eq. (5) contains no transmitted homogeneous wave behind the array and no reflected homogeneous wave before the array. Hence, the incident wave p_0 is completely absorbed by the array of monopole–dipole resonators. The total field before the array consists of the incident homogeneous wave and an infinite number of inhomogeneous waves, and the total field behind the array consists of inhomogeneous waves only.

The results obtained above suggest that sound absorption by monopole–dipole resonators in a multimode waveguide is possible. Indeed, total field (5) satisfies the relations

$\dfrac{\partial p}{\partial x} = 0$ at $x = \dfrac{L}{2}(1 + 2q)$ and $\dfrac{\partial p}{\partial y} = 0$ at $y = \dfrac{l}{2}(1 + 2s)$, where q and s are any integers. This means that formula (5) also describes the field in a waveguide with rigid walls determined by the equations $x = \dfrac{L}{2}(1 + 2q)$, $y = \dfrac{l}{2}(1 + 2s)$. The shapes of the cross sections of such waveguides are shown in the figure, with the resonator

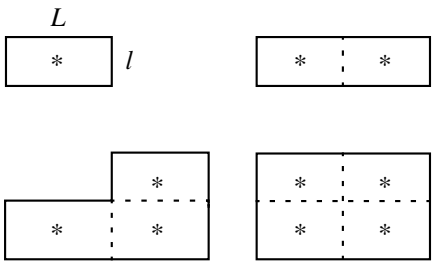

Shapes of the waveguide cross sections. The asterisks show the resonator positions.

positions represented by asterisks. Formula (5) describes the field in a waveguide with a cross section consisting of $(L \times l)$ rectangles that contain resonators at their centers. The values of L and l can be varied, but they must not exceed the wavelength of sound. The minimum number of resonators that is necessary to provide for the absorption of the zero-order mode in a multimode waveguide is equal to the minimum number of $(L \times l)$ rectangles in the cross section of this waveguide.

REFERENCES

1. A. D. Lapin, Akust. Zh. **49**, 855 (2003) [Acoust. Phys. **49**, 731 (2003)].
2. M. A. Isakovich, *General Acoustics* (Nauka, Moscow, 1973) [in Russian].
3. P. Morse and U. Ingard, *Theoretical Acoustics* (McGraw-Hill, New York, 1986).
4. N. G. Kanev and M. A. Mironov, Akust. Zh. **49**, 372 (2003) [Acoust. Phys. **49**, 312 (2003)].
5. A. D. Lapin and M. A. Mironov, in *Proceedings of XI Session of the Russian Acoustical Society* (GEOS, Moscow, 2001), Vol. 1, p. 192.
6. S. N. Rzhevkin, *Course of Lectures on the Theory of Sound* (Mosk. Gos. Univ., Moscow, 1960) [in Russian].
7. T. Johansson and M. Kleiner, J. Acoust. Soc. Am. **110**, 1315 (2001).

Translated by E. Golyamina

Acoustical Physics, Vol. 51, No. 3, 2005, pp. 365–366. Translated from Akusticheskiĭ Zhurnal, Vol. 51, No. 3, 2005, pp. 431–432.

CHRONICLE

In Memory of Ivan Vladimirovich Anisimkin (July 16, 1976–December 9, 2003)

On December 9, 2003, Ivan Vladimirovich Anisimkin, an outstanding young scientist from the Institute of Radio Engineering and Electronics of the Russian Academy of Sciences, was killed in a terrorist attack.

Today, we live in a troubled time, when one often hears about explosions, holding of hostages, or killings of innocent people. Many of us think that these crimes are committed somewhere far away and that the probability of becoming a victim of such an attack is very small.

However, our young colleague and one of our most promising young scientists, Ivan Anisimkin, accidentally found himself at the epicenter of an explosion detonated by a terrorist. On that day, Anisimkin, as usual, walked towards his institute, which was situated in the central part of Moscow, near the National Hotel. It was there, next to the State Duma building, that the fatal explosion took place.

Ivan Anisimkin was born on July 16, 1976, in Ramenskoe, Moscow region. In 1999, he graduated from the Moscow Institute of Physics and Technology and started working at the Institute of Radio Engineering and Electronics, Russian Academy of Sciences, where he simultaneously took post-graduate courses. In 2002, Anisimkin received the degree of Candidate of Science for his brilliant work "Influence of Sorption and Thermal Processes on the Acoustic Wave Propagation in Solid-State Structures."

As early as his student years, Anisimkin showed outstanding abilities in research and published three papers devoted to the study of heat transfer in subsonic gas flows. In total, Anisimkin published 26 scientific papers, which have made important contributions to condensed-matter physics, physical acoustics, environmental monitoring, analytical chemistry, biology, and a number of interdisciplinary sciences. He put forward ideas that have opened up new possibilities for obtaining important information on the environment and on the processes that occur on the surfaces of solids. He developed new experimental techniques for studying adsorption and desorption in gaseous media. He constructed high-sensitivity detectors and sensor arrays for electronic systems that identify gaseous and liquid substances. He studied the sensitivity of normal plate modes to external actions and revealed a much greater difference in the responses of these than had been known before.

The striking features shown by Anisimkin in his work were his thoroughness and persistence in achieving his aim. In studying acoustic vibrations in piezoelectric crystals, which had already been much studied before, Anisimkin discovered a new type of acoustic waves: quasi-longitudinal normal modes. They represent a new, tenth, type of acoustic vibrations that may exist in a solid in the form of an exact solution to the boundary-value problem. This result, which proved to

1063-7710/05/5103-0365$26.00

be the last one obtained by Anisimkin, is of fundamental significance for physical acoustics and will undoubtably be included in future textbooks devoted to this area of research.

Despite his youth, Anisimkin was well known among Russian and foreign scientists. He gave some brilliant talks at Russian and international conferences. He received a number of Russian and international research grants and was a laureate of the National Science Support Foundation for "Outstanding Scientists, Young Doctors and Candidates of Science." The news that he was the winner of a grant from the President of the Russian Federation arrived after his death.

Being 27 years old, Anisimkin undoubtedly belonged to the group of those gifted and active people who form the elite of the nation and determine its progress. He did not have enough time to make his main discoveries, but the contributions to science that he had already made during his short and brilliant life will serve as the basis for new lines of research.

Anisimkin was a well-rounded, educated person: he knew four foreign languages, loved music, and read much about the history and culture of Russia, Italy, Greece, India, China, and the Near East. Friends and colleagues of Anisimkin appreciated his personal qualities: his charm, even temper, respectful manners, honesty, tact, and his wide scope of interests—all the features that have always been associated with a Russian intellectual and with the best representatives of Russian science. Everyone around him was glad to see his scientific achievements, his active interest in life, his good prospects, and his youth.

This terrorist attack has ruthlessly cut down the life of Ivan Anisimkin on its launching pad: it did not allow him to fulfil his plans, to have a family of his own, and to experience many other beautiful things that occur in a human life. The shining memory of this wonderful person and outstanding scientist will forever remain in our hearts.

Translated by E. Golyamina